Effect of Damage, Temperature, and Helium on Irradiated Nanoprecipitation Stability and Helium Sequestration Ability in an Advanced Ferritic/Martensitic Fe-9Cr Steel

by

Theresa Mary Kelsy Green

A dissertation submitted in partial fulfillment
of the requirements for the degree of
Doctor of Philosophy
(Nuclear Engineering and Radiological Sciences)
in the University of Michigan
2023

Doctoral Committee:

Professor Todd Allen, Co-Chair
Professor Kevin Field, Co-Chair
Professor Adrien Couet
Professor Yue Fan
Research Scientist Kai Sun

Theresa Mary Kelsy Green

tmkgreen@umich.edu

ORCID iD: 0000-0002-8259-6674

Dedication

To the passionate teachers and professors who, through their dedication as educators, instilled a sense of scientific curiosity in me.

To society writ large, I only did this work in the hopes that in some small way I might positively contribute to the continued efforts of the progression of the human endeavor.

Lastly, to my hard work and perseverance, as cultivated by my family, my mentors, and the academic institutions I've had the honor to attend.

Acknowledgements

I would first like to thank my advisors, Professor Todd Allen and Professor Kevin Field. Professor Allen, I will forever be grateful for you providing me with the opportunity of a lifetime to study at two of the world's most premier universities. I also thank you for your support not only in the development of my technical skills but also in my professional development skills. I was able to attend programs and conferences many students would never dream of being able to attend. Importantly, your advice on scientific writing has always stuck with me and it has helped me immensely in my dissertation. Professor Field, it was an honor to be one of your first graduate students. It has been rewarding and instructive to see how you've grown the research group and all that the group has accomplished since the very beginning. I have learned so much from your mentorship – and not just how to make a good presentation or write a good research proposal. You've also taught me how to respond constructively to my failures, how to ask probing questions, and how to critically think about my work. To both Professor Allen and Professor Field, I am deeply grateful for your scientific insights and professional guidance. You have helped me develop a dedication to scientific integrity that I will always carry with me.

I would also like to thank my committee members, Professor Adrien Couet, Dr. Kai Sun, and Professor Yue Fan, for their input and guidance as well. In addition, I would like to thank my collaborators at Oak Ridge National Laboratory, Dr. Lizhen Tan, Dr. Ying Yang, Dr. Tim Graening, and Dr. Weicheng Zhong, for their important contributions. Dr. Ying Yang kindly shared the Thermo-Calc data needed to perform this work and offered many insights in

conversations. This work would also not have been possible without the years of work and effort from Dr. Lizhen Tan.

I would like to sincerely thank past and present graduate students and postdoctoral researchers from my research group and others, Dr. Stephen Taller, Dr. David Woodley, Dr. Priyam Patki, Dr. Charles Hirst, Gabriella Bruno, Mackenzie Warwick, Hangyu Li, Robert Renfrow, Matthew Lynch, Timothy Defranco, Ethan Polselli, Wyatt Peterson, Logan Clowers, and Valentin Pauly. Thank you all for your scientific discussions, help in the laboratory, revisions to my presentations, and general support. There are countless others from before my time at Michigan that laid the groundwork for successful experiments, especially in the Michigan Ion Beam Laboratory, who I could not have accomplished this work without.

Thank you to the past and present staff members at the Michigan Ion Beam Laboratory, Dr. Gary Was, Dr. Kevin Field, Dr. Ovidiu Toader, Thomas Kubley, Robert Hensley, Dr. Fabian Naab, Dr. Kai Sun, Prashant Niraula, Alex Flick, and Dr. Zhije (George) Jiao. I could not have completed my ion irradiation experiments without your expert help and guidance, and I am truly grateful. I want to thank the staff in the Nuclear Engineering and Radiological Sciences department, Cherilyn Davis, Garnette Roberts, Besnik Topulli, and Rebecca Duguay. I also want to thank the staff at the Michigan Center for Materials Characterization for training me on and supporting my work on FIB, SEM, and S/TEM, Bobby Kerns, Dr. Allen Hunter, Dr. Tao Ma, Dr. Haiping Sun, Deanna Hecht, and Dr. Kai Sun. Kai, you get a special shout out for patiently teaching me so many microscope techniques and answering countless questions I've had over the years. Thank you immensely for sharing your vast S/TEM knowledge with me. Thank you to the Fusion Energy Sciences program for providing the main source of funding for this work (DOE-FOA-0002173). Thank you to the Nuclear Regulatory Commission for supporting me with a

Graduate Fellowship in 2017-2018. Research presented in this thesis was also partially supported by the Laboratory Directed Research and Development program of Los Alamos National Laboratory under project number XXPV under the mentorships of Dr. Benjamin Eftink and Dr. Aaron Kohnert.

I would also like to thank my family from the bottom of my heart. You have consistently been there for me my entire life in more ways than I can list and I could not have accomplished this without you all. Mom, thank you for encouraging me to go to college since the time I was little. No other kid in our community went to college, and I am forever grateful for you for teaching me to not only dream big, but to stick to following through with those dreams no matter how hard it might be. You always knew how to challenge me to be better while also supporting me through the process. Dad, thank you for being the only one in the family to ever ask me about my research and to try to understand what I do! You truly taught me the value and meaning of hard work, no matter the circumstances. I have tried to emulate that in my own career. Thank you for being a role model to me in honesty and in doing the right thing. To my sisters, Heather and Jessica, thank you for your constant love and support. You have both been role models to me (in what to do and what not to do!) and offered me guidance like only sisters can. To my sweet nieces, Avary, Andie, and Mary, I hope that I serve as the role model to you three that I never had myself. I love you three with my whole heart.

Beni, you were my rock in the hard times, my voice of reason when I was unsure, my motivation when I lacked the will. Thank you, I couldn't have done it without you.

Lastly, to my dog, Orpheus. I got you when I first started graduate school and you have made every day a good day. I could not have asked for a better pup, or a better running buddy.

Table of Contents

List of Tables

List of Figures

List of Appendices

Abstract

Fusion first-wall and blanket materials need to withstand the synergistic effects of atomic displacements, transmutation products such as helium, and elevated temperatures. Particularly, helium can have significant effects on the microstructural evolution of materials under irradiation, including increased cavity swelling, changes in solute segregation, altered secondary phase evolution, and/or altered point defect transport [1–6]. Methods for mitigating helium effects, which can in turn improve swelling resistance, include the introduction of microstructural sinks to disperse and sequester helium homogeneously. This delays the localized accumulation of helium to a single or few sites within the microstructure, such as in each cavity, and lengthens the onset to steady-state swelling. One such microstructural sink is secondary phases and precipitates [7]. Previous studies have shown the interfaces of Ti-rich MX precipitates in Ti-modified 316 austenitic stainless steel were able to sequester most or all of helium generated during neutron irradiation and extend the onset of steady-state swelling [3]. In addition, helium has also been shown to bind to solute atoms [5]. Hence, helium is predicted to have strong interactions with solutes and precipitate-matrix interfaces and to have significant consequences for the swelling behavior of steels.

However, there exists no conclusive experimental evidence in literature that semi-coherent nanoprecipitates in current fusion candidate materials will act as sites for helium sequestration. The objective of this work centers on filling the knowledge gap on the evolution of such precipitates and their interfaces under simultaneous atomic displacements and helium

transmutation. This research aims to understand the co-evolution of helium and MX-TiC semi-coherent precipitates using dual-beam ion irradiations on a reduced activation ferritic/martensitic (RAFM) Fe-9Cr alloy that is a candidate fusion first-wall and blanket material. This work examines the precipitate behavior under ion irradiation without helium and then with helium to assess the helium effects on precipitate stability as well as on the precipitate interface.

This work found that co-injected helium suppressed the radiation-assisted coarsening response of precipitates. This is hypothesized to occur due to helium atoms binding to solutes in the matrix and rendering those helium-solute clusters immobile. MX-TiC precipitates were also found to sequester helium atoms in the form of nano-scale bubbles on the precipitate-matrix interface as a function of temperature prior to precipitate dissolution. Such helium sequestration is desired for greater swelling resistance, but it was found that the MX-TiC precipitates were not present at high enough densities or stable to high enough damage levels to affect the onset of steady-state swelling or the steady-state swelling rate, as compared with prior generations of RAFM steels.

This work provides insights into the single and combined effects of damage rate, damage, temperature, and helium co-injection on the stability of nanoprecipitates and their effect on swelling resistance in an advanced RAFM Fe-9Cr steel alloy. The consequences of this research are to assess the current state of advanced fusion structural materials and to inform future alloy designers on the relationship of precipitation and swelling. This work will pave a roadmap for understanding the irradiation stability and function of secondary phases that have been specifically designed to provide radiation resistance during fusion operation.

Chapter 1 Introduction

Nuclear energy has held the promise of being a reliable, near-inexhaustible energy source since its initial entrance into the commercial power sector in the 1950s. The fulfillment of this promise is needed especially now, as a growing world population demands low-carbon, sustainable, 24/7 energy production. Though great strides have been made in light-water and advanced non-light-water nuclear fission energy technologies, fusion energy remains the gold standard to be achieved. Fusion energy does not require the mining of uranium, emits no carbon during operation, cannot melt down, has reduced radioactive waste, and has the greatest theoretical capacity for power output achievable from any energy source [8]. However, just as with fission technology, designing and manufacturing structural materials that can operate optimally in the harsh environment of a fusion reactor core for long life spans has eluded scientists thus far. As such, it is of extreme importance to dedicate resources to the research of designing and manufacturing the next generation of structural materials for fusion energy reactors. In particular, this work focuses on the materials needs of a first of a kind (FOAK) fusion reactor such as the International Thermonuclear Experimental Reactor (ITER) Tokamak fusion reactor.

As no fusion reactors with the relevant neutron flux and temperature are in operation today, it is necessary to build from the historical legacy of fission neutron and ion irradiation data of structural materials and combine this knowledge with the design specifications of materials for fusion reactors. Austenitic steels have been used as structural materials in light water reactors, but these materials have unacceptable irradiation creep and void swelling for non-light-water fission reactor applications. Materials in fast fission reactors need to withstand the synergistic effects of

atomic displacements, elevated temperatures, irradiation creep, and void swelling from helium transmutation. As such, ferritic/martensitic (FM) steels are the leading candidate structural materials for fast fission reactors. FM steels have a body-centered cubic (BCC) structure and typically contain 7-15 weight % Cr with 1-3 weight % alloying solutes. The remaining composition is Fe. FM steels have a complex, hierarchical structure consisting of prior austenite grains, sub-grains, martensitic laths, secondary phases, and a high dislocation density. Beneficial secondary phases induced by heat treatment(s) include MX (M=metal, X=C and/or N) precipitates. The complexity of FM materials is theorized to provide greater radiation resistance than austenitic steels [9]. The higher expected radiation resistance of FM steels, as determined by steady-state swelling and mechanical properties under irradiation, and the similarities between the end-of-life dose between fission and fusion reactors means FM steels are also being adopted as primary candidates for structural materials in fusion energy applications.

FM steels in fusion reactors need to withstand the environmental stressors listed for advanced fission reactors, but they must also withstand an increased level of helium transmutation (~10-20 appm He/dpa) due to the unique neutron spectrum in fusion reactors. The effects from helium-induced degradation can be lifetime-limiting for materials, including void swelling, helium embrittlement at grain boundaries, and alteration of phase stabilities. This work focuses on the effects of helium on swelling and how to mitigate swelling during fusion operation. Methods for improving swelling resistance include the introduction of microstructural sinks to sequester helium in a homogeneous fashion, thereby delaying the rate of helium accumulation in each cavity and lengthening the onset of swelling [10–12]. Precipitates, such as MX precipitates in FM steels, are one such microstructural sink to sequester helium. MX precipitates have also been shown to improve creep strength [13]. While MX precipitates have been studied in detail in austenitic steels,

particularly MX-TiC precipitates, the stability of MX precipitates and their helium sequestration ability has not been systematically documented in FM steels under fusion-relevant irradiation conditions. In addition, the ability of these precipitates to sequester helium and prevent matrix void swelling has also not been conclusively proven in FM steels across all possible irradiation environments for a fusion reactor. This work is the first to provide a systematic roadmap of MX precipitate stability and helium sequestration ability in FM steels.

This research aims to understand the co-evolution of helium and MX-TiC precipitates under ion irradiation in an advanced engineering Fe-9Cr alloy that is an analogue for a more complex candidate fusion structural material. This work will look at the precipitate behavior under ion irradiation with and without helium co-injection to assess helium effects on precipitate stability. A combination of ion irradiation experiments, with careful post-irradiation characterization techniques coupled with computational models were used to achieve this objective. Chapter 2 provides a background on FM alloys and the effects of irradiation on their microstructures, with a focus on the development of advanced FM steels in the United States and current knowledge on precipitation and helium evolution. Chapter 3 summarizes the objective of the thesis and the approach taken to achieve the objective. Chapter 4 describes the experimental procedures and techniques used for ion and electron irradiation experiments and post-irradiation characterization. Chapter 5 summarizes the results gathered from the experiments. Chapter 6 offers an interpretation and discussion of the experimental results and address the objective. Chapter 7 provides the conclusions drawn from the thesis and suggests future work.

Chapter 2 Background

This chapter will provide the background necessary to understand the outcomes of this work and place them in the context of existing literature. A general overview of FM steels and FeCr alloys will be provided followed by a comprehensive review of the existing experimental and theoretical work regarding MX precipitate evolution and helium effects on the microstructural evolution of Fe-based alloys under neutron and ion irradiation. Various factors affecting MX precipitate evolution under irradiation as well as thermal stability will be considered.

2.1 Fusion Environment

The fusion environment represents one of the most extreme man-made devices for materials to operate in (Table 2.1) [14]. In a tokamak type fusion reactor, the deuterium-tritium (D-T) plasma at the core of the reactor has the following reaction:

$$^{2}H + {}^{3}H \rightarrow {}^{3}He\ (3.5\ MeV) + n\ (14.1\ MeV) \qquad \text{Eq. 2.1}$$

The products of this reaction interact with the surrounding first wall and blanket structures (Figure 2.1). These structures support heat extraction for energy production and tritium breeding for continued operation. Current candidate materials for plasma-facing components of the first wall structure include beryllium and tungsten [15]. Materials for the underlying structure that support the plasma-facing components and for the blanket structure need to be able to withstand high temperatures, high neutron fluxes causing radiation damage, degradation from transmutation products, creep, and fatigue cycling. Several structural alloys have been considered for these

components such as austenitic alloys, Ni-based alloys, and ferritic/martensitic (FM) steels [16]. Due to studies on mechanical property evolution and neutron flux activation concerns, the development of reduced activation FM (RAFM) steels began in the 1980s and continue today.

Open questions on the role of atomic displacements and helium transmutation on RAFM steel performance remain. This work addresses the combined effects of atomic displacements and helium transmutation in an advanced Fe-9Cr RAFM steel that is a candidate material for the underlying structure that support the plasma-facing components and for the blanket structure. The manufacturing and development of such steels for fusion applications will now be discussed.

Table 2.1 Environmental design considerations for FM steels as first wall and blanket structures in a tokamak fusion reactor [14,16].

System	Temperature (°C)	Neutron Flux ($m^{-2}s^{-1}$) (E>0.1 MeV)	Heat Flux (MW/m^2)	Transmutation Products
First Wall	300-600	3×10^{17}	~1-5	^2H, ^3H, ^4He
Blanket Structure	300-600	2×10^{17}	~0.1	^2H, ^3H, ^4He

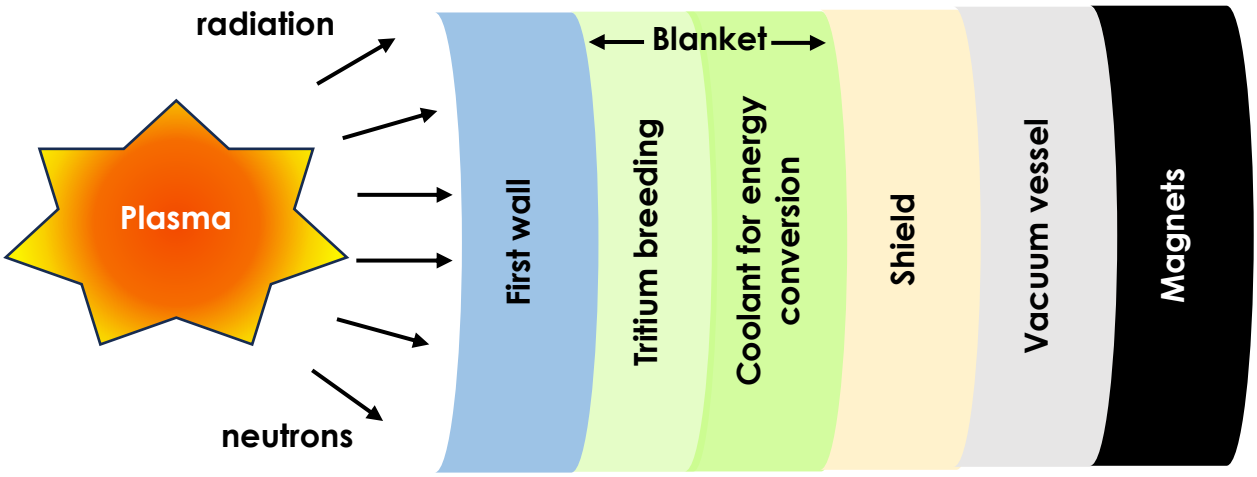

Figure 2.1 Schematic of the materials in a tokamak fusion reactor. Adapted from [17].

2.2 Overview of FM Steels

2.2.1 General Metallurgy of FM Steels

FM steels have better thermal conductivity, lower thermal expansion ratio, and superior swelling resistance than austenitic steels [16]. FM steels are commonly produced using traditional ingot metallurgy and forging processes. They are preferred to be used in the normalized and tempered condition as this condition provides good strength, ductility, and toughness [18]. Normalization consists of annealing above the austenitizing temperature (AC_1), which is the equilibrium temperature where ferrite with a body centered cubic structure (BCC) transforms to austenite with a face centered cubic structure (FCC). Normalization is often followed by air cooling. Typically for 9-12 weight % Cr FM steels, the AC_1 is between 950^o-1150^{o}C. Normalization temperature and time primarily dictates the final prior austenite grain size and precipitate kinetics.

Upon cooling from the austenitizing temperature, the austenite should fully transform into martensite. Martensite is formed from austenite by quenching from a temperature above the AC_1 temperature. It is a diffusion-less process. As such, transformations that require diffusion, such as austenite to ferrite, are suppressed. The martensite transformation involves the martensite start temperature (M_s) and the martensite finish temperature (M_f), which are dependent on the carbon content in the alloy. The M_s temperature is highly dependent on the C and N content of the steel [19]. After the transformation to as-quenched martensite is complete, the C and N contents will be interstitials in solid solution and they provide the main contribution to the hardness of the material at this point [19].

After normalization and air cooling, the tempering process takes place to increase toughness and ductility. The tempered microstructure and the precipitate sequence that take place

during tempering determine the pre-irradiation microstructure and the corresponding strength of the material [3]. Tempering will remove interstitials like C and N by forming various complex carbide, nitride, and carbonitride compounds and precipitates. The removal of the C and N also reduces lattice strain thus decreasing hardness. Tempering typically takes place around 700-750°C to provide the optimal properties. For instance, Vitek *et al*. found that a temperature range of 700-780°C is necessary to complete the precipitation process during tempering for 1 hour in a 9Cr-1Mo-V-Nb alloy [20]. Alamo *et al*. found that tempering above 700°C in RAFM steels resulted in optimal impact properties [21]. The resulting microstructure, if tempered around ~750ºC, consists of a body centered cubic lattice with a fully tempered martensite microstructure. $M_{23}C_6$ precipitates (60–200 nm) and smaller MX precipitates (20–80 nm) are located on and within lath and prior austenite grain boundaries [22]. Tempering also reduces the high number density of dislocations present in the normalized condition [23]. Normalized and tempered specimens typically contain a dislocation density in the range of $10^{13\text{-}14}$ m^{-2} [18,24]. The general microstructure of an FM steel is shown in Figure 2.2.

The effects of heat treatment on microstructure and mechanical properties of FeCr steels have been well documented [7,9,10]. Parameters that affect the final material properties include composition, time at temperature, and cooling rates. Alloying elements have significant effects on the phase transformation temperatures. Figure 2.3 shows the AC_1 (A_s) and AC_3 (A_f) transformation temperatures for ferrite/martensite into austenite for seven RAFM steels. W and Cr were found to have significant effects on the austenite transformation temperatures. Continuous Cooling Temperature (CCT) and Time-Temperature-Transformation (TTT) diagrams are shown for the same alloys in Figure 2.4 and Figure 2.5. Such diagrams are useful in determining optimal heat treatment schedules given specific compositions of alloys. Care should also be taken to consider

the geometry of the material being heat treated, as the heating and cooling rates can be quite different from the various points in a large geometry material, such as in an ingot of a commercially fabricated steel alloy.

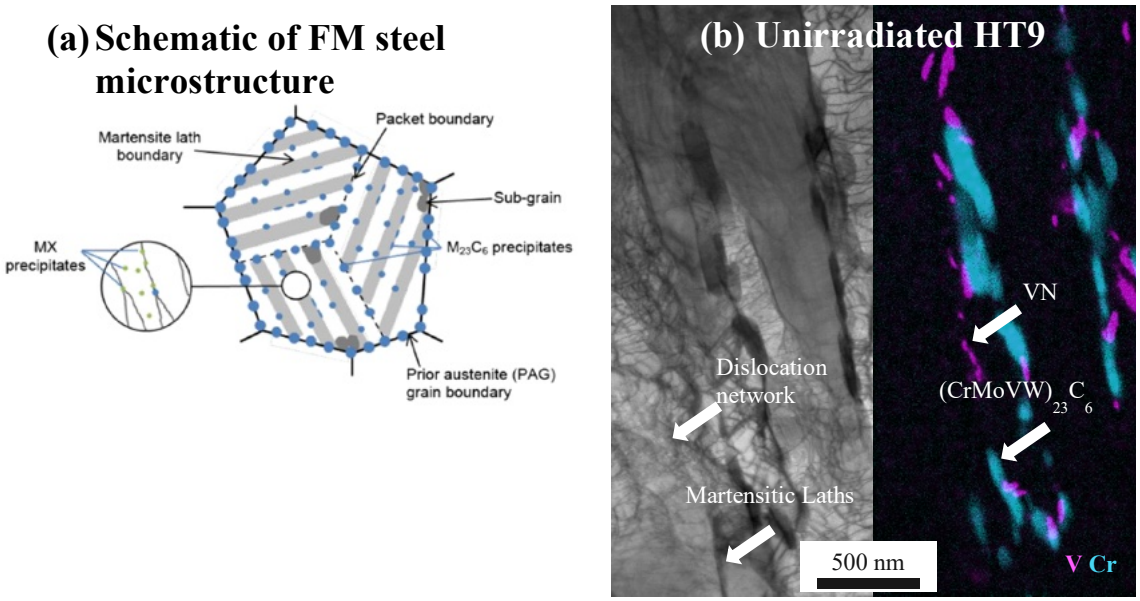

Figure 2.2 Microstructure of normalized and tempered FM steel taken from [97]. (b) Example electron microscope micrograph and corresponding composition map of a traditional Fe12Cr FM steel called HT9 (unpublished data from Green, Li, Allen).

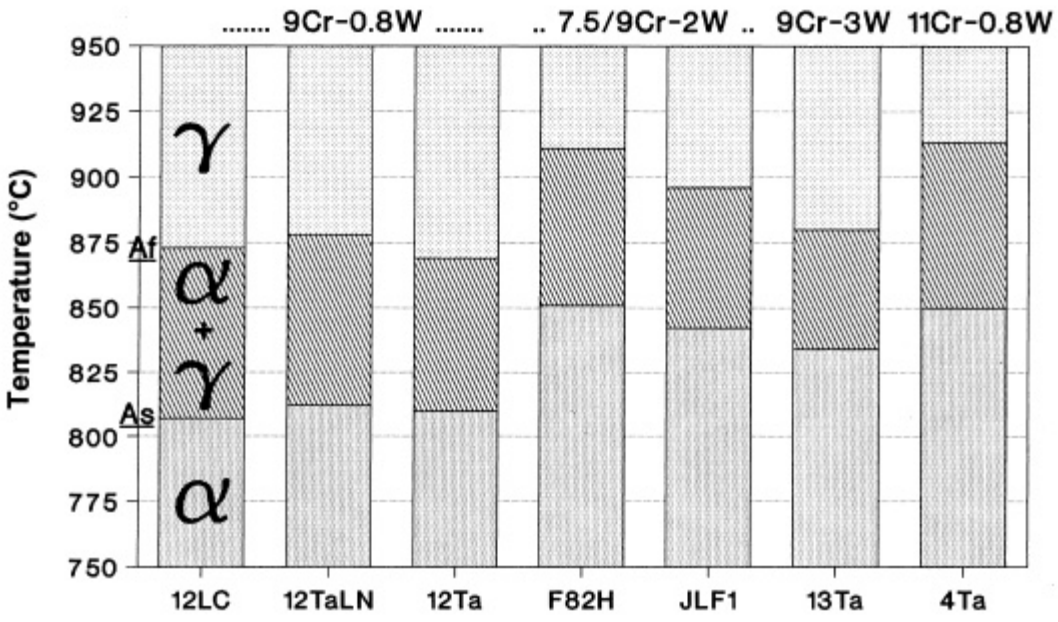

Figure 2.3 Austenite start (A_s, AC_1) and finish (A_f, AC_3) temperatures for various RAFM steels [21].

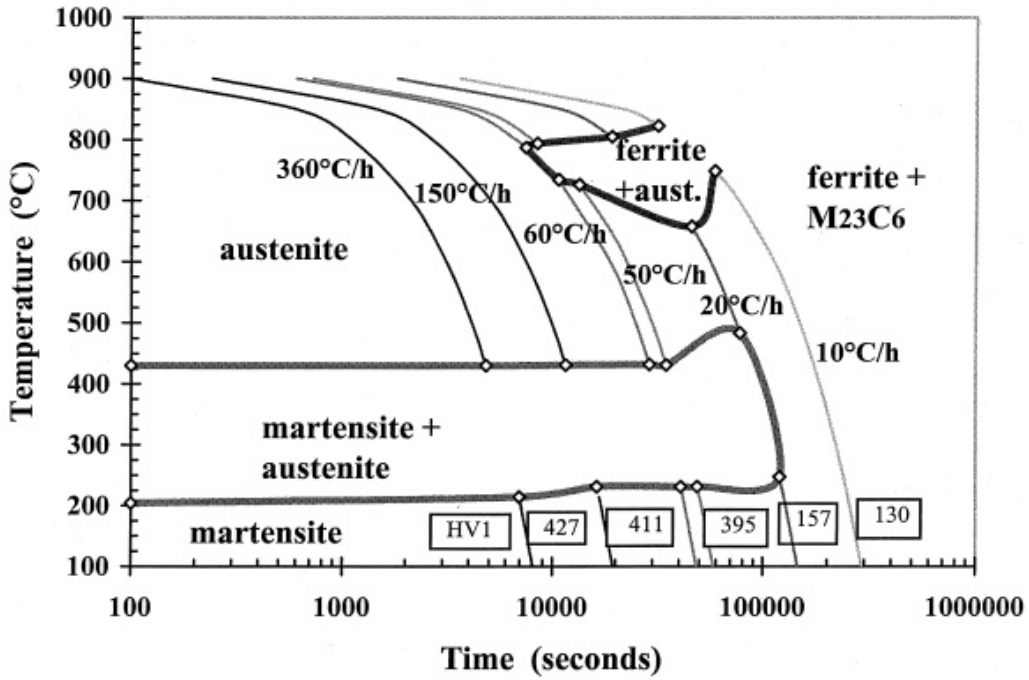

Figure 2.4 CCT diagram of F82H steel after austenitization for 30 minutes at 1050°C [21].

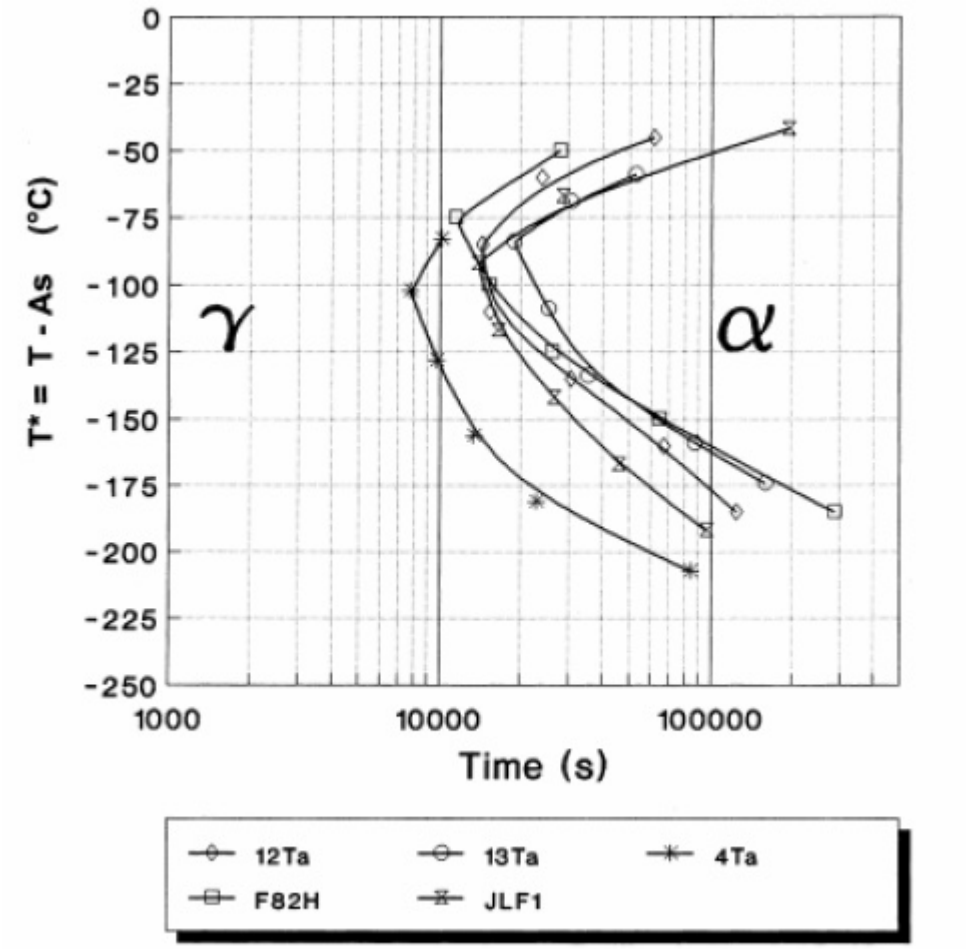

Figure 2.5 TTT diagrams for several steels. T* represents the shift of the temperature of isothermal transformation from starting temperature [21].

2.2.2 Development of Advanced FM Steels – Reduced Activation FM Steels and Castable Nanostructured Alloys

Traditional FM steels with 7-15 weight % Cr, such as Grade 91 and HT9, have been studied for decades. In the 1980s, research began on developing reduced activation FM steels (RAFM) to achieve superior mechanical properties and reduced radioactivity during operation for fusion applications over traditional FM steels [16]. As such, computational thermodynamics to tailor the composition of RAFM steels and optimized thermomechanical treatments (TMT) to improve properties were utilized [12]. For instance, Mo was replaced with W and Nb with Ta to meet the

activation limits of shallow land burials for radioactive waste. The most promising compositions of RAFM steels included 7-9 weight % Cr, including the steels known as (F82H Fe–8Cr–2W–0.2V–0.04Ta) and EUROFER97 (Fe–9Cr–1W–0.2V–0.12Ta), due to this Cr content range minimizing the radiation-induced ductile-brittle transition temperature (DBTT) while preserving beneficial corrosion resistance [16,27]. These steels also draw from the literature of fossil energy and other advanced steel research programs [13,28–30]. The performance of these steels is benchmarked by comparing their properties, such as tensile, creep, and Charpy impact properties, to those of Grade 91(Fe–9Cr–1Mo–V–Nb) and similar FM steels.

The properties of RAFM steels are derived from their high dislocation density, fine martensite lath structure, and high number density of precipitates – effectively, identical key features to FM steels. Precipitates include $M_{23}C_6$ and MX precipitates on and within grain boundaries. The MX precipitate populations will vary based on steel composition and heat treatment. Particularly, computational thermodynamics and TMT, such as hot working, have been used to increase the density of desirable MX precipitates. The MX precipitates are typically either (V,Ta)N (*i.e.*, MN) or TaC (*i.e.*, MC) [31]. However, while F82H and EUROFER97 have achieved comparable yield stresses to Grade 91, they still suffer from poor high temperature creep resistance as compared to Grade 91 [16,27]. This is partially due to the presence of $M_{23}C_6$ carbides, which do not effectively pin the grain boundaries during creep due to their ease of coarsening above 550°C [32]. MX precipitates have been shown to pin grain boundaries effectively in thermal conditions, but they are not present in high enough densities in F82H or EUROFER97 to provide the necessary level of creep strength at high temperature (>500°C) [33]. Hence, a greater density of fine, stable MX precipitates is desired to provide improved creep strength.

Precipitates are also used to increase radiation resistance. Precipitate-matrix interfaces can serve as trapping sites for point defects, thereby decreasing the overall point defect concentration during irradiation and limiting the negative effects of irradiation. Such interfaces are called sinks. Microstructural features that can efficiently accommodate a high flux of point defects by trapping and/or annihilating them during irradiation are considered to have a high sink strength. MX precipitates in RAFM steels are therefore desired to provide both creep and sink strengthening attributes [12]. Oxide dispersion strengthened (ODS) RAFM steels have also been investigated to provide elevated creep resistance and sink strength [12]. However, the typical manufacturing process of ODS alloys, which includes ball milling and extrusion, is expensive and results in anisotropic mechanical properties and low toughness.

Thus, an effort spearheaded by Oak Ridge National Laboratory aimed to increase the MX precipitation in RAFM steels through computational thermodynamics and traditional manufacturing methods with TMT. This new family of steels was called Castable Nanostructured Alloys (CNAs) and they use traditional TMT methods to achieve the desired microstructural features [27,34]. CNAs are designed to have a volume fraction of MX precipitates of ~0.5 vol%, which is lower than the oxide clusters in ODS steels ($\gtrsim$0.7 vol%) but greater than the MX phase fraction in traditional RAFM steels (<0.2 vol%) and in Grade 91 (~0.4%). CNAs are also designed to have a reduced fraction of $M_{23}C_6$ carbides [27]. CNAs have been developed over the past 7 years with several different generations and heats studied. Here, the development strategy over these different generations is presented in detail.

Two methods for increasing the amount of MX nanoprecipitates in CNAs over traditional RAFM steels were considered for the first set of CNAs (CNA1, CNA2, and CNA3): 1) increasing V, Ta, and N content to promote the formation of (V,Ta)N and 2) adding Ti and restricting N to

promote formation of (Ti,Ta)C [27]. Nitride-strengthened CNA1 contained (V,Ta)N while carbide-strengthened CNA2 and CNA3 contained (Ti,Ta)C. A reduction in $M_{23}C_6$ precipitates is expected in CNA2/3 as compared to CNA1 due to C being consumed by the MC precipitates prior to the later phase formation of $M_{23}C_6$ precipitates [31]. In addition, the N content in CNA1 was expected to result in the formation of the detrimental Laves and Z phases during operation. CNA1-3 were normalized at 1150°C and tempered at 750°C for 1 hour and fabricated in laboratory-scale heats. CNA1-3 underwent tensile tests in air from room temperature up to 800°C, creep tests at 600 and 650°C, and Charpy impact tests. The tests helped determine which MX precipitate type, nitride or carbide, provided better mechanical properties. CNA1-CNA3 displayed a yield strength 100-300 MPa higher than traditional RAFM and FM steels up to 800°C with a slight reduction in ductility. CNA2 had the greatest yield strength at all temperatures tested followed by CNA3 and then CNA1, but CNA1 had slightly greater ductility than CNA2 and CNA3. CNAs exhibited improved Charpy impact toughness as compared to Grade 91 and ODS RAFM steels. CNA3 had the highest upper shelf energy (USE) of the three CNAs tested, followed by CNA2 and CNA1. The CNAs also had improved creep resistance from preliminary tests at 600 and 650°C, particularly at higher stresses. The overall sink strength of the initial generations of CNA steels was one order of magnitude greater than previous RAFM steels mainly due to dislocations and MX precipitates. The results of the testing concluded that the MX carbides in CNA2 and CNA3 provided better mechanical properties than the MX nitrides in CNA1. It was also determined that the carbide-strengthened CNA3 tended to have better helium management capability than the carbonitride-strengthened CNA1 based on deuterium retention studies [35]. In addition, CNA3 demonstrated greater Charpy impact energies. Figure 2.6, Figure 2.7, and Figure 2.8 provide the mechanical property data of CNAs as compared to FM and RAFM steels.

Hence, three more generations of CNAs were then fabricated in laboratory-scale heats, CNA4-CNA6 [34] strengthened with MX carbides. TiC and TaC or complex (Ti,Ta)C precipitates were chosen over nitrides based on the previous work on CNA1-CNA3 and due to data on the stability of TaC, TiC, and VN precipitates under ion irradiation [36,37] (see Section 2.4.2). CNA4-6 were normalized at 1150°C and tempered at 750°C for 1 hour. The six generations of CNAs exhibited comparable yield and tensile strength to one another, which was ~200-300 MPa greater than Grade 91 and EUROFER97. The CNAs also had creep resistance comparable to ODS-EUROFER97. The impact toughness of the CNAs was also improved, with USE values ~2.5 times greater than Grade 91, F82H, and EUROFER97.

CNA7 was produced but limited results or details have been published in open literature and thus is not discussed within this work [38]. Two additional heats of CNAs, CNA8 and CNA9, were developed to test the effects of C content on $M_{23}C_6$ precipitate formation while maintaining the MX carbide level constant [39]. CNA8 has twice the amount of C than CNA9. CNA8 was estimated with computational thermodynamics to contain ~1.05 mol% of $M_{23}C_6$ carbides where CNA9 is estimated to have <0.1 mol%. As will be detailed in future chapter, no $M_{23}C_6$ precipitates were found in CNA9 experimentally. Both CNA8 and CNA9 were designed to have ~0.5 mol% of TiC precipitates [39]. EBSD investigations found that CNA9 has a coarser grain structure than CNA8, which led to CNA8 having a lower DBTT (

Figure 2.9). The C content also led the CNA9 to have a higher upper shelf energy (USE) than CNA8 [39]. CNA1-9 were fabricated as lab scale heats. Currently, ORNL is generating a new CNA heat that is produced using conventional steel making at industrial heat scales >1/4 ton but results on this variant are limited at the time of this work.

In summary, composition tailoring, computational thermodynamics, and TMT have been used to develop advanced RAFM and CNA steels for fusion applications. In particular, the increases in precipitate number density (10^{21}-10^{22} m^{-3}, which is ~2-3 orders of magnitude greater than earlier generations of 9Cr RAFM steels [27,34]) in combination with smaller grain sizes and higher dislocation densities in CNA steels have led to greatest improvements in mechanical properties over traditional FM steels. As such, CNA steels are promising as the leading candidate materials for fusion energy applications. However, data on the stability of MX nanoprecipitates under irradiation in the CNA materials is sparse. The MX nanoprecipitates are the main source of the improved mechanical properties and radiation resistance in the CNA steels, and therefore their stability is of the utmost scientific and engineering interest. The next section will discuss irradiation effects in steels, including a general overview of phase stability and examples of MX phase stability in austenitic, FM, RAFM, and CNA steels. An emphasis on the literature gap in phase stability under irradiation for RAFM and CNA steels will be highlighted.

Table 2.2 Summary of the various generations of CNA steels.

	MX Type	MX Phase Percentage (%)	$M_{23}C_6$ Phase Percentage (%)	Mechanical Testing
CNA1	(V,Ta)N [27]	0.47 [35]	1.8 [35]	Tensile tests, creep tests, and Charpy impact tests
CC22	(V,Ta)(C,N) [35]		1.3 [35]	
CNA2	(Ti,Ta)C [27]	0.43 [35]	1.5 [35]	
CNA3	(Ti,W,Ta)C [35]	0.41 [35]	1.3 [35]	
CNA4	TiC and TaC or complex (Ti,Ta)C	0.40 [35]	1.4 [35]	
CNA5	TiC and TaC or complex (Ti,Ta)C	0.32 [35]	1.4 [35]	
CNA6	TiC and TaC or complex (Ti,Ta)C	0.44 [35]	2.1 [35]	
CNA7	Carbides	0.84 [35]	1.4 [35]	
CNA8	TiC (not published)	0.3 (this work)	Not published	
CNA9	TiC and (Ti,W)C (this work)	0.3 (this work)	0 (this work)	

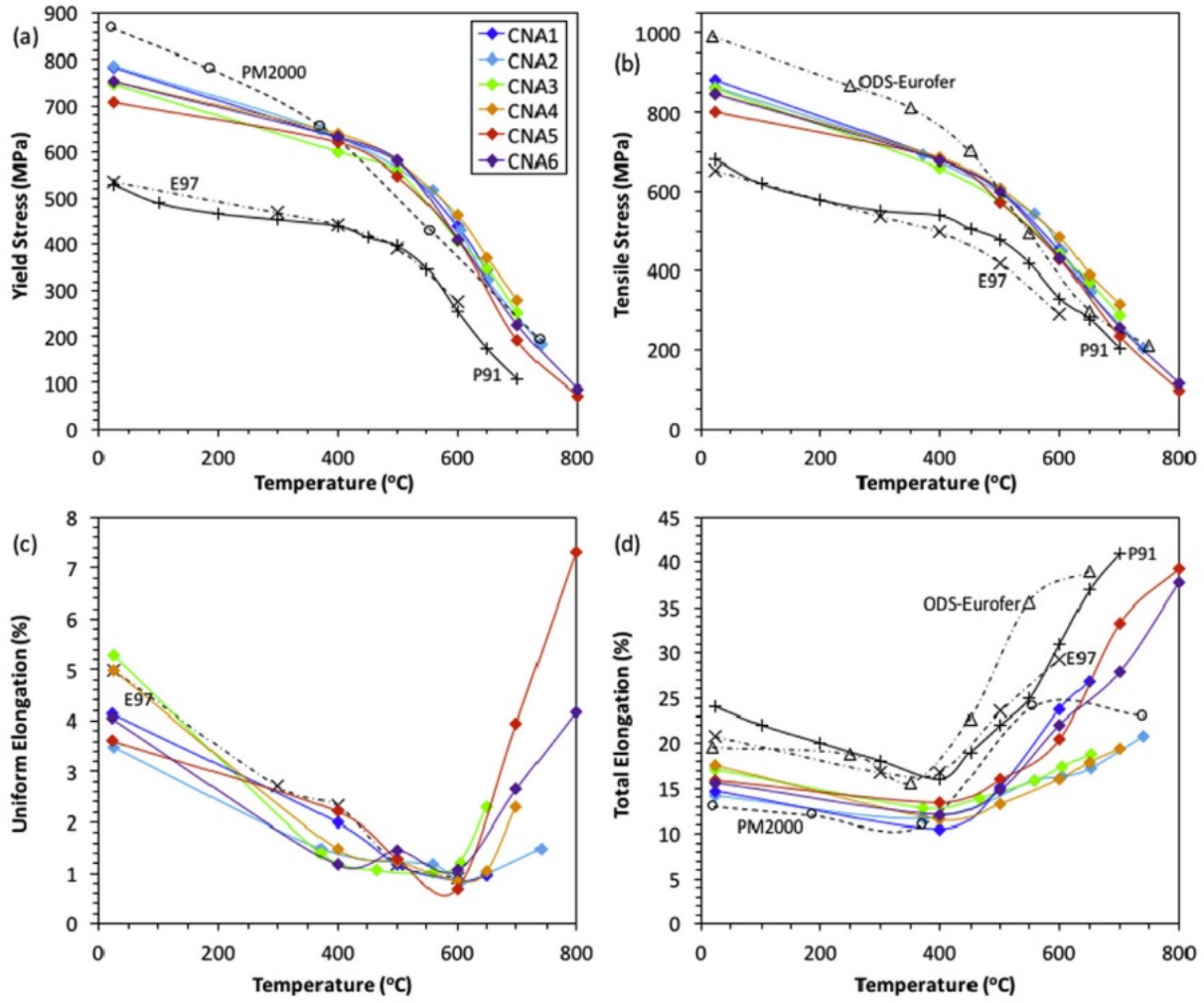

Figure 2.6 (a) Yield strength, (b) tensile strength, (c) uniform elongation, and (d) total elongation of CNA1 through CNA6 compared with literature data of Grade 91, EUROFER97, ODS-EUROFER, and PM2000 [34].

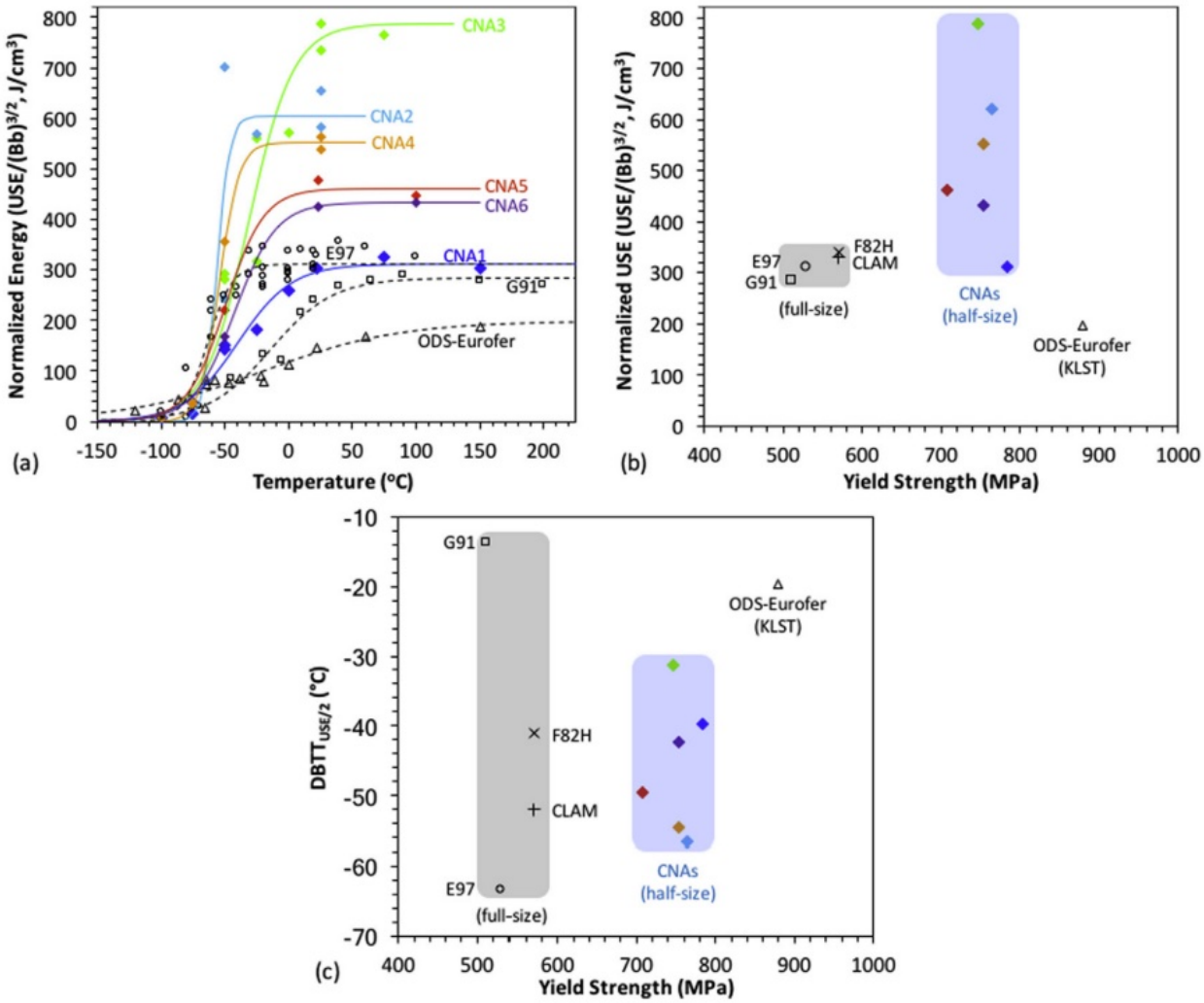

Figure 2.7 (a) Temperature-dependent Charpy impact absorbed energy of CNA1 through CNA6 compared with Grade 91, EUROFER97, and ODS-EUROFER; (b) Normalized USE to nominal fracture volume and (c) DBTT at USE/2 as a function of room-temperature yield strength of the CNAs compared with Grade 91, F82H, Eurofer97, CLAM, and ODS-EUROFER [34].

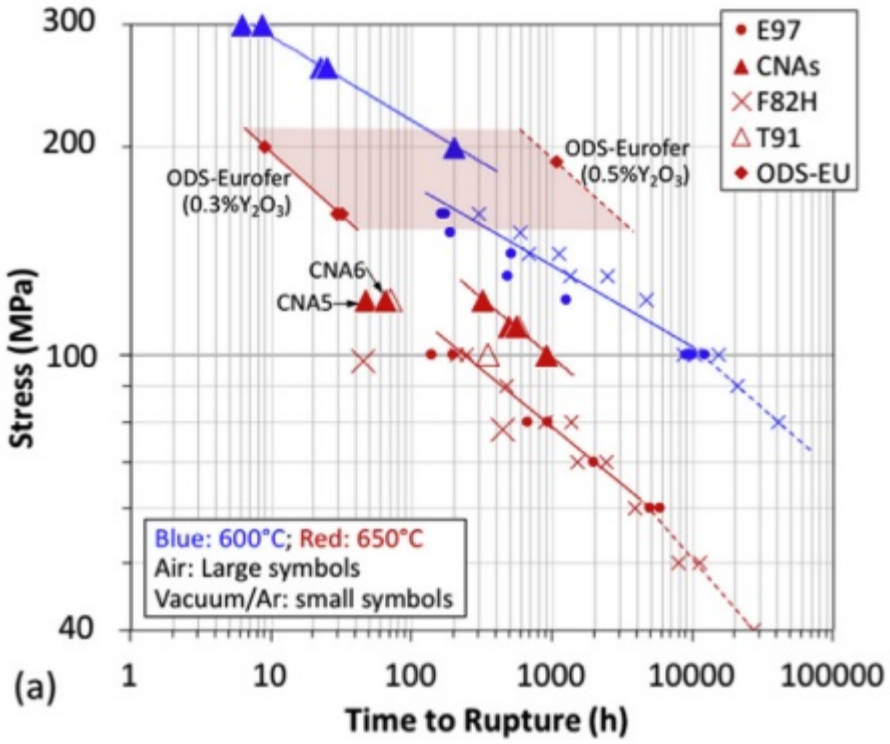

Figure 2.8 Stress as a function of time to rupture of CNAs compared with T91, F82H, EUROFER97 and ODS-EUROFER creep-tested at 600 and 650°C [34].

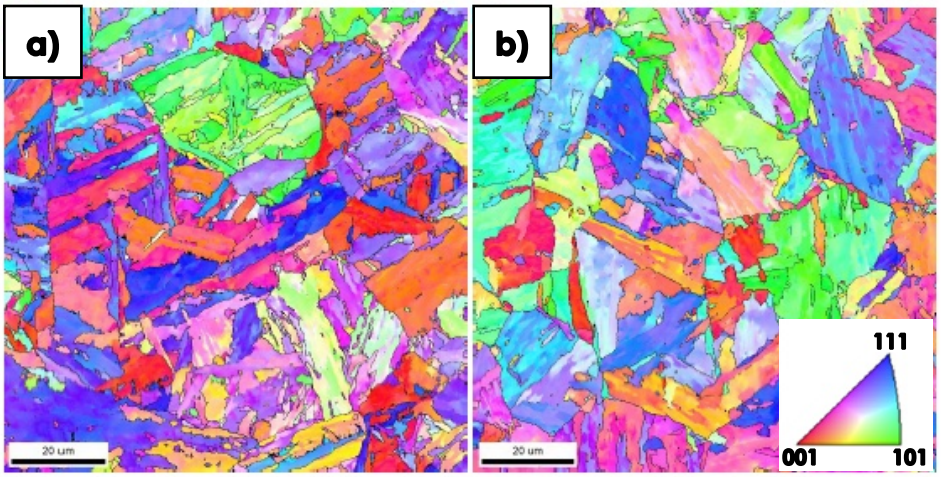

Figure 2.9 Inverse pole figure for (a) CNA8 and (b) CNA9 [40].

2.3 Irradiation Effects: Phase Instability and Dimensional Instability

Radiation damage phenomena will alter the microstructure in two main ways [41]:

- Bombarding particles transfer recoil energy to lattice atoms, which will cause displacement and a Frenkel pair defect to be created if the recoil energy exceeds the threshold energy of displacement.
- Bombarding particles can cause transmutation reactions leading to new elements, such as helium.

This section will discuss the above interconnected effects of radiation damage on phase stability in steels (both austenitic and FM steels) as well as discuss how helium affects phase stability. A generalized theory of phases under irradiation will be provided. Then general effects of helium on the microstructure will be discussed. Specific examples of phase and dimensional instability will be offered, as well as comparing the phase stability under irradiation at temperature versus thermal annealing.

2.3.1 Radiation Damage

Bombarding high energy particles such as heavy ions, neutrons, electrons, and protons have extreme effects on the microstructure and properties of materials. If the energy of an impinging particle exceeds the threshold displacement energy for a lattice atom, that atom will be knocked off its original lattice site. This atom is known as a primary knock-on atom (PKA). The PKA will initiate a branching damage cascade event where lattice atoms will be knocked off their lattice sites by other recoiling lattice atoms if the displacement energy threshold is exceeded. Eventually, the atoms will come to rest in new sites in the lattice as their energy decreases with increasing numbers of lattice atom interactions. This process creates Frenkel pairs of vacancies and

interstitials. The amount of displacements per atom (dpa) is the general model used for describing the extent of the damage inflicted on the lattice. The annihilation, clustering, and diffusion of Frenkel pairs determines the altered properties of materials under irradiation. The ability of materials to resist negative changes to their microstructure from radiation damage is termed radiation resistance. The damage cascade event proceeds in the following steps [1]:

- Collisional: Primary recoil atom kicks off atomic displacements until no further displacements occur (<0.1 ps)
- Thermal spike: the collisional energy causes a high density of deposited energy in surrounding lattice atoms (0.1 ps)
- Quenching: thermodynamic equilibrium is established (~10 ps)
- Annealing: thermally activated diffusion of lattice defects which lasts until the defects escape the cascade region and leads to observable effects of irradiation (nanoseconds to months)

Importantly, the cascade size and the effects of radiation damage are based on the energy, mass, and fluence of the particles. Electron irradiation creates Frenkel pairs but does not produce damage cascades. Protons, due to their light mass, produce small damage clusters with isolated Frenkel pairs. Heavy ions and neutrons, on the other hand, produce dense damage cascades. One method of comparing effects from bombarding particles of different mass and energy is the primary recoil spectrum. The primary recoil spectrum refers to the density of recoil atoms with energies in a certain range created during radiation damage and is dependent on projectile mass and energy. The concept describes the density of displacement damage occurring during irradiation. The weighted recoil spectra, *W(T)*, refers to the recoil density weighted by the damage energy produced in each recoil, which describes defect production. *W(T)* for various ions can be

assessed and compared to neutron data. From Figure 2.10, it can be seen that heavy ions mimic the shape of the curve for neutrons but have different *W(T)* magnitudes and different behaviors at higher energy.

As can be seen from Table 2.3, each type of irradiation has its advantages and disadvantages when studying radiation effects in materials. As fusion reactors are not yet in operation, researchers must rely on fission neutron and ion irradiations to simulate fusion environments. Fission neutron irradiations, however, take long times (on the order of months to years) to achieve the desired damage levels (<50 dpa), activate the materials such that they cannot be studied for months to years after irradiation, do not allow for simple single effects studies, and have lower rates of helium production via transmutation reactions than those expected for a fusion reactor. Ion irradiations, on the other hand, allow for fast experiments (hours to days) and highly controllable single effects studies (including the desired helium co-injection rates for fusion operation). Ions have a long history of being able to replicate key radiation phenomena such as swelling, segregation, and dislocation loop formation [42–45]. But direct comparisons from ion and neutron data is difficult and thus trends either in dose, temperature, dose rate, and composition are best to elucidate key mechanisms controlling radiation resistance. Hence, this work will utilize heavy ion irradiations for these reasons and because its weighted recoil spectra is similar to that of neutrons. Radiation effects phenomena in steel alloys such as RAFM steels include effects to secondary phases, which is the topic of the next section.

Table 2.3 Overview of the damage induced from various bombarding particles. Table content extracted from Ref. [1].

Particle	Damage Induced	Displacement efficiency (Frenkel pairs that survive the cascade quench)	Advantages	Disadvantages
Electrons	Isolated Frenkel pairs No damage cascade	50-100%	Simple source High dose rate Short irradiation times Single effects study	No cascades No transmutation No activation Convoluted results from surface effects of thin foils
Protons	Small, low density cascades with isolated Frenkel pairs	25%	Intermediate dose rate Moderate irradiation times Relatively flat damage profile Single effects study	Limited transmutation Minor activation
Heavy ions	Large, dense cascades	4%	High dose rate Short irradiation times Dense cascade production No activation Single effects study	No transmutation Depth-dependent damage profile
Neutrons	Large, dense cascades	2%	Best simulation of commercial power operation environments	High activation Convoluted data from multiple effects Low dose rate Long irradiation times

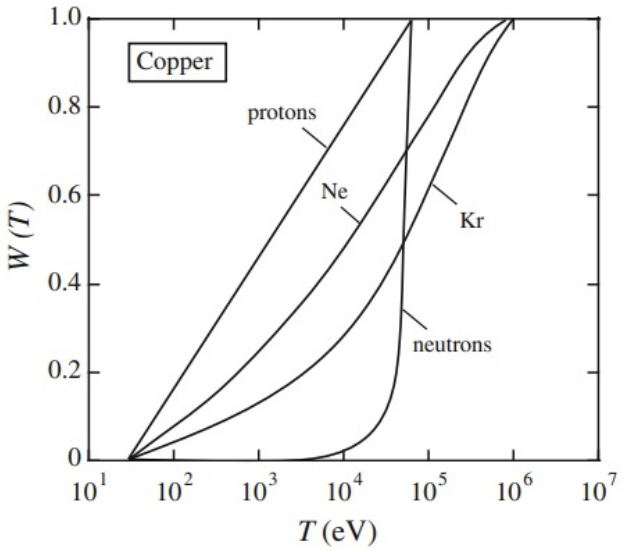

Figure 2.10 Weighted recoil spectra (W(T)) for 1 MeV protons, Ne ions, Kr ions, and neutrons in copper. Reproduced from Ref. [1].

2.3.2 Phase stability under irradiation

Phase stability under irradiation is a complex phenomenon that includes [46,47]:

- Precipitation of phases that are not thermally stable without irradiation
- Dissolution of thermally stable precipitates
- Disordering of ordered precipitates
- Amorphization of crystalline phases
- Coarsening via Ostwald ripening or inverse Ostwald ripening
- Solute segregation causing phase formation or dissolution

This work will focus on two main factors that are theorized to control phase stability under irradiation: radiation-enhanced diffusion (RED) and ballistic dissolution (or recoil resolution). Diffusion of solutes under irradiation is enhanced compared to thermal diffusion due to the excess amount of point defects. As solute diffusion is often coupled to point defects, these species diffuse faster. Hence, material phenomena that could only occur at very high temperatures under thermal conditions, or perhaps would never occur under thermal conditions, can occur under irradiation conditions at lower temperatures. The concentration gradients at the interface can also influence back diffusion of elements away from precipitates. Alternatively, concentration gradients can cause solutes to flow to the precipitates [48].

Ballistic dissolution refers to the solute atoms in a precipitate being ballistically ejected during a damage cascade event from the precipitate to the matrix. The rate of this process is proportional to the surface area of the precipitate and the damage rate [48]. This is not to be confused with the flux of atoms which may recoil from the particle to the matrix [48]. Generally, it is theorized that ballistic dissolution acts to dissolve precipitates under irradiation while RED acts to stabilize precipitates by causing the back diffusion of solute atoms from the matrix to

precipitates. This theory will be explored further with experimental examples of phase stability in steels and with theoretical frameworks for predicting phase stability under irradiation.

2.3.3 Dimensional stability under irradiation

Radiation damage also causes the transmutation of new elements, most importantly that of helium through the (n,α) reaction [49]. Helium has been shown to cause changes in precipitation during irradiation, such as radiation-induced precipitation, alteration in kinetics of phase transformations, and changes in phase composition [2,3,7,48]. Helium also causes changes to cavity pressurization, atomic transport, microstructural sink strengths, and localized compositions which can lead to helium embrittlement and enhanced void swelling. This work focuses on the effects of helium on swelling and how to mitigate swelling during fusion operation.

Helium has been shown to reduce the critical cavity size needed to reach vacancy biased-driven cavity growth. Excess vacancies, caused by interstitial bias of dislocations, migrate and form clusters. Helium has a strong binding to vacancies and stabilizes these clusters. Once these clusters reach a critical size, vacancy biased-driven cavity growth occurs. The resultant swelling is an important phenomenon in the range of $0.3T_m \lesssim T \lesssim 0.5T_m$, where T_m is the melting point of the steel. Below $0.3T_m$, slow diffusion causes the recombination of interstitials and vacancies to dominate and swelling does not occur. Above $0.5T_m$, the thermal vacancy concentration is greater than the radiation-induced concentration and cavities thermally emit vacancies [42].

Swelling occurs in three regimes: an incubation regime, a transient regime, and a linear or steady-state swelling regime. Swelling is generally negligible in the incubation regime [50]. The nucleation of cavities is dominant in the transient regime. BCC FM steels exhibit a longer transient regime than FCC austenitic steels (Figure 2.11). After the transient regime, steady-state swelling at a linear rate is reached at a certain critical damage level and is dominated by cavity growth. The

steady-state swelling rate in FM steels is quoted at ~0.2%/dpa and in austenitic steels at ~1%/dpa [50]. Steady-state swelling is determined by intrinsic material properties and microstructural evolution, but the duration of the transient regime can be changed depending on microstructural features, temperature, and damage rate.

One method to increase swelling resistance is to introduce a high density of traps for helium such as precipitate-matrix interfaces to increase the number of cavities and slow the accumulation rate of helium in each cavity, increasing the critical dose to the onset of swelling [7]. This is akin to studies on grain size effects on steady-state swelling rates in 304 stainless steel. The average swelling rate in coarse-grained 304 stainless steel was ~0.18%/dpa whereas ultra-fine grained 304 stainless steel had a rate of ~0.03%/dpa [50]. Examples of the evolution of secondary phases and the interdependent effects of helium in literature will now be described.

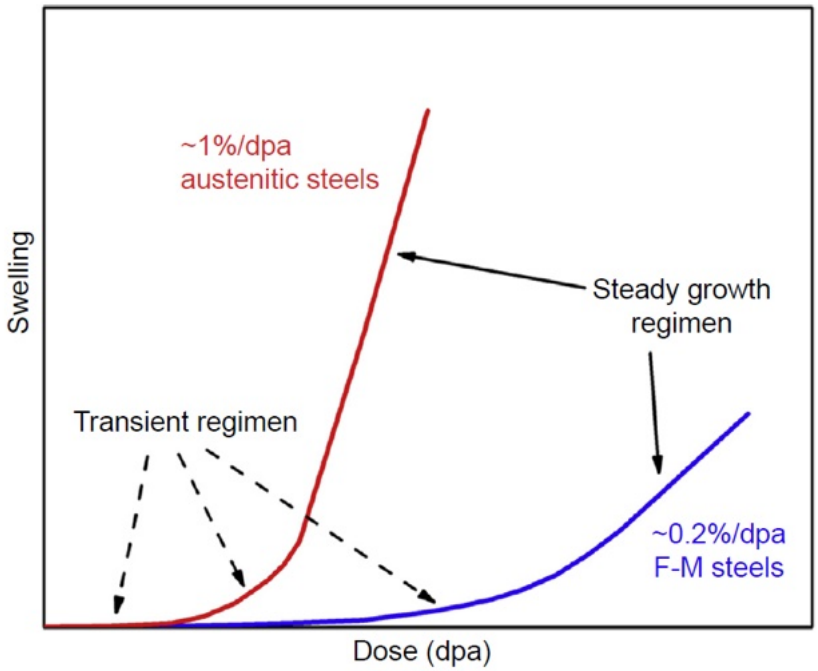

Figure 2.11 Comparison of transient and steady-state swelling regimes in austenitic and FM steels [50].

2.3.4 Coupling of helium and phase stability

Due to the increased level of helium transmutation in fusion reactors over fission reactors, helium is theorized to be as important as displacement damage for materials operation. Helium and precipitation evolution are theorized to be coupled in a manner of ways [48,51]:

- Direct processes that control the nucleation and growth of cavities at precipitate-matrix interfaces through:
    - The trapping of helium at the precipitate-matrix interfaces, due to the cavity-precipitate pair being a larger sink than a cavity alone, and possible diffusion of point defects to attached cavity.
    - Interactions between point defects and the precipitate-matrix interfaces (for instance, the interfacial energy of the attached cavity may be different than the matrix cavity).
    - The development of precipitate shells at cavity surfaces.
- Indirect processes that affect the sink strengths of features besides cavities, such as through:
    - Precipitation causing a change in the overall sink strength and hence a change in the partitioning of point defects.
    - The alteration of dislocation capture efficiencies through precipitation on dislocations, which changes the net point defect bias.
    - The preferential bias of precipitation for interstitials or vacancies.
- Mediating processes such that the chemical composition and diffusion of solutes and point defects is affected, such as through:
    - Changes in concentration of major and minor alloying elements in the matrix due to precipitation formation or dissolution.

The following sections discuss the interrelated evolution and effects between secondary phases and helium under irradiation in austenitic steels, traditional FM and RAFM steels, and CNA steels. Emphasis will be placed on MX-type precipitation, but other relevant phases will also be discussed to understand the relationship of helium with precipitates, though this review is not meant to be an exhaustive look at all possible secondary phases.

2.4 Examples of Phase and Dimensional stability under irradiation

2.4.1 Austenitic Steels

Most historical data on the stability of MX precipitates derives from austenitic steels. Though the same mechanisms of phase stability may not be present in austenitic and FM steels, it is still instructive to understand the history of phase stability in the literature of austenitic steels. The stability of MX precipitates, G phase, and Laves phase have been extensively studied in Ti-modified austenitic stainless steel. These precipitates are theorized to have different effects on swelling based on the nature of their interfaces. The MX precipitates are found to form and evolve with the cold-worked dislocation structure and are typically MX-TiC precipitates [52]. Thermal aging at and above 600°C will also result in the formation or coarsening of MX particles, but its formation and evolution will be altered under irradiation [53]. The stability of the MX phase in austenitic steels is dependent on changes in matrix composition (such as caused by irradiation-induced precipitation of other secondary phases) and to the generation rate of helium.

In Ref. [48,54], a Ti-modified stainless steel was neutron irradiated to 35 dpa over a temperature range of 425-650°C. The G and Laves phases had attached cavities to their interfaces at every temperature considered. The attached cavities were larger than the matrix cavities and accounted for the majority of the swelling, suggesting the importance of the particle interface for cavity nucleation and subsequent growth [52]. This experimental result was viewed to back up a

theory put forward by Mansur, that precipitate interfaces can act to collect point defects and channel them to the attached cavity (see Section 2.5.3). This causes the attached cavity to grow at a faster rate than the matrix cavities.

To test Mansur's theory, stainless steel was irradiated to a dose of 70 dpa, at which point G phase particles formed [3,52,55] (Figure 2.12). Then, the steel was injected with 400 appm helium. Helium-filled bubbles nucleated at the G phase interfaces and on dislocations. The material was then subjected to another irradiation to a further 20 dpa. During this last stage of irradiation, the cavities attached to the G phase particles grew faster than those on the dislocations. These results were viewed as consistent with Mansur's point defector collector theory of precipitates and cavities. This work and further work with G phase particles created a theory for the sequence of precipitate and attached cavity evolution: the particle-matrix interface traps mobile helium atoms, point defects accumulate with the helium atoms and form bubbles at the interface, and the bubbles coarsen under bias-driven growth at a rate faster than the matrix cavities as the dislocation network evolves [48].

In contrast to the evolution of helium with G phase particles, Maziasz found that MX-TiC particles in Ti-modified stainless steel are associated with 1-2 bubbles each after irradiation [52]. As such, the transition to bias-driven growth of the attached cavities is delayed as compared to the observed transition for G phase particles due to the MX-TiC particle-interface not exerting a strong point defect collector effect due to their small size (<10 nm). It is theorized that if the MX-TiC particles coarsen, the attached cavities will likewise grow. Mansur theorized that geometrically enhanced collection would not be important for TiC particles due to their small size but rather the bias modification function due to their high misfit with the matrix would be important [56].

The rate of helium generation was also found to affect the MX-TiC particle stability [3,57]. Austenitic Ti-modified type 316 stainless steel irradiated with Ni ions to 70 dpa at 675°C with either 0.4 appm He/dpa or 20 appm He/dpa. The increased helium co-injection rate prevented the formation of G phase and increased the stability of the MX-TiC phase. Small bubbles were found attached to the MX-TiC particle-matrix interfaces. It was theorized this was due to the greater helium co-injection rate creating a greater overall sink strength from the enhanced numbers of helium-vacancy clusters, hence affecting the diffusion of solutes and reducing the solute segregation per site needed to form the G phase. Importantly, the migration of Ti from MX-TiC particles to G phase leads to MX-TiC precipitate dissolution, but helium prevented that in this study.

Pulsed ion irradiation studies of modified 316 stainless steels [2,58] have shown that MX-TiC particles without helium co-injection form at damage levels less than 10 dpa due to thermal affects or radiation-enhanced effects at 675°C. The MX-TiC particle volume fraction is maximized around 40 dpa before dissolving in favor of Ti solutes migrating to G phase particles. With helium co-injection, the MX-TiC particles have small helium bubbles attached to their interfaces by 10 dpa. The number density of MX-TiC particles is greater with helium co-injection, suggesting helium influenced the nucleation process of the MX particles. The process of the replacement of MX-TiC particles with G phase was also slowed, as the MX-TiC particles were still present at 70 dpa with helium co-injection. At 70 dpa, the bubbles attached to MX-TiC particles remained small whereas the bubbles attached to the G phase grew relatively larger.

The behavior of MX-TiC precipitates was also reported in Ref. [59] for proton irradiated cold-worked Ti-modified 316 stainless steel. The MX-TiC precipitates were not initially formed during manufacturing, but nucleated and grew at low dose (0-10 dpa) during irradiations at 600°C,

and then gradually began to dissolve between 10 and 45 dpa. The dissolution of the MX-TiC precipitates coincided with the nucleation and growth of the Ti-containing Fe_2P phase. Hence, Ti solute redistribution was the reason for MX-TiC precipitate dissolution between intermediate and high dose. The dissolution of MX-TiC precipitates and the subsequent loss of sink strength was theorized to cause greater void swelling. This work did not study the correlation of bubbles at precipitate-matrix interfaces.

The stability of the TiC phase in relation to helium was also addressed in Ref. [48]. Ti-modified stainless steel was irradiated with 4 MeV Ni ions at 675°C to 100 dpa with a damage rate of 6×10^{-3} dpa/s and a helium co-injection rate of 4 appm He/dpa. The pre-existing cuboidal TiC precipitates (edge length of ~85 nm) were surrounded by fine MX-TiC particles of diameter ~3 nm. Each small MX-TiC particle had a helium bubble attached to it. This effect was not found at 20 dpa. Hence, displacement cascades at high damage levels may have caused solute atoms within MX-TiC particles to recoil into the matrix, where they renucleated with or on helium bubbles.

Maziasz found that the helium trapping at the MX-TiC precipitate-matrix interface minimized swelling in solution-annealed stainless steel and cold-worked Ti-modified steel irradiated in the High Flux Isotope Reactor (HFIR) from 550-680°C between 30-57 dpa [6]. The final helium concentrations were 1,850-3,600 appm helium. It was found that 90% of the overall cavity density was located at or close to the MX-TiC particle interfaces, with the cavities decreasing in size with decreasing proximity to the interface. The matrix and Laves phase were denude of cavities. The cold-worked Ti-modified steel contained two variants of MX-TiC precipitates: an equiaxed variant with a cube-on-cube orientation relationship and a rod-shaped variant, which was dominant. TEM observations showed that the helium trapping ability did not depend on the precipitate variant, but rather on the nature of the interfacial structure. Both precipitates were found to be incoherent. In

the solution-annealed stainless steel before irradiation, the equiaxed MX-TiC precipitates were heterogeneously dispersed in the matrix with a density of (1-4)×10^{19} particles/m^3. After irradiation, the rod variant dominated and increased in number density. It was also uniformly distributed, suggesting the pre-existing equiaxed MX-TiC precipitates dissolved during irradiation. Maziasz summarizes that the trapping ability of MX-TiC precipitates in general is effective over a range of damage rate, fluence, irradiation temperature, and He/dpa ratio. Trapping occurred in the following irradiation environments for Ti-modified 316 stainless steel:

- Lower temperature and lower fluence for HFIR irradiation
- Pre-injection of 30 appm helium followed by creep testing at 800°C and 120 mPa for 100 hours
- High temperature dual beam ion irradiation at 600°C and 70:1 appm He/dpa to 2.5 dpa
- High temperature EBR-II irradiation at 650°C to 39 dpa and 19 appm helium

Based on this knowledge, Ref. [6] concludes that all helium being generated during the HFIR irradiation was trapped in bubbles at the MX-TiC-matrix interface. This was possibly due to the interfacial dislocations on the MX-TiC-matrix interface providing nucleation sites for helium bubbles. It is assumed that helium-vacancy clusters migrate long distances and have preferential accumulation at the interfaces due to the TiC precipitates being biased for vacancies and helium-vacancy complexes. The TiC phase's volume misfit allows it to resist interstitial absorption. The presence of bubble nucleation but absence of growth at the TiC particles is due to the high helium/low vacancy concentrations in the adjacent matrix.

Kesternich [57] studied the role of interfaces and dislocations on helium trapping in two austenitic stainless steels that contained large (~100 nm) TiC precipitates, small (~6 nm) MX-TiC precipitates distributed on dislocation networks, and $M_{23}C_6$ carbides. The steels were implanted

with helium concentrations from 30 to 1,000 appm and subsequently annealed at 700, 750 and 800°C with and without applied tensile stress. As helium becomes mobile above 700°C by the detrapping mechanism or diffusion via interstitial or vacancy mechanism, helium bubbles formed after annealing. Overall, a greater dislocation density was found to correlate to greater helium bubble density and smaller helium bubble sizes. A $M_{23}C_6$ carbide at a triple grain boundary junction was imaged in TEM. It had one semi-coherent interface (cube-on-cube orientation relationship) with one grain and was incoherent with the other two grains (with no interfacial dislocations observable). Bubbles in higher density and smaller sizes were found preferentially decorated at the interfacial mismatch dislocations on the semi-coherent interface versus the incoherent interfaces. Small MX-TiC precipitates, located on dislocations, were found to have 2-3 bubbles attached to their interfaces per precipitate. These precipitate-attached bubbles were smaller than bubbles associated with only dislocations. No noticeable differences were found between bubbles associated with the smaller MX-TiC precipitates and the larger TiC precipitates, which was not hypothesized by Mansur [56]. Kesternich concluded that the interfacial dislocations did not determine the helium trapping ability of the TiC-matrix interfaces. Rather, the helium sequestration ability arose from the large lattice mismatch between TiC precipitates and the matrix (~20%) which causes a high interfacial energy. A high interfacial energy corresponds to a greater likelihood of bubble nucleation. In addition, the volume of helium bubbles (average volume per bubble times the bubble density) was higher at the TiC-matrix interfaces than the $M_{23}C_6$ carbide-matrix interfaces. Kesternich hypothesized this was due to the interfacial energy as well, driving the Ostwald ripening process of helium bubbles. The bubbles at higher energy interfaces (*i.e.,* the TiC interfaces) have lower pressure due to the gain of energy from the interface, causing the bubbles at higher energy interfaces to grow at the expense of bubbles on lower energy interfaces.

Kesternich concluded that finely dispersed TiC precipitation can strongly suppress the adverse effects of helium [57].

In summary, MX precipitates formed either during cold-working in Ti-modified stainless steel or during low dose irradiation (<10d pa) were found to dissolve around intermediate dose (~40 dpa) as the Ti solute atoms in the MX precipitates redistributed, perhaps through a combined effect of displacements into the matrix and radiation-enhanced diffusion, in favor of the formation of new particles such as G phase or phosphides. This process was prevented or slowed with the presence of helium, the effect increasing in magnitude as the helium implantation rate also increased. Small helium bubbles attached to the TiC precipitate-matrix interface also had longer transient regimes than matrix cavities or cavities attached to other particles such as G phase. Helium, therefore, affected solute transport and segregation of elements and led to greater stability of MX-TiC precipitates in austenitic steels. Helium also had unique interactions with different precipitates, with the MX-TiC precipitates providing the most stable interfaces for the creation of a high density of small bubbles, thereby preventing void swelling. Thus far, there are a number of theories regarding MX precipitation in relation to helium in austenitic steel, including MX phase stability and helium accumulation at MX interfaces. The most notable and relevant to this work are listed in Table 2.4.

Table 2.4 Summary of the work conducted on MX precipitate stability and helium sequestration in austenitic steels.

Ref.	Theory
MX Phase instability with helium	
[3,57]	Alteration of solute diffusion and segregation, leading to reduced radiation-induced precipitate formation
[48,59]	A disturbance in the balance between loss of Ti atoms by cascade dissolution and back diffusion of Ti causes MX-TiC dissolution. For instance, this could occur if Ti solutes are diverted to the formation of a new phase as cascade dissolution dominates.
[48,59]	If dissolution of MX particles occurs, MX particles may renucleate with the help of helium, since helium bubbles lower the interfacial energy of the MC particle-interface.
Preferential helium accumulation and Cavity Development at the MX precipitate-matrix interfaces	
[3,56]	Point defect collection - The precipitate-matrix interface may serve as a sink for point defects and provide an easy diffusion path for the collected point defects to the attached cavity. The size of the precipitate radius governs the geometric enhancement factor, and thus allows for greater point defect collection and greater growth of precipitate-attached cavities as compares to matrix cavities.
[3]	Helium trapping
[3,60]	Surface energy credit - Work has already been done to create the particle-matrix interface and a cavity created at this interface yields that energy to help create a particle-cavity pair at the interface.
[61]	Interfacial dislocations serve as preferred storage sites for helium, leading to the formation of helium bubbles on interfacial dislocations on the MX precipitate-matrix interface.
[57]	Interfacial dislocations do not determine the helium trapping ability of the TiC-matrix interfaces. Rather, the helium sequestration ability arises from the large lattice mismatch between TiC precipitates and the matrix (~20%) which causes a high interfacial energy.
[6]	TiC particles are strongly biased for vacancies (due to a large positive volume misfit with the austenite matrix) and since helium-vacancy complexes are more likely the migrating species than vacancy-only complexes, helium will also accumulate at the TiC interface.

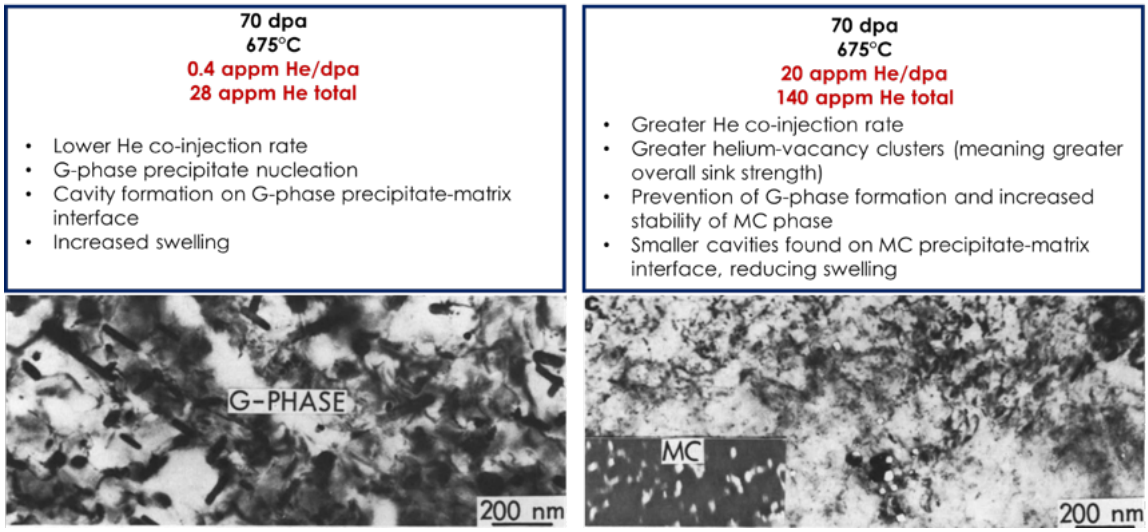

Figure 2.12 Summary and corresponding TEM micrographs showing the effect of helium co-injection rate on phase stability under irradiation in a Ti-modified austenitic steel [3,57].

2.4.2 Traditional FM and RAFM Steels

MX precipitation in FM steels has garnered considerably less research interest than austenitic steels. In their normalized-and-tempered state in FM steels, MX precipitates are typically 5-10 nm in diameter but upwards of ~30 nm in EUROFER97 [62]. MX precipitates can exist as VN, TaC, TiC, and or NbC depending on the composition of the steel and are typically present with a number density of 10^{19}-10^{21} particles/m^3. The ageing effects on MX precipitates in F82H have been studied at 400-650°C with 100,000 hours of ageing. MX precipitates were found to coarsen after ageing at these conditions [31]. MX precipitates have also been found to be unstable at high temperature creep testing, where TaN and TaC precipitates have been shown to coarsen under high temperature creep [63]. For instance, TaC precipitates were ~5 nm before creep testing. After creep testing, the TaC precipitates became cuboidal and rod-like in morphology and ranged in size from 6-40 nm.

Ref. [62] studied the irradiation effects of MX precipitates in EUROFER97 steel irradiated at 300°C to ~20 dpa using the Swiss Spallation Neutron Source (SINQ). The number density of MX precipitates was not assessed, but atom probe tomography (APT) was used to assess the composition modifications of MX precipitates under irradiation. MX precipitates in EUROFER97 contained less V and Ta but more Cr, Fe, Mn, and W after irradiation. A broadening interface at the VN precipitate-matrix, with greater levels of V and N in the matrix, interface suggested dissolution of VN in EUROFER97. In general, undersized solutes (Mn, Si, and Cu) were found enriched at the interface and oversized elements (W, V and Ta) were found depleted at the interface between the MX precipitate and the matrix.

A 9Cr-1MoVNb and a Ni-doped 9Cr-1MoVNb steel was irradiated in HFIR to 39 dpa at 300-600°C [64]. After tempering at 760°C for 1 hour, fine MC particles (both VC and (V,Nb)C)

with a phase fraction of 15% were on and within subgrain boundaries. Between 300-500°C, the smallest MC particles had dissolved by 39 dpa but coarser ones were present in both steels. In addition, the Ni-doped 9Cr-1MoVNb steel had radiation-induced precipitation of $M_{23}C_6$ carbides, M_6C (η), M_2X rods, and coarse χ particles. Irradiation also caused a change in MC composition in both steels. V-rich MX precipitates were dominant after irradiation. Both the VC and (V,Nb)C precipitates contained less V and more Cr, Mo, Fe, and Si after irradiation.

The composition of MC carbides was found unchanged using TEM-EDS analysis of carbon extraction replicas of a modified 9Cr–1Mo FM steel exposed at 32–57°C to a mixed proton/neutron particle flux and spectrum at the Los Alamos Neutron Science Center (LANSCE) to 0.5–9.6 dpa [65]. The initial size of the Nb-rich MC precipitates (~50 nm) was unchanged by irradiation and remained crystalline. Number densities were not reported.

Ref. [66] irradiated F82H, JLF-1, aged F82H-IEA (600°C at 30,000 hours) and Fe–Ta–C model alloy (700°C at 500 hours) to 10 or 20 dpa at 300°C or 500°C with 6.4 MeV Fe^{3+} ions for single beam irradiations or with 6.4 MeV Fe^{3+} ions + degraded 1 MeV He^{+} ions (15 appm He/dpa) for dual beam irradiations. In the single beam irradiation at 300°C to 10 dpa, the smaller MX precipitates became dominant and decreased in number in F82H as compared to the unirradiated condition. But in the JLF-1 specimen, while the precipitate size distribution overall became smaller, the smallest of the MX precipitates had dissolved. This was also observed in JLF-1 and ORNL9Cr steel specimens neutron irradiated to 5 dpa at 300°C [67]. The MX-TaC precipitates in the Fe–Ta–C model alloy dissolved in all conditions. The authors suggest that the resolution of TaC precipitates is from radiation-enhanced diffusion. In addition, the authors of [67] suggest that TaC precipitates do not dissolve thermally and that dissolution under neutron irradiation may occur

due to irradiation-induced changes to the solubility limit of Ta or the C concentration in the matrix being changed by irradiation.

In response to Ref. [66], Ref. [68,69] fabricated a model alloy (Fe-0.2 wt.% TaC) to simulate the MX precipitate behavior in F82H steel under high energy electron irradiations (0.75 to 2.5 MeV) in a high voltage electron microscope (HVEM). Irradiations were conducted at 400°C to simulate the environment of first wall materials in fusion reactors. The TaC precipitates were stable under irradiation with 0.75 MeV electrons, but their size and number density decreased with electron energies above 1 MeV. Electron energies above 1 MeV cause atomic displacements in Fe and hence cause radiation-enhanced diffusion. Due to the gradient in atomic displacements in the Fe matrix caused by the gradient in electron flux of the 1 MeV electron beam, vacancies are expected to flow from the beam center (higher flux of electrons) to the outer (lower flux of electrons). The authors concluded that displacements within the TaC precipitates caused direct dissolution of the precipitates (by Ta dissolving into the matrix) at high electron energies and that radiation-induced vacancies in the matrix enhanced Ta diffusion away from the TaC precipitates through vacancy-type diffusion. The displacement of Ta may have also caused the formation of non-stoichiometric unstable $Ta_{1-x}C$ precipitates. It was concluded that displacements of Ta atoms destabilize the TaC precipitates, but C has no effect.

Ref. [70] studied ion irradiation effects in two heats of F82H steel, F82H-BA12 and F82H-IEA, at 400°C to 20 or 50 dpa using 2.8 MeV Fe^{2+} ions at a rate of 1.4×10^{-3} dpa/s. This study aimed to further the findings in Ref. [68], where the disappearance and decreasing size of MX precipitates was observed with increasing displacement damage due to enhanced vacancy diffusion. In this study, the F82H-IEA sample did not have pre-existing MX precipitates. The shrinkage rate of MX precipitates in the F82H-BA12 sample was 0.06 nm/dpa under irradiation,

meaning it resisted radiation-induced size instability. The Ta-rich MX precipitates had a number density 2.5 times greater than the V-rich MX precipitates after irradiation. (Ta,V)-rich MX precipitates were not found. The MX precipitates were less than 40 nm in all irradiated specimens. The MX precipitate size remained stable under irradiation, changing from an average size of 26 nm in the control specimen to 23 nm at 50 dpa.

MX precipitates in EUROFER97 underwent significant growth but had no changes in number density after irradiation to 32 dpa at 332°C in the irradiation experiment ARBOR [71]. Pre-existing spherical Ta(C,N) precipitates were distributed in the matrix. A low amount of V-rich MX precipitates was also detected. No differences in precipitate type or composition were detected before and after irradiation. Before irradiation, MX precipitates had a diameter of 21.1 nm and after irradiation at 332°C the MX precipitates had a diameter of 29.7 nm.

Ref. [72] studied MX precipitate density and size distribution in EUROFER97 after irradiation to 15 dpa at 300°C in the mixed spectrum HFIR and in the BOR-60 reactor. Pre-existing MX precipitates were enriched with Ta and V. The mean MX precipitate diameter after irradiation to 15 dpa at 300°C in HFIR was 27 nm and in BOR 60 was 29 nm, which represent increases in size over the control specimen size of ~21 nm. The HFIR samples had a total precipitate density of 7.9×10^{19} m^{-3} and a volume fraction of visible precipitates of 1.71%, including both MX and $M_{23}C_6$ precipitates. The BOR-60 samples had a total precipitate density of 9.5×10^{19} m^{-3} and a volume fraction of visible precipitates of 2.89%, including both MX and $M_{23}C_6$ precipitates. It was suggested by the authors, though not numerically verified, that irradiation caused the growth of pre-existing MX precipitates and hence increased their volume fraction. Samples in the BOR-60 reactor were also irradiated up to 32 dpa, and the MX precipitates did not show considerable changes in size or density changes from the 15 dpa condition in BOR 60.

To further gauge the stability of MX precipitates, three model alloys were fabricated labeled TaC, TaN, and VN and irradiated under 5 MeV Fe^{2+} ion irradiation at 500°C for damage levels up to 49 dpa with a dose rate in the range of $(1.2–7.6)\times10^{-4}$ dpa/s [36]. The precipitates were analyzed with S/TEM. Irradiation caused:

- Moderate reprecipitation (number density increase) and slight dissolution (size decrease) of the oval-shaped TaC precipitates
- Significant dissolution and moderate size changes (decreased particle length but increased thickness) of the disc-shaped TaN precipitates
- Slight reprecipitation and moderate growth in particle length (no change in thickness) of the disc-shaped VN precipitates

Hence, TaC was concluded to have the best radiation stability. Irradiation did not alter the crystallinity of any precipitate type. This work also indicated that displacement rate is an important factor in precipitate evolution, with a higher displacement rate inducing precipitate dissolution [37]. This work concluded that the morphology of the precipitates governed their stability under irradiation [18]. The stability of the TaC, TaN and VN nanoprecipitates was also studied under thermal aging (600 and 700°C) and creep (600°C) [37]. TaC was also found to have the best resistance to thermal aging-induced and creep-induced instability, including resistance to dissolution and coarsening.

Ref. [73] investigated HT9 irradiated in the Advanced Test Reactor up to 4.16 dpa from 300 to 600°C. The pre-existing VN precipitates were found to be enriched in Cr after irradiation due to radiation-induced segregation (RIS). VN precipitates have been shown to be thermodynamically unstable and morph into Cr-rich Z phase when annealed at elevated

temperatures. It is hypothesized that RIS enhances the transformation of VN precipitates into Cr-rich precipitates.

In summary, MX particles in FM steels have been shown to coarsen at elevated temperature ageing and creep testing and have been shown to either coarsen or dissolve under irradiation. But sparse systematic research on the mechanisms governing MX precipitate stability in FM steels has been conducted, especially in relation to helium. This is partially due to the low density of MX precipitates present in FM and RAFM steels, making their behavior statistically difficult to characterize.

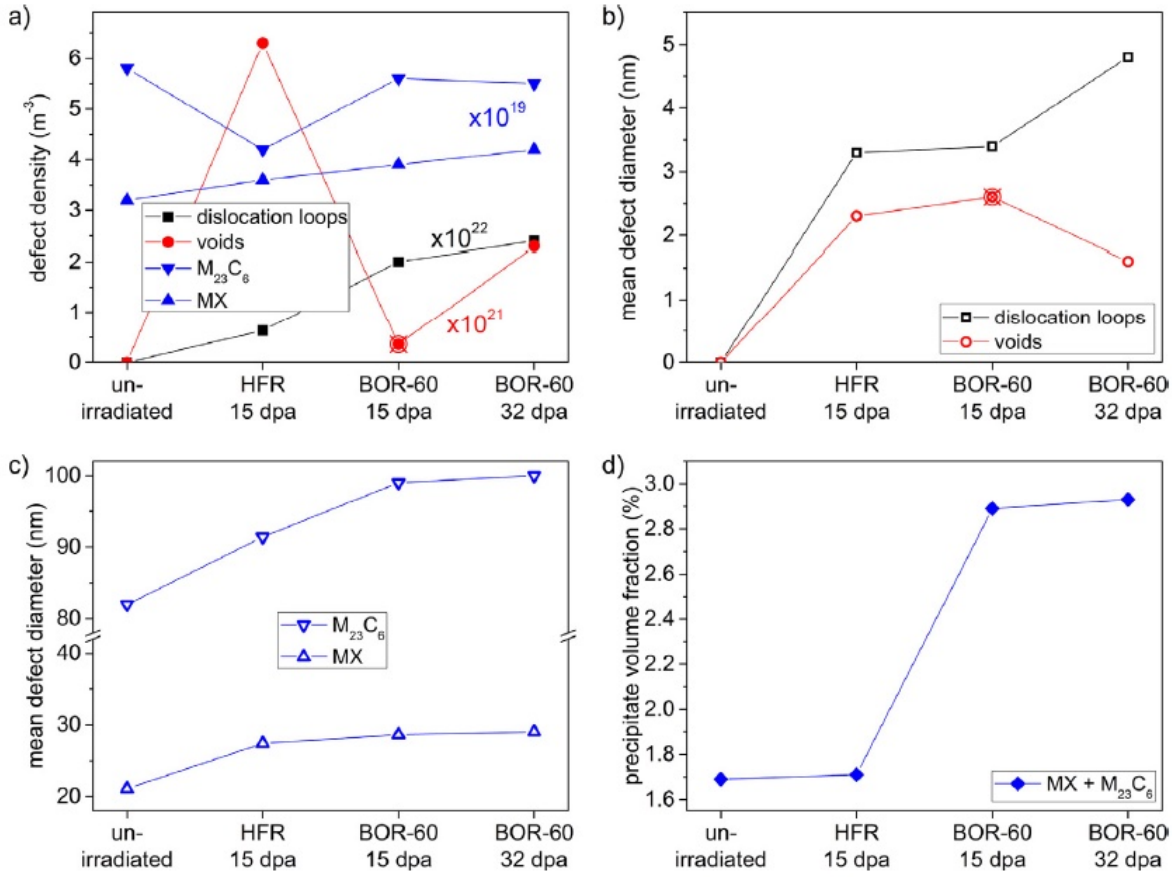

Figure 2.13 (a) Density, (b,c) diameter, and (c) volume fraction of loops, voids, MX precipitates, and $M_{23}C_6$ carbides in EUROFER97 after irradiation [72].

2.4.3 CNA Steels

Though there are currently nine generations of CNA steels, only CNA1 and CNA3 have been tested for helium and/or radiation damage effects at the time of this work. A summary of the experiments conducts on CNAs is given in Table 2.5.

CNA3 underwent single, dual, and triple beam irradiation at 400-600 °C to a damage level of 50 dpa at a damage rate of 1×10^{-3} dpa/s with He and H injection rates of 10 and 40 appm/dpa, respectively [39,74]. In all conditions, the MX-(Ti,W,Ta)C precipitates in CNA3 were partially or fully dissolved. CNA3 had a greater swelling than F82H, which was co-irradiated with CNA3, at 500°C, which was the peak swelling temperature studied.

In Ref. [75], the precipitates in CNA3 survived Fe + He dual ion beam irradiation to 50 dpa at 650°C with 15 appm He/dpa. Bubbles in the matrix had a mean radius of 8.4±2.9 nm and a density of $\sim5\times10^{21}$ m^{-3}. Bubbles associated with precipitates had a mean radius of 4.6±1.8 nm and a density of 143 m^{-3}. Hence, the bubbles on the precipitates were smaller than those in the matrix. A total of 32% of cavities were found associated with precipitates, though not all of these precipitates were the MX-(Ti,W,Ta)C precipitates. There were also Cr-rich precipitates and oxycarbides present. This percentage of cavity population attached to cavities was on par with the other materials investigated, including a FeCrAl alloy and an ODS alloy.

Helium bubble formation was examined in CNA3 and 14YWT with in-situ and ex-situ helium implantation to 10,000 appm He at 500-900°C [76]. The bubble number densities were comparable to the nanoparticle densities in both alloys. Helium bubbles at the MX precipitate interfaces were observed. The bubble size in CNA3 was greater than in 14YWT, and the bubble density in CNA3 was smaller than in 14YWT. This difference was greater with increasing temperature, suggesting that CNA3 did not contain enough precipitates to suppress swelling at

higher temperatures. The sink strength of precipitates in CNA3 was estimated to be 2×10^{15} m^{-2}, but this was derived from MX and $M_{23}C_6$ precipitates. The MX carbides in CNA3 were shown to have favorable binding energies for helium up to a temperature of 600°C. The paper concluded the nanoparticles in both alloys were beneficial at sequestering helium and suppressing swelling.

Helium bubble formation was also investigated in CNA1 as well as 9YWT and 14YWT after helium ion irradiation to ~7,500 appm He and ~0.3 dpa at 500 and 700°C [77]. All materials had small spherical bubbles at the precipitate-matrix interfaces, but 9YWT and 14YWT exhibited better trapping ability than CNA1 at 700°C. The authors suggest that MX precipitate binding energy with helium may be insufficient at elevated temperatures or that the sink strength of MX precipitates at higher temperature is not enough to sequester all of the helium due to a greater helium migration rate. The sink strength of precipitates in CNA1 was estimated to be ~10^{15} m^{-2}, but this was derived from MX and $M_{23}C_6$ precipitates. It was estimated that a sink strength of 10^{16} m^{-2} is needed to resist swelling at higher temperatures.

Table 2.5 Summary of irradiation and helium implantation experiments conducted for CNA alloys.

CNA	Irradiation Conditions	Irradiation Results
CNA3	Dual beam (Fe^{3+} + He^{+}) irradiation at 650°C [35,75]	• 32% carbide-bubble association in CNA3 compared with ~40% cluster-bubble association in ODS alloys [35,75]
CNA3	Single ion beam (Fe^{2+}), dual ion beam (Fe^{2+} + He^{2+}), and triple ion beam (Fe^{2+} + He^{2+} + H^{+}) irradiations were conducted at 500°C to a damage level of 50 dpa and dual and triple beam irradiation experiments were conducted at 450°C to 50 dpa at a damage rate of ~1×10^{-3} dpa/s [39,74]	• 500°C had greater swelling than 450°C [39,74] • Average cavity size, density, and swelling were on par between CNA3 and F82H [39,74] • Precipitates partially or fully dissolved in CNA3 [39,74] • CNA3 swelling was 0.56% and F82H was 0.88% as 450°C [39,74] • CNA3 swelling was 1.6% and F82H was 0.95% as 500°C [39,74]
CNA1, CNA3	He implantation at elevated temperature [76,77]	• Bubbles were found attached to MX particles but the MX particles did not maintain high helium sequestration ability above 600°C [76,77]

2.5 Models of Phase Stability and Helium Effects on Precipitation

Based on the experimental literature, numerous models for precipitate stability under irradiation and the role of helium on cavity co-development with precipitates have been developed. Below, relevant models are described.

2.5.1 Frost and Russell Model of Recoil Resolution

Frost and Russell described a method for modelling the behavior and dissolution of precipitates under irradiation [78]. The model considers the competing mechanisms of resolution by radiation recoil and thermal coarsening. Resolution by radiation recoil describes the process of solute atoms in a precipitate recoiling into the matrix as a result of radiation damage, causing the eventual dissolution of the precipitate. This is identical to later references in literature on ballistic dissolution. On the other hand, thermal coarsening hastens the growth of precipitates by causing the recoiled solute atom to return to the precipitate. A steady-state is reached when a balance between these two processes occurs. This model was an expansion of the work by Nelson [46] and considers the solute deposition rate to be a function of proximity to the precipitate, which was not previously included in Nelson's model [47]. To the author's knowledge, the Frost and Russell model has not previously been explicitly applied to understand experimental results of precipitate stability.

The applicability of recoil resolution to precipitate behavior can be inferred from the solute matrix concentration, since dissolution and growth is dependent on the solute concentration profile. Thermal coarsening is assumed to be driven by the differences in solute concentration near large and small precipitates. The deviation from equilibrium solute concentration determines the dominant factor on precipitate behavior: dissolution via recoil resolution or growth via thermal coarsening. For instance, if the matrix concentration under irradiation is close to thermal

equilibrium, thermal coarsening will proceed, which is expected to occur at higher temperatures. To make this assessment, Frost and Russell derived an equation to compare the matrix concentration of solute in thermal equilibrium with the precipitates to the maximum matrix solute concentration attained from recoil resolution. The equation is derived by solving the steady-state concentration profile from the diffusion equation, modified by the rate of recoil resolution:

$$c_{max}(r_p + R) = c_e + \frac{SR^2}{12D}\left(1 - \frac{R}{4r_p}\right) \quad \text{Eq. 2.2}$$

where R is the recoil distance, S is the recoil rate (in dpa/s), D is the diffusion of the rate-limiting species (in m^2/s), r_p is the mean precipitate radii (in m), and c_e is the thermal concentration (in atom fraction). The recoil distance R refers to the distance that the recoil solute atom travels outside of the precipitate after a collision.

Frost and Russell furthered the model by explicitly determining the dominant precipitate behavior operating at given irradiation conditions, thermal coarsening or dissolution by recoil resolution, by taking account of the matrix solute concentration from thermal coarsening and from recoil resolution. Frost and Russell derived the following equation for the concentration in the matrix as a function of particle size, $c(r_p)$:

$$c(r_p) = c_e\left(1 + \frac{2\sigma V_m}{r_p(k_bT)}\right) + \frac{SR^2}{12D}\left(1 - \frac{R}{4r_p}\right) \quad \text{Eq. 2.3}$$

The first term in the equation, $c_e\left(1 + \frac{2\sigma V_m}{r_p(k_bT)}\right)$, is the Ti concentration in the matrix from the Gibbs-Thomson equation [79]. The Ostwald ripening process is an example of Gibbs-Thomson effect, where concentration gradients cause larger precipitates to grow at the expense of the smaller precipitates. The second term, $\frac{SR^2}{12D}\left(1 - \frac{R}{4r_p}\right)$, is the the concentration from recoil resolution. $c(r_p)$ changes sign when:

$$S = c_e \frac{96 D \sigma V_m}{R^3 (k_b T)} \quad \text{Eq. 2.4}$$

where σ is the surface tension of the precipitate-matrix interface and V_m is the molar volume of the precipitates (m^3/mol). σ is taken to be the standard value of 0.5 J/m^2 [80]. The reason to ascertain when $c(r_p)$ is negative or positive is because concentration gradients cause coarsening or dissolution. This equation can be plotted as a function of temperature. The curve delineates the boundary of the dominant mechanism on precipitate behavior (Figure 2.14). Below the curve, thermal coarsening is dominant. Above the curve, recoil resolution is dominant.

In summary, Frost and Russell's model of recoil resolution predicts that the matrix concentration of solute tends to a steady-state value dictated by recoil resolution and thermal equilibrium considerations. Recoil resolution becomes an important factor in precipitate stability when the equilibrium solute concentration differs from the steady-state concentration under irradiation. Otherwise, thermal coarsening proceeds. A summary of resultant precipitate behavior based on the steady-state concentration of solute under irradiation is given in Table 2.6.

Table 2.6 Summary of findings from the recoil resolution model on concentration effects on precipitate stability under irradiation.

Steady-state concentration	Resultant Precipitate Behavior
Differs little from the equilibrium solute concentration	Recoil resolution is not important and thermal coarsening will proceed normally
Large compared to the equilibrium solute concentration but not high enough to nucleate new particles	Recoil resolution will produce an inverse coarsening in which all particles tend toward the same size
Large compared to the concentration needed to nucleate new second-phase particles but lower than the volume fraction	Re-precipitation will become an important process
Exceeds the volume fraction of particles present	Dispersion will be entirely dissolved at steady-state

2.5.2 Muroga, Kitajima, and Ishino (MKI) Model on Recoil Resolution

Another model developed by Muroga, Kitajima, and Ishino (MKI) extended Frost and Russell's work [81]. The MKI model quantitatively predicts the size change and dissolution of precipitates under irradiation using recoil resolution as a guiding principle [81]. The MKI model uses computer simulations to obtain recoil range distributions from collisional cascades of primary recoils with precipitates atoms. The recoil distribution is then used to calculate the recoil resolution efficiency, ε_{res}. The recoil resolution efficiency is defined as the number of atoms moved from inside to outside the precipitate with collision cascades divided by the number of atomic displacements within the precipitate:

$$\varepsilon_{RES} = \frac{\left(-R^4/_{12} + r_p^2 R^2\right)\pi S/_R}{4\pi r_p^3 S/_3} \quad \text{Eq. 2.5}$$

$$\varepsilon_{RES} = \frac{12\left(R/_{r_p}\right) - \left(R/_{r_p}\right)^3}{16} \quad \text{Eq. 2.6}$$

Hence, the recoil resolution efficiency is a function of damage rate, recoil range, and precipitate size. As the recoil range increases, more solute atoms are moved from inside to outside the precipitate and the recoil resolution efficiency increases. As the precipitate size increases, the fraction of recoil atoms that stop within the precipitate also increases and the recoil resolution efficiency decreases. A decreased recoil resolution efficiency translates to enhanced precipitate stability. An increased recoil resolution efficiency translates to more solute atoms recoiling away from the precipitate and hence more precipitate dissolution.

The rate of change in the initial size distribution of the precipitates, assumed to be unimodal in the paper, can be derived from the precipitate volumetric change as a function of recoil resolution efficiency:

$$\frac{dr_p}{dt} = \frac{-r_p S \varepsilon_{RES}}{3} \quad \text{Eq. 2.7}$$

From here, the final precipitate size as a function of irradiation damage level can be calculated using integration, ensuring that ε_{RES} is a function of r_p:

$$\int_{r_0}^{r_1} \frac{1}{r_p \varepsilon_{RES}} dr_p = \int_{t_0}^{t_1} -\frac{S}{3} dt \quad \text{Eq. 2.8}$$

$$\int_{r_0}^{r_1} \frac{1}{r_p \left(\frac{12\left(R/r_p\right) - \left(R/r_p\right)^3}{16} \right)} dr_p = \int_{t_0}^{t_1} -\frac{S}{3} dt \quad \text{Eq. 2.9}$$

The recoil range distribution, R, can be calculated computationally. The MKI model used the MARLOWE code. R is physically a range of values since it represents recoils resulting from primary knock-on atoms as well as from atoms at the end of cascade branches.

A more accurate model of ε_{RES} to describe precipitate dissolution via recoil resolution and growth via solute back diffusion can be developed with the use of an effective range, R_{eff}. R_{eff} considers the recoil range, R (solute displacements outside of the precipitates as calculated by MARLOWE or more recently by SRIM), and the capture radius, r_{cap} (solutes diffusion back to precipitate from the matrix). The MKI model does not explicitly explain how to calculate R_{eff} from R and r_{cap} but explains that r_{cap} is a function of solute size, irradiation environments (such as temperature), precipitate coherency, and stress fields. Ref. [81] used survey calculations of representative values of R_{eff} to understand precipitate behavior under irradiation. The results of these calculations are shown in Figure 2.15, which show the estimated precipitate radius as a function of damage level for four conditions. It is observed that pre-existing small precipitates (with radius <1 nm) dissolve by several tens of dpa. This suggests the importance of carrying out

experiments to damage levels greater than 10 dpa to understand the dissolution behavior of dispersoids. It also suggests that the starting size distribution of precipitates is a key factor in the resulting size distribution at transient precipitate dose regimes.

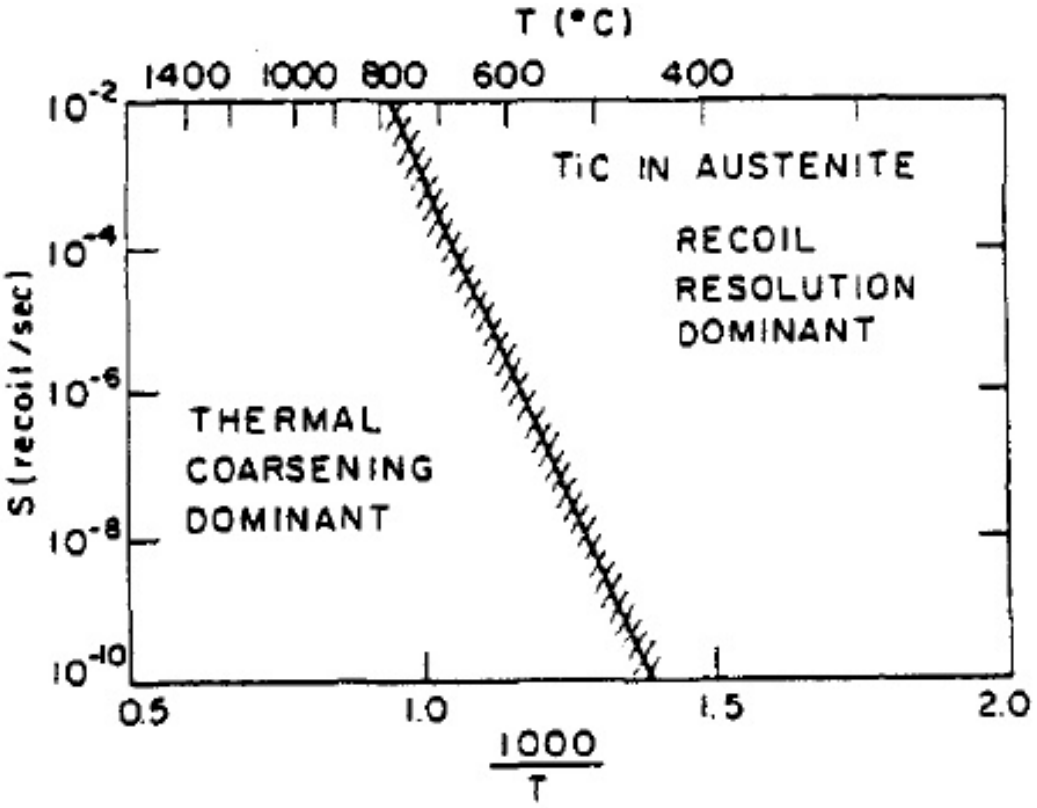

Figure 2.14 Prediction calculated by the Frost and Russell model of when thermal coarsening or recoil resolution will determine TiC precipitate stability [81].

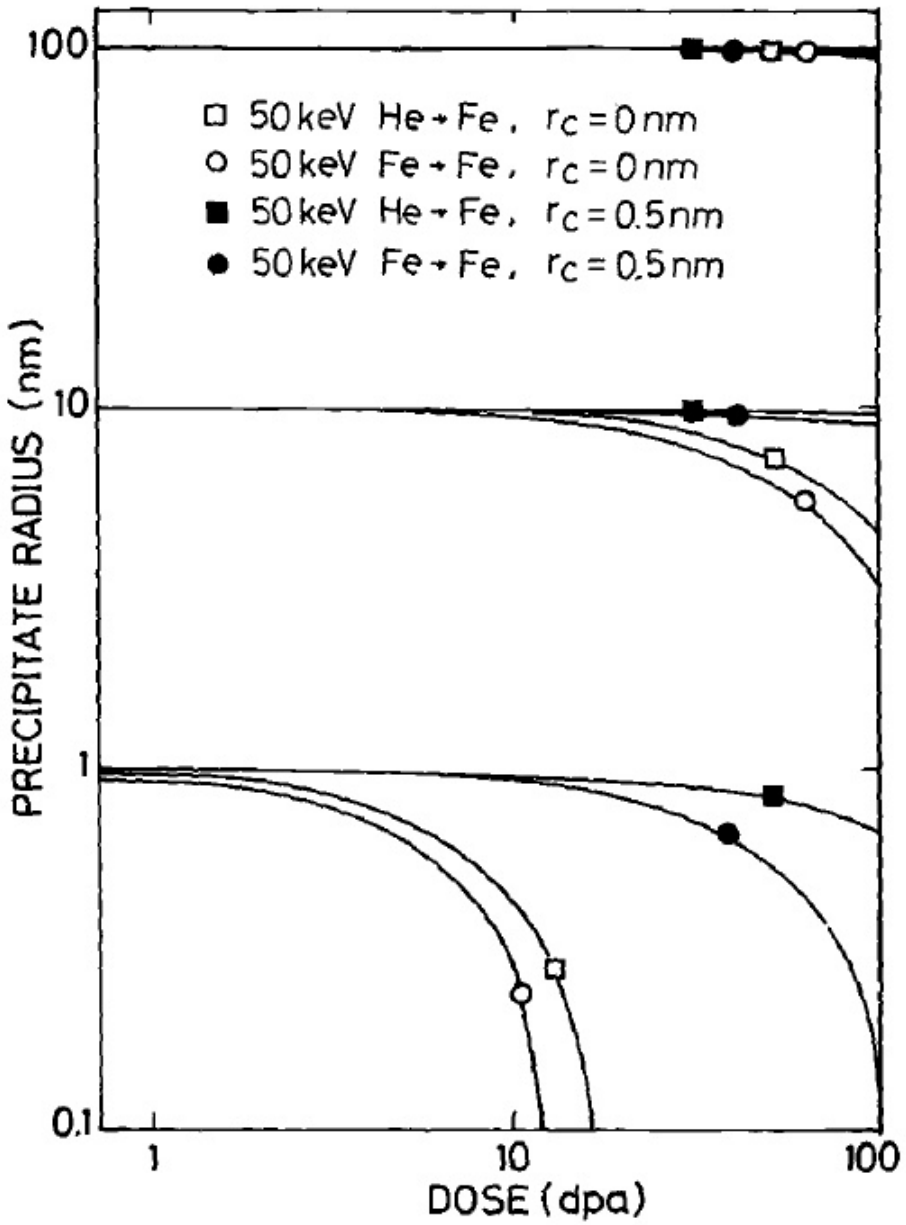

Figure 2.15 Dose dependence of precipitate radius calculated with the MKI model of recoil resolution [81].

2.5.3 Mansur's Theory on Precipitation and Cavities under Irradiation

Mansur studied the relationship of precipitate-matrix interfaces to cavity development, theorizing that the rate of growth of the matrix cavities versus the precipitate-attached cavities is governed by the sizes of the precipitate-attached cavities and the precipitates, a bias modification

function that addresses the capture efficiencies and sink strengths of cavities and precipitate-cavity pairs, and a sink strength modification variable to allow comparison between microstructures with different sink strengths [56]:

$$\frac{dr_{cp}}{dr_c} = \left[\frac{r_c r_b}{r_{cp}^2}\right]\left[\frac{Z_v^b S_i^{(1)} - Z_i^b S_v^{(1)}}{Z_v^c S_i^{(2)} - Z_i^c S_v^{(2)}}\right]\left[\frac{\left(1 + \frac{4RG}{D_v D_i S_v^{(1)} S_i^{(1)}}\right)^{1/2} - 1}{\left(1 + \frac{4RG}{D_v D_i S_v^{(2)} S_i^{(2)}}\right)^{1/2} - 1}\right] \quad \text{Eq. 2.10}$$

where the first term in brackets is the geometric enhancement term, the second term is the composite bias modification term, and the third term is the sink strength modification term. The superscripts (1) and (2) refer to two materials systems that can be compared with this equation. If comparisons are being made in one system, these simplify to $S_i^{(1)} = S_i^{(2)} = S_i$ and $S_v^{(1)} = S_v^{(2)} = S_v$ and the sink strength modification term simplifies to unity. The variable r_b is the composite sink radius of a precipitate (r_p) with an attached cavity (r_{cp}). The variable r_c is the radius of a matrix cavity. r_b is given by [56]:

$$r_b = -\frac{r_{cp} r_p}{rc_p + r_p}\left[2\gamma_E + \varphi\left(\frac{r_p}{r_{cp} + r_p}\right) + \varphi\left(\frac{r_{cp}}{r_{cp} + r_p}\right)\right] \quad \text{Eq. 2.11}$$

$$= \begin{cases} r_b \to r_p \; when \; r_p \gg r_{cp} \\ r_b \to r_{cp} \; when \; r_p \ll r_{cp} \end{cases}$$

Hence, the theory also suggests that swelling is influenced by the size of the precipitates through the geometric enhancement term, as long as cavities are not the dominant sink in the material and is influenced by the biases (capture efficiencies and sink strengths) of the precipitate-cavity pair and the matrix cavity through the bias modification term. The bias modification term would be unity if $Z_v^b = Z_v^{bc}$ and $Z_i^b = Z_i^{bc}$. Mansur theorized this would be the case if the absorption of point defects was diffusion-controlled at both the precipitate-cavity pairs and the

matrix cavities, but not the case if absorption was interface-controlled. The bias modification term is expected to be unity if the precipitates are not highly misfitting with the matrix [48].

2.6 Summary

In summary, a systematic understanding of the mechanisms of MX phase stability under irradiation and the co-evolution of MX precipitates and cavities under irradiation, particularly in FM and RAFM steels, is lacking in the literature. In addition, theoretical frameworks for precipitate stability and for the relationship between precipitates and cavities have been put forward, but experimental validation in FM and RAFM steels has not been conducted. Such experimental work is necessary to understand degradation mechanisms in steels and to better design future advanced steels for fusion power plants. In addition, while studies of helium implantation effects on MX precipitates in CNA steels have been reported, there is no literature on the combined effects of helium co-implantation and ion irradiation damage of precipitation in such steels. These gaps in knowledge will be addressed in this work through single effects ion irradiation experiments of a CNA steel.

Chapter 3 Objectives

The overarching objective of this work is to inform advanced alloy design and manufacturing for structural materials in nuclear power applications through the evaluation of key microstructural features for alloy performance. This objective will be accomplished through accelerated fusion power plant-relevant radiation environmental exposures via ion irradiation experiments at temperature with co-injected helium of an advanced Fe-9Cr steel alloy called CNA9, which is an engineering alloy in the leading RAFM steel class developed by the United States. Specifically, the stability of pre-existing TiC nanoprecipitates and the development of cavities with co-injected helium will be assessed. Two related hypotheses, one tailored towards a scientific objective and one towards an engineering centric objective, were developed to guide the investigation into the behavior of TiC precipitates in the presence of helium and to examine the effects of TiC precipitation on the swelling response of CNA9. The objectives as outlined below were met through a systematic study using accelerated ion irradiations and advanced characterization as outlined in Chapter 4.

The hypothesis for the **scientific objective** is:

Co-injected helium will prevent the radiation-enhanced growth of pre-existing TiC nanoprecipitation within ion irradiation environments at temperatures of 0.3 to 0.4 of the melting point of advanced steels. This will occur due to injected helium atoms binding to Ti solute atoms in the matrix, of which could have been already present in the matrix or which were recoiled into the matrix from irradiation-produced cascades. Helium is known to suppress the diffusion of

helium-solute complexes by increasing the energy activation barrier needed to be overcome for movement of the complex [3–5,82–84]. *Hence, the helium-Ti solute clusters formed under dual beam irradiation will suppress Ti solute diffusion, thereby preventing the growth of pre-existing TiC nanoprecipitates in comparison to single beam irradiations without co-injected helium. However, helium is hypothesized to have no effect on the ballistic dissolution of precipitates, as it is not expected to affect the cascade behavior leading to the ballistic ejection of Ti into the matrix from TiC precipitates. But the suppressed diffusion of Ti solutes by helium co-injection may lead to a quicker onset of dissolution.*

To achieve the scientific objective and to either confirm or refute the hypothesis, further sub-objectives were established. The **first scientific sub-objective** was aimed at determining *the single and combined effects of damage level, damage rate, temperature, and co-injected helium* on the pre-existing size distribution and number density of TiC precipitates. To complete this sub-objective, a series of experiments were performed in the laboratory with varying conditions. This required the establishment of a controlled and consistent process of performing the experiments as well as analyzing and processing the experimental data. The development of the following methods was essential in acquiring the relevant experiment data:

- A method for consistent and controlled ion irradiation experiments at temperature.
- Development of proper procedures for the extraction of electron transparent samples from both the ion irradiated and thermally exposed regions of the bulk CNA9 specimens.
- Coupled and complimentary post-characterization techniques using scanning transmission electron microscopy (STEM) equipped with energy dispersive spectroscopy (EDS) ability for spatially correlated composition information.

- A method for consistent quantification of the TiC precipitation evolution, both the evolution that resulted from irradiation at temperature and from only thermal annealing at the same temperature to differentiate between thermal and radiation effects.

The **second scientific sub-objective** was aimed at understanding *why* a change in irradiation parameters did or did not result in changes to the pre-existing and/or formed TiC precipitate population. A detailed analysis of the TiC precipitate size distributions in the control specimen, irradiated specimens (with and without helium), and in the thermally annealed regions of the irradiated specimens accomplished this sub-objective. Evaluation of the precipitate populations after different environmental exposures, such as irradiation at temperature or just thermal exposure, enables decoupling of thermal coarsening responses from combined influence of temperature and radiation. Existing radiation precipitate stability models including the Frost and Russell model [78] and the MKI model [81] were applied to the data from this work to provide insight into the roles of displacement damage, temperature, and helium on ballistic dissolution and growth of precipitates. In addition, this work sheds light on the validity of such models to TiC precipitates in advanced Fe-9Cr steel engineering alloys. This is a critical step in establishing a fundamental understanding and predictive model of MX-type precipitate stability in RAFM steels for fusion applications.

The hypothesis for the **engineering objective** is:

Precipitates will sequester helium atoms during irradiations with co-injected helium in the form of individual nano-scale bubbles on the precipitate-matrix interface as a function of temperature. In line with previous theoretical work, it is hypothesized that this occurs due to the attraction of helium to misfitting dislocations at the precipitate-matrix interfaces [61,85,86]. *However, the relatively low density of pre-existing TiC precipitates is hypothesized to not prevent*

the overall un-constrained helium-driven swelling in the matrix. The helium sequestration response of the precipitate-attached cavities is hypothesized to be dependent on:

a) *Temperature – Temperature may cause increased diffusion of helium and vacancies to the helium-filled bubbles attached to the TiC interfaces, thereby decreasing the time to reach the onset of biased-driven void growth.*
b) *Coherency of interfaces – Semi-coherent platelets such as those studied within have misfitting dislocations on the precipitate-matrix interface to relieve stress at the interface. It is hypothesized that these interfacial dislocations will sequester helium in small bubbles and will serve as sites of growth for voids.*
c) *Level of helium co-implantation – A greater helium co-implantation rate is expected to cause the nucleation of greater amounts of cavities in the matrix and at the precipitate-matrix interfaces due to the greater driving force from higher helium concentrations.*

The first **engineering sub-objective** was aimed at determining *the helium and vacancy sequestration ability of TiC precipitates.* To complete this sub-objective, a subset of the irradiation experiments as described above were used. These irradiations varied temperature and the level of helium co-injection. The development of the following methods was essential in acquiring the relevant experiment data:

- A method for consistent and controlled ion irradiation experiments at temperature
- Development of proper procedures for the extraction of electron transparent samples from both the ion irradiated and thermally exposed regions of the bulk CNA9 specimens

- Coupled and complimentary post-characterization techniques utilizing STEM equipped with EDS ability and conventional off zone axis bright field TEM imaging for spatially correlated composition and cavity development information
- A method for consistent quantification of the TiC precipitation evolution and cavity development.

The **second engineering sub-objective** was aimed at understanding *why* a change in irradiation parameters did or did not result in changes to the helium sequestration ability at the TiC precipitate-matrix interface and how those changes affect the overall swelling behavior of the steel. A detailed analysis of cavities attached to precipitates and cavities located in the matrix provided a comprehensive picture of the relative importance of precipitate interfacial characteristics to helium sequestration and their influences to swelling.

Hence, the scientific-relevant hypothesis will explore the helium-mediated mechanisms on precipitate size, number density, and volume fraction as a function of varying thermal and irradiation conditions, while the engineering-relevant hypothesis will investigate how helium sequestration evolves at the precipitate-matrix interface as a function of temperature and coherency. The hypotheses were tested via a combination of heavy ion irradiation experiments with and without co-injected helium followed by detailed characterization of the microstructure using advanced scanning transmission electron microscopy (S/TEM) techniques.

Chapter 4 Experimental Procedures and Methodology

This chapter will describe the experimental procedures used in this work to prepare, irradiate, and characterize a model advanced reduced activation ferric/martensitic (RAFM) steel to address the hypotheses presented in Chapter 3.

4.1 Alloy and Sample Preparation

This work used a model alloy variant of the U.S. developed advanced ferritic/martensitic steel class deemed Castable Nanostructured Alloys, or CNA(s) for short [39,40,87,88]. Specifically, the laboratory-scale Castable Nanostructured Alloy #9 (CNA9) was used within. The composition in weight percent is reported in Table 4.1. The bulk chemistry evaluation was performed by Dirats Laboratories using quantitative analysis by inductively coupled plasma spectroscopy optical emission spectroscopy (ICP OES) for metallic elements, combustion for C and S, and inert gas fusion (IGF) for O and N. According to Dirats Laboratories, the uncertainty of each measurement was determined to be either 1% of the absolute composition value or two in the last reported digit, whichever is least. This method was used to determine the error of the analysis in Table 4.1. The alloy and compositional information were provided by Oak Ridge National Laboratory (ORNL). CNAs were developed primarily at ORNL to achieve high number densities of MX-type precipitates using traditional steel manufacturing methods, resulting in improved mechanical properties and radiation tolerance [12,27,31,34,36,89–92]. CNAs are considered in the family of advanced reduced activation ferritic/martensitic (RAFM) steels. Prior to this work, there were seven previous generations of laboratory-scale CNAs, CNA1-CNA7,

where each CNA generation was tailored to evaluate specific properties or environmental responses – see Chapter 2 for additional details. At the inception of this work, CNA8 and CNA9 were created as advanced engineering alloys to test the effects of C content on nanoprecipitation development, based on current understanding from the prior CNA generations. Please refer to Chapter 2 for an in-depth description of CNA properties and development. CNA8 was also irradiated in the experiments conducted for this work, but its characterization was out of the scope of this work because this work hypotheses, and thus scope, does not consider the effects of carbon on microstructural evolution under irradiation and is left for future studies. Due to having twice the amount of carbon, CNA8 contained $M_{23}C_6$ precipitation whereas CNA9 did not. See Appendix A for details. CNA9 was chosen for work because it did not contain $M_{23}C_6$ precipitation. CNA9 was selected to avoid any possible influence that the $M_{23}C_6$ precipitation may have on the MX-TiC precipitate stability by either increasing or decreasing the free carbon in the alloy under irradiation. Thus, eliminating the role of $M_{23}C_6$ precipitates simplifies the evaluation of precipitate behavior and enables the detailed evaluations of the hypotheses proposed in Chapter 3.

CNA9 was normalized at 1050°C for 1 h in Ar atmosphere then hot-rolled at 1050°C to 0.3 inch-thick with ~21% reduction per pass. It was briefly reheated at 1050°C if needed followed by water quenching. The ingot of CNA9 was then cut into two halves, top and bottom. The bottom half was tempered at 750°C for 30 min, air cooled, and de-scaled. A 1 cm piece from the top half was used for composition analysis [39,40,87,88].

Samples in the form of 1.5 × 1.5 × 10 mm^3 bars were cut from the laboratory-scale ingot of CNA9 using electrical discharge machining (EDM) and shipped to the University of Michigan for ion irradiation studies. The samples were mounted on a puck with crystal bond and mechanically ground and polished using successively finer grits with each step. The samples were

bonded to the puck as flat as possible to ensure a uniformly flat surface of all samples on the puck, which is important to obtain a uniform ion implantation depth (or ion range) during the irradiation experiments and hence have confidence in the measurements of ion damage beneath the sample surface Mechanical grinding consisted of using 400, 600, 800, and 1200 grit in succession. Polishing consisted of using pads with 3, 1, and 0.25 μm polycrystalline diamond suspension (Pace Technologies item numbers PC-1003-500, PC-1001-500, and PC-0125-500, respectively) resulting in a mirror-like surface finish. An optical microscope was used after each step to ensure the damage layer from the previous grit was removed by observing the absence of prior polishing step scratches. On average, the samples retained a thickness of 1 mm after the final mechanical polishing step. CNA9 samples were prepared simultaneously with three other FM steel bars of the same geometry as well as two FM guide bars. The three other FM steels were CNA8, additively nanostructured alloy # 2b (ANA2b), and ANA2a. The guide bars served as points of contact for thermocouples during irradiations for temperature control. The guide bars had dimensions of 1.5 × 1.5 × 20 mm^3 before undergoing identical grinding and polishing steps to the target samples. Each set of six samples, CNA9 plus the three other FM steels and the two FM guide bars, were irradiated side-by-side during experiments Figure 4.1. CNA9, the three other FM steel alloys, and the FM guide bars will be referred to as the irradiation stage. It was important to polish the samples in the same configuration that would be used in the irradiation experiment to ensure uniform thickness across samples and good contact with the stage. The FM bars were chosen because they had similar thermal conductivity to the FM steels being irradiated, which is important as only thermocouples for temperature monitoring during irradiation experiments were welded to the guide bars. Thus, a similar thermal conductivity ensures a similar temperature distribution during experimentation.

Electropolishing was then performed on all samples to remove any remaining deformation layers from grinding and polishing. The electropolishing solution was 10% perchloric acid solution, 90% methanol solution, cooled to -45°C using a methanol bath with dry ice. The perchloric acid solution was 70% perchloric acid and 30% water. Typical volumetric ratios used in the electropolishing step were 50 mL of perchloric acid and 450 mL of methanol solution mixed in a 1,000 mL beaker to enable sufficient solution to electropolish all samples simultaneously. A magnetic stirrer was used to create a ~20 mm in diameter vortex in the electropolishing solution. The bars were connected to an anode (the sample itself then becoming the anode) and the surface of the bars to be irradiated were submerged next to the vortex in the electrolyte solution facing a Pt mesh (the cathode). The samples were electropolished at an applied voltage of -40 V for approximately 20 seconds. Voltage was applied using a Circuit Specialists CSI6010X power supply. A diagram of the electropolishing set-up is shown in Figure 4.2. The samples were electropolished for approximately 20 seconds, timed using a simple handheld digital timer. This procedure removed an estimated 2 μm of material resulting in final sample geometries of approximately 1.5 × 1× 10 mm^3 and 1.5 × 1 × 20 mm^3 for the irradiation samples and guide bars, respectively. The sample preparation was completed with cleaning samples in beakers of acetone, methanol, and ethanol in succession for 20 seconds minimum in each beaker. The quality of the samples were visually inspected to verify no significant scratches, discoloration, surface pitting, or other irregularities existed after the final electropolishing procedure [93].

All samples were labeled to ensure proper tracking. Each material had their own unique marking that would be engraved on the middle of the back side of the sample. The side to be irradiated would be engraved with a ‘+’ on the back side of the sample, and the side to only be thermally exposed would be marked with a ‘-’ on the back side.

Table 4.1 Chemical compositions (wt%) of CNA9 provided by Dirats Laboratories.

Element	CNA9 (wt.%)
Fe	89.27±0.02
Cr	8.688±0.08688
W	1.026±0.0126
Mn	0.516±0.00516
Si	0.141±0.00141
Ta	0.090±0.0009
Ti	0.141±0.00141
V	0.049±0.00049
C	0.049±0.00049
Al	<0.002±0.0002
B	<0.0005±0.00005
Co	<0.005±0.0005
Cu	<0.002±0.0002
Mo	0.004±0.0004
Nb	<0.002±0.0004
Ni	<0.007±0.0007
P	0.004±0.0004
Zr	<0.002±0.0002
S	0.002±0.0002
O	0.0012±0.00012
N	0.0013±0.00013

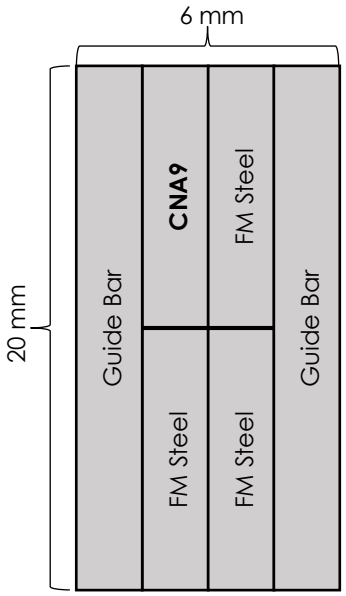

Figure 4.1 An example of a set of samples to be irradiated simultaneously on an irradiation stage. CNA9 and three other FM steels were irradiated side-by-side in each experiment in this configuration. FM guide bars served as sites for thermocouple placement for temperature control.

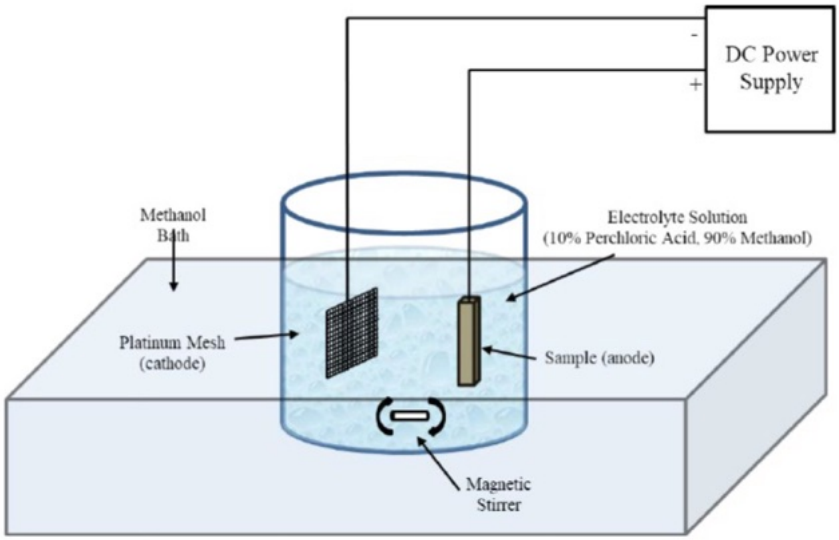

Figure 4.2 Schematic of the electropolishing set-up from [93].

4.2 Ex-Situ Dual Ion Irradiations

4.2.1 Ion Irradiation Experiments

All ex-situ ion irradiation experiments were performed at the University of Michigan-Ann Arbor's Michigan Ion Beam Laboratory (MIBL) (Table 4.2). A total of 16 ex-situ irradiation experiments were completed. Each irradiation consisted of one sample of CNA9, three other FM steels, and two FM guide bars as described in the previous section. The irradiation experiments were split into five series that each tested the effects of a single irradiation parameter on the behavior of TiC precipitates (Table 4.3): the dose rate series, dose series, temperature series, helium co-injection series at various temperatures, and helium co-injection series at various helium rate. The parameters chosen were motivated by fusion relevant conditions [94,95] while balancing incremental variations in single effects for fundamental studies of precipitate behavior. The target damage rates were 7×10^{-4} or 1×10^{-4} dpa/s. The dose rate of 7×10^{-4} dpa/s was chosen because previous work showed that it creates a neutron-like swelling response in FM steels for advanced fission reactors [42] and 1×10^{-4} dpa/s was chosen as a reasonably low dose rate to study dose rate effects. The target damage levels ranged were 1, 5, 15, 50, and 100 dpa. First-wall and blanket structures are expected to undergo damage more than 100 dpa [11,12,94,96]. Hence, a damage level of 100 dpa was used to assess the effects of fusion-relevant high damage levels on CNA9. Target damage levels of 1, 5, 15, and 50 dpa were used to gain a fundamental and mechanistic understanding of CNA9's evolution. The target temperatures used were 300, 400, 500, and 600°C. This range encompasses fusion-relevant temperatures and allows for a granular understanding of thermal effects by encompassing regimes that are expected to have different mechanisms governing CNA9's evolution (*i.e.*, dissolution at the two lower temperatures and thermal diffusion at the two higher temperatures). In addition, the temperatures tested encompass the peak swelling

regime for FM steels, which is around 420-440°C for neutron irradiations at 450-500 for ion irradiations [42]. The peak swelling temperature for heavy ion irradiations occurs at higher temperatures than for neutron irradiations due to the higher displacement rates used ion irradiations [18]. The target helium co-injection rates were 0, 10, and 25 appm He/dpa. A rate of 0 appm He/dpa was used to establish the effects of damage without helium co-injection first. Rates of 10 and 25 appm He/dpa were then used to assess how helium changed CNA9's evolution as compared to the single beam experiments. The helium co-injection rates of 10 and 25 appm He/dpa were chosen because they represent the fusion-relevant helium rates for FM steels [11,95,96]. The rate of 25 appm He/dpa is the maximum rate attainable experimentally to assess helium rate effects.

Table 4.2 Ex-situ ion irradiation parameters for the project organized by Sample ID name. All irradiations were completed with 9 MeV Fe^{3+}. The cells are filled as follows: target parameter/achieved parameter experimentally. For simplicity, the target experimental parameters for each irradiation will be shown in the rest of this work. T_{irr} = temperature of irradiation.

Sample ID	Total dpa	Dose rate (dpa/s)	T_{irr} (°C)	Helium co-injection rate (appm He/dpa)	Time at temperature (h)	Completion date
A1	15/15.1	$7\times10^{-4}/7\times10^{-4}$	300/298.2	0	~6	1/4/2023
A2	50/50.4	$7\times10^{-4}/7\times10^{-4}$	300/294	0	~20	4/25/2022-4/26/2022
A3	50/50	$1\times10^{-4}/9.97\times10^{-5}$	300/300	0	~139	5/25/2021-6/1/2021
B1	15/15	$7\times10^{-4}/7.2\times10^{-4}$	400/399	0	~6	8/4/2022
B4	15/15.1	$7\times10^{-4}/7.1\times10^{-4}$	400/401.6	10/10.3	~6	1/30/2023
C1	1/1.1	$7\times10^{-4}/7.4\times10^{-4}$	500/503	0	~0.4	9/7/2022
C2	5/5.3	$7\times10^{-4}/6.8\times10^{-4}$	500/502	0	~2	8/1/2022
C3	15/15	$7\times10^{-4}/7.1\times10^{-4}$	500/500.6	0	~6	1/6/2023
C4	50/50	$7\times10^{-4}/7.3\times10^{-4}$	500/499.8	0	~6	7/19/21-7/29/21
C5	100/100	$7\times10^{-4}/7.4\times10^{-4}$	500/499.6	0	~6	7/14/21
C6	15/15	$7\times10^{-4}/7.3\times10^{-4}$	500/498	10/9.96	~6	7/29/21
C7	50/50.1	$7\times10^{-4}/7.4\times10^{-4}$	500/499	10/9.96	~6	7/19/21-7/29/21
C8	100/100	$7\times10^{-4}/7.3\times10^{-4}$	500/500	10/10.1	~6	6/19/2021
C9	15/15.4	$7\times10^{-4}/7.2\times10^{-4}$	500/504.5	25/25.4	~6	2/3/2023
D1	15/15.4	$7\times10^{-4}/6.9\times10^{-4}$	600/601	0	~6	8/29/2022
D2	15/15.1	$7\times10^{-4}/7.1\times10^{-4}$	600/599.5	10/9.8	~6	2/1/2023

Table 4.3 Ex-situ ion irradiation parameters for the project organized by single effects testing. T_{irr} = temperature of irradiation.

Series	Sample ID	Total dpa achieved	Dose rate (dpa/s)	T_{irr} (°C)	Helium co-injection rate (appm He/dpa)
Dose Rate	A2	50	7×10^{-4}	300	0
	A3	50	1×10^{-4}	300	0
Dose	C1	1	7×10^{-4}	500	0
	C2	5	7×10^{-4}	500	0
	C3	15	7×10^{-4}	500	0
	C4	50	7×10^{-4}	500	0
	C5	100	7×10^{-4}	500	0
Temperature	A1	15	7×10^{-4}	300	0
	B1	15	7×10^{-4}	400	0
	C3	15	7×10^{-4}	500	0
	D1	15	7×10^{-4}	600	0
Helium (at various temperatures)	B4	15	7×10^{-4}	400	10
	C6	15	7×10^{-4}	500	10
	D2	15	7×10^{-4}	600	10
Helium (at different co-injection levels)	C3	15	7×10^{-4}	500	0
	C6	15	7×10^{-4}	500	10
	C9	15	7×10^{-4}	500	25

4.2.2 Ion Damage and Helium Co-implantation Calculations

A valid region of analysis in the irradiated samples must be determined to avoid surface-related and injected interstitial effects. This was evaluated by reviewing previous work completed on similar FM steel and ion irradiation conditions. Specifically, Getto [97] and Getto *et al.* [43] explains that near the surface (~300 nm or less) there is a larger vacancy-to-interstitial ratio due to the preferential loss of interstitials because of their higher mobility and increased survival efficiency of vacancies to interstitials near the surface in damage cascades. The excess vacancies promote void nucleation and hence induce artifacts into the analysis within the near-surface regime. The width of the near-surface zone also increases with increasing temperature, approaching widths of ~1 μm at high temperatures [98]. On the other hand, injected interstitials at the end of the heavy ion implantation can also artificially change the microstructural evolution by suppressing swelling with excessive interstitials and/or chemical effects. Ref. [99] found that the implanted ion profile can also broaden due to both thermal and radiation-enhanced diffusion. The longer the irradiation time or the greater the temperature, the greater the reduction of the region available for safe analysis due to the broadening. The authors concluded that ion energies in excess of 8 MeV are needed to create a broad enough region for safe analysis. Hence, 9 MeV Fe^{3+} ions were used to create a profile of injected ions such that the valid region of interest did not suffer from surface or injected interstitial effects. 3.42 MeV He^{2+} ions were used for helium co-implantation to obtain the desired helium concentration profile that matched the 9 MeV Fe^{3+} safe region damage profile.

Depth-dependent damage of 9 MeV Fe^{3+} ions and implantation of 3.42 MeV He^{2+} into CNA9 was calculated using the Stopping and Range of Ions in Matter (SRIM 2013) [100]. SRIM takes the ion type, ion energy, incident angle of ions, composition of the sample target in atomic

percent, and the thickness of the sample target as inputs to calculate the damage and implantation of ions. The SRIM damage calculations were conducted using “quick” Kinchin-Pease (KP) mode which has been documented to more accurately calculate damage levels of heavy ion irradiation experiments than other methods [101,102] The simulation used to calculate damage and helium implantation on CNA9 was developed based on previous studies in Grade 91 [42]. The simulation by Taller was run for 85,000 ions to obtain a visually smooth damage curves and adequate counting statistics. The compositions between CNA9 and Grade 91 are similar enough to create the same results from SRIM. Both CNA9 and Grade 91 have a Cr content of ~8.7% and both contain minor alloying elements less than 2%, with the rest of the content being Fe. Thus, it was assumed on first evaluation that variation in the calculated dose rates were to be within the error of the assumptions accounted for in SRIM, such as not incorporating temperature or lattice structure effects. The validity of this assumption was confirmed by running a shorter SRIM calculation within this work to 10,000 ions into CNA9 (Figure 4.3). This was done because a full SRIM calculation with 85,000 ions is computationally expensive. Figure 4.3 shows that it is indeed accurate to use the SRIM calculation of Grade 91 for CNA9 when accounting for simulation inaccuracies using SRIM including factors such as crystal structure. A displacement energy of 40 eV was used for Fe, Cr, Ni, V, and Mn, and 60 eV for Nb and Mo for both the initial simulation using Grade 91 and for the shorter CNA9 simulation. For all other elements, a displacement energy of 25 eV was used [1,42].

Figure 4.4a shows the damage curve of Fe ions and the level of helium implantation as a function from the surface of CNA9. Both are depth dependent. As such, the depth range of 1,100-1,300 nm beneath the surface of the sample was chosen as the nominal damage and helium co-implantation region to be assessed for microstructural characterization. At this depth range, the target irradiation parameters for dose, dose rate, and helium co-implantation are met. This region

is also far enough from the surface to avoid surface-related artifacts while avoiding artifacts from the injected Fe ions (Figure 4.4b). All microstructural characterization probing irradiation effects was carried out at this depth range. To probe only thermal effects on precipitate behavior, microstructural characterization was completed past a depth of 3 μm which is past the ion range (2.5 μm) and thus limited to no effects from irradiation exist past this range or characterization was completed on liftouts taken from the thermal-only region of the bulk sample that was irradiated.

Eq. 4.1 was used to achieve the desired experimental damage dose and dose rate. The damage rate due to the ion flux was attained from SRIM simulation and had a value of 0.3589 displacements/Å-ion for the 9.0 MeV Fe^{3+} ion beam used in all experiments. The desired ion beam current was calculated to achieve the desired damage rate and was configured by MIBL staff for each experiment. An estimation of the total ion fluence was calculated through periodic measurements of the Fe^{3+} beam current during irradiations and integrating it over the time of irradiation. The damage rate from the energy degraded helium ions was determined to be several orders of magnitude lower than the damage rate for the 9.0 MeV Fe^{3+} ion beam and considered negligible [103,104]. Ref. [97] pre-implanted helium with energies of 80, 140, 220, 310 and 420 keV into HT9. The damage caused by pre-implantation of 1000 appm helium was estimated to be 0.02 dpa. The 3.42 MeV He^{2+} ions after the foil degrader were between 520 keV and 1.26 MeV. While these energies are higher than used in Ref. [97], they are not expected to cause significant levels of damage due to the light mass of helium [1].

$$dpa = \frac{(SRIM\ damage\ rate)\sum(ion\ beam\ current \times time)}{(number\ density\ of\ sample)(ion\ charge)(specimen\ area\ irradiated)} \quad \text{Eq. 4.1}$$

For dual ion irradiations, the rate of helium co-implantation was controlled by an aluminum foil degrader in the MBC. The implementation of, design of, and calculations for the use of this

foil degrader was completed by a previous student, Dr. Stephen Taller, and is now part of standard MIBL procedures for dual ion irradiations with helium co-injection [42,105]. Dr. Taller used SRIM to calculate the energy, E, position vector in three dimensions, $\boldsymbol{r}$, and direction vector ($\boldsymbol{\varphi}$) in three dimensions for each ion exiting the aluminum foil degrader and for each angle of the foil rotation ($\boldsymbol{\theta}$) in one-degree increments. The direction vectors calculated with SRIM were used to simulate the trajectory of individual helium ions from the foil to the sample surface. A schematic of this description is shown in Figure 4.5. The foil degrader was controlled by a LabView™ script during irradiations. The result of the degrader system is the helium/dpa ratio can be maintained constant in the nominal damage region, as seen in Figure 4.4.

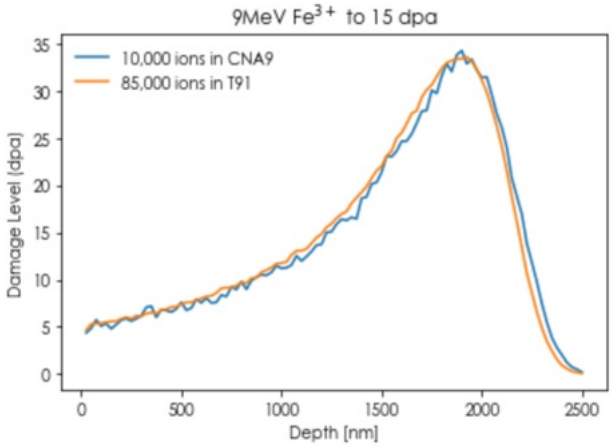

Figure 4.3 A quick KP SRIM calculation was run using 10,000 incident 9 MeV Fe^{3+} ions into CNA9 to check that the SRIM results from running 85,000 ions into Grade 91 could be used.

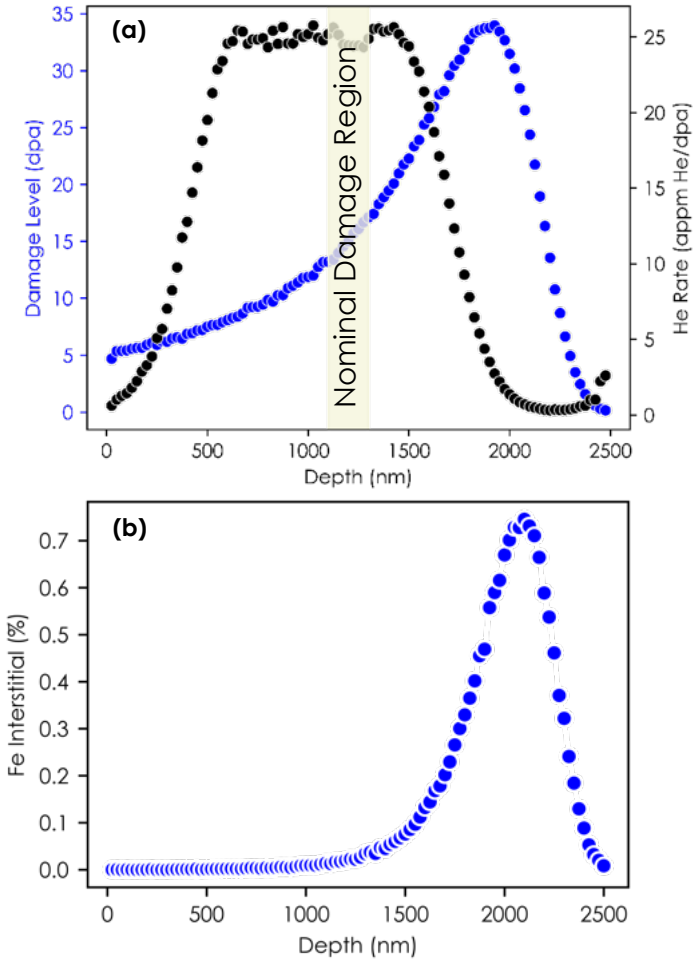

Figure 4.4 (a) Plot showing the damage curve for Fe ions (blue, left axis) and the level of He implantation (black, right axis), both as a function of depth beneath CNA9's surface. (b) The percent of Fe interstitials implanted from irradiation with Fe ions.

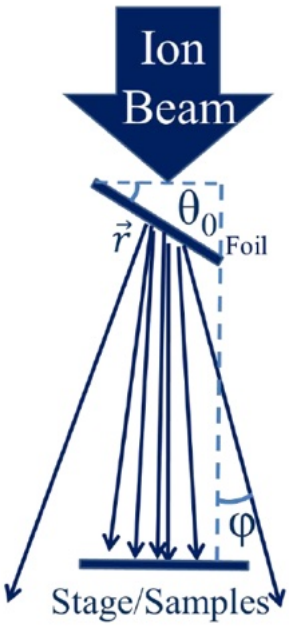

Figure 4.5 A schematic of the foil degrader geometry used for helium co-implantation during dual ion irradiations, taken from [42].

4.2.3 Ion Irradiation Details and Set-Up

Irradiations were conducted in two different beamlines of the MIBL facility, chosen based off of experimental parameters and facility scheduling. Irradiation A3 was conducted using Beamline 2 while all other irradiations used the multi-beam chamber (MBC) connected to Beamlines 4, 5, and 7 (Figure 4.6). Beamline 2 is a single-beam chamber with no helium co-implantation ability. The MBC chamber is connected to three beamlines but only Beamlines 4 and 7 were used. Beamline 4 delivered 9 MeV Fe^{3+} ions from the NEC Pelletron accelerator normal to the surface of the samples to induce the highest range of ions into the samples possible. Beamline 7 delivered 3.42 MeV He^{2+} ions from the 1.7 MV General Ionex Tandem Accelerator for dual beam irradiations at an angle of 60° from the surface of the samples. Since helium is a light

element, an off normal configuration for the helium beam enables similar ranges to the on-axis Fe^{3+} implantation.

A photo of a completed irradiation stage and a schematic of an irradiation stage mounted in the MBC is given in Figure 4.7. After the samples finished the polishing process as described previously, they were loaded onto the appropriate irradiation stage. The samples were arranged on top of a copper foil and Au paste to ensure good thermal conductivity with the irradiation stage. A hold down bar, as shown in Figure 4.7, was used to keep the samples in place during the experiment. The area for irradiation (4×6 mm^2) was marked by an engraver. Type J thermocouples were made by weaving Fe and Constantan (Cn) metal wires through ceramic pieces, taking care that the wires did not touch at any point. One side of the wires were connected to a feedthrough port on the irradiation stage to allow for digital control and the other side of the wires were spot welded onto a guide bar. The only point at which the Fe and Cn wires touched was at the point of welding on the guide bar surface. Each guide bar had two sets of thermocouples. The irradiation stage was then loaded into the appropriate chamber using a copper gasket and tightly bolted to ensure good vacuum. A cartridge heater was inserted to the back of the stage for temperature control. Cables from a computer readout were attached to thermocouple feedthroughs. The thermocouple cables connect to a National Instruments Module *NI-9213* and the module is plugged into a National Instruments cRIO *cRIO-9074*. The Thermocouple Voltage Signal is digitized in the module and converted to Celsius in the cRIO's Real Time OS running LabVIEW™. These values are saved to the laboratory network and are available to save and are shown on available PC's. The chamber with the loaded stage was pumped down to ~10^{-1} torr using an Edwards Model nXDS10i roughing pump and plasma cleaned for 2-3 hours using an Evactron EP Series Plasma De-Contaminator to prevent C contamination. Typically, the stage would also be heated to ~150°C to

allow for outgassing of the stage during the plasma cleaning step. The chamber would then be brought down to room temperature and pumped down further overnight using a CTI-CRYOGENICS Model TORR 8 Cryopump turbomolecular pump to achieve a pressure in the range of ~1×10^{-7} torr. Standard procedures for starting the irradiation would begin the following day.

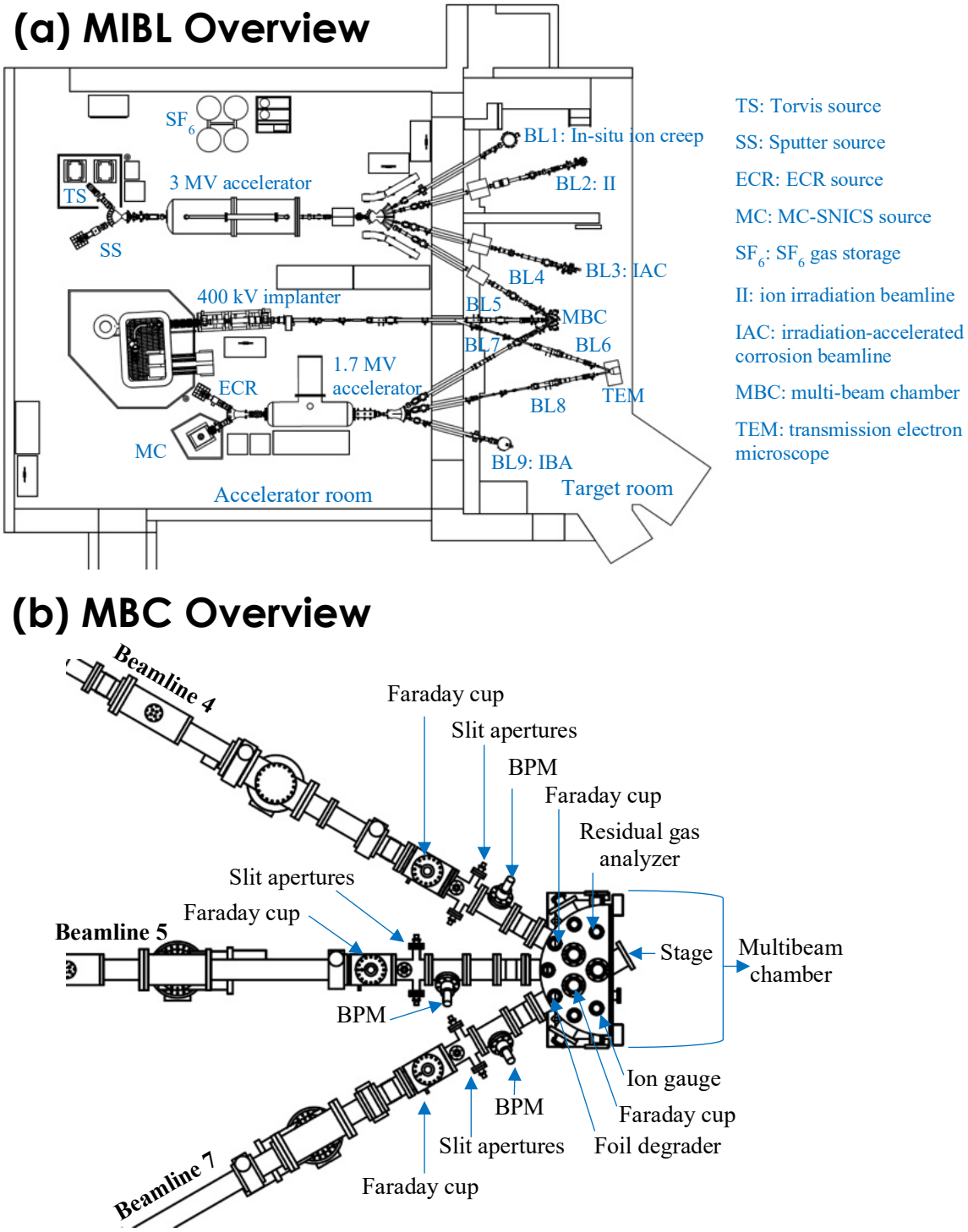

Figure 4.6 (a) Layout of the MIBL facility showing the various beamlines, accelerators, and sources. (b) Schematic showing the MBC chamber used for the majority of irradiations. Schematics taken from [42].

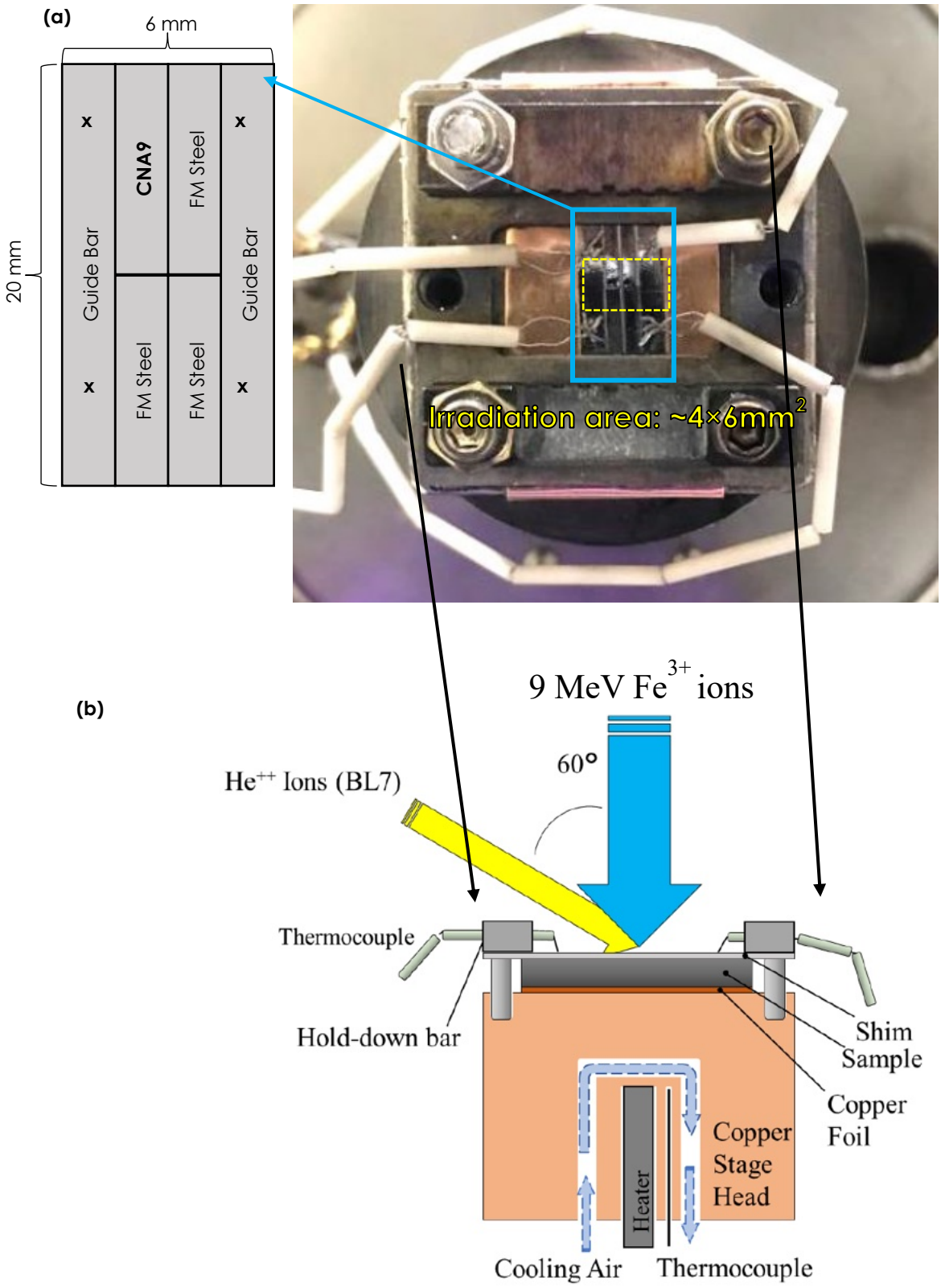

Figure 4.7 (a) Picture of an actual irradiation stage used for an experiment for this work with a schematic showing the samples irradiated. (b) Schematic of the MBC chamber used for the majority of irradiations, taken from [42].

4.2.4 Details on the Day of Ion Irradiation Experiments and Running the Experiments

On the day of the irradiation before the experiment started, the alignment of the beams and heating of the stage to approximately 5°C below the target temperature of the irradiation would be completed to compensate for beam heating once the beam was set onto the samples. The beams were aligned to hit the desired area on the samples using high-powered lasers that were directed down the ion beamlines parallel to the directions of the beams (Figure 4.9). The laser would illuminate the samples and the markings from the engraver would allow for precise alignment of the beams. A ceramic piece was also used for final adjustments of the alignments for the irradiations conducted in the MBC. The ceramic piece located in the chamber can be positioned directly in front of the samples for alignment of the ion beams, then positioned below the stage so as not to block the beams from hitting the samples.

The temperature on the stage was maintained using a 2D FLIR® infrared thermal pyrometer (Teledyne Model A655sc) which was focused onto the stage through a Ge window. The thermocouple readings were used to calibrate the 2D FLIR® before the start of the irradiation. The heating process before the start of the irradiation would take several hours to allow for the entirety of the stage to reach steady-state at elevated temperature. If the target temperature was not held constant for at least 45 minutes, the 2D FLIR® calibrations would drift during the irradiation as the entire stage continued to heat up. The time at temperature before irradiation is not expected to have any noticeable effects on the microstructure of the FM steels. This can be ascertained by the fact that the precipitates in the thermally exposed portions of CNA9 during irradiations at 300, 400, 500, and 600°C that were at temperature for ~6 hours during the irradiation, plus however long it took to reach temperature before the irradiation started, had no significant differences in size, density, or volume fraction to the precipitates in the control sample

(refer to Chapter 5). The 2D FLIR® was calibrated to the thermocouple readings using areas of interest (AOI) drawn on the samples in the LabView™ program (Figure 4.8). The emissivity of the AOIs was adjusted to achieve agreement with the thermocouples before irradiation was started.

In parallel, MIBL staff would prepare the sources and accelerators to achieve the desired energy and current of the Fe and He ions. The area of irradiation was controlled with a slit aperture system for each beamline. The width of the apertures in the X and Y directions were set to define the desired irradiation area on the samples. Note, X direction denotes the direction parallel to the floor of the laboratory and Y perpendicular to X. The slits also measured the current of the beam incident on them and could be monitored during the irradiation. A slit aperture was used for both the Fe and He beams, but the 60° incident angle of the He beam to the Fe beam had to be taken into consideration when setting the slit apertures to create a 10×10 mm^2 over scanning area of the helium beam. The slit apertures for both beams were positioned approximately 1,000 mm from the sample surface. The helium ions were delivered via a rastered beam. The Fe beam, however, was defocused to achieve a uniform damage profile on the samples (within 10%). In addition, previous work has shown that defocused beams represent neutron irradiations more accurately and in particular do not induce experimental artifacts to precipitate responses that rastered Fe beams may induce [106].

While the sources were being prepared, the cold trap was started. A copper piece in the beam chamber, called the cold trap, encircles the irradiation stage. The cold trap is cooled internally with a liquid nitrogen tank and serves to prevent contamination during irradiation and achieve better pressure. On average, the cold trap was replenished with LN_2 every 1 h to ensure proper cooling and prevent outgassing of the cold trap during the irradiations. Replenishing was controlled by a LabView™ program.

Once the stage was at temperature and the beams were ready, the beams were allowed to impinge on to the samples. During the irradiations, temperature, pressure, beam current, and beam profiles were recorded and displayed on computers using custom built LabView™ programs. The temperature was monitored using the 2D FLIR® and thermocouple readings. The irradiations were maintained within ±10°C of the desired target temperature. The temperature could be changed using the digitally controlled heater cartridge. The partial pressure of each gas species in the vacuum was monitored using an Inficon Transpector® MPS Residual Gas Analyzer. The beam current on each slit was constantly monitored with current readings and a live beam profile (Figure 4.8). The slit on the currents could be adjusted if needed to maintain a flat profile of the defocused Fe beam. The current on the source could also be digitally controlled to maintain the desired current on the stage. In addition, Faraday cups were inserted into the iron and helium beamlines in front of the stage periodically (typically every 30 min or every 1 h, depending on stability of the beam and irradiation length) and measurements of the iron and helium total currents impacting the stage were recorded. These measurements were inserted into an Excel sheet that calculated the dose achieved, He/dpa ratio, and time left in the irradiation. If the temperature, slit current, or stage current deviated from a set tolerance, the LabView™ programs controlling these parameters would trigger an alarm. The pressure in the vacuum chamber was monitored using an InstruTech Inc. model IGM402 hot cathode ionization vacuum gauge. The target pressure for all irradiations was below 1×10^{-7} torr. However, this was hard to achieve with the high temperature experiments at 600°C. These experiments were started around 3×10^{-7} torr. The only samples to have oxidation layers develop were irradiations C8, C9, and D2. At higher temperatures, the helium beam will cause oxidation even if the pressure is kept at ~1×10^{-7} torr. The oxidation layers were not expected to significantly affect the results, as no significant differences in the microstructure were found in

areas of oxidation and in areas of no oxidation. Typical irradiation parameters are shown in Table 4.4.

Once the desired damage level was reached, the irradiation was stopped and shutdown procedures were followed. The beams were blocked from hitting the stage. The heater was set to 0 V and a supply of air was set to maximum flow rate to quickly cool the samples to reach below 100°C within 10 minutes. The samples would be unloaded the next day and then prepared for characterization. Data from all experiments can be found in Appendix B.

Table 4.4 Various parameters measured during all irradiations and their typical values.

9 MeV Fe^{3+} Current (measured with a Faraday inserted directly in front of the irradiation stage)	189.9 nA
Typical average Fe^{3+} current on the X slits	0.15 μA
Typical average Fe^{3+} current on the Y slits	0.15 μA
3.42 MeV He^{2+} Current (measured with a Faraday inserted directly in front of the irradiation stage)	707.4 nA (25 appm He/dpa) 279.3 nA (10 appm He/dpa)
Typical average He^{2+} current on the X slits	0.05 μA
Typical average He^{2+} current on the X slits	0.05 μA
He/Fe Ratio	1.47
Typical pressure	$< 3\times10^{-7}$ torr

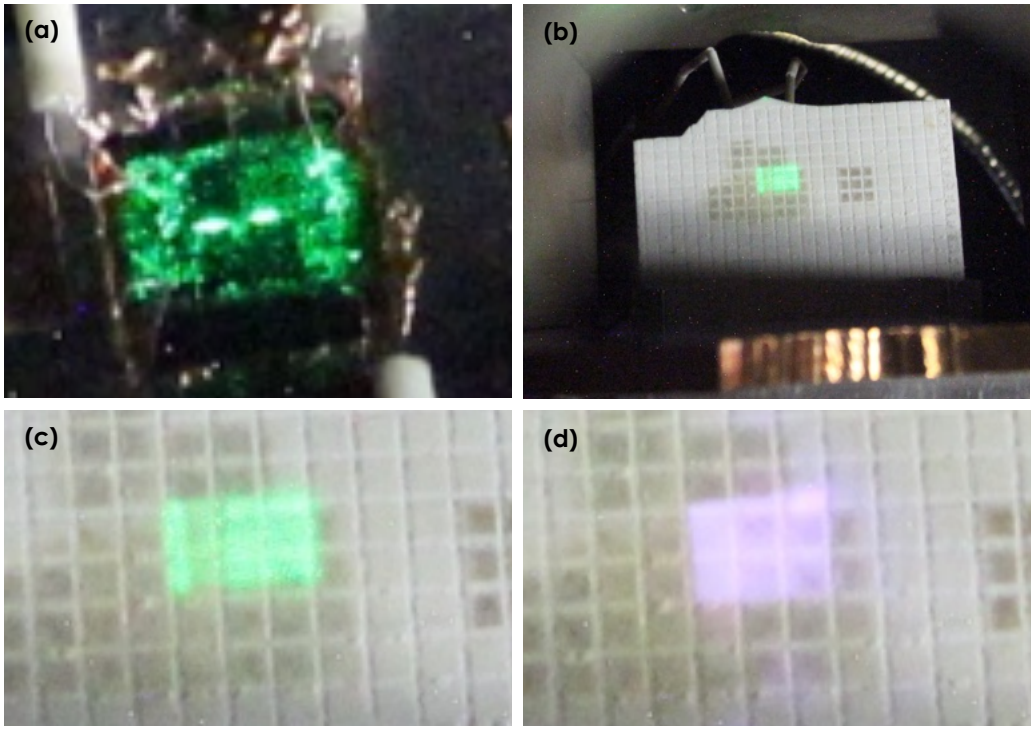

Figure 4.9 (a) Image showing the irradiation stage from Irradiation D2 with the green laser simulating the location of the Fe beam on the samples. (b) Image showing the ceramic piece that is inserted in front of the samples to be irradiated in the MBC. (c) Close up image of (b). (d) The purple laser simulates the He beam location on the samples. The purple laser was aligned to the location of the green laser (Fe beam) to ensure that both beams hit the samples simultaneously in the same region.

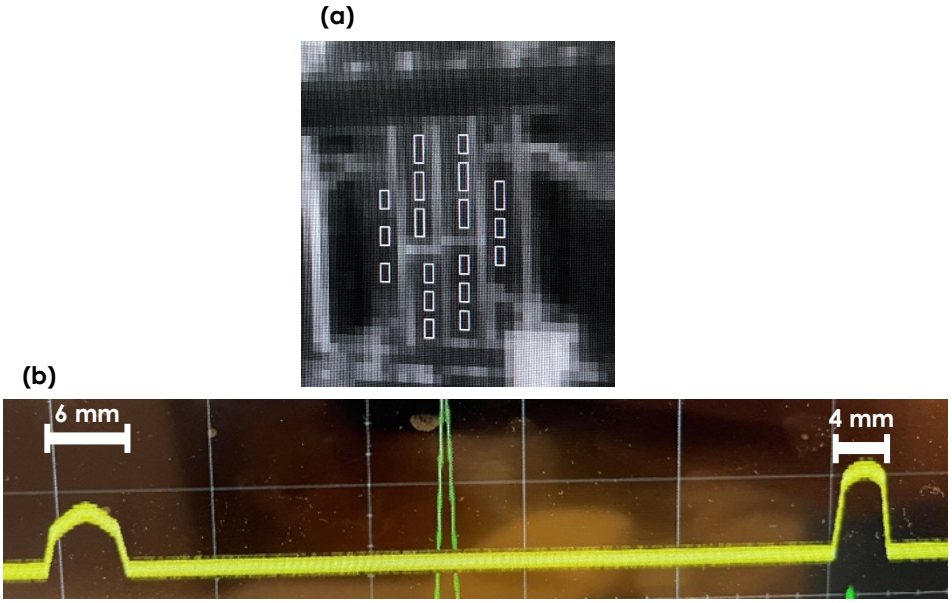

Figure 4.8 (a) Example of AOIs located on each sample in the 2D FLIR program to record temperature during irradiations. (b) Example of the defocused Fe beam profile.

4.3 S/TEM Sample Preparation

This section details the preparation and analysis methods used to examine the microstructure of CNA9 after it was irradiated. It consists of TEM sample preparation, imaging with TEM and STEM, and the characterization and analysis of the images.

All TEM sample preparation was conducted on dual Scanning Electron and Focused Ion Beam Instruments (SEM/FIB) at the Michigan Center for Materials Characterization $(MC)^2$ at University of Michigan-Ann Arbor. The $(MC)^2$ facility houses three FIB/SEM instruments: the Thermo Fisher Nova 200 Nanolab SEM/FIB, the Thermo Fisher Helios 650 Nanolab SEM/FIB, and the Thermo Fisher Helios G4 PFIB UXe. All instruments were used to create TEM samples using the same procedures, except for slight variations in ion beam energy and current which is dependent on the instrument used. All instruments have an electron beam (used mainly for imaging) perpendicular to the surface of the bulk sample at 0° and a gallium (Thermo Fisher Nova 200 Nanolab SEM/FIB, the Thermo Fisher Helios 650 Nanolab SEM/FIB) or Xenon (Thermo Fisher Helios G4 PFIB UXe) ion gun 52° from the electron beam for imaging and milling.

A typical TEM sample preparation methodology was used for the extraction of cross-sectional slices of material penetrating a few microns beneath the irradiated sample surface, encompassing the full damage region from irradiation and past the ion implantation depth (Figure 4.10). After irradiation, the bulk sample of CNA9 was cleaned in acetone, methanol, and ethanol and mounted on a stub with conductive adhesive (either Cu tape or Au paste) with the irradiated side facing up. The stub containing the bulk sample of CNA9 was loaded into a dual SEM/FIB and pumped down. A thin layer of carbon ($(12\text{-}25\mu m)^X \times 2\mu m^Y \times 0.3\mu m^Z$) was deposited at 0° (perpendicular to the electron beam) using a 3-5keV/6nA carbon beam within the irradiated region to define the location of the lift-out. The carbon layer protected that area from potential milling

from the ion beam, which would affect accurate estimations of the nominal damage region. The stage was then tilted to 52° (perpendicular to the ion beam) and a layer of 100% platinum or a layer of 80% platinum/20% carbon was deposited on top of the carbon layer using a gallium or Xenon beam with a current of about 0.3-1nA and ion energy of 12-15keV. Using a higher current of 20-60nA and energy of 30 keV, the gallium or Xenon beam was used to create trenches parallel to the long sides of the C/Pt layer using a regular cross section pattern about 8 μm deep. The long sides of the deposition were cleaned up using successively lower currents (0.3-4nA) with the cleaning cross section pattern. The stage was then tilted back to 7° and the gallium or Xenon beam was used to cut underneath the lift-out in a U-cut shape. After this was completed on both sides of the lift-out, the lift-out was only connected to the bulk sample on one side. A micromanipulator (called an Omniprobe™ needle) was inserted and positioned such that it was just next to the free-standing edge of the lift-out. A small amount of platinum (deposition of ~0.125 μm^3) was used to weld the Omniprobe™ needle to the sample. The connecting edge was cut through with the gallium beam to free the TEM specimen from the bulk sample and the Omniprobe™ needle with the lift-out was retracted to its original position. The dual SEM/FIB was then vented, the bulk sample removed, and FIB grid holder with an empty FIB grid was loaded into the chamber and pumped down. The Omniprobe™ needle with the lift-out was lowered to the FIB grid position and the two lower corners of the lift-out sample were welded to the grid. The needle was cut free from the sample and retracted from the chamber. The stage was then rotated 180° to weld the back sides of the connected lift-out.

After this procedure, the resulting lift-out was about 2 μm thick and 6-8 μm long. Thinning procedures were then commenced to thin the sample from 2 μm thick to the desired thickness through successive milling steps at various angles, ion energies, and ion currents. The long sides

of the lift-out were first cleaned using a gallium or Xenon beam with 30keV energy and 0.3-4nA current with a rectangular milling box. This was done at 52° on both sides of the lift-out until the lift-out was approximately 1 µm thick. The sample was then tilted to 54° and windows of dimensions (3-8)μm^X × (4-8)μm^Y were milled on the side of the lift-out, viewable in the electron beam. The sample was rotated 180° and the same window-making procedure was completed. Windows were used to prevent bending of the liftout as it reached its target thickness of approximately 100 nm. The windows were thinned further at 56° and 48° using ~30 keV/1nA and ~16 keV/ 0.2nA until the sample contrast in the electron beam became slightly white in the area of interest when viewed at 5 keV/0.4 nA. The procedure to create lift-outs used only for compositional analysis with STEM-EDS was completed here. Otherwise, samples underwent final cleaning steps to mill away as much FIB-induced damage as possible. Each side of the lift-out was cleaned at 57° and 47° for 10-20 minutes per side using both 5keV and 2keV beams. The final thickness of the foil was approximately 80-130 nm in the nominal damage region. A completed liftout and general microstructure of CNA9 at various conditions is shown in Figure 4.11.

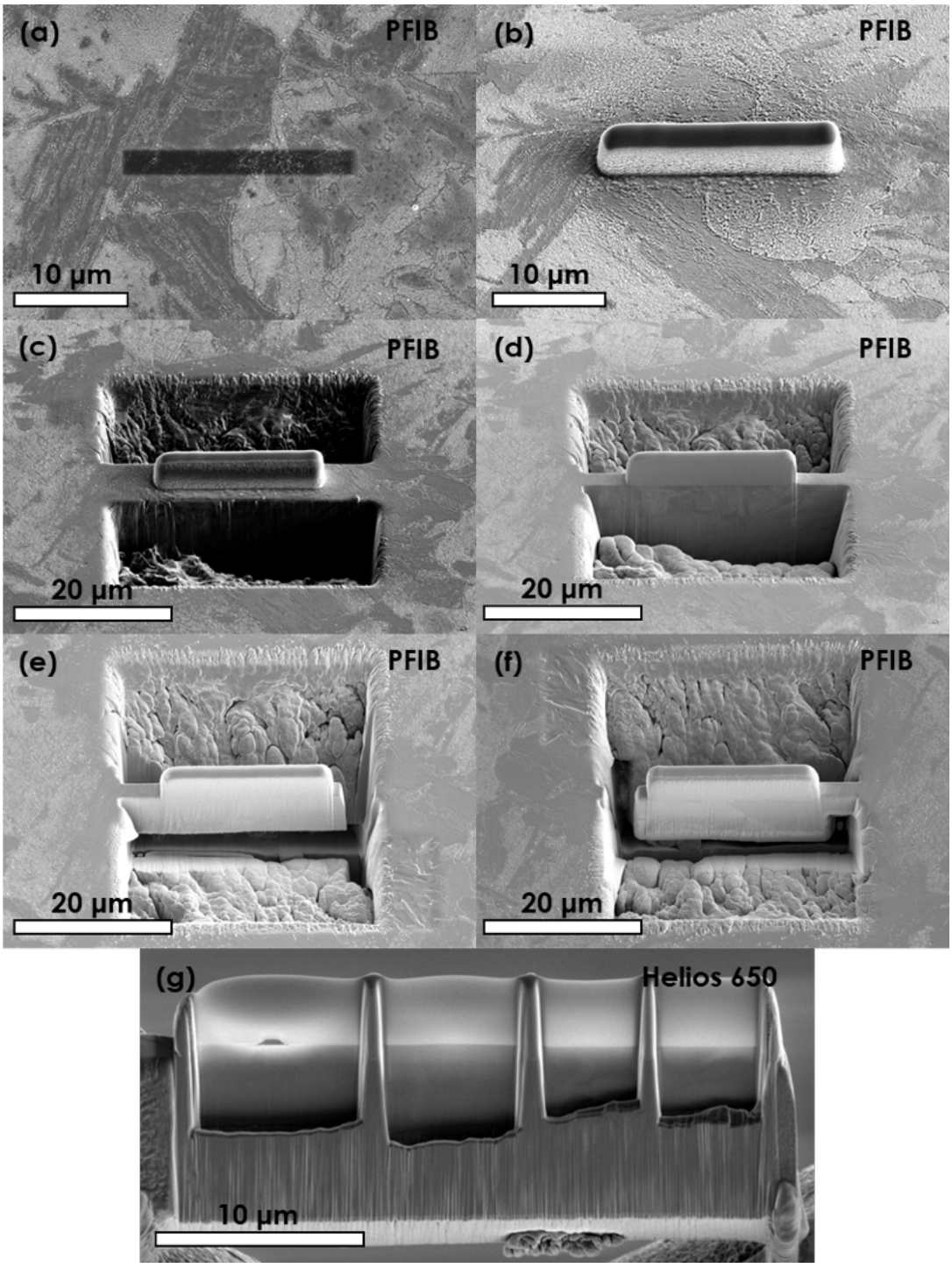

Figure 4.10 Various steps in the TEM sample-making process: (a) C deposition perpendicular to the electron beam on an irradiated sample surface, (b) Pt/C cap deposition on top of the C layer perpendicular to the ion beam, (c) trenching on either side of the protective Pt/C layer to penetrate the ion irradiated material, (d) successive thinning steps tothin the TEM sample to ~1 µm, (e) creating a U-cut so the sample is only connected to the bulk specimen on one side, and (f) rotating 180° to ensure that the U-cut is complete. After step (f), the sample was removed from the bulk specimen with a Pt-welded needle and placed in a valley on a grid. The grid was then successively thinned to electron transparency, as shown in (g).

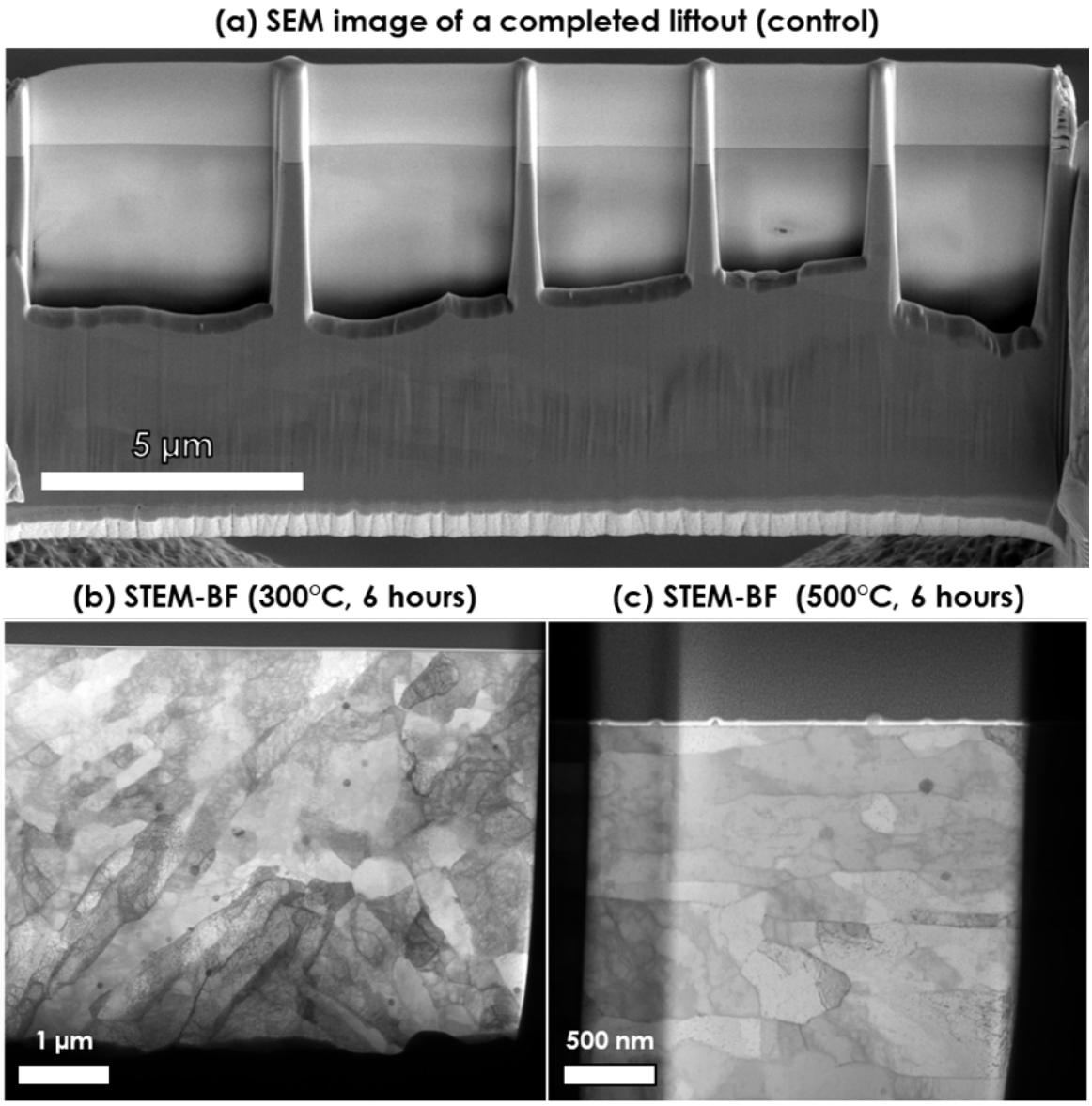

Figure 4.11 (a) Example of a TEM sample after final thinning procedures. This liftout was taken from the control specimen. It was thinned to 20-50 nm for high resolution imaging of TiC precipitates. Examples of the CNA9 grain structure taken from thermally annealed portions of two different conditions (b,c). The grain structure did not noticeably change from the control specimen as a function of irradiation.

4.4 S/TEM Sample Thickness Measurements

The thicknesses of the lift-outs were obtained with the use of energy-filtered TEM (EFTEM)-based thickness mapping [107] (Figure 4.12). EFTEM is an analytical technique based off the inelastic scattering that occurs when a monoenergetic beam of electrons passes through an

electron transparent sample. During inelastic interactions of the monoenergetic electron beam produced by the electron gun with the TEM lift-out, inelastically scattered electrons will lose a finite amount of energy based off the composition and thickness of the sample. This results in an energy spread of the electron beam exiting the sample. EFTEM uses an energy filter to choose which electrons will contribute to the final image. Thickness maps using EFTEM are formed by filtering the final electron spectrum to consist of only electrons that were inelastically scattered but only lost a small amount of energy.

Thickness mapping was completed on the Thermo Fisher Tecnai G2 F30 TWIN Electron Microscope (TF30) as part of the $(MC)^2$ facility. The TF30 is equipped with a Gatan® Imaging Filter (GIF) for electron energy loss spectroscopy (EELS) and EFTEM. The GIF was controlled by Gatan's Digital Micrograph® (DM) user interface for EFTEM. At the beginning of every session, the TEM was aligned and then put in EFTEM mode. An optimal objective lens strength of 89.9022% (vendor indicated) was used. The GIF was calibrated using DM's automatic procedures. A 1024×1024-pixel thickness map was acquired using the built-in function in DM. DM would obtain an elastic image and an unfiltered image. From the total intensity in the unfiltered image, I_t, and the zero-loss intensity in the elastic image, I_0, DM calculated the thickness of the sample. User inputs for the software calculation consisted of the collection angle (defined by the apertures) and the mean free path of inelastic electron scattering, λ. λ was estimated for pure Fe and found to be 121 nm. The thickness, t, was calculated using the following equation:

$$t = -\lambda \ln\left(\frac{I_t}{I_0}\right) \qquad \text{Eq. 4.2}$$

where λ was estimated from the following equations taken from Ref. [108] using E_0 = 300 kV for the electron beam, Z=26 for Fe, and β=10 mrad for the collection angle:

$$E_m = 7.6Z^{0.36} \quad \text{Eq. 4.3}$$

$$F = \frac{1 + {E_0}/{1022}}{\left(1 + {E_0}/{511}\right)^2} \quad \text{Eq. 4.4}$$

$$\lambda = \frac{106FE_0}{E_m \ln\left(\frac{2\beta E_0}{E_m}\right)} \quad \text{Eq. 4.5}$$

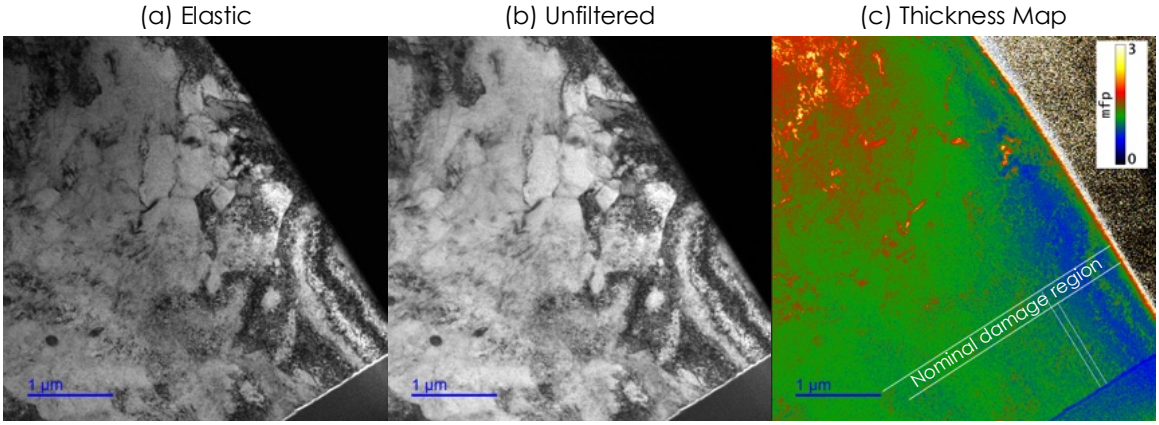

Figure 4.12 Example of an (a) elastic image, (b) unfiltered image, and (c) thickness map taken with EFTEM from the B4 irradiation condition.

4.5 S/TEM-EDS Composition Mapping of TiC Precipitates

Characterization of the TiC precipitates was completed through compositional mapping using STEM equipped with Energy Dispersive X-ray Spectroscopy (EDS) capability. During EDS acquisition, the incident electron beam from the TEM hits the sample and excites electrons in the inner electron shells of atoms, such that these electrons get ejected from their lower energy shells. Outer shell electrons will fill the electron holes left in the inner shell electrons. X-rays with energy equal to the difference between the higher and lower energy shells will be ejected in the process and absorbed by the EDS detectors. These characteristic X-rays allow for elemental identification with high accuracy. STEM-EDS acquisition was carried out on the Thermo Fisher Talos F200X G2 S/TEM within the $(MC)^2$ facility using the high-visibility low-background double-tilt (α =

±35°, β = ±30°) holder for optimized EDS acquisition and the Velox software. The EDS system on the Talos is equipped with a Super-X window-less detector consisting of four equal crystals with an active area of 4 × 30 mm^2 and a solid angle of 0.9 mrad. The resolution of STEM on the Talos is <0.16 nm. If TEM samples for EDS analysis are too thin, statistics will suffer from a lack of counts. If TEM samples are too thick, the X-rays may be absorbed by the sample before hitting the detectors. Hence, all samples (except for one) for EDS were between 80-130 nm thick. Parameters for STEM-EDS acquisition are shown in Table 4.5. TiC precipitates were identified by their Ti composition. Due to detector limitations of accurately identifying light elements, carbon can be identified with EDS but it is not as reliable as heavier elements like Ti. Hence, Ti was used for best and most consistent results.

Table 4.5 Parameters used for STEM-EDS acquisitions.

Parameter	Average Values
Sample Thickness	80-130 nm (one sample was 150 nm)
Pixel Size	519.0 pm
Dwell Time	8-20 µs, depending on drift
Count rate	~80-140 kcps
Dead time	~10-20%
Screen current	0.6-1.2 nA
Map time	45 min – 1 h
Gun	3
Spot Size	2
Camera Length	205 mm
Post-processing	Net filter, 3×3-pixel average filtering
Image Size	512×512
Magnification	450kx, except for a few 320 and 245kx maps

4.6 Characterization of TiC Precipitates

Individual STEM-EDS maps were characterized to ascertain TiC precipitate diameter, number density, and volume fraction as a function of irradiation parameters. The number of maps

per condition varied as a function of the density of precipitates. A minimum of two lift-outs per condition were taken to account for material heterogeneity.

The location of each STEM-EDS map was correlated to its location in the appropriate EFTEM thickness map and the average thickness of the area of the EDS map was extracted. Precipitates in the nominal damage region on each map were identified. The major axis, *a*, and minor axis, *b*, of each precipitate was measured in a freely available image processing suite called FIJI, or ImageJ. An example of a counted map, including the manual labels, is shown in Figure 4.13. The equivalent diameter was then calculated as:

$$d_{eq} = \sqrt{a \times b} \qquad \text{Eq. 4.6}$$

The major axes, minor axes, and equivalent diameters of each STEM-EDS map were digitally recorded. The mean equivalent diameters of the precipitates present in each map for a given condition were calculated, and the final average equivalent diameter for each condition was calculated as the average of the mean equivalent diameters of each map. The same was done for the equivalent radii. The error was calculated as the standard error of the mean equivalent diameters of each map. The volume of each precipitate in every map was summed and divided by the total volume assessed per map. Final values for the volume fraction of each condition were calculated as the average and standard error of the volume fractions of each map. The number density of each map was calculated as the number of precipitates counted divided by the total volume assessed for each map. Final values for the number density of each condition were calculated as the average and standard error of the number densities of each map for that condition. This method of error analysis allows for a quantitative understanding of the heterogeneity present in the precipitate size, number density, and volume fraction for each condition.

Outlier analysis was also conducted for all precipitates in each condition. Outliers for each condition were found by calculating the interquartile range. Any measured diameters outside of the interquartile range were removed from the analysis (Figure 4.14). All data presented within for precipitate equivalent diameter (*e.g.*, size), number density, and volume fraction reflect data free from outliers.

Precipitate size distributions were calculated using Gaussian kernel density estimation with the built-in Python 3.7 Seaborn violin plot function. The violin plots were scaled by the number of observations present for each condition. The optimal bandwidths for the violin plots were assessed individually for each condition using the built-in Scott criterion [109]. Box plots showing the mean diameters and interquartile range were also calculated with the built-in Python 3.7 Seaborn box plot function overlaid onto the violin plots. Individual measurements of precipitate diameters were also overlaid onto the violin and box plots using markers.

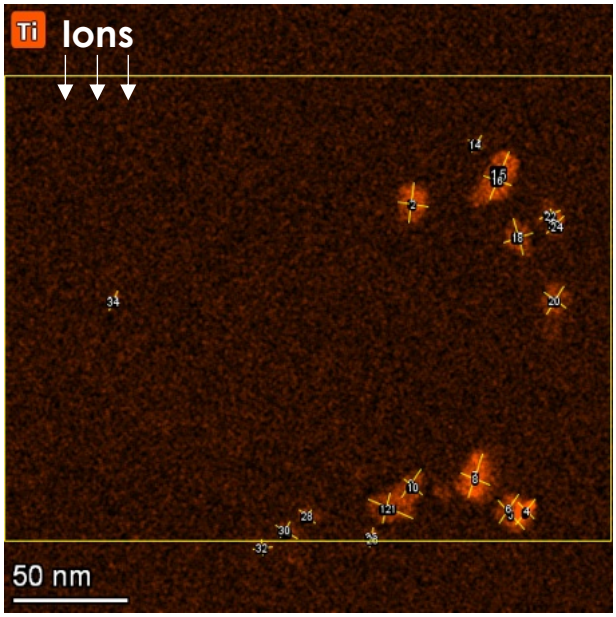

Figure 4.13 An example of a STEM-EDS map for Ti showing TiC precipitates in the nominal damage region (in between yellow brackets). Only precipitates in this region or touching the edges of this region were counted for the irradiation conditions.

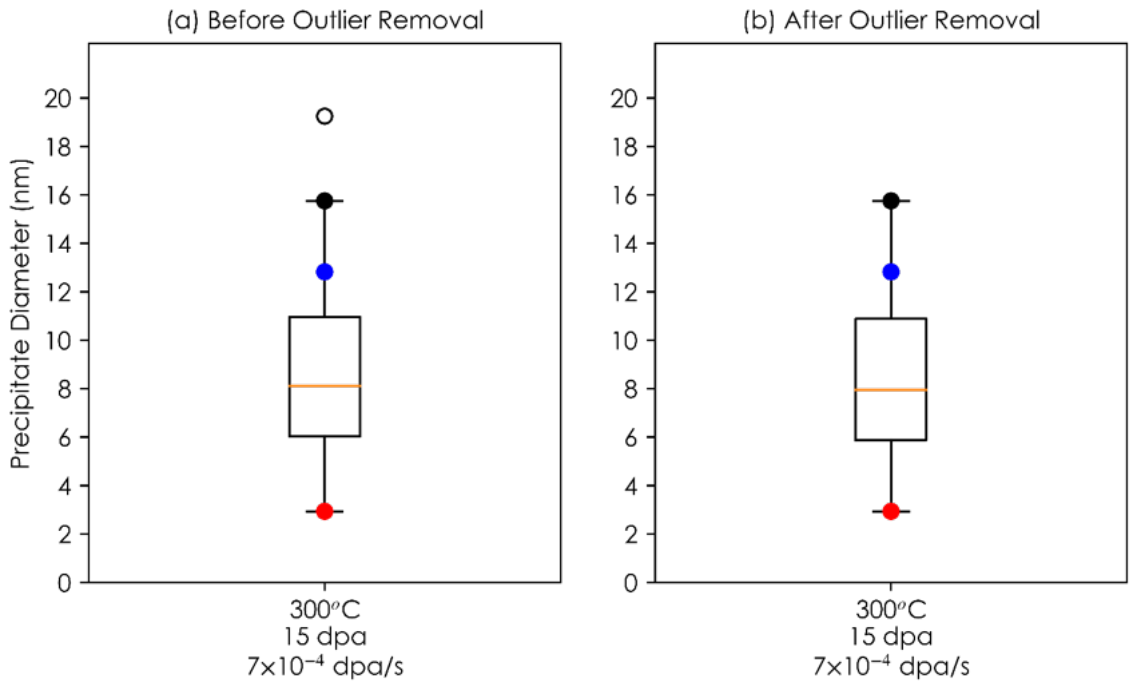

Figure 4.14 Outlier analysis was conducted on each condition studied. This is an example of the analysis for the single beam 15 dpa condition at 300°C, where one only outlier (the white circle in (a)) was removed.

4.7 Characterization of Size and Density of Cavities

Imaging of cavities in the matrix and on precipitates in dual ion irradiated CNA9 specimens was also completed on the Thermo Fisher Talos F200X G2 S/TEM. Conventional TEM off-zone bright-field (BF) imaging using Fresnel contrast was utilized to image cavities. A standard procedure for consistent imaging of cavities across all samples was used. Cavity images were taken with Gatan One View bottom mount camera at 245kx with an acquisition time of 2-8 μs and a resolution of 4k. The magnification at 245kx allowed for a field of view of 250.2 nm × 250.2 nm and a resolution of 0.061 nm/pixel. Cavity imaging occurred in regions of interest that had been compositionally mapped with STEM-EDS to allow for spatial correlations to be made between location of cavities (in the matrix or on the precipitate-matrix interface) to the size and density of cavities.

A series of underfocused and overfocused images were collected in each region of interest from a focus value of -1 μm to +1 μm in incremental 0.5 μm steps. Cavities do not have noticeable contrast when imaged in focus. However, deviating the focus value from the in-focus condition causes contrast of the cavities to become noticeable due to their mass difference with the Fe matrix. In underfocused images, cavities appear as lighter features with a darker fringe around them. In overfocused images, the cavities appear as darker features with a lighter rim around them. The underfocused images taken at -0.5 μm were used to estimate the size and density of the cavities per condition. The images taken at -0.5 μm, +1 μm, and -1 μm were used to help verify that the feature identified as a cavity in the -0.5 μm image was indeed a cavity. Example images of underfocused and overfocused cavities in the matrix are shown in Figure 4.15. This region of interest in the C9 condition had no MX-TiC precipitates present. Cavities on the precipitate-matrix interface were observed by overlaying CTEM BF images on top of STEM-EDS maps of Ti. This way TiC precipitates, and any correlated cavities, could be assessed. An example of a CTEM BF image in the -1 μm underfocused condition overlaid on top of a STEM-EDS map of Ti is shown in Figure 4.16. The diameters of the cavities in the matrix and on the TiC precipitate-matrix interfaces were assessed with ImageJ.

Cavity size distributions were plotted in two different manners. In the first method, the distribution was calculated using a Gaussian kernel density estimation with the built-in Python 3.7 Seaborn violin plot function. The violin plots were scaled by width. Width, instead of the number of counts as was done for precipitates, was used to scale the plots because the number of matrix cavities greatly outnumbered those attached to precipitates. Hence, the width of the size distribution would be too small to properly observe if the number of counts was used to scale the distributions. The optimal bandwidths for the violin plots were assessed individually for each

condition using the built-in Scott criterion [109]. The second method to visualize the cavity distributions of both matrix and precipitate-attached cavities was completed by plotting a log-log scale of the cavity sizes versus the cavity density. The density bins were calculated with a 0.5nm size resolution per bin below 5 nm and a 1 nm size per bin for cavities greater than 5 nm in diameter. The distribution was calculated using the built-in Matplotlib histogram function in Python 3.7. A smoothed curve was then plotted to outline the shape of the histogram.

To assess swelling from the total number of cavities, the volume of each cavity assessed in the nominal damage region of each map was calculated assuming all cavities were spheres. The total volume of all cavities in each map was summed and divided by the total volume of the map assessed:

$$Swelling\ (\%) = \frac{\Delta V_{cavities}}{\Delta V_{map} - \Delta V_{cavities}} \times 100\% \qquad \text{Eq. 4.7}$$

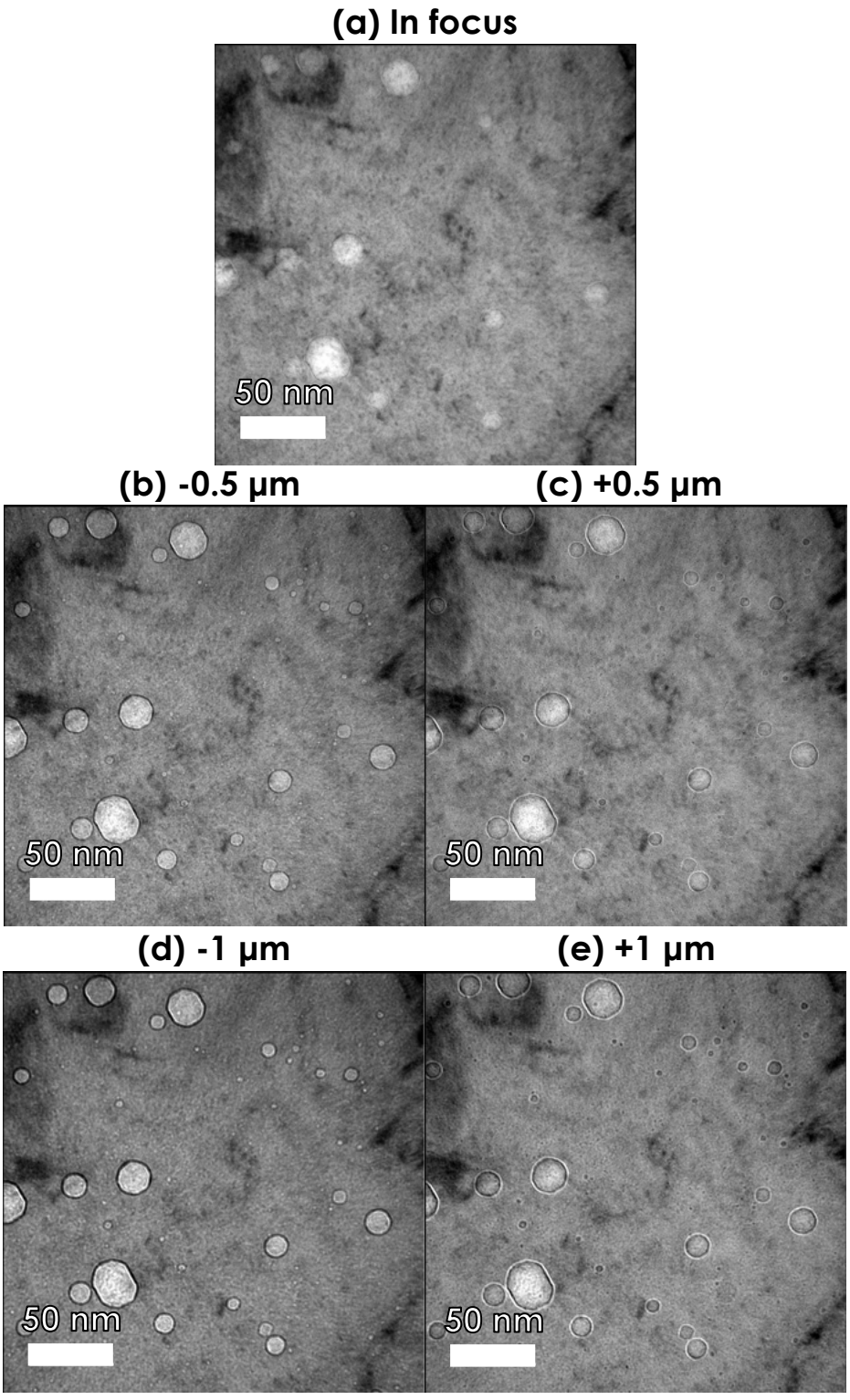

Figure 4.15 CTEM BF micrographs (a) in focus, (b) underfocused by 0.5 µm, (c) overfocused by 0.5 µm, (d) underfocused by1 µm, and (e) overfocused by 1µm in the same area on a CNA9 specimen irradiated to 15 dpa at 500°C with 10 appm He/dpa and 7×10^{-4} dpa/s.

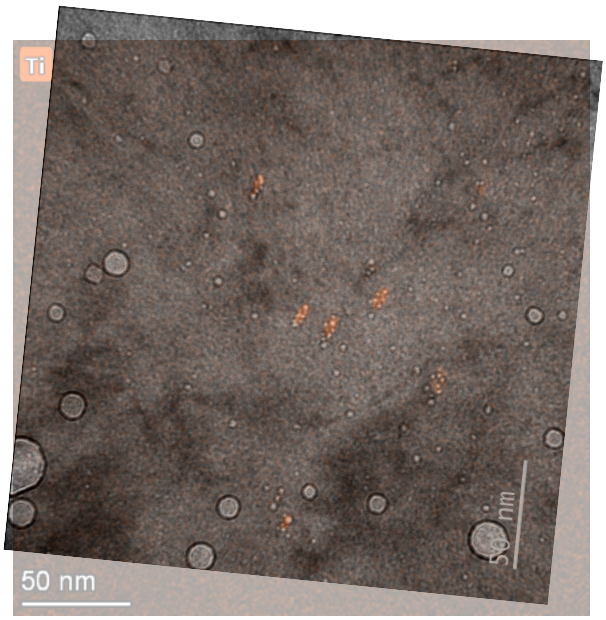

Figure 4.16 An example showing how cavities in the matrix and on precipitate-matrix interfaces were identified. A CTEM BF image in the underfocused condition was carefully aligned to match the same region of interest from a STEM-EDS map of Ti.

4.8 Further Considerations of Error Analysis

Error for the precipitate size was previously discussed. The standard errors of precipitate diameter provide a measurement of heterogeneity of precipitate sizes between maps of the same condition. Another method of deriving error comes from resolution of the EDS maps used for precipitate analysis. The resolution was approximately 0.5 nm/pixel in ImageJ. Hence, the error for each diameter could also be calculated as:

$$\mu_{diameter} = \frac{0.52}{d} \qquad \text{Eq. 4.8}$$

where d is the diameter of the precipitate. This method of error was calculated for the control condition. All error propagations were completed with the uncertainties package (version 3.1.6) in Python. The error for each precipitate diameter measurement was calculated and was propagated. First, the average diameter of each EDS map was calculated. Then, the average of those averages

was taken. The final precipitate diameter for the control condition was 7.8 ± 0.008 nm. The value calculated using the other method described in section 4.2.8 was 7.8 ± 0.3 nm.

Since the fractional error is dependent on the size of the measurement, this analysis was also carried out for the D1 condition, as it had the largest precipitate sizes. The value of the average diameter calculated using the error from the ED resolution was 14.9 ± 0.01 nm, whereas an error of 14.9 ± 2.2 nm was derived from the heterogeneity between EDS maps. As can be clearly seen, the error derived from the heterogeneity between EDS maps is significantly greater than that from the EDS map resolution. As such, the error from the EDS map resolution was ignored and thus not reported in further quantification of the microstructures.

Error for void swelling values were calculated as follows. For each irradiation condition, multiple CTEM images were taken to assess the cavity structure. The cavity diameters in each image were measured and stored digitally. The volume of each image was also calculated and stored. The error associated with the cavity diameters was calculated by taking the TEM resolution into consideration. The TEM used for cavity imaging as a 0.25 nm point-to-point resolution. Hence, the fractional error for each diameter was calculated as:

$$\mu_{diameter} = \frac{0.25}{d} \qquad \text{Eq. 4.9}$$

where *d* is the diameter of the cavity. The error for each cavity diameter was calculated. The error associated with the volume of each image derived from the EFTEM thickness mapping. An error of 10% is assumed to account for the error in this method of obtaining TEM lamellae thickness [110]. The error in the cavity number density also derives from the 10% thickness measurement error. Since swelling depends on both the errors associated with the cavity diameter and the volume of the images, the final error for swelling was propagated with the uncertainties Python package during swelling calculations.

One further point to consider is the grain-to-grain variability of CNA9, which adds additional uncertainty in a bulk-like measurement of cavity-induced swelling. Swelling was not found to significantly vary from grain to grain, but the number density of TiC precipitates could vary significantly at times. It is thought this variation is due to the variation of Ti present from grain-to-grain and is a result of the material fabrication process. To minimize this uncertainty, a minimum of two TEM specimens were extracted for each condition from different regions of the irradiated sample characterization was completed in multiple grains per lift-out. However, only one liftout was taken for conditions with no precipitates and only one liftout used for the control specimen characterization. Additional control specimen characterization was completed prior to this work by ORNL collaborators.

4.9 Calculation of Interstitials and Vacancies under Irradiation and Sink Strength

To calculate the point defect concentrations, a standard rate equation for the change in defect concentration for interstitials and vacancies with time was used from [1]:

$$\frac{dC_v}{dt} = \xi K_0 - K_{iv} C_i C_v - K_{vs} C_v C_s \quad \text{Eq. 4.10}$$

$$\frac{dC_i}{dt} = \xi K_0 - K_{iv} C_i C_v - K_{is} C_i C_s \quad \text{Eq. 4.11}$$

where C_v is the vacancy concentration, C_i is the interstitial concentration, ξ is the production efficiency for heavy ion irradiations (shown to be ~ 0.1 [111]), K_0 is the defect production rate, K_{iv} is the vacancy–interstitial recombination rate coefficient, K_{vs} is the vacancy–sink reaction rate coefficient, K_{is} is the interstitial–sink reaction rate coefficient, and C_s is the sink concentration. Hence, the second term in the equations represents the annihilation of point defects due to mutual recombination and the final terms represent the loss of point defects (interstitials or vacancies) to sinks.

The vacancy–interstitial recombination rate coefficient is defined as:

$$K_{iv} = \frac{z_{iv}\Omega(D_i + D_v)}{a^2} \quad \text{Eq. 4.12}$$

where z_{iv} is the combinatorial factor equal to 500, Ω is the atomic volume of the matrix, and a is the lattice parameter of the matrix.

The reaction rate constants ($K_{(i,v)x}$) describe the reaction between an interstitial or vacancy with a sink. The reaction rate constants are a function of the diffusion coefficient of point defects and the tendency of the reaction to occur, called the sink strength ($k^2_{(i,v)x}$):

$$K_{(i,v)x}C_{(i,v)}C_x = k^2_{(i,v)x}C_{(i,v)}D_{(i,v)} \quad \text{Eq. 4.13}$$

The point defect rate equations can be rewritten to include sink strengths by substituting the definition of the reaction rate constants into Eq. 4.10 and Eq. 4.11:

$$\frac{dC_{(i,v)}}{dt} = \xi K_0 - K_{iv}C_iC_v - k^2_{(i,v)}D_{(i,v)}C_{(i,v)} \quad \text{Eq. 4.14}$$

where $k^2_{(i,v)}$ is the sink strength for either vacancies or interstitials and $D_{(i,v)}$ is the diffusion coefficient for either vacancies or interstitials. The sink strengths for interstitials and vacancies were calculated for each irradiation condition using the measured values of cavities and precipitates (given in Chapter 5) from this work and the measured values of dislocation lines and loops, prior austenite grains (PAGs), and laths from [42] and [33] for Grade 91. The total sink strengths (k^2) for interstitials and vacancies are the sum of the sink strengths of the individually measured sinks, accounting for the bias of interstitials for dislocations:

$$k_v^2 = \sum_s k_{vs}^2 = k_{gb}^2 + k_{cav}^2 + k_{ppts}^2 + k_{dis}^2 \quad \text{Eq. 4.15}$$

$$k_i^2 = \sum_s k_{is}^2 = k_{gb}^2 + k_{cav}^2 + k_{ppts}^2 + k_{dis}^2 \quad \text{Eq. 4.16}$$

$$k^2 = k_v^2 + k_i^2 \quad \text{Eq. 4.17}$$

where k_{gb}^2 is the grain boundary sink strength from PAGs and laths, k_{cav}^2 is the sink strength from voids and bubbles, k_{ppts}^2 is the precipitate sink strength from the MX-TiC precipitates, and k_{dis}^2 is the dislocation sink strength.

The sink strength of cavities was calculated by assuming all cavities below 5 nm are helium-pressurized bubbles and all cavities over 5 nm are voids:

$$k_{cav}^2 = k_{bub}^2 + k_{void}^2 \quad \text{Eq. 4.18}$$

$$k_{bub}^2 = k_{bub,i}^2 + k_{bub,v}^2 \quad \text{Eq. 4.19}$$

$$k_{bub,i}^2 = 4Y_i \pi \rho_{bub} r_{bub} \quad \text{Eq. 4.20}$$

$$k_{bub,v}^2 = 4Y_v \pi \rho_{bub} r_{bub} \quad \text{Eq. 4.21}$$

$$Y_i = \frac{(\alpha_{v,cavity} - \alpha_{i,cavity})\left({}^{T_m}/_{T}\right)^{1/3}}{r_v + r_{bub} + \alpha_{bub,v}\left({}^{T_m}/_{T}\right)^{1/3}} \quad \text{Eq. 4.22}$$

$$Y_v = 1 \quad \text{Eq. 4.23}$$

$$k_{void}^2 = 4\pi \rho_{void} r_{void} \quad \text{Eq. 4.24}$$

where $k_{bub,i}^2$ is the sink strength of bubbles for interstitials, $k_{bub,v}^2$ is the sink strength of bubbles for vacancies, k_{bub}^2 is the total bubble sink strength, ρ_{bub} is the number density of bubbles, r_{bub} is the average radius of bubbles, Y_i is the bias of bubbles for interstitials, Y_v is the bias of bubbles for vacancies, r_v is the radius of a vacancy (taken as the radius of an Fe atom), and $\alpha_{v,cavity}$ and $\alpha_{i,cavity}$ are fitting parameters derived from Ref. [112]. $\alpha_{v,cavity}$ and $\alpha_{i,cavity}$ are equal to 0.83Å and 3.19 Å, respectively. Voids are assumed to be neutral sinks.

The sink strength of MX-TiC precipitates was calculated as [61]:

$$k_{ppt}^2 = 4\pi\rho_{ppt}r_{ppt} \quad \text{Eq. 4.25}$$

where ρ_{ppt} is the number density of precipitates and r_{ppt} is the average equivalent radius of the precipitates [1].

The sink strength of dislocations was calculated as:

$$k_{dis}^2 = k_{loop}^2 + k_{line}^2 \quad \text{Eq. 4.26}$$

$$k_{(loop,line),i}^2 = 2B_i\pi\rho_{(loop,line)}r_{(loop,line)} \quad \text{Eq. 4.27}$$

$$k_{(loop,line),v}^2 = 2B_v\pi\rho_{(loop,line)}r_{(loop,line)} \quad \text{Eq. 4.28}$$

$$k_{(loop,line)}^2 = k_{(loop,line),i}^2 + k_{(loop,line),v}^2 \quad \text{Eq. 4.29}$$

where k_{loop}^2 is the sink strength of dislocation loops, k_{line}^2 is the sink strength of dislocation lines, B_i is the bias factor of dislocations for interstitials, and B_v is the bias factor of dislocations for vacancies. B_v is assumed to be 1, meaning dislocations are not biased toward vacancies, based off of literature [1]. B_i was calculated to be 8% from Ref. [112]. B_i was calculated by using the bias-driven criterion to determine the critical bubble radius. The bias-driven criterion in Ref. [112] is defined as a model of cavity behavior in which growth of small cavities is driven by helium accumulation until a critical radius is reached, whereby cavities grow via bias-driven partitioning of point defects. The critical bubble radius is the radius of cavities where the cavities transition from being stabilized by helium gas to a vacancy-biased growth regime. The critical bubble radius is solved for by setting the biases for dislocations and cavities equal and solving for the cavity radius that allows this criterion to be true:

$$r_{crit}^{bias-driven} = \frac{\left(\alpha_{i,cavity} - \alpha_{v,cavity}\right)(T_m/T)^{1/3} - B_i\left(r_{vac} + \alpha_{v,cavity}(T_m/T)^{1/3}\right)}{B_i} \quad \text{Eq. 4.30}$$

It was determined that the critical bubble radius from this equation matched experimental data at 500°C if B_i was equal to 8%.

The sink strength of grain boundaries was calculated using the following equation:

$$k_{gb}^2 = k_{PAG}^2 + k_{lath}^2 \quad \text{Eq. 4.31}$$

where

$$k_{PAG,lath}^2 = \frac{6\sqrt{k_{inside\ grain}^2}}{d_{PAG,lath}} \quad \text{Eq. 4.32}$$

$$k_{inside\ grain}^2 = k_{cav}^2 + k_{ppts}^2 + k_{dis}^2 \text{ (SI)} \quad \text{Eq. 4.33}$$

$$k_{inside\ grain}^2 = k_{cav}^2 + k_{ppts}^2 + k_{dis}^2 + k_{bub}^2 + k_{void}^2 \text{ (DI)} \quad \text{Eq. 4.34}$$

The diffusion of interstitials and vacancies were assumed to have an Arrhenius dependence:

$$D_{(i,v)} = \alpha_{(i,v)}\omega_{(i,v)}e^{\left(-E_m^{(i,v)}/kT\right)} \quad \text{Eq. 4.35}$$

where α is 1/6 for interstitials and 1 for vacancies, ω is the jump frequency for either vacancies or interstitials, k is the Boltzmann constant, T is the temperature, and E_m is the migration energy of interstitials or vacancies [1,42].

The previous equations were used to solve for the point defect concentration from Eq. 4.14 by setting $\frac{dC_{(i,v)}}{dt} = 0$ to solve for steady-state from Ref. [1]:

$$N_v^{ss} = \frac{-k_{is}^2 D_i}{2K_{iv}} + \sqrt{\frac{\xi K_0 k_{is}^2 D_i}{K_{iv} k_{vs}^2 D_v} + \frac{(k_{is}^2)^2 D_i^2}{4K_{iv}^2}} \quad \text{Eq. 4.36}$$

$$N_i^{ss} = \frac{-k_{vs}^2 D_v}{2K_{iv}} + \sqrt{\frac{\xi K_0 k_{vs}^2 D_v}{K_{iv} k_{is}^2 D_i} + \frac{(k_{vs}^2)^2 D_v^2}{4K_{iv}^2}} \quad \text{Eq. 4.37}$$

The vacancy and interstitial fractions present at certain irradiation conditions are:

$$C_v^{ss} = \frac{N_v^{ss}}{N_{matrix}} \quad \text{Eq. 4.38}$$

$$C_i^{ss} = \frac{N_i^{ss}}{N_{matrix}} \quad \text{Eq. 4.39}$$

All error associated with the input values to the equations above were propagated with the use of the uncertainties Python package. The results of the calculations for point defect concentrations are shown in Table 4.6. Sink strength calculations for select single ion irradiation experiments are shown in Table 4.7and for dual ion irradiation experiments in Table 4.8.

The same values for dislocation loops and lines were used for the single and dual beam calculations. Dislocation loop size and density for 300°C was taken from Ref. [113]. Ref. [113] irradiated Grade 91 to 30 dpa at 300°C with a dose rate 2×10^{-3} dpa/s. As dislocation loop size and density are a function of temperature, dose, and dose rate, it can be assumed that the value used here will not exactly match CNA9's value at 300°C but were appropriate for use due to lack of literature data [114]. Values for dislocation loop size and density and for dislocation line density for all temperatures besides 300°C were taken from Ref. [42]. Dislocation line density for 300°C assumed to be same as at 400°C, as data was lacking from literature. Values from Ref. [42] did not match the experimental conditions in this work exactly. Ref. [42] used Grade 91 irradiated at 406°C-16.6dpa-7×10^{-4} dpa/s-4.3 appm He/dpa, 480°C-16.6dap-7×10^{-4} dpa/s-4.3 appm He/dpa, and 570°C-15.4dpa-7×10^{-4} dpa/s-4.3 appm He/dpa. Hence, values from Ref. [42] input for 400°C in these calculations were taken from the experiment run at 406°C. Values input for 500°C in these calculations were taken from the experiment run at 480°C. Values input for 600°C in these

calculations were taken from the experiment run at 570°C. Errors for dislocation loop size and density from Ref. [42] were reported in the reference. As explained in Section 4.2.2 Grade 91 is an appropriate surrogate material due to the similarity in composition to CNA9 and the similar grain and lattice structures. Hence, it is assumed that values of dislocation line densities of Grade 91 can be used for CNA9, within appropriate reason. However, the helium rate used in this thesis was 2.3× greater than used in Ref. [42]. Helium implantation level has been shown to affect the dislocation structure by altering the ratio of dislocation loop type in BCC Fe-Cr steel alloys, but not by altering the number density of total dislocation loops [115]. Hence, it is assumed that using the dislocation loop size and densities from Ref. [42] is appropriate within reason.

Values for the prior austenite grain (PAG) size was taken from Ref. [42] and the martensite lath size was taken from Ref. [24]. Error for the lath size was assumed to be 10% to cover the spread of lath sizes found in literature [33]. Values for MX-TiC precipitates, bubbles, and voids were from this work. The errors for MX-TiC precipitates, bubbles, and voids have been explained previously in this chapter.

It can be observed from Table 4.7 that sink strength is mainly derived from the dislocations in single ion irradiated samples. In samples that underwent dual beam irradiation (Table 4.8), bubbles contributed the most significantly to the sink strength of the samples. This led to total sink strengths 8-9 orders of magnitude greater than the total sink strengths calculated for the single beam conditions. The MX-TiC precipitates contributed minimally to the total overall sink strength in all conditions. It can also be noticed that the precipitates contributed a greater percentage to the overall sink strength as temperature increased, due to the increase in volume fraction of precipitates with temperature. A comparison between the precipitate sink strength and total sink strengths in single and dual ion irradiated conditions are shown in Figure 4.18 and Figure 4.17.

Table 4.6 Calculated vacancy (N_v^{ss}) and interstitial (N_i^{ss}) concentrations for the irradiation conditions in the single and dual ion temperature series.

Temperature	Irradiation Parameters for Single and Dual Ion Conditions	N_v^0 (Vacancy)	N_v^{ss} (Vacancy concentration in vac/m^3)	N_i^0 (interstitial)	N_i^{ss} (interstitial concentration in int/m^3)
300°C	15 dpa, 7×10^{-4} dpa/s	6.3×10^{15}	$(52.5\pm112.4)\times10^{19}$	9.1×10^{-16}	$(7.0\pm1.7)\times10^{19}$
400°C	15 dpa, 7×10^{-4} dpa/s	7.7×10^{17}	$(10.1\pm0.6)\times10^{19}$	3.1×10^{-9}	$(3.1\pm0.2)\times10^{19}$
	15 dpa, 7×10^{-4} dpa/s, 10 appm He/dpa		$(9.0\pm0.5)\times10^{19}$		$(2.6\pm0.1)\times10^{19}$
500°C	15 dpa, 7×10^{-4} dpa/s	2.7×10^{19}	$(9.5\pm0.6)\times10^{19}$	2.1×10^{-4}	$(5.3\pm0.3)\times10^{19}$
	15 dpa, 7×10^{-4} dpa/s, 10 appm He/dpa		$(5.0\pm0.2)\times10^{19}$		$(2.6\pm0.1)\times10^{19}$
600°C	15 dpa, 7×10^{-4} dpa/s	4.3×10^{20}	$(6.1\pm0.6)\times10^{19}$	1.2×10^{0}	$(5.6\pm0.5)\times10^{19}$
	15 dpa, 7×10^{-4} dpa/s, 10 appm He/dpa		$(3.2\pm0.2)\times10^{19}$		$(2.6\pm0.1)\times10^{19}$

Table 4.7 Values input to calculate sink strength for single ion irradiation conditions in the temperature series to 15 dpa with 7×10^{-4} dpa/s. N.C. means not calculated.

Dislocation Lines	Number density (m^{-3})	300°C: 3.8×10^{14} 400°C: 3.8×10^{14} 500°C: 0.4×10^{14} 600°C: N.O.	k^2_{line} (m^{-2})	300°C: 7.9×10^{14} 400°C: 7.9×10^{14} 500°C: 8.7×10^{13} 600°C: N.C.
Dislocation Loops	Number density (m^{-3})	300°C: 4.1×10^{22} 400°C: 12×10^{21} 500°C: 0.46×10^{22} 600°C: N.O.	k^2_{loop} (m^{-2})	300°C: $(2.3\pm1.1)\times10^{15}$ 400°C: $(1.6\pm0.2)\times10^{15}$ 500°C: $(1.7\pm0.2)\times10^{14}$ 600°C: N.C.
	Radius (nm)	300°C: 4.3±2.1 400°C: 10.1±1.2 500°C: 29±3.8 600°C: N.O.		
MX-TiC precipitates	Number density (m^{-3})	300°C: $(8.8\pm1.8)\times10^{20}$ 400°C: $(1.4\pm0.2)\times10^{21}$ 500°C: $(1.7\pm0.3)\times10^{21}$ 600°C: $(1.3\pm0.2)\times10^{21}$	k^2_{MX} (m^{-2})	300°C: $(4.8\pm1.0)\times10^{13}$ 400°C: $(6.9\pm1.0)\times10^{13}$ 500°C: $(1.1\pm0.2)\times10^{14}$ 600°C: $(1.2\pm0.2)\times10^{14}$
	Radius (nm)	300°C: 4.4±0.09 400°C: 3.8±0.06 500°C: 5.2±0.1 600°C: 7.4±0.4		
Grain Boundaries	Diameter of PAGs (μm)	15	k^2_{GB} (m^{-2})	300°C: $(7.0\pm0.7)\times10^{14}$ 400°C: $(6.1\pm0.6)\times10^{14}$ 500°C: $(2.4\pm0.2)\times10^{14}$ 600°C: $(1.4\pm0.1)\times10^{14}$
	Diameter of laths (nm)	500±50		
Total			k^2_{tot} (m^{-2})	300°C: $(4.6\pm1.1)\times10^{15}$ 400°C: $(3.7\pm0.2)\times10^{15}$ 500°C: $(9.7\pm0.6)\times10^{14}$ 600°C: $(5.1\pm0.5)\times10^{14}$

Table 4.8 Values input to calculate sink strength for dual ion irradiation conditions in the temperature series to 15 dpa with 7×10^{-4} dpa/s and 10 appm He/dpa. N.C. means not calculated.

Dislocation Lines	Number density (m^{-3})	400°C: 3.8×10^{14} 500°C: 0.4×10^{14} 600°C: N.O.	k^2_{line} (m^{-2})	400°C: 7.9×10^{14} 500°C: 8.7×10^{13} 600°C: N.C.
Dislocation Loops	Number density (m^{-3})	400°C: 12×10^{21} 500°C: 0.46×10^{22} 600°C: N.O.	k^2_{loop} (m^{-2})	400°C: $(1.6\pm0.2)\times10^{15}$ 500°C: $(1.7\pm0.2)\times10^{14}$ 600°C: N.C.
	Radius (nm)	400°C: 10.1±1.2 500°C: 29±3.8 600°C: N.O.		
MX-TiC precipitates	Number density (m^{-3})	400°C: $(9.2\pm1.8)\times10^{20}$ 500°C: $(1.8\pm0.1)\times10^{21}$ 600°C: $(1.6\pm0.2)\times10^{21}$	k^2_{MX} (m^{-2})	400°C: $(4.9\pm0.9)\times10^{13}$ 500°C: $(8.5\pm0.7)\times10^{13}$ 600°C: $(1.1\pm0.2)\times10^{14}$
	Radius (nm)	400°C: 4.2±0.07 500°C: 3.8±0.06 600°C: 5.6±0.2		
Grain Boundaries	Diameter of PAGs (μm)	15	k^2_{GB} (m^{-2})	400°C: $(6.6\pm0.6)\times10^{14}$ 500°C: $(3.7\pm0.4)\times10^{14}$ 600°C: $(2.4\pm0.2)\times10^{14}$
	Diameter of laths (nm)	500±50		
Bubbles	Number density (m^{-3})	400°C: $(3.3\pm0.2)\times10^{22}$ 500°C: $(1.8\pm0.07)\times10^{22}$ 600°C: $(1.9\pm0.07)\times10^{22}$	k^2_{bub} (m^{-2})	400°C: $(4.8\pm0.3)\times10^{14}$ 500°C: $(5.5\pm0.2)\times10^{14}$ 600°C: $(3.6\pm0.1)\times10^{14}$
	Radius (nm)	400°C: 0.47±0.0049 500°C: 0.99±0.0039 600°C: 0.65±0.0040		
Voids	Number density (m^{-3})	400°C: N.O. 500°C: $(1.4\pm0.05)\times10^{21}$ 600°C: N.O.	k^2_{void} (m^{-2})	400°C: N.O. 500°C: $(1.0\pm0.0)\times10^{14}$ 600°C: N.O.
	Radius (nm)	400°C: N.O. 500°C: 5.70±0.0019 600°C: N.O.		
Total			k^2_{tot} (m^{-2})	400°C: $(4.3\pm0.2)\times10^{15}$ 500°C: $(1.9\pm0.1)\times10^{15}$ 600°C: $(1.1\pm0.1)\times10^{15}$

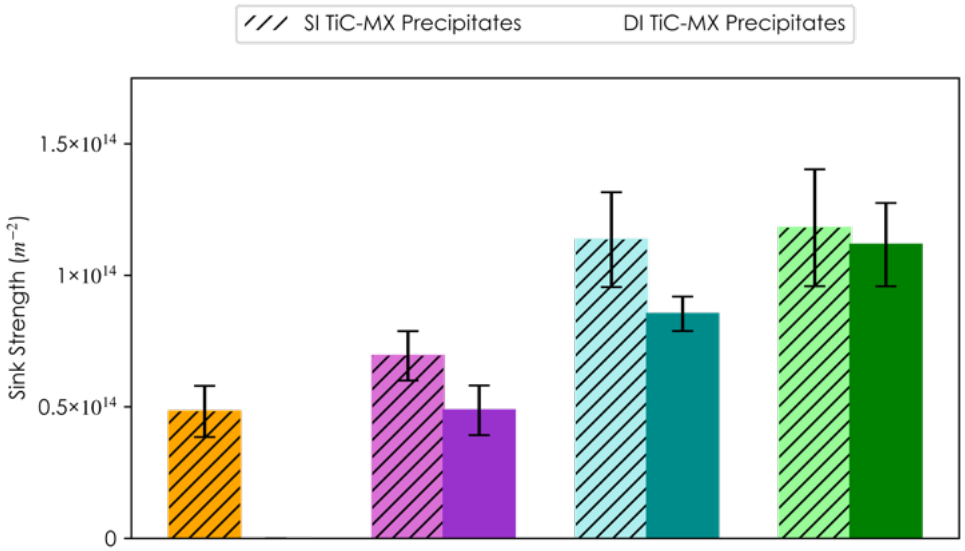

Figure 4.18 Calculated MX precipitate sink strength values for single ion irradiation experiments and dual ion irradiations. All irradiations were completed with a damage rate of 7×10^{-4} dpa/s to 15 dpa. All dual beam irradiations were completed with 10 appm He/dpa.

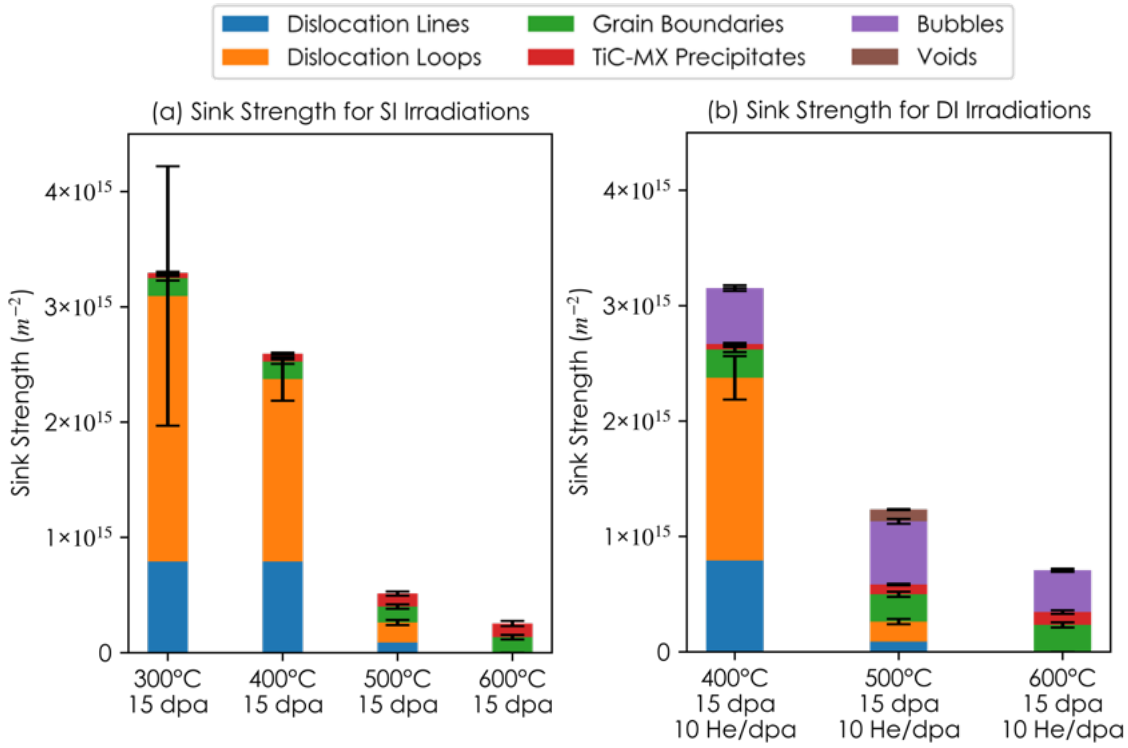

Figure 4.17 Calculated total sink strength values for single ion irradiation experiments and dual ion irradiations. All irradiations were completed with a damage rate of 7×10^{-4} dpa/s to 15 dpa. All dual beam irradiations were completed with 10 appm He/dpa.

Chapter 5 Results

This chapter presents the results of the microstructural characterization of the samples irradiated in the experiments described in Chapter 4. The following sub-sections summarize the significant findings of the nanoprecipitate evolution in CNA9 as a function of damage rate, damage level, irradiation temperature, and helium co-implantation rate. The results are separated into four sections based on the five series of irradiation experiments explained in Chapter 4, each probing a single irradiation parameter response. The five series of irradiation experiments were damage rate, damage, temperature, constant helium implantation rate at various temperatures, and various helium implantation rates at constant temperature (Table 4.3). The first section describes the results of the damage rate series to establish damage rate effects and to choose an appropriate damage rate for the remaining irradiation series. The second section describes the results of the damage level series to determine the significance of damage level to precipitate stability. The third series assesses the effects of temperature on nanoprecipitate behavior with a fixed dose rate and dose. The three remaining series explore the effects of helium rate on the microstructure and how helium interplays with temperature and dose, including the effects of various helium co-injection rates. Quantitative cavity results and corresponding discussion will only be provided for the dual beam conditions, as no cavities and thus swelling was observed in the single beam conditions studied.

STEM-EDS micrographs of Ti showing the TiC nanoprecipitates and precipitate size distributions in the form of violin plots will be shown for each condition. In addition, the number of STEM-EDS maps taken, the number of precipitates counted, the number density of precipitates,

the equivalent diameters of precipitates, and the volume fraction of precipitates are given in Appendix C. These statistics will also be shown in the appropriate sections. Refer to Chapter 4 for a complete explanation of how these values and their errors were calculated for each condition/sample. TEM-BF micrographs of cavities and cavity size distributions will also be shown. The methods of quantification for cavities were also explained in Chapter 4.

It is important to first understand the size and density of the TiC precipitates before irradiation to better understand how irradiation can alter precipitates, if at all. STEM-EDS micrographs and corresponding STEM-BF images of the control specimen are shown in Figure 5.1. Precipitate size distributions and statistics derived from the analyzed STEM-EDS micrographs of the control sample are shown in Figure 5.2. The control sample was never irradiated or thermally annealed and was in the as-received condition. Figure 5.2 shows the number of precipitates counted per map (N), number density of precipitates (ρ), average equivalent diameter (d), and volume fraction (f) for each map. The size distribution labeled 'Control' was created from all precipitates counted in the control sample from all four maps. The errors for the statistics of the individual maps of the control sample are the standard errors of the average values of each map. The circular markers on Figure 5.2 are the individual precipitate diameter measurements. The mean solid and dashed interquartile lines are shown via box plots overlaid onto the violin plots.

In this chapter, the statistical parameters of the precipitates in each irradiated condition will be compared to those of the control specimen by taking ratios of the number density, size, and volume fraction of precipitates in the irradiated condition to those in the control specimen. For instance, the ratio of the average equivalent diameter of precipitates in each irradiation condition to the average equivalent diameter of precipitates of the control specimen will be used to interpret the precipitate size response. However, it is important to carefully analyze the error values

associated with the resulting ratio parameters to avoid falsely claiming statistical significance. This can be done through careful error analysis and propagation and by understanding the inherent variability in individual parameters in the control specimen itself.

To try to understand and quantify the variability present in the control sample, the number density, size, and volume fraction of precipitates of each individual STEM-EDS map of the control specimen were compared to the same parameter calculated from the average of all maps (shown in the 'Control' column in Figure 5.2). The resulting ratios are shown in Figure 5.2 labeled as ρ/ρ_{CTRL} d/d_{CTRL}, and f/f_{CTRL}. These parameters represent the range of values that ratios calculated from irradiated samples must be smaller than or larger than to be considered statistically significant. For instance, a calculated ratio of $\rho_{IRRADIATED}/\rho_{CTRL}$ equal to 2 would be considered statistically significant as it is larger than the largest value of ρ/ρ_{CTRL} in Figure 5.2

It should be justified why the comparison of irradiated precipitate statistical parameters to the control specimen was chosen instead of the comparison of the irradiated size distributions to the corresponding thermally annealed size distributions. An assessment of the TiC precipitates in each thermally exposed areas of the bars used for irradiation experiments at each temperature used in irradiation experiments (300, 400, 500, and 600°C) was conducted. Figure 5.3 shows the analysis between the control and thermally annealed precipitate size distributions. The samples were annealed for approximately 6 h, which is the time to complete a 15 dpa irradiation with damage rate of 7×10^{-4} dpa/s (Table 4.2). No significant deviation in number density or equivalent diameter from the control specimen was found (Figure 5.3). As such, it was determined that the most accurate and consistent representation of the evolution of TiC precipitates under irradiation would be to compare irradiated size distributions to the aggregated control size distribution.

Just as explained for Figure 5.2, the ratios of number density, size, and volume fraction

between the thermally annealed and control specimens represent the limit of statistical significance. Hence, the conservative values will be chosen from Figure 5.2 and Figure 5.3 to determine statistical significance of the changes in irradiated precipitate response. The ratios of number density, size, and volume fraction between the irradiated and control specimens will be deemed significant if they differ by more than the most conservative value of that parameter from Figure 5.2 and Figure 5.3. Those values are shown in Table 5.1.

Table 5.1 Tabulated values from Figure 5.2 and Figure 5.3 that represent the range of statistical significance for future ratio calculations between irradiated and control specimens.

Ratio	Significant if less than/Lower bound	Significant if greater than/Upper bound
ρ/ρ_{CTRL}	0.61	2
d/d_{CTRL}	0.87	1.3
VF/VF_{CTRL}	0.63	3.2

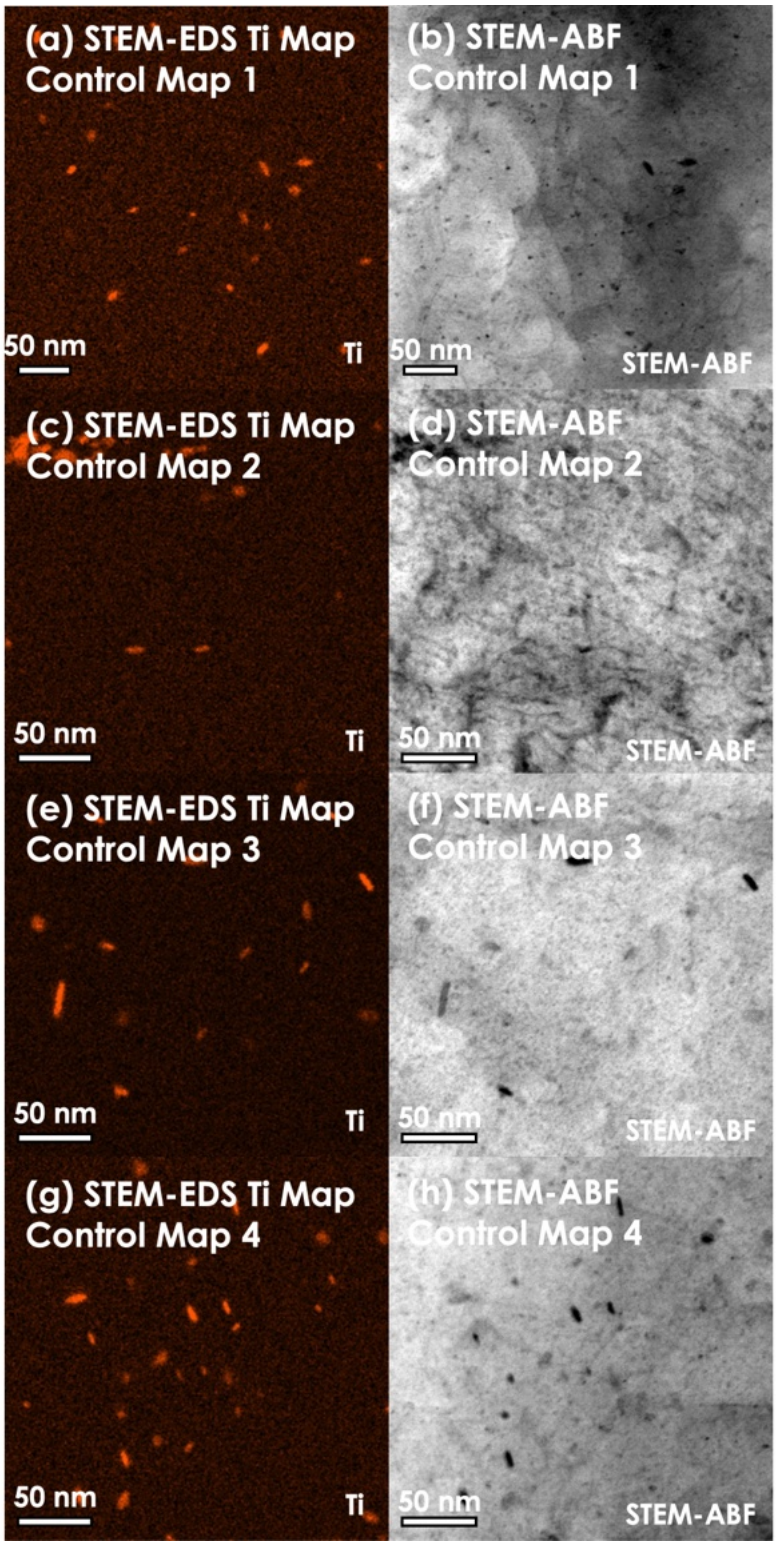

Figure 5.1 STEM-EDS micrographs of Ti (a,c,e,g) and corresponding STEM-ABF micrographs (b,d,f,g) taken from the control CNA9 specimen, which was never irradiated or thermally annealed.

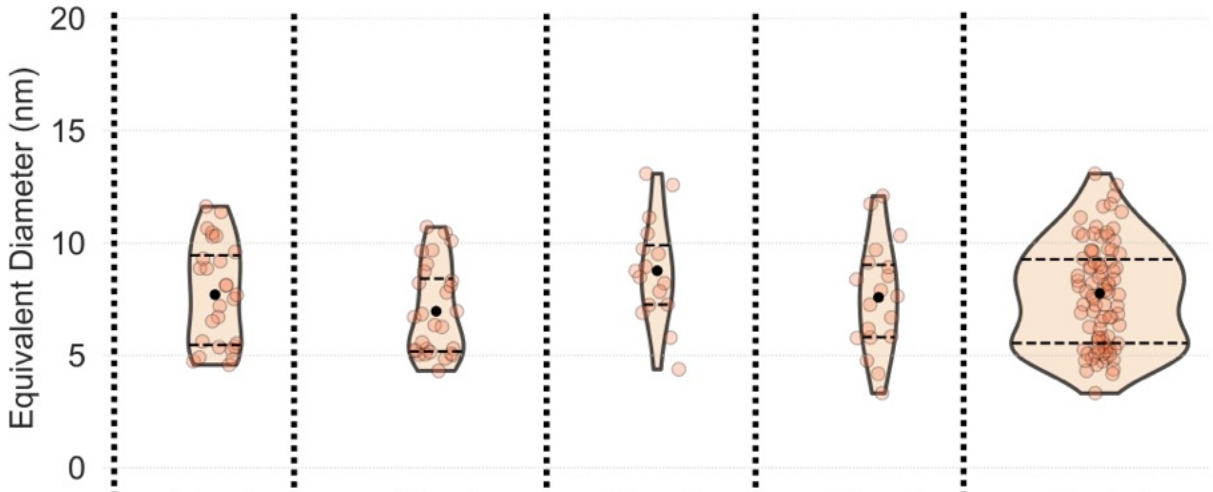

	Map 1	Map 2	Map 3	Map 4	Control
N	27	28	16	19	**90**
ρ (m^{-3})	1.6×10^{21}	3.1×10^{21}	2.0×10^{21}	2.4×10^{21}	$\mathbf{(2.3\pm0.3)\times10^{21}}$
d_{eq}(nm)	7.7	7.0	8.8	7.6	**7.8±0.3**
f	4.9×10^{-4}	6.9×10^{-4}	8.3×10^{-4}	7.0×10^{-4}	$\mathbf{(6.8\pm0.6)\times10^{-4}}$
ρ/ρ_{CTRL}	0.7±0.09	0.7±0.09	1.4±0.2	0.9±0.1	
d/d_{CTRL}	1.0±0.04	0.9±0.03	1.1±0.04	1.0±0.04	
f/f_{CTRL}	0.7±0.07	0.7±0.06	1.0±0.09	1.2±0.1	

Figure 5.2 Size distribution plots of precipitates counted in each STEM-EDS map of the control sample. Number of precipitates counted per map (N), number density of precipitates (ρ), average equivalent diameter (d_{eq}), and volume fraction (f) are shown for each map.

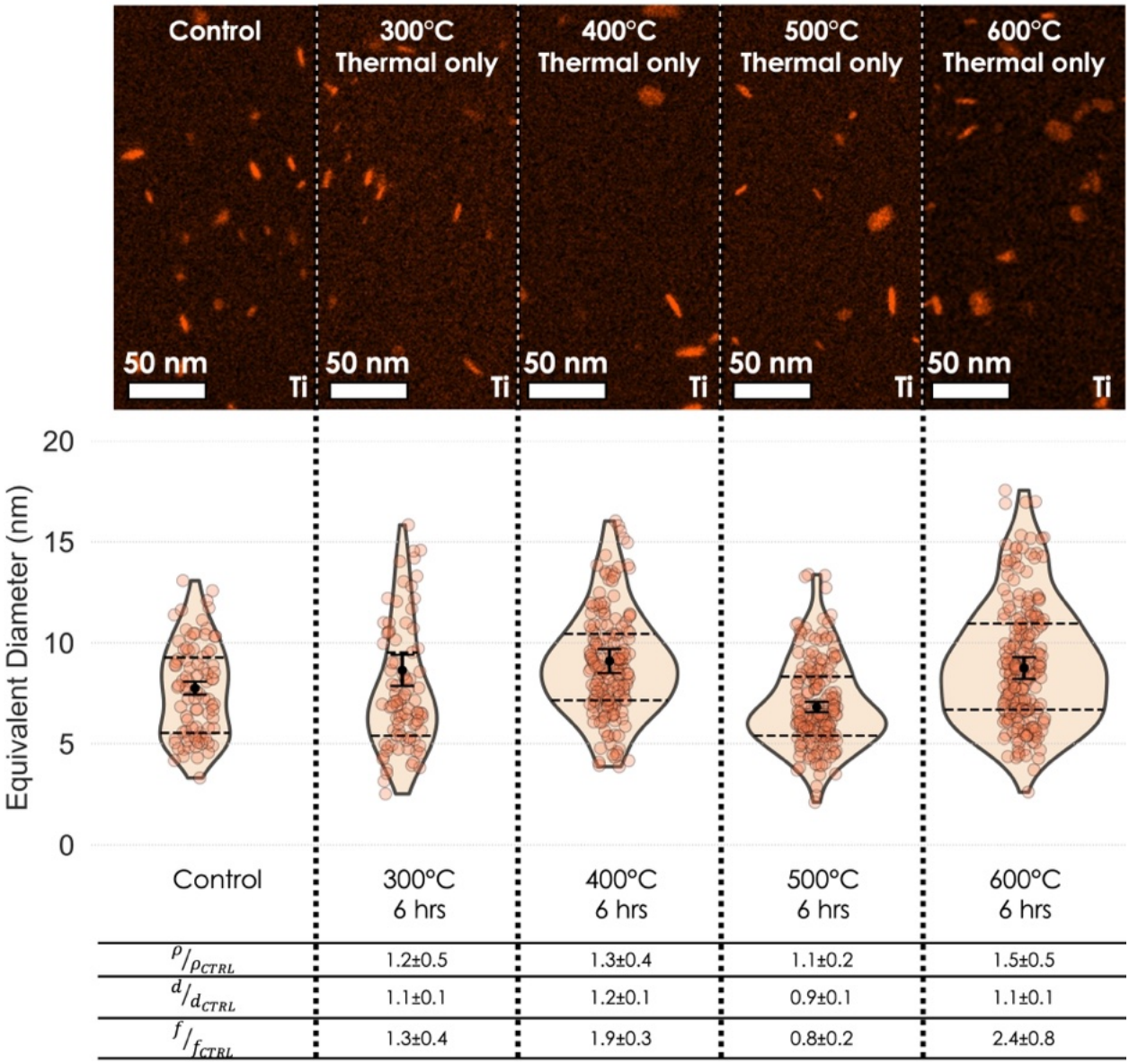

Figure 5.3 STEM-EDS micrographs with corresponding size distributions and precipitation statistics for thermally annealed conditions at 300, 400, 500, and 600°C. Each condition was annealed for 6 hours.

5.1 Microstructure Evolution with Variable Damage Rate for Fixed Temperature and Damage Level

For heavy ion irradiation, ballistic dissolution has been shown to be a function of dose rate when the energy of the incoming projectile is greater than the displacement energy of the precipitate atoms [1]. Back diffusion is mainly a function of temperature. To isolate the effects of ballistic dissolution and to minimize the effects of back diffusion on precipitate stability, two low temperature/high dose irradiation conditions were chosen: A2 (300°C, 50 dpa, 1×10^{-4} dpa/s) and A3 (300°C, 50 dpa, 7×10^{-4} dpa/s). The only target irradiation parameter that was varied was dose rate. The dose rate of 7×10^{-4} dpa/s was chosen because previous work showed that it creates a neutron-like swelling response in FM steels for advanced fission reactors [42] and 1×10^{-4} dpa/s was chosen as a reasonably low dose rate to study dose rate effects. 50 dpa was chosen as a reasonable damage level to be able to ascertain ballistic dissolution effects. Refer to Chapter 4 for a full discussion of how parameters were chosen.

5.1.1 MX-TiC Precipitation Results

The MX-type TiC precipitates dissolved in both conditions. This can be seen in the STEM-EDS maps taken in the nominal damage region in Figure 5.4. To isolate the effects of irradiation versus temperature, STEM-EDS maps were taken in the region beneath the ion implantation depth where only thermal effects were present in the A2 condition. As can be observed in Figure 5.5, the MX-type TiC precipitates were still present in the thermal region. It was assumed that MX-TiC precipitates were also present in the A3 condition, as the precipitates past the implantation depth were annealed for ~19.8 h as opposed to ~138.9 h in the A2 condition. Hence, damage level had a

dominant effect over damage rate in determining the precipitate stability for the specific conditions studied in this series. In particular, it can be assumed that the MX-TiC precipitates dissolve at higher damage levels (such as at 50 dpa), and that assumption will be tested in the next series. Hence, all future experiments used a dose rate of 7×10^{-4} dpa/s to allow for faster irradiation experiments. It should be noted that damage rate may have an effect on precipitate behavior at other conditions, such as at higher temperatures and lower damage levels. However, that is not the focus of this work and is left to future work. Refer to Section 6.1.1 for an in-depth discussion of damage rate effects found in literature.

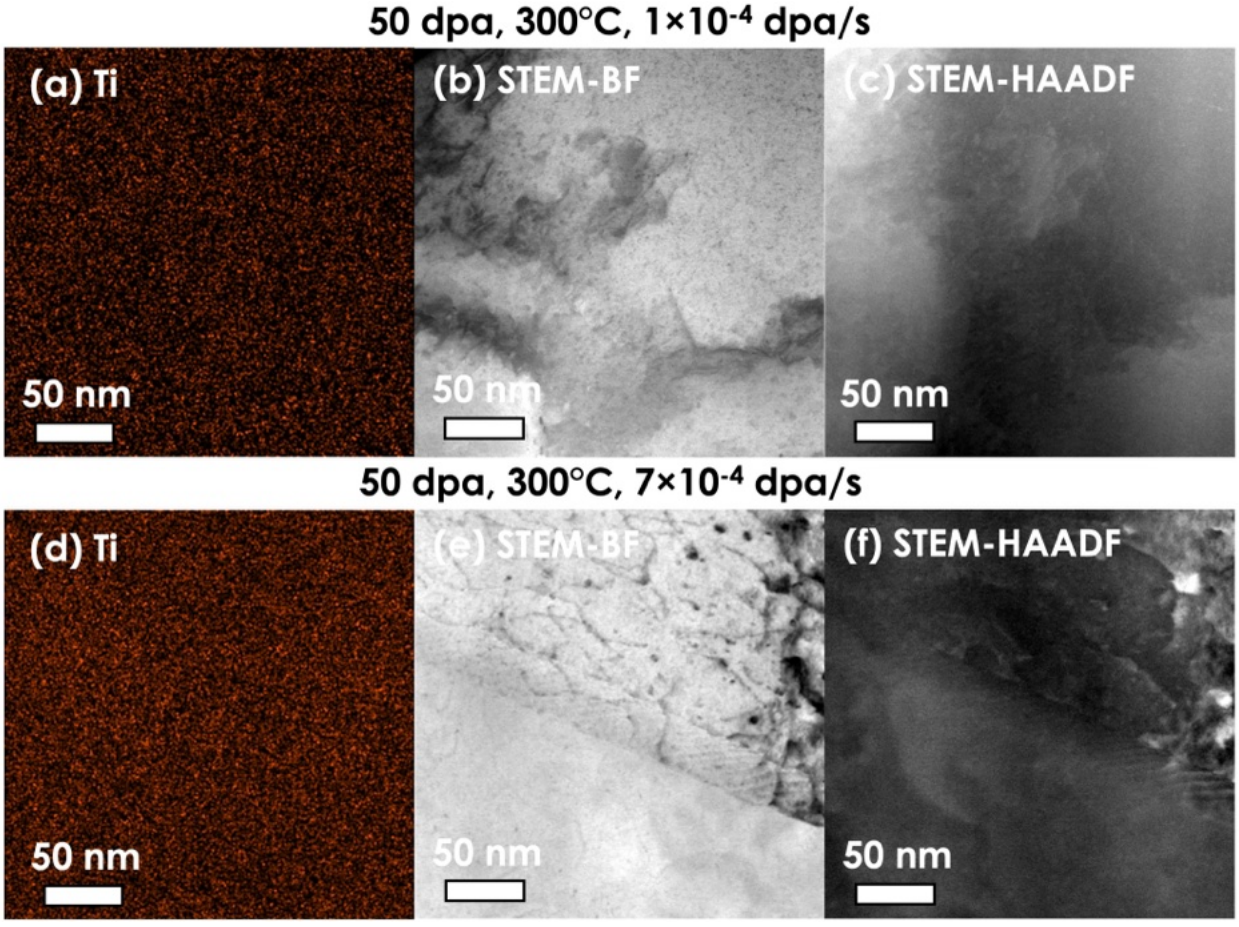

Figure 5.4 (a) STEM-EDS map of Ti with corresponding (b) STEM-BF and (c) STEM-HAADF micrographs for the A2 irradiation condition (300°C, 50 dpa, 1×10^{-4} dpa/s). (d) STEM-EDS map of Ti with corresponding (e) STEM-BF and (f) STEM-HAADF micrographs for the A3 irradiation condition (300°C, 50 dpa, 7×10^{-4} dpa/s). Images encompass the nominal damage region that is 1.1-1.3 μm beneath the sample surface, as outlined in Chapter 4.

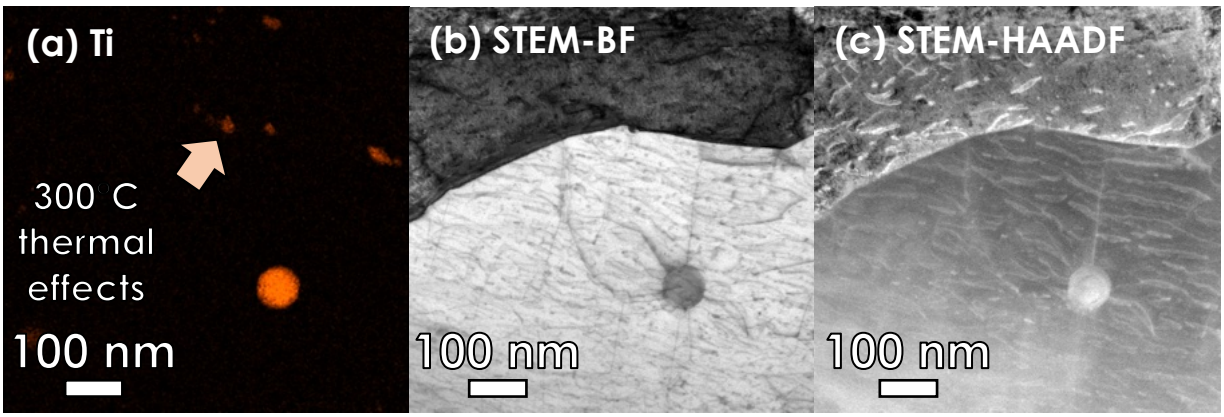

Figure 5.5 (a) STEM-EDS map of Ti with corresponding (b) STEM-BF and (c) STEM-HAADF micrographs for the unirradiated portion of the A2 irradiation condition (300°C, 50 dpa, 1×10^{-4} dpa/s). The micrographs show the effects of thermal aging of MX-TiC precipitates after exposure to 300°C for 19.8 hours. This is the time of the irradiation for the condition shown in Figure 5.2 (a-c). The MX-TiC precipitates remained.

5.2 Microstructure Evolution with Variable Damage Level for Fixed Temperature and Damage Rate

Based on the previous set of experiments that showed dissolution at 50 dpa at both 1×10^{-4} dpa/s and 7×10^{-4} dpa/s at 300°C, the effects of dose were singled out for further study. In this set of experiments, the doses studied were 1, 5, 15, 50, and 100 dpa, which correspond to conditions C1-C5 in Table 4.2, respectively. Temperature and dose rate were kept constant at 500°C and 7×10^{-4} dpa/s for all irradiations in this series. The temperature of 500°C was used, as opposed to the previously used 300°C, to assess the effect of back diffusion which was assumed to be more dominate at 500°C compared to 300°C. Chapter 4 also discussed the reasoning for choosing these irradiation parameters. This series will help to establish the damage level to use in future dual beam irradiations with helium co-injection to understand the role of helium on precipitate and cavity evolution.

5.2.1 MX-TiC Precipitation Results

It can be observed from Figure 5.6 that damage level plays a critical role in precipitate dissolution. In the low to intermediate dose regimes (1, 5, and 15 dpa) the precipitates maintained a similar number density to the control specimen. The precipitates at low doses (1 and 5 dpa) maintained a similar size distribution to the control specimen as well, but precipitates at the intermediate dose of 15 dpa displayed growth. This is reflected in the size distributions of the conditions irradiated to 1, 5, and 15 dpa as compared to the size distribution of the control specimen. The size distributions of the 1 and 5 dpa conditions are nearly the same as that of the control condition, with near exact size statistics. But the size distribution of the 15 dpa sample shifted upward toward larger diameters. This trend is reflected in the increase in equivalent diameter and the resulting increase in volume fraction of the precipitates in the 15 dpa sample as compared to the control condition (Figure 5.6). The average equivalent diameter increased by a factor of 1.3±0.1 and the volume fraction increased by a factor of 1.6±0.4 in the 15 dpa sample over the control sample. It should be noted that the average number density increased over the control specimen in the 1 and 5 dpa samples, though the increase was within the standard error and hence was deemed insignificant. The average number density of the 15 dpa sample decreased from that of the control sample but was also within error.

However, by 50 dpa and 100 dpa the MX-TiC precipitates completely dissolved. The only type of precipitate that remains at these high damage levels is the large non-MX-TiC precipitate with a diameter of about 90 nm. They remain stable most likely due to their larger size shielding them from dissolution. Solutes in the precipitate are less likely to ballistically eject from the precipitate and more likely to be displaced within the precipitate at larger precipitate sizes. For

future investigations of temperature effects, a dose of 15 dpa will be used because it encompasses an observed change but with the precipitates still being present.

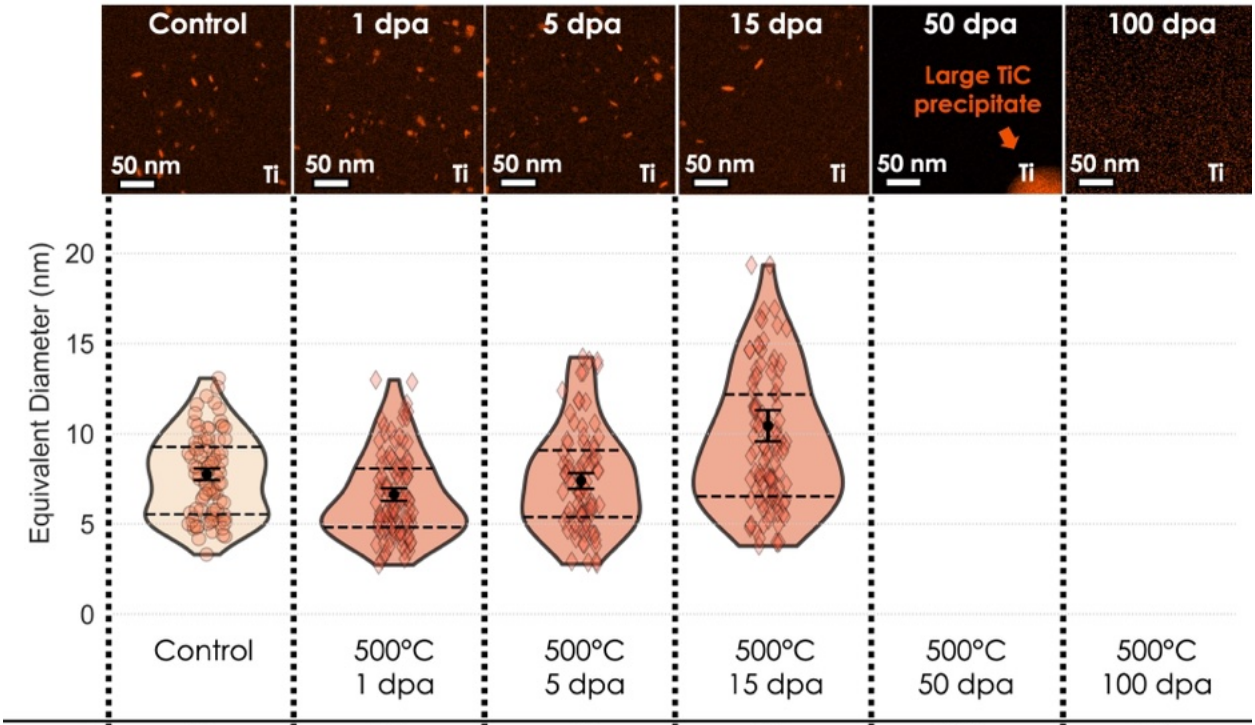

	Control	500°C 1 dpa	500°C 5 dpa	500°C 15 dpa	500°C 50 dpa	500°C 100 dpa
N	90	106	86	109	N.O.	N.O.
ρ (m^{-3})	$(2.3\pm0.3)\times10^{21}$	$(3.3\pm0.9)\times10^{21}$	$(2.9\pm0.9)\times10^{21}$	$(1.7\pm0.3)\times10^{21}$	N.O.	N.O.
d_{eq} nm)	7.8±0.3	6.6±0.4	7.4±0.4	10.4±0.9	N.O.	N.O.
f	$(6.8\pm0.6)\times10^{-4}$	$(6.9\pm0.2)\times10^{-4}$	$(9.3\pm3.4)\times10^{-4}$	$(11.1\pm2.3)\times10^{-4}$	N.O.	N.O.
ρ/ρ_{CTRL}	-	1.4±0.4	1.3±0.4	0.8±0.2	N.O.	N.O.
d/d_{CTRL}	-	0.9±0.1	1.0±0.1	1.4±0.1	N.O.	N.O.
f/f_{CTRL}	-	1.02±0.3	1.4±0.5	1.6±0.4	N.O.	N.O.

Figure 5.6 STEM-EDS micrographs of Ti with corresponding MX-TiC precipitate size distributions and statistics for the control specimen and specimens irradiated at 500°C with 7×10^{-4} dpa/s to 1 dpa, 5 dpa, 15 dpa, 50 dpa, and 100 dpa. Individual measurements of precipitates are shown by markers overlaid on the violin plot size distributions. Circles represent precipitate sizes from the control specimen and diamonds represent precipitate sizes from the irradiated specimens. N.O. means not observed.

5.3 Microstructure Evolution with Variable Temperature for Fixed Damage Rate and Damage Level

The third series assesses the effects of temperature at 300, 400, 500, and 600°C with a dose rate of 7×10^{-4} dpa/s to 15 dpa. These correspond to conditions A1, B1, C3, and D1. By analyzing the STEM-EDS maps of TiC precipitates for each condition to obtain and compare the size distributions, number densities, and volume fractions, an understanding of how single beam ion irradiation affects the precipitate stability as a function of temperature is established. Refer to Chapter 4 for a discussion on how these temperatures were chosen.

5.3.1 MX-TiC Precipitation Results

The results of these series are visualized with Figure 5.7 and Figure 5.8. Figure 5.7 shows the size distributions with a mirrored violin plot for each condition. Corresponding number of precipitates counted, precipitate number density, precipitate equivalent diameter, and precipitate volume fraction per condition are shown. Figure 5.8 shows the STEM-EDS micrographs for the control specimen and each irradiated condition in this series, along with the corresponding split violin plots displaying how the irradiation conditions changed the size distribution of TiC precipitates. The split violin plots show the same control size distribution on the left-hand sides coupled with the various irradiated conditions on the right-hand sides. The ratios of the number densities (ρ), equivalent diameters (d), and volume fractions (f) of the irradiated conditions to those of the control condition are shown at the bottom of the figure. The ratios show the irradiation response as compared to the control specimen. The interquartile lines on the violin plots are shown as dashed lines. The mean sizes and associated standard error are shown points with error bars. The counts of the precipitates are overlaid on the violin plots with symbols.

As can be seen in Figure 5.8, the ratios of the irradiated precipitate number densities to the control precipitate number densities (ρ/ρ_{CTRL}) at 300 and 400°C are less than 1 for each temperature (0.4±0.1 and 0.6±0.1, respectively), meaning that the number density decreased significantly with irradiation. At 300 and 400°C, the ratios of the irradiated precipitate diameters to the thermal precipitate diameters (d/d_{CTRL}) are equal to about 1 (1.1±0.1 and 1.0±0.1, respectively), meaning the precipitate sizes did not change significantly after irradiation. Hence, the ratios of the volume fractions (f/f_{CTRL}) at 300 and 400°C show there was a nominal decrease in volume fraction of TiC precipitates after irradiation resulting from the decrease in number density and stable sizes.

Similarly, the precipitate number densities in the 500 and 600°C conditions decreased in comparison to the control precipitate number density (0.8±0.2 and 0.6±0.1, respectively), though it was not a significant decrease at 500°C. On the other hand, the volume fractions in the 500 and 600°C conditions increased with irradiation, most notably at 600°C. The increase in the ratio of equivalent diameters for both 500 and 600°C was significant (1.4±0.1 and 1.9±0.3, respectively), but only the volume fraction increase at 600°C (6.2±1.7) can be deemed significant as it is greater than the aforementioned cutoff (Table 5.1). The volume fraction ratio for 500°C was 1.6±0.4, which is less than the cutoff for significance at 3.2. However, there is a clear lengthening of the tail of the size distribution at 500°C as shown in Figure 5.8. In addition, the interquartile lines of the 500°C size distribution have shifted upward with irradiation, most noticeably the 75% interquartile line. The shift upward of the distribution and interquartile lines are more pronounced in the 600°C condition, which is interpreted to be consistent with coarsening.

The precipitate size behavior at 500 and 600°C may be consistent with radiation-enhanced Ostwald ripening, where solutes from smaller precipitates migrate to larger precipitates [19]. This

may be shown from the shift upward in both the 500 and 600°C size distributions of the smallest precipitate sizes, evident from the shift upward of the interquartile range and the mean sizes at those temperatures. It is also possible that solutes from TiC nanoclusters and precipitates smaller than the STEM-EDS resolution are migrating to larger TiC precipitates. Even if radiation-induced Ostwald ripening is not occurring, diffusion-mediated coarsening seems to be the dominant factor in precipitate stability at 500 and 600°C. Though importantly other mechanisms like ballistic dissolution are still operating. This will be discussed in depth in Chapter 6. This series established the importance of temperature to TiC precipitate stability under irradiation to intermediate dose (15 dpa).

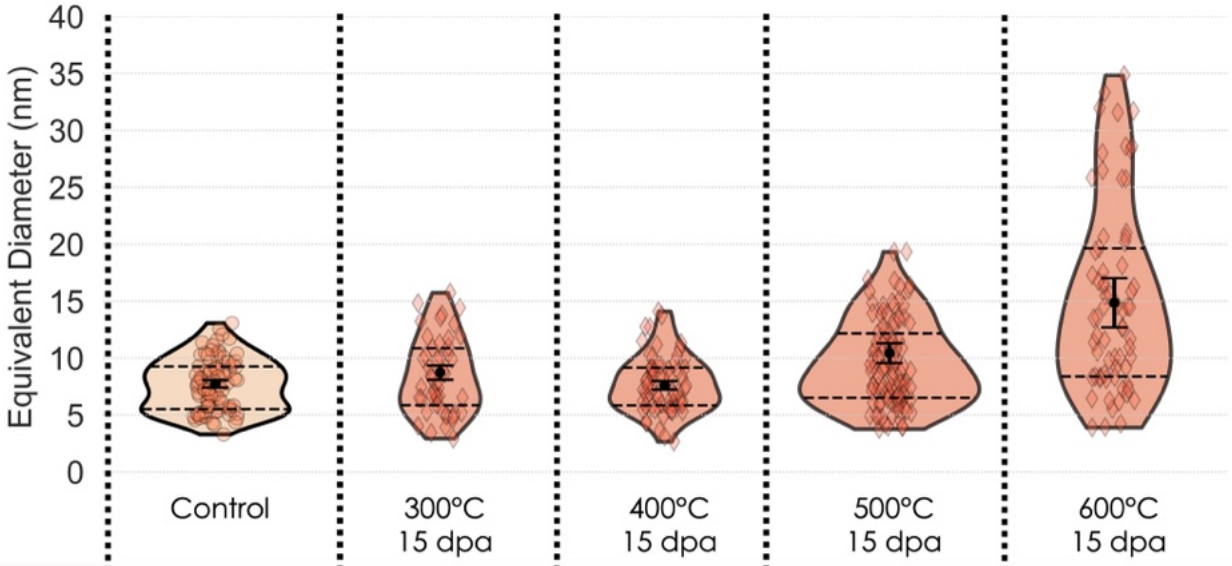

	Control	300°C 15 dpa	400°C 15 dpa	500°C 15 dpa	600°C 15 dpa
N	90	49	67	109	69
ρ (m^{-3})	$(2.3\pm0.3)\times10^{21}$	$(0.9\pm0.2)\times10^{21}$	$(1.5\pm0.2)\times10^{21}$	$(1.7\pm0.3)\times10^{21}$	$(1.3\pm0.2)\times10^{21}$
d_{eq} (nm)	7.8±0.3	8.7±0.6	7.6±0.4	10.4±0.9	14.9±2.2
f	$(6.8\pm0.6)\times10^{-4}$	$(3.9\pm1.0)\times10^{-4}$	$(4.4\pm0.9)\times10^{-4}$	$(11.1\pm2.3)\times10^{-4}$	$(42.0\pm11.0)\times10^{-4}$

Figure 5.7 Size distributions and corresponding statistics for the control specimen and specimens irradiated to 15 dpa with 7×10^{-4} dpa/s at 300, 400, 500, and 600°C. Size increased with increased temperature.

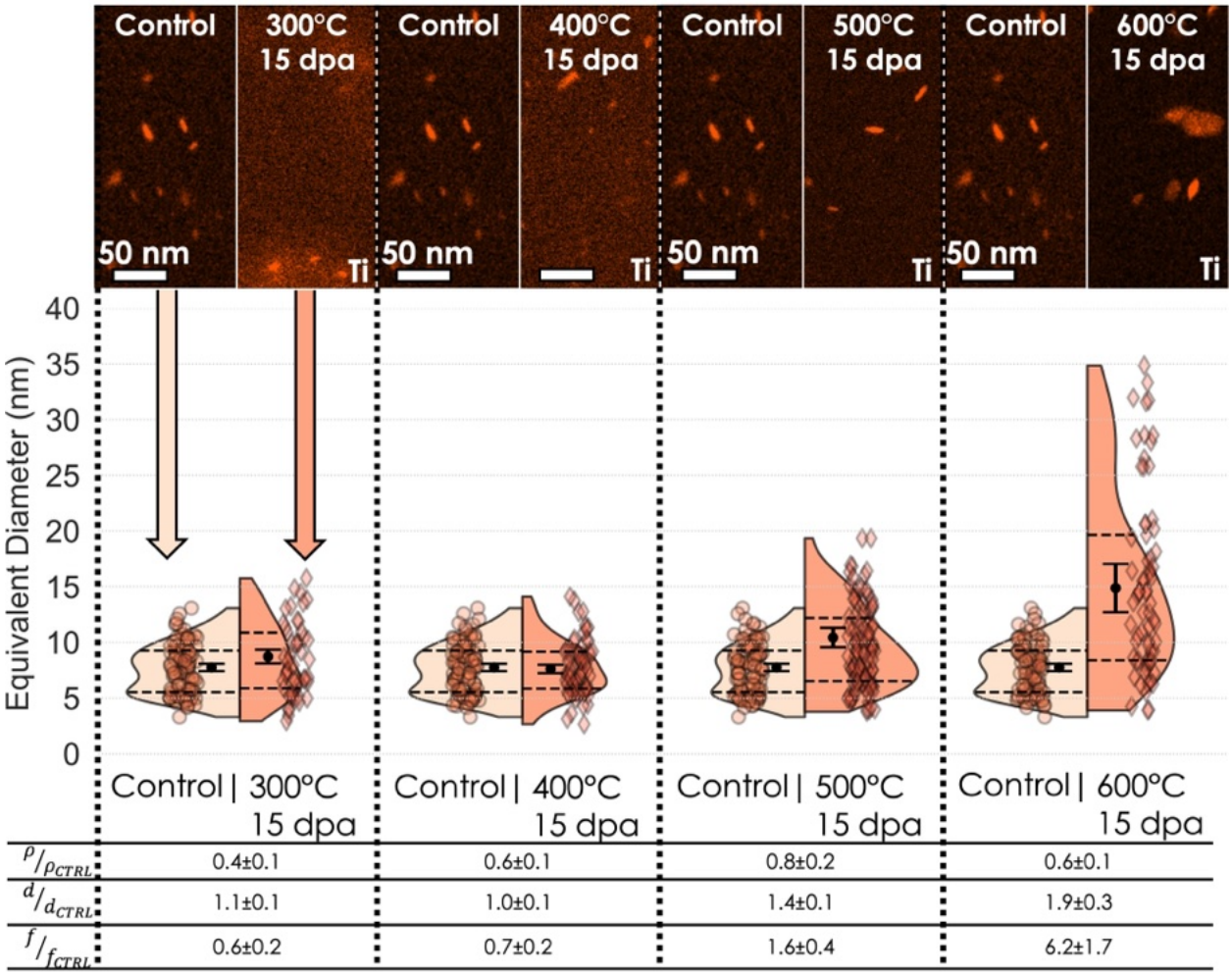

	Control | 300°C 15 dpa	Control | 400°C 15 dpa	Control | 500°C 15 dpa	Control | 600°C 15 dpa
ρ/ρ_{CTRL}	0.4±0.1	0.6±0.1	0.8±0.2	0.6±0.1
d/d_{CTRL}	1.1±0.1	1.0±0.1	1.4±0.1	1.9±0.3
f/f_{CTRL}	0.6±0.2	0.7±0.2	1.6±0.4	6.2±1.7

Figure 5.8 STEM-EDS micrographs for the control specimen and each irradiated condition in the single beam temperature series, along with the corresponding split violin plots and ratios of number density (ρ), average equivalent diameter (d), and volume fraction (f).

5.4 Microstructure Evolution with Variable Damage Level for Fixed Temperature, Damage Rate, and Helium Co-Implantation

5.4.1 MX-TiC Precipitation Results

As can be seen in Figure 5.9, helium had no observable effect on the MX-TiC precipitate dissolution at 50 or 100 dpa at 500°C and a displacement rate of 7×10^{-4} dpa/s. All MX-TiC precipitates dissolved at these high damage levels regardless of helium level, solidifying that

damage level is the dominant effect on precipitate stability above 15 dpa for the conditions studied. However, there were differences in precipitate evolution as a function of helium at 15 dpa. These results will be discussed in detail in Section 5.5.

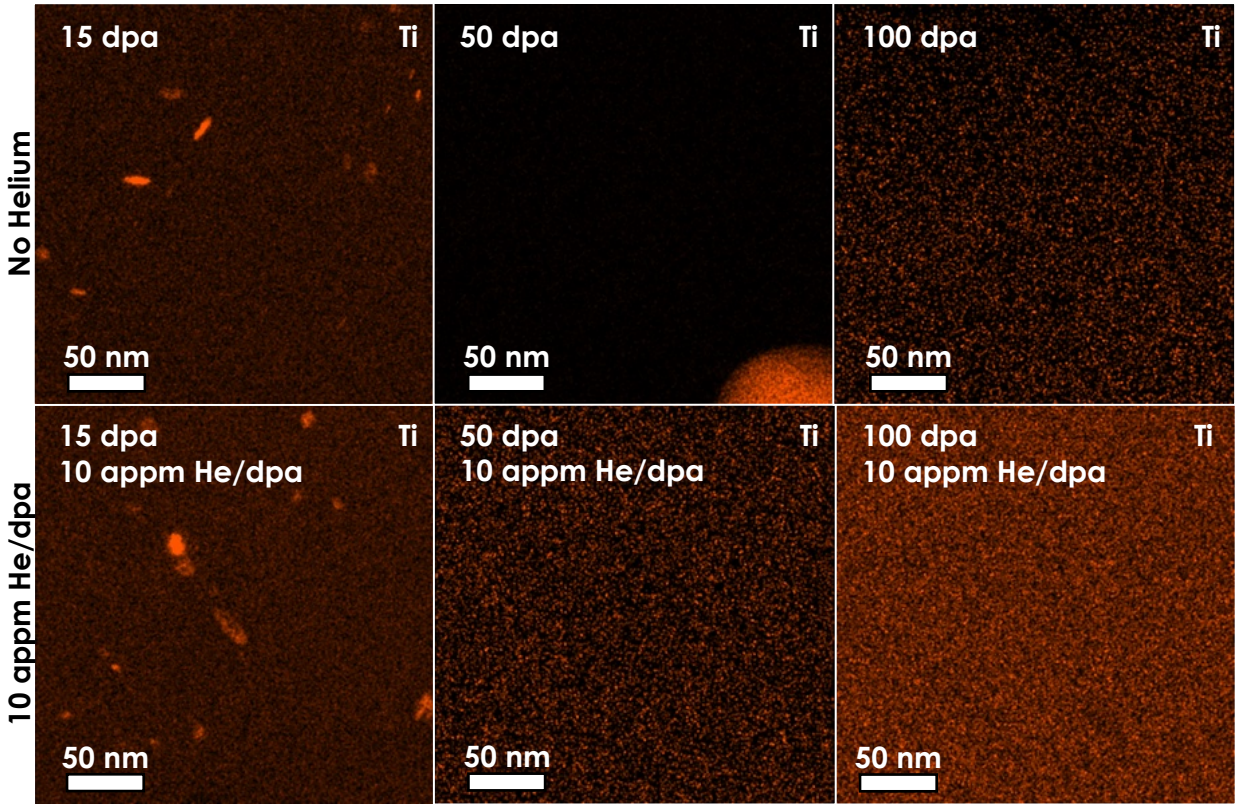

Figure 5.9 STEM-EDS micrographs of Ti for single beam conditions irradiated to (a) 15, (b) 50, and (c) 100 dpa. STEM-EDS micrographs of Ti for dual beam conditions irradiated to (d) 15, (e) 50, and (r) 100 dpa with 10 appm He/dpa. All conditions were irradiated at 500°C and rate 7×10^{-4} dpa/s.

5.4.2 Cavity Results

Figure 5.10 shows representative TEM-BF micrographs of cavities for the dual beam irradiations at 500°C to 15, 50, and 100 dpa with 10 appm He/dpa and 7×10-4 dpa/s. The number of cavities counted, diameter of cavities, and the swelling values are tabulated in Table 5.2. From the table, these conditions exhibited bimodal cavity distributions.

Table 5.2 Statistics of cavity analysis for select dual beam irradiations at 500°C to 15, 50, and 100 dpa with 10 appm He/dpa and 7×10^{-4} dpa/s. The 15 dpa condition includes cavities in the matrix and attached to TiC precipitates. See Table 5.3 for a detailed analysis of cavities in the 15 dpa condition.

Parameter	15 dpa	50 dpa	100 dpa
Number of total cavities	792 total 738 (<5nm) 54 (>5nm)	568 total 539 (<5nm) 29 (>5nm)	619 total 548 (<5nm) 71 (>5nm)
Diameter of matrix cavities	1.3±0.01 nm (<5nm) 10.1±0.4 nm (>5nm)	1.6±0.07 nm (<5nm) 11.8±0.6 nm (>5nm)	1.9±0.02 nm (<5nm) 16.3±0.8 nm (>5nm)
Density of cavities	$(2.1\pm0.08)\times10^{22}$ m^{-3} total $(1.8\pm0.07)\times10^{22}$ m^{-3} (<5nm) $(0.1\pm0.01)\times10^{22}$ m^{-3} (>5nm)	$(2.5\pm0.2)\times10^{22}$ m^{-3} total $(2.3\pm0.2)\times10^{22}$ m^{-3} (<5nm) $(0.1\pm0.01)\times10^{22}$ m^{-3} (>5nm)	$(3.2\pm0.3)\times10^{22}$ m^{-3} total $(2.8\pm0.3)\times10^{22}$ m^{-3} (<5nm) $(0.4\pm0.02)\times10^{22}$ m^{-3} (>5nm)
Swelling from all cavities	0.2±0.01%	0.2±0.03%	1.9±0.4%
Swelling per dpa	0.01±0.0007 %/dpa	0.004±0.0006 %/dpa	0.02±0.004 %/dpa

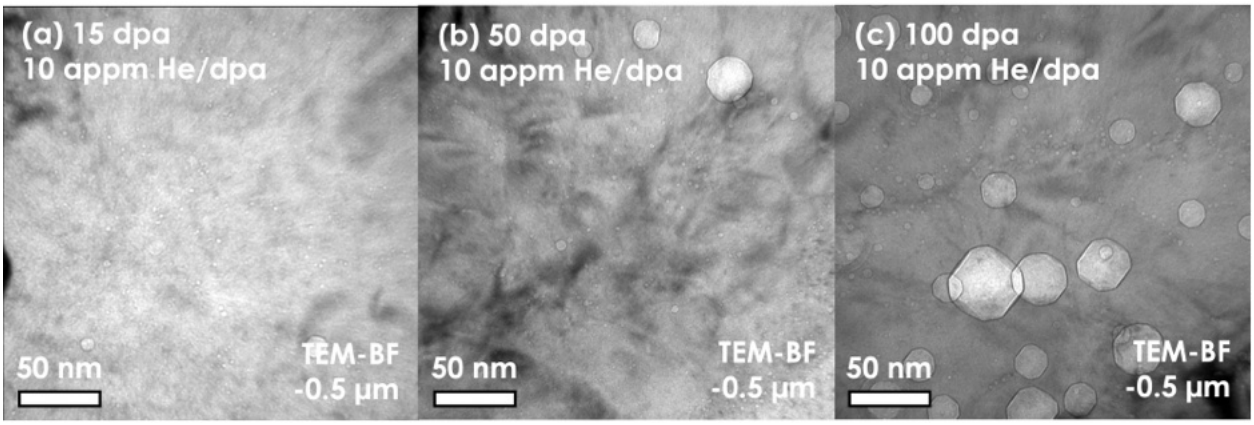

Figure 5.10 Cavity results for dual beam irradiations irradiated to (a) 15, (b) 50, and (c) 100 dpa. All conditions irradiated with 10 appm He/dpa at 500°C with a dose rate of 7×10^{-4} dpa/s. Images are TEM-BF micrographs in the -0.5 µm underfocused condition.

5.5 Microstructure Evolution with Variable Temperature for Fixed Helium Co-Implantation, Damage Rate, and Damage Level

The second set of helium experiments held the variable of dose, dose rate, and helium co-implantation constant (15 dpa, 7×10^{-4} dpa/s, 10 appm He/dpa) with varying temperature (400, 500, and 600°C) to explore the interaction of helium and temperature. These conditions correspond to B4, C6, and D2. The damage level of 15 dpa was chosen because it was shown to encompass effects of precipitate dissolution with single beam irradiation and the effects of helium co-injection at this damage level can be explored.

5.5.1 MX-TiC Precipitation Results

Figure 5.11 and Figure 5.12 shows the dual beam precipitate responses at various temperatures as compared to the control specimen. The response of the TiC precipitates at 400°C with 10 appm He/dpa co-implanted is nearly identical to the response found at 400°C with no helium co-implanted: the number density of precipitates decreased, the size of precipitates remained stable, and volume fraction decreased with irradiation.

However, helium did influence the responses at 500 and 600°C. The helium appears to have decreased the irradiation-enhanced growth of the TiC precipitates as compared to the single beam conditions as shown by the tail of the size distribution in Figure 5.12. At 500°C, the average equivalent diameter remained stable after the dual beam irradiation. The ratio of the average size of the precipitates at 500°C under dual beam irradiation compared to the control specimen was 1.0±0.1. Whereas the single beam response at 500°C of this parameter was 1.4±0.1. This is also reflected in the size distribution at 500°C. In Figure 5.12, the distribution of the dual beam 500°C is almost the same as the control size distribution. This was not the case for the single beam irradiation at 500°C, which skewed to larger sizes. As already described, the change in average

equivalent diameter in the single beam irradiation at 500°C to 15 dpa was significant, but the change in diameter in the corresponding dual beam condition was not.

The difference in responses between the single and dual beam conditions at 500°C can also be observed in Figure 5.13. This figure compares the size distributions of the single and dual beam irradiations as well as the ratios of the number densities, equivalent diameters, and volume fractions of the dual beam to the single beam conditions. The ratio between the number densities of the single and dual beam conditions at 500°C (1.0±0.2) shows that this parameter was not affected by the presence of helium and hence helium co-injection is not significantly affecting the dissolution. However, the average size did decrease with helium at 500°C (0.7±0.1), leading to a reduction in the volume fraction (0.5±0.1). This can be observed in the shortening of the tail of the dual beam irradiation at 500°C as compared to the single beam irradiation, as shown by the black arrow in Figure 5.13.

The dual beam response at 600°C as compared to the single beam response at 600°C followed the same pattern as observed at 500°C: no change in number density, decrease in average size, decrease in volume fraction, and shortening of the tail of the size distribution with helium co-injection. Next, the general cavity behavior will be discussed. Figure 5.14 summarizes the size, number density, and volume fraction of for all single and dual beam conditions (10 appm He/dpa) irradiated to 15 dpa with a damage rate of 7×10^{-4} dpa/s.

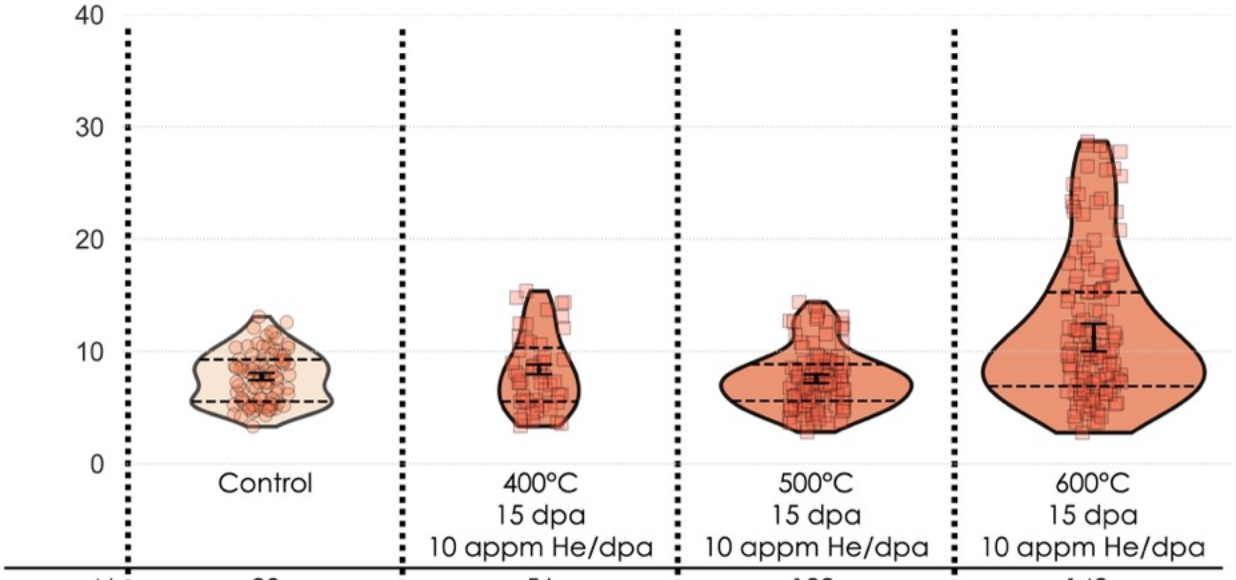

	Control	400°C 15 dpa 10 appm He/dpa	500°C 15 dpa 10 appm He/dpa	600°C 15 dpa 10 appm He/dpa
N	90	56	122	142
ρ (m^{-3})	$(2.3\pm0.3)\times10^{21}$	$(0.9\pm0.2)\times10^{21}$	$(1.8\pm0.1)\times10^{21}$	$(1.6\pm0.2)\times10^{21}$
d_{eq} (nm)	7.8±0.3	8.4±0.4	7.6±0.4	11.2±1.2
f	$(6.8\pm0.6)\times10^{-4}$	$(3.8\pm0.9)\times10^{-4}$	$(5.3\pm0.5)\times10^{-4}$	$(27.7\pm11.0)\times10^{-4}$

Figure 5.11 Size distributions and corresponding statistics for the control specimen and specimens irradiated to 15 dpa with 7×10^{-4} dpa/s and 10 appm He/dpa at 400, 500, and 600°C.

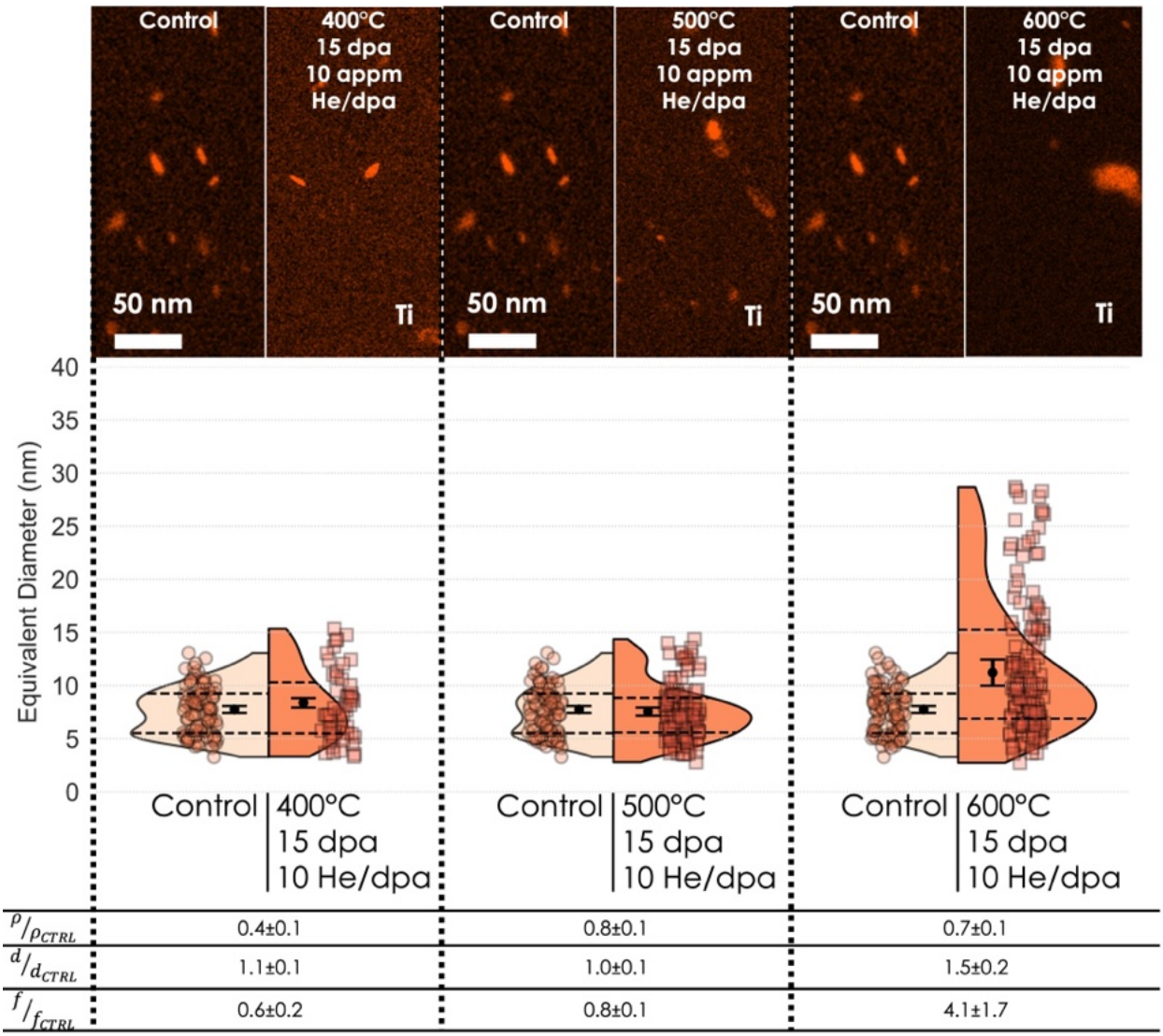

ρ/ρ_{CTRL}	0.4±0.1	0.8±0.1	0.7±0.1
d/d_{CTRL}	1.1±0.1	1.0±0.1	1.5±0.2
f/f_{CTRL}	0.6±0.2	0.8±0.1	4.1±1.7

Figure 5.12 STEM-EDS micrographs for the control specimen and each irradiated condition in the dual beam temperature series, along with the corresponding split violin plots and ratios of number density (ρ), average equivalent diameter (d), and volume fraction (f).

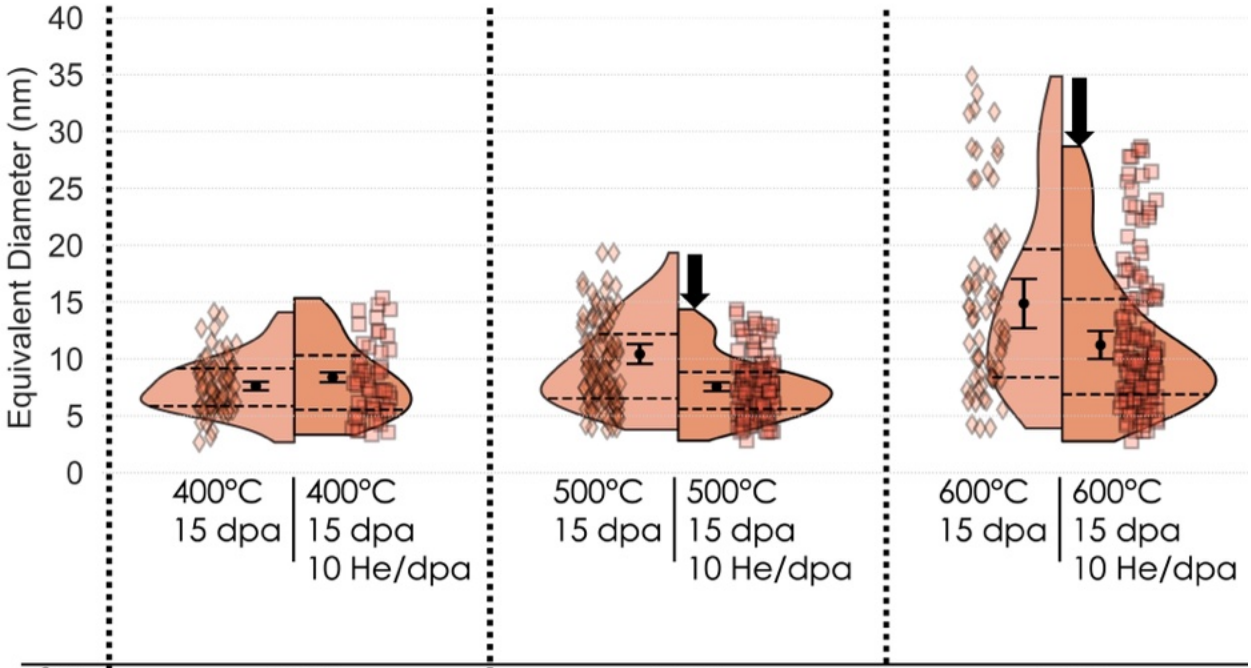

	400°C 15 dpa | 400°C 15 dpa 10 He/dpa	500°C 15 dpa | 500°C 15 dpa 10 He/dpa	600°C 15 dpa | 600°C 15 dpa 10 He/dpa
ρ_{DI}/ρ_{SI}	0.7±0.2	1.0±0.2	1.3±0.3
d_{DI}/d_{SI}	1.1±0.1	0.7±0.1	0.8±0.1
f_{DI}/f_{SI}	1.1±0.3	0.5±0.1	0.7±0.3

Figure 5.13 The comparison in responses between the single and dual beam conditions at 500°C. The ratios now show the change in parameters from the dual to the single beam conditions. Diamonds represent precipitates from single beam irradiations and squares from dual beam irradiations.

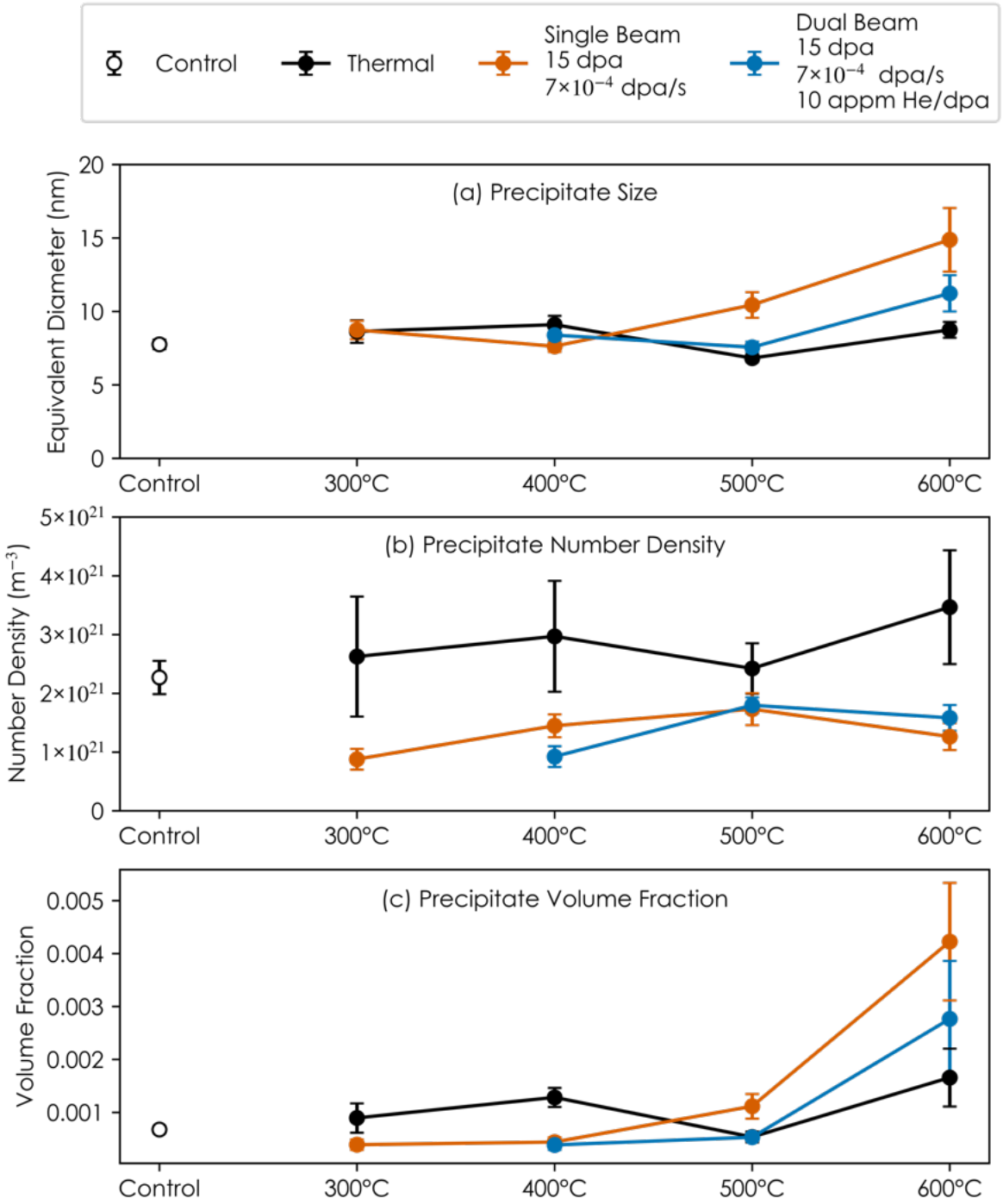

Figure 5.14 Overview of (a) equivalent diameter, (b) number density, and (c) volume fraction of MX precipitates in CNA9 under single and dual ion beam conditions. If no error bars are visible for markers, the error was smaller than the size of the marker at that condition.

5.5.2 Cavity Results

The general cavity behavior was assessed at each temperature tested with 10 appm He/dpa (Figure 5.15). Small, spherical cavities (~1-2 nm in diameter) were found in the 400°C (Figure 5.15a) and 600°C (Figure 5.15c) dual beam conditions homogeneously dispersed in the matrix. The peak swelling condition for the temperatures tested occurred at 500°C, where a bimodal cavity size distribution was evident (Figure 5.15b). The bimodal size distribution is explained in literature, which describes the occurrence of a critical cavity size above which the cavity is stable enough to grow with vacancy accumulation and below which is stabilized through the amount of gas pressure from helium [20]. Cavity statistics for three conditions are shown in Table 5.3.

In addition, the TiC-matrix interface was studied to assess the TiC precipitates' ability to trap helium in the form of helium-filled bubbles. Representative STEM-EDS maps of Ti and corresponding TEM-BF micrographs in the underfocused condition are shown for 400°C, 500°C, and 600°C in Figure 5.16, Figure 5.17, and Figure 5.18, respectively. As described in Chapter 4, the STEM-EDS maps and TEM-BF images were taken in the same location so as to allow for spatial correlation of the cavities (*i.e.,* in the matrix or attached to precipitates). This allowed for accurate counting and measuring of the precipitate-attached cavities. It should be noted that TEM-BF images are 2D projections of the 3D volume of the TEM lamellae. As such, it is possible to incorrectly identify cavities in the volume of the lamellae as being attached to a precipitate, if the 2D projection renders the distance between the cavity in the matrix and the precipitate flat. However, typically a clear 'halo' of cavities around the circumference of precipitates was observed. The possibility of miscounting cavities in the matrix as being being attached to precipitates cannot be fully accounted for, however. It is assumed that this error is small such as not to affect the overall results of the analysis.

It was found that the interfaces of TiC precipitates sequestered helium in the form of bubbles at all temperatures tested, but that the most efficient helium sequestration occurred at 500 and 600°C. Only 14 precipitate-attached cavities were observed in the 400°C condition, which is not enough to be statistically relevant. On the other hand, 162 and 366 precipitate-attached cavities were observed for the dual beam conditions at 500 and 600°C. This resulted in an average of 5.3±0.4 and 4.8±0.4 TiC-attached bubbles per precipitate respectively for the dual beam conditions at 500 and 600°C. All precipitate-attached cavities were spherical and less than 5 nm in diameter, and hence were considered helium-filled bubbles.

The size distributions of the cavities attached to precipitates and cavities in the matrix are shown in Figure 5.19. The uniform distributions of small matrix (<5 nm) cavities are displayed for the 400°C-15 dpa-7×10^{-4} dpa/s-10 appm He/dpa condition (irradiation condition B4, Table 4.2) and in the 600°C-15 dpa-7×10^{-4} dpa/s-10 appm He/dpa condition (irradiation condition D2, Table 4.2). A bimodal cavity size distribution was found in the 500°C-15 dpa-7×10^{-4} dpa/s-10 appm He/dpa condition, which can be inferred from the lengthened size of matrix cavities in the 500°C condition in Figure 5.19 and can be more clearly seen in the log-log plot in Figure 5.20. Figure 5.20 shows the size distribution of the precipitate-attached cavities (light blue) and the matrix cavities (dark blue) in 500°C-15 dpa-7×10^{-4} dpa/s-10 appm He/dpa condition. The precipitate-attached cavities remain small (below 5 nm) while the matrix cavities display a bimodal distribution. The precipitate-attached bubbles also remained smaller than the critical bubble radius at 500°C. Refer to Section 4.9 for a detailed description of how the critical bubble radius was determined.

Table 5.3 Statistics of cavity analysis for select dual beam irradiations at 400, 500, and 600°C to 15 dpa with 10 appm He/dpa and 7×10^{-4} dpa/s. N.M. means not measured.

Parameter	**400°C**	**500°C**	**600°C**
Number of total cavities	856 total	792 total	926 total
Number of TiC-attached cavities	14 (<5nm) 0 (>5nm)	162 (<5nm) 0 (>5nm)	366 (<5nm) 0 (>5nm)
Number of matrix cavities	842 (<5nm) 0 (>5nm)	576 (<5nm) 54 (>5nm)	560 (<5nm) 0 (>5nm)
Diameter of TiC-attached cavities	1.0±0.1 nm (<5nm)	1.2±0.03 nm (<5nm)	1.6±0.04 nm (<5nm)
Diameter of matrix cavities	1.0±0.04 nm (<5nm) 0 (>5nm)	1.3±0.02 nm (<5nm) 10.1±0.4 nm (>5nm)	1.2±0.02 nm (<5nm)
Density of TiC-attached bubbles	$(0.06\pm0.02)\times10^{22}$ m^{-3} (<5nm)	$(0.5\pm0.05)\times10^{22}$ m^{-3} (<5nm)	$(0.8\pm0.07)\times10^{22}$ m^{-3} (<5nm) 0 (>5nm)
Density of matrix cavities	$(3.3\pm0.1)\times10^{22}$ m^{-3} (<5nm) 0 (>5nm)	$(1.7\pm0.06)\times10^{22}$ m^{-3} (<5nm) $(0.1\pm0.01)\times10^{22}$ m^{-3} (>5nm)	$(1.3\pm0.08)\times10^{22}$ m^{-3} (<5nm) 0 (>5nm)
Ratio of TiC-attached bubbles to the number of TiC precipitates observed	0.4±0.1	5.3±0.4	4.8±0.4
Fraction of precipitate-attached bubbles to total bubble count	0.02±0.006	0.3±0.03	0.5±0.04
Swelling from all cavities	0.002±0.0002%	0.2±0.01%	0.005±0.0002%

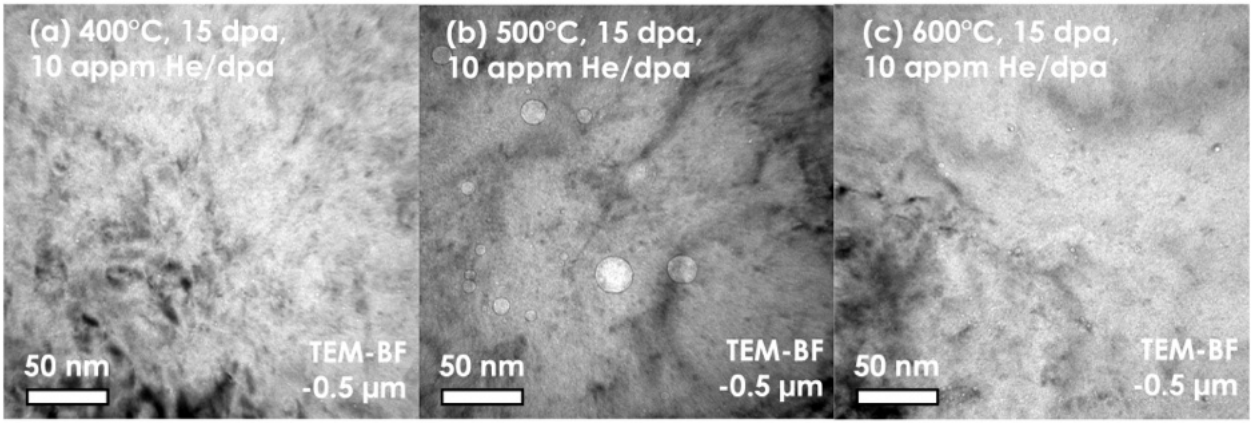

Figure 5.15 TEM-BF micrographs in the underfocused condition showing cavities at (a) 400°C, (b) 500°C, and (c) 600°C irradiated to 15 dpa with 7×10^{-4} dpa/s and 10 appm He/dpa.

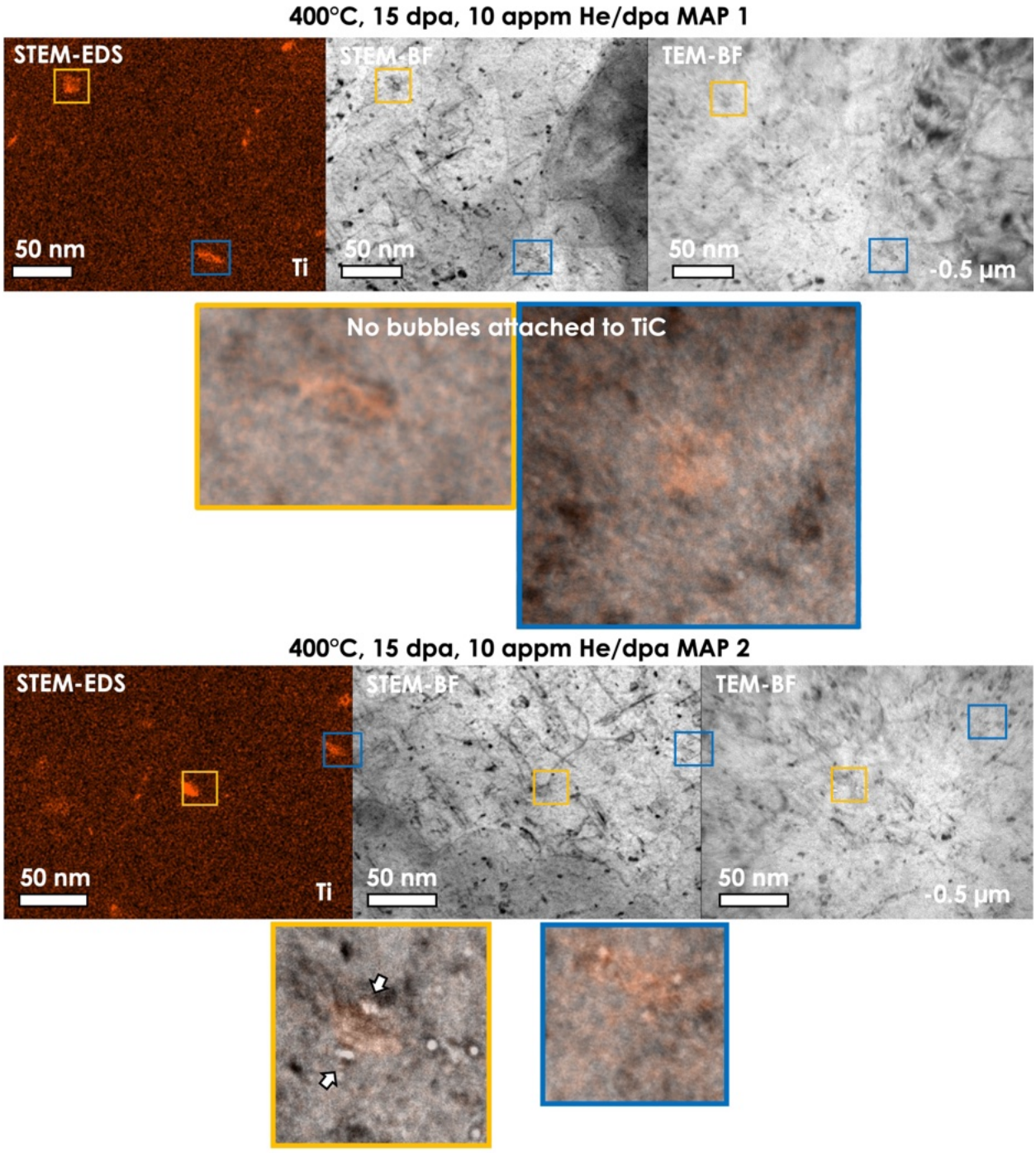

Figure 5.16 Two sets of representative STEM-EDS maps of Ti with corresponding STEM-ABF and TEM-BF micrographs in the underfocused condition for the 400°C-15 dpa-7×10^{-4} dpa/s-10 appm He/dpa condition. The spatial relationship between cavities and MX-TiC precipitates was established by carefully overlaying the STEM-EDS images of Ti over the underfocused TEM-BF micrographs. These overlays are shown in the insets outlined by yellow and blue.

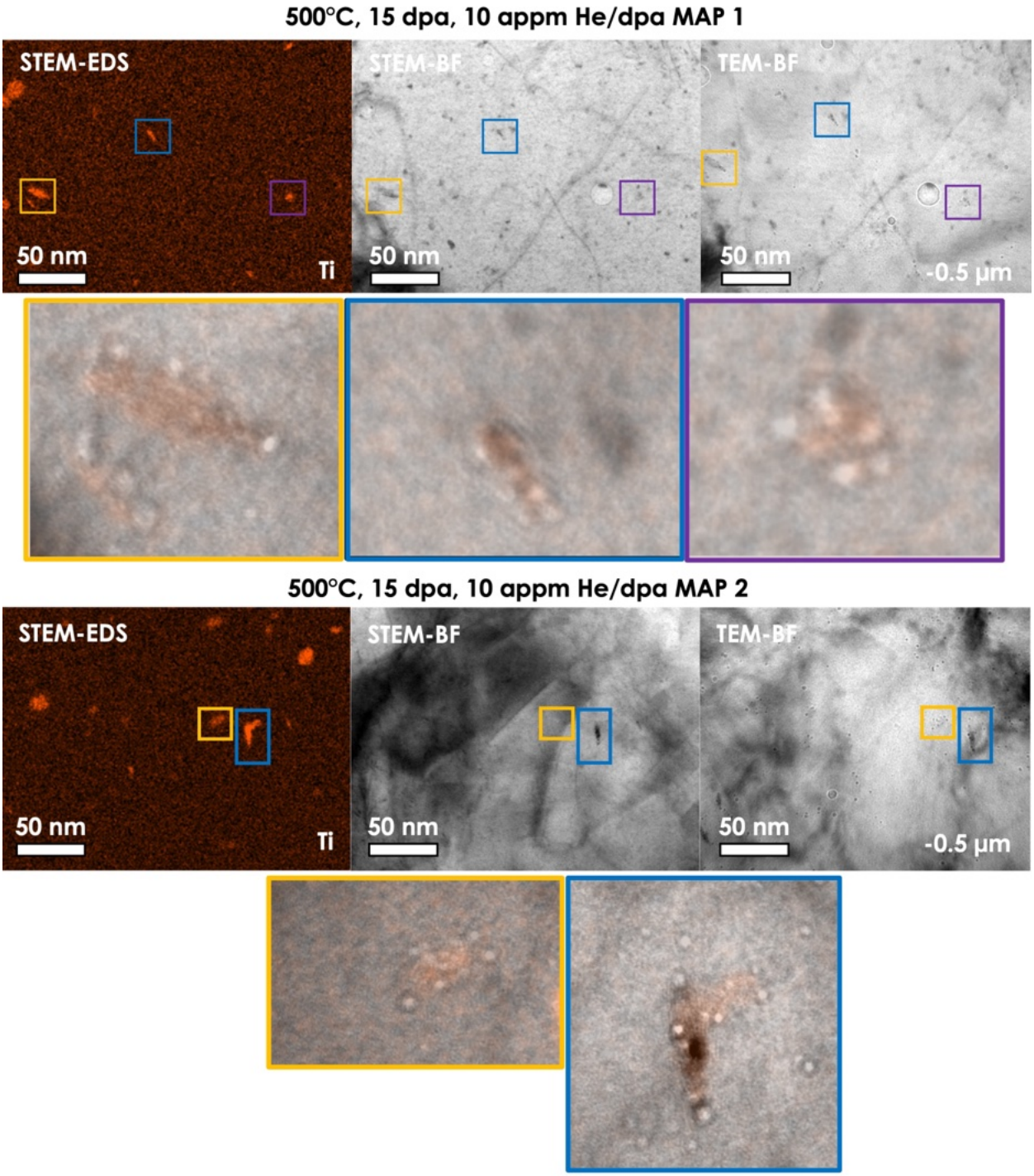

Figure 5.17 Two sets of representative STEM-EDS maps of Ti with corresponding STEM-ABF and TEM-BF micrographs in the underfocused condition for the 500°C-15 dpa-7×10^{-4} dpa/s-10 appm He/dpa condition. The spatial relationship between cavities and MX-TiC precipitates was established by carefully overlaying the STEM-EDS images of Ti over the underfocused TEM-BF micrographs. These overlays are shown in the insets outlined by yellow, blue, and purple.

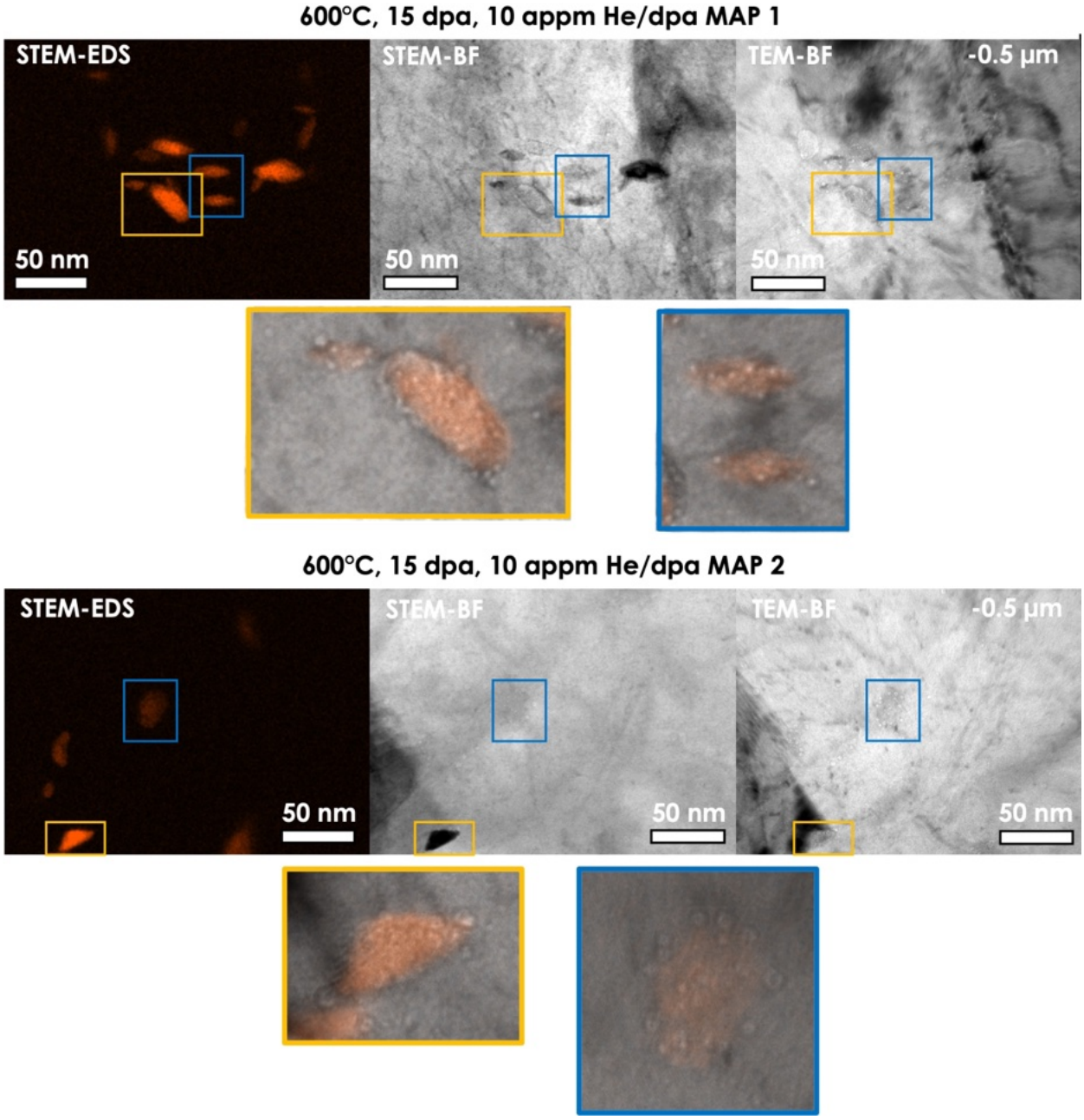

Figure 5.18 Two sets of representative STEM-EDS maps of Ti with corresponding STEM-ABF and TEM-BF micrographs in the underfocused condition for the 600°C-15 dpa-7×10^{-4} dpa/s-10 appm He/dpa condition. The spatial relationship between cavities and MX-TiC precipitates was established by carefully overlaying the STEM-EDS images of Ti over the underfocused TEM-BF micrographs. These overlays are shown in the insets outlined by yellow and blue.

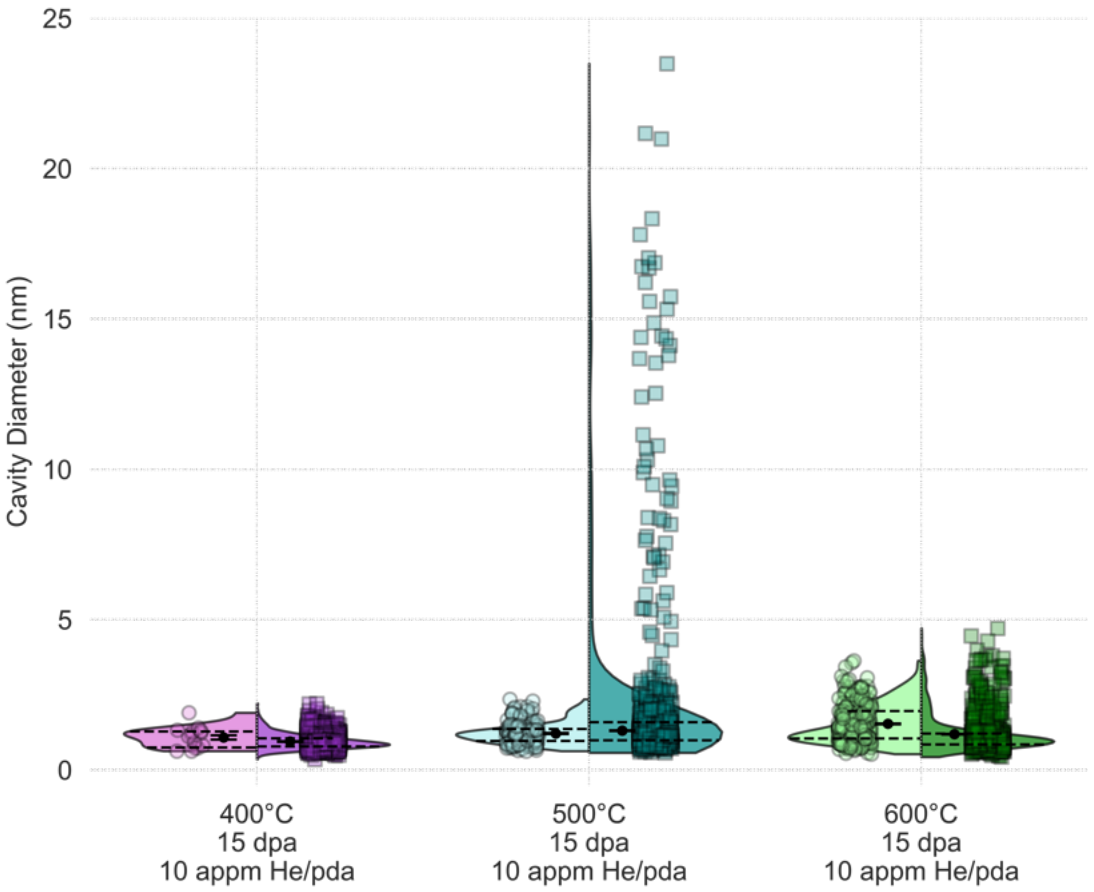

Figure 5.19 Comparison of the size distributions of the cavities attached to precipitates (left-hand side of each split violin plot, circles) and cavities in the matrix (right-hand side of each split violin plot, squares) for 400°C (purple), 500°C (blue), and 600°C (green) irradiated to 15 dpa with 7×10^{-4} dpa/s and 10 appm He/dpa.

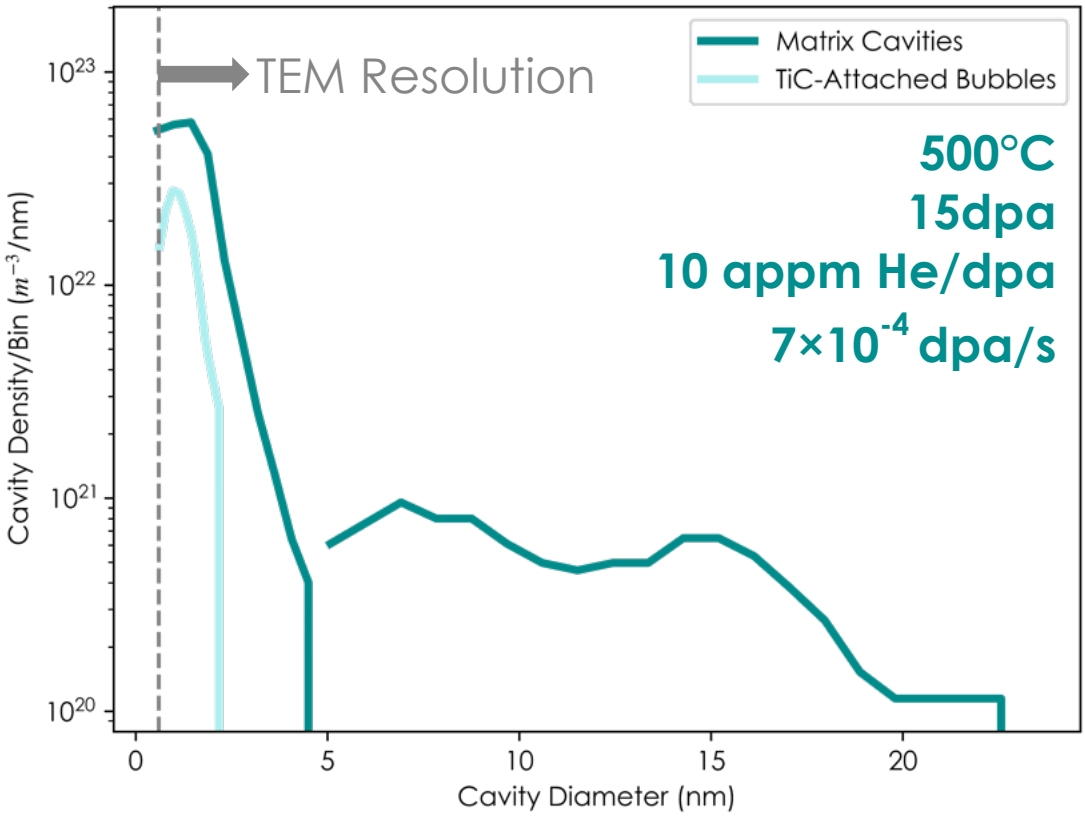

Figure 5.20 A log-log plot showing the cavity density per bin width as a function of cavity diameter for the 500°C-15 dpa-7×10^{-4} dpa/s-10 appm He/dpa condition.

5.6 Microstructure Evolution with Variable Helium Co-Implantation for Fixed Temperature, Damage Rate, and Damage Level

The last set of experiments assessed the effects of helium rate on precipitate stability. The variables of dose (15 dpa), dose rate (7×10^{-4} dpa/s), and temperature (500°C) were held constant while helium co-implantation varied (0, 10, and 25 appm He/dpa). These conditions correspond to C3, C6, and C9. The helium co-injection rate of 25 appm He/dpa was chosen because it encompasses the fusion-relevant helium rate regime for FM steels and because it was the maximum rate attainable experimentally to assess the effects of helium rate.

5.6.1 MX-TiC Precipitation Results

Representative STEM-EDS maps of Ti for the 500°C-15 dpa-7×10^{-4} dpa/s-25 appm He/dpa condition is shown in Figure 5.21. Statistics for each condition in this irradiation series is shown in Figure 5.22. The results of the control specimen and conditions C3 and C6 have already been presented. The TiC precipitation structure of condition C9 (500°C-15 dpa-7×10^{-4} dpa/s-25 appm He/dpa) was nearly exactly that of the condition C6 (500°C-15 dpa-7×10^{-4} dpa/s-10 appm He/dpa). The larger precipitate sizes present in the single beam 500°C-15 dpa-7×10^{-4} dpa/s condition were not observed in either of the dual beam conditions, regardless of helium co-injection rate.

Most likely, the helium co-injection rates (10 and 25 appm He/dpa) were not significantly different enough to result in different observable precipitation behavior. CNA9 has a high intrinsic sink strength and hence a greater difference in helium co-injection rate would most likely be necessary to notice effects on precipitate evolution. However, 25 appm He/dpa was the upper limit achievable in MIBL and hence no further studies could take place at MIBL to increase the helium co-injection rate to observe the effects of helium rates greater than 25 appm He/dpa. However, as 25 appm He/dpa is within the calculated helium generation range for structural steels for fusion reactors, this implantation rate is relevant to fusion studies. A greater helium rate would be more suitable for fundamental studies. Future work could utilize other ex-situ ion beam laboratories and in-situ ion irradiation facilities that are able to achieve greater helium co-injection rates. Pre-implantation may also be used to achieve the desired greater helium concentrations, however pre-implantation can cause cavity swelling results that are not consistent with reactor-relevant irradiations and hence a dynamic understand of precipitates and cavity development may not be able to be garnered [3,116], though one study found that precipitates in HT9 were not affected by the method of helium implantation [117].

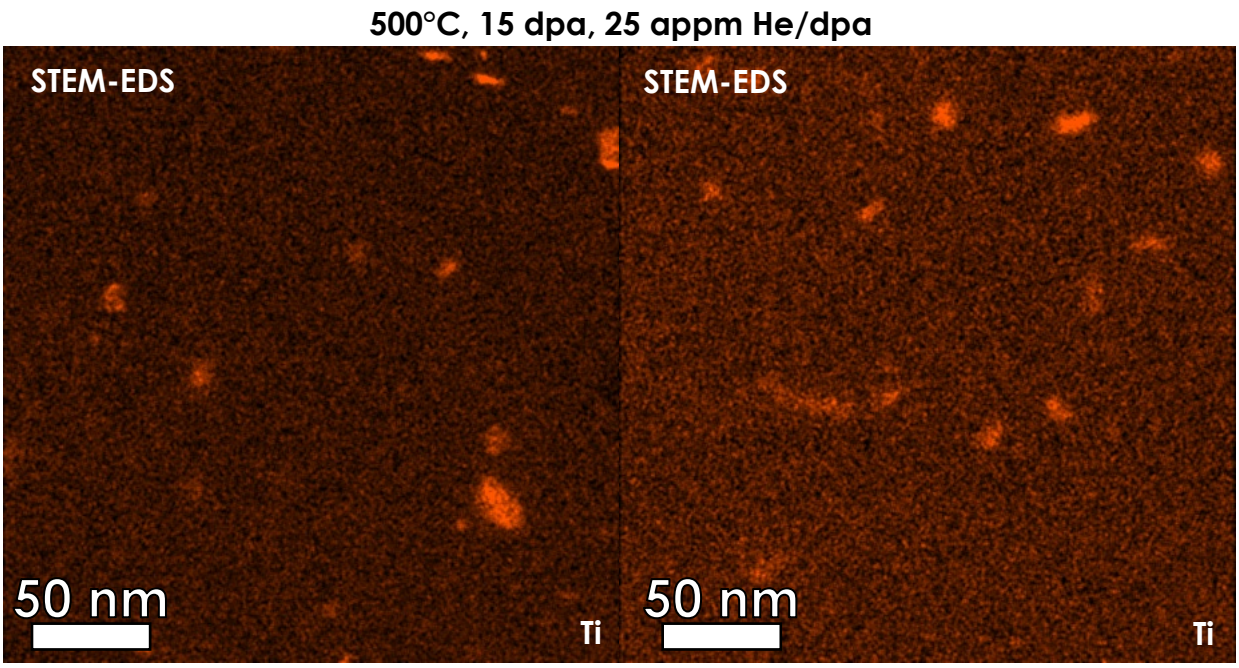

Figure 5.21 Representative STEM-EDS maps of Ti for the 500°C -15 dpa-7×10^{-4} dpa/s-25 appm He/dpa condition.

5.6.2 Cavity Results

The general cavity behavior of the 500°C-15 dpa-7×10^{-4} dpa/s-25 appm He/dpa condition can be seen in Figure 5.23. The sequestration of helium at the precipitate-matrix interfaces is also shown in Figure 5.24. Table 5.4 shows that there is no statistically significant difference in the density or size of cavities in the 25 appm He/dpa condition versus in the 10 appm He/dpa condition. Hence, the MX-TiC precipitates remain efficient helium sequestration sites at 25 appm He/dpa condition.

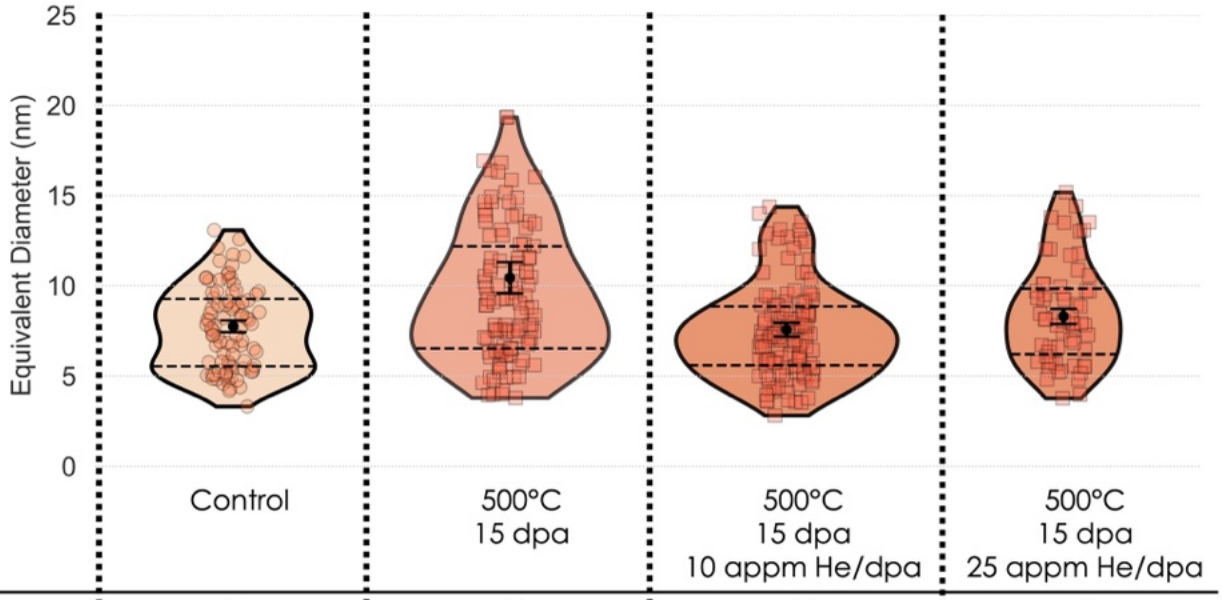

	Control	500°C 15 dpa	500°C 15 dpa 10 appm He/dpa	500°C 15 dpa 25 appm He/dpa
N	90	109	109	63
ρ (m^{-3})	$(2.3\pm0.3)\times10^{21}$	$(1.7\pm0.3)\times10^{21}$	$(1.8\pm0.1)\times10^{21}$	$(1.5\pm0.2)\times10^{21}$
d_{eq} nm)	7.8±0.3	10.4±0.9	7.6±0.4	8.3±0.4
f	$(6.8\pm0.6)\times10^{-4}$	$(11.1\pm2.3)\times10^{-4}$	$(5.3\pm0.5)\times10^{-4}$	$(6.1\pm1.1)\times10^{-4}$

Figure 5.22 Statistics for the helium co-injection series at 500°C (0, 10, 25 appm He/dpa) as compared to the control specimen.

Table 5.4 Statistics of cavity analysis for select dual beam irradiations at 500°C to 15 dpa with 25 appm He/dpa and 7×10-4 dpa/s.

Parameter	15 dpa 25 appm He/dpa
Number of total cavities	896 total
Number of TiC-attached cavities	173 (<5nm) 0 (>5nm)
Number of matrix cavities	670 (<5nm) 53 (>5nm)
Diameter of TiC-attached cavities	1.4±0.04 nm (<5nm)
Diameter of matrix cavities	1.5±0.01 nm (<5nm) 11.7±0.4 nm (>5nm)
Density of TiC-attached bubbles	$(0.7\pm0.1)\times10^{22}$ m^{-3} (<5nm)
Density of matrix cavities	$(3.1\pm0.1)\times10^{22}$ m^{-3} (<5nm) $(0.2\pm0.03)\times10^{22}$ m^{-3} (>5nm)
Ratio of TiC-attached bubbles to the number of TiC precipitates observed	5.6±0.0.3
Fraction of precipitate-attached bubbles to total bubble count	0.2±0.0.007
Swelling from all cavities	0.3±0.05%

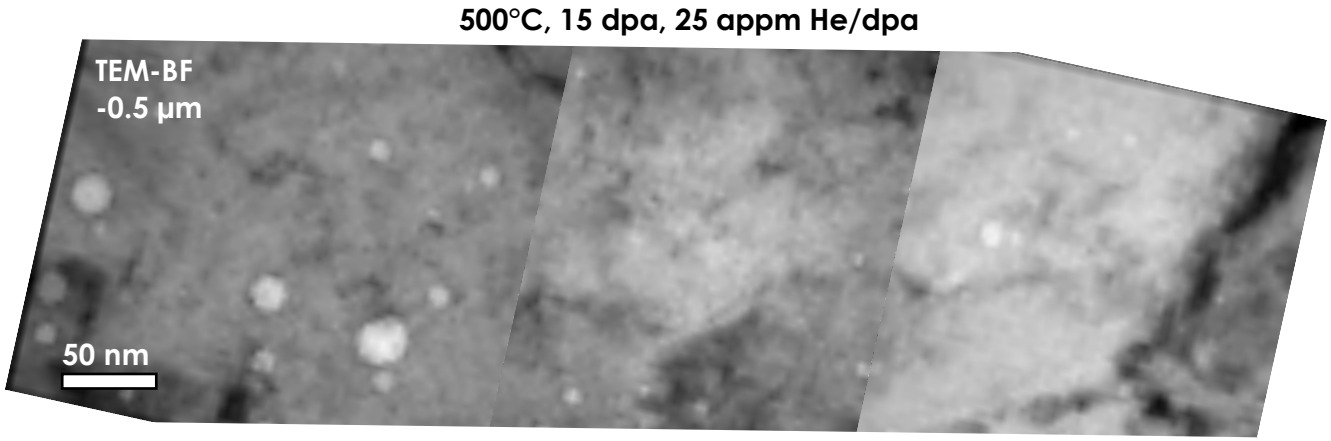

Figure 5.23 The general cavity behavior in the nominal damage region of the 500°C-15 dpa-7×10^{-4} dpa/s-25 appm He/dpa condition.

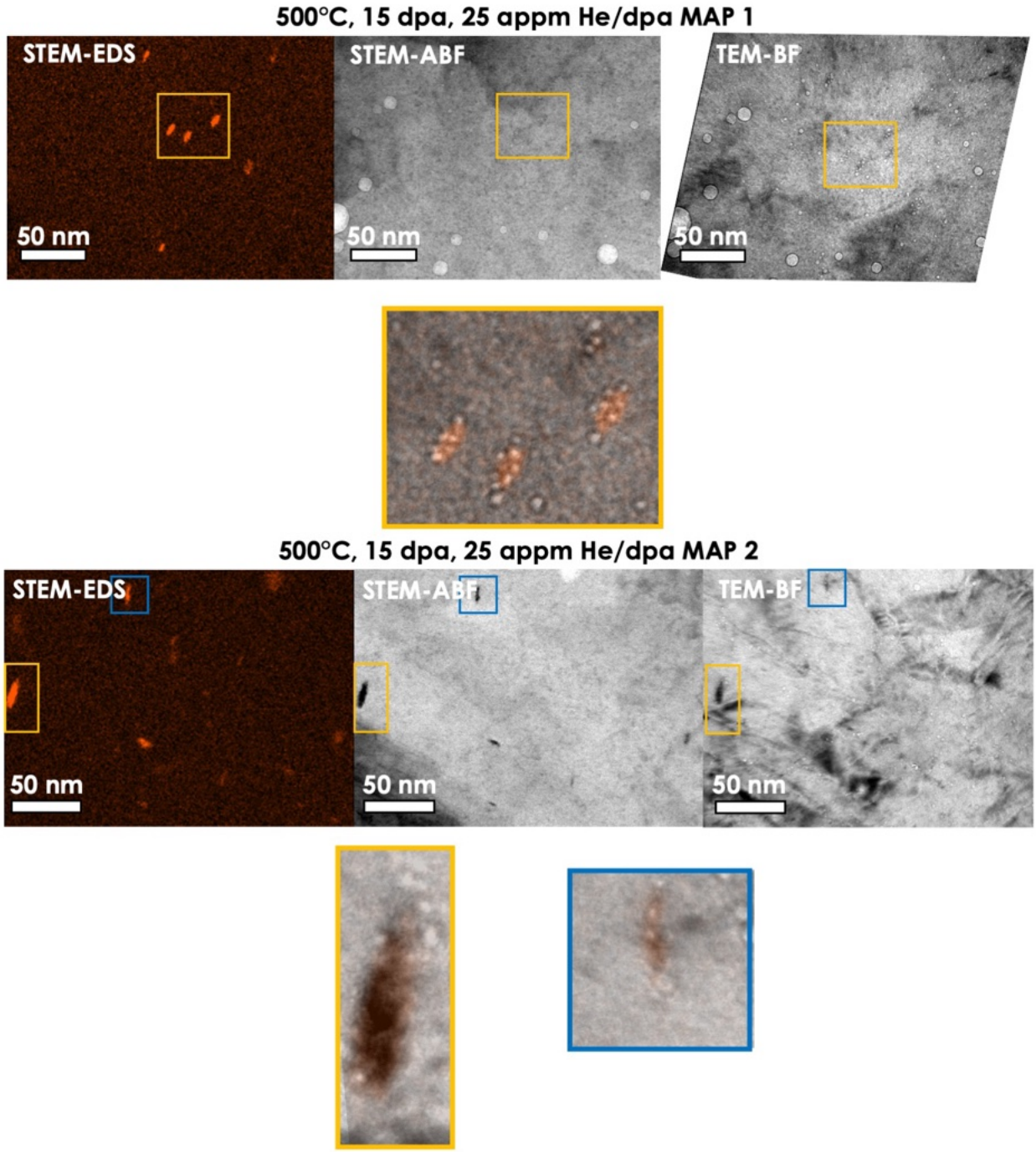

Figure 5.24 Two sets of representative STEM-EDS maps of Ti with corresponding STEM-ABF and TEM-BF micrographs in the underfocused condition for the 500°C-15 dpa-7×10^{-4} dpa/s-25 appm He/dpa condition. The spatial relationship between cavities and MX-TiC precipitates was established by carefully overlaying the STEM-EDS images of Ti over the underfocused TEM-BF micrographs. These overlays are shown in the insets outlined by yellow and blue.

Chapter 6 Discussion

The discussion of the results presented in Chapter 5 will be divided into two main sections. The first section will assess the results in the context of the scientific hypothesis as described in Chapter 3, that co-injected helium will suppress the growth of the pre-existing TiC precipitates versus ion irradiations conducted without co-injected helium due to helium-solute binding. The sub-sections will describe helium's role on precipitate coarsening and dissolution. The effects of damage, damage rate, and temperature will also be discussed. The second section will assess the results in the context of the engineering hypothesis to understand the helium sequestration ability of TiC precipitates and its effect on swelling.

An important note is that the irradiations described in Chapters 4 and 5 were conducted to varying damage levels of 1, 5, 15, 50, and 100 dpa and varying damage rates of 1×10^{-4} dpa/s and 7×10^{-4} dpa/s. However, these values were calculated for the CNA9 matrix (which is mostly composed of Fe) and not for the MX-TiC precipitates. As such, a SRIM calculation was conducted to find the equivalent damage rate and damage level for TiC. For now on, the damage rate and levels will be referred to in the following format: XX_{TiC} or YY_{matrix} where XX refers to the value of the damage rate or level for the MX-TiC precipitates and YY for the matrix (Table 6.1). See Appendix D for full details. In addition, the helium rate is expected to be different within the MX-TiC precipitates as compared to the matrix value. However, this value is not relevant as it is assumed that helium migration to the surface from the matrix is greater than the helium accumulation and transport within the nanoscale precipitates.

Table 6.1 Equivalent damage levels and damage rates for the CNA9 matrix and the MX-TiC precipitates.

Damage Level for CNA9 Matrix (dpa)	1	5	15	50	100
Equivalent Damage Level for MX-TiC Precipitates (dpa)	0.5	2.3	7	23	47
Damage Rate for CNA9 Matrix (dpa/s)	1×10^{-4}		7×10^{-4}		
Equivalent Damage Rate for MX-TiC Precipitates (dpa/s)	0.5×10^{-4}		3.3×10^{-4}		

6.1 Precipitate Stability under Ion Irradiation

6.1.1 Overview of MX Precipitate Stability at Various Damage Levels

The MX-TiC precipitates dissolved by $23_{TiC}/50_{matrix}$ dpa in all single beam experiments and remained dissolved by $47_{TiC}/100_{matrix}$ dpa, no matter the damage rate ($(0.5\times10^{-4}$ dpa/s$)_{TiC}/(1\times10^{-4}$ dpa/s$)_{matrix}$, $(3.3\times10^{-4}$ dpa/s$)_{TiC}/(7\times10^{-4}$ dpa/s$)_{matrix}$) or temperature (300, 500°C) tested. It should be noted that it is possible that not all the TiC precipitates dissolved, but that their density was so low as to not be observed in the volume of material assessed or their sizes so small as to not be detectable given the resolution of STEM-EDS (~0.5 nm). It was expected that the precipitates would undergo less ballistic dissolution at the lower dose rate, meaning the rate of dissolution would be less [111]. Likewise, it was expected that for the same damage rate and damage level the small MX-TiC precipitates may fully or partially succumb to ballistic dissolution at lower temperature (300°C) but that back diffusion would prevent such dissolution at higher temperature (500°C), due to the increased diffusion with temperature. The experiments conducted proved these hypotheses to be incorrect for these conditions. It is possible that at higher temperatures than 500°C the precipitates may be stable at $23_{TiC}/50_{matrix}$ dpa, but determination of that critical temperature is left to future work. As a reference, MX-(Ti,W,Ta)C precipitates in CNA3 were stable under irradiation to 50 dpa at 650°C (damage rate was not reported) [75]. This irradiation condition was

not conducted here as experimental conditions were constrained to those relevant to first wall and blanket environments and the evaluation of precipitate-helium evolution at and near peak swelling. *These experiments show that damage level is the dominant factor in precipitate stability at and above* $23_{TiC}/50_{matrix}$ *dpa for the temperatures (300, 500°C) and damage rates* $((0.5\times10^{-4}\ dpa/s)_{TiC}/(1\times10^{-4}\ dpa/s)_{matrix}$, $(3.3\times10^{-4}\ dpa/s)_{TiC}/(7\times10^{-4}\ dpa/s)_{matrix})$ *studied.*

It should be noted that though the different damage rates tested here did not result in observable precipitate differences, literature highlights the importance of damage rate on phase stability in ion irradiation studies. The complete dissolution of MX-(Ti,W,Ta)C precipitates by 50 dpa was observed in heavy ion irradiation of CNA3 at 450 and 500℃ using a damage rate of 1×10^{-3} dpa/s [74]. TaN, TaC, and VN experienced slight to significant dissolution under irradiation to ~49 dpa with ~5×10^{-4} dpa/s at 500°C. As damage rate is increased in heavy ion irradiation of FM steels containing the α′ phase, α′ becomes unstable and eventually dissolves or not capable of forming under irradiation [111,118]. A critical damage rate can also be determined at which α′ is unstable, related to the temperature of the irradiation. This critical damage rate was determined to be around 10^{-4} dpa/s for α′ [111,118]. There is most likely a critical damage rate for MX precipitates in FM steels as well. This work mapped out the stability at irradiation conditions relevant to fusion structural materials for dose, temperature, and helium injection rate using two different damage rates, but determination of the critical damage rate is left to future fundamental studies such as in-situ TEM ion irradiations and/or neutron irradiations in materials test reactors. It can be ascertained from this work that the critical damage rate for precipitate stability is below 1×10^{-4} dpa/s_{matrix} for temperatures between 300-500°C, which is pushing the limits of what is achievable with ion irradiation experiments due to time and resource constraints. Relatedly, damage rate will also affect the point defect concentrations under irradiation and thus can affect

various phenomena related to precipitation, such as radiation induced segregation [119]. Thus, careful consideration of the full range of damage rate effects should be accounted for when mapping the stability of MX precipitates as a function of damage rate. Another related consideration is the applicability of MX precipitate stability under heavy ion irradiation to their stability in a fusion environment. Levine *et al.* considered this by irradiating a FeCrNi austenitic steel in the BOR60 fission reactor at 9.4×10^{-7} dpa/s to 318°C to ~5, 10, and 50 dpa [120]. An additional ~5 and 40 dpa were added to the BOR60-irradiated 5 dpa material with heavy ion irradiation at $\sim10^{-3}$ dpa/s from 320-420°C to compare the evolution of the microstructure. The study analyzed the stability of radiation-enhanced Cu-rich and radiation-induced Ni-Si-Mn-rich nanoclusters, not MX precipitates. The analysis showed that the accelerated damage rate under ion irradiation altered the development of nanoclusters. Cu nanoclusters remained after neutron irradiation to 50 dpa but dissolved under ion irradiation to the same dose. Ni-Si-Mn-rich nanoclusters, however, remained present in both types of irradiations, though the clusters grew into G phase precipitates under neutron irradiation whereas the cluster evolution under ion irradiation was dependent on temperature. Using a cluster stability model, Levine *et al.* found that the size of nanoclusters evolved in a similar fashion under both kinds of irradiation, however the behavior of the nanoclusters with ion irradiation was shifted to high temperatures. However, the size of nanoclusters under both types of irradiations converged as temperature increased and was nearly the same at an elevated temperature of 500°C. Levine *et al.* further highlights the importance of damage rate and temperature on phase stability [120]. Understanding the evolution of MX precipitates in FM steels requires low damage rate neutron irradiations. Work is ongoing on this front, as CNA9 was part of an irradiation campaign in the High Flux Isotope Reactor.

In addition, helium co-injection did not prevent the dissolution of the MX-TiC precipitates at $23_{TiC}/50_{matrix}$ dpa or $47_{TiC}/100_{matrix}$ dpa nor did helium cause re-precipitation, as had been hypothesized in Refs. [48,59]. *This suggests that damage level is the dominant factor over helium co-injection for the MX-TiC precipitate dissolution in CNA9 at the lab conditions studied, or effectively helium does not impact the final stability of MX-TiC precipitates.* Importantly, helium co-injection may have affected the onset of dissolution, but it did not affect the complete dissolution of precipitates by $23_{TiC}/50_{matrix}$ dpa.

While precipitate dissolution occurred at high damage levels, precipitates were still present in the intermediate dose regime at $7_{TiC}/15_{matrix}$ dpa at 300, 400, 500, and 600°C with and without helium co-injection. The precipitate response at low to intermediate damage level was governed by temperature and helium co-injection. At lower temperatures (300,400°C) in either single or dual beam irradiations, no coarsening of precipitates was observed. Rather ballistic dissolution is assumed to have played a dominant role, as the size distributions remained the same as the control specimen but there were significant reductions in precipitate number density. Helium co-injection had no effect on this response. However, the pre-existing size distributions of the MX-TiC precipitates coarsened under single beam irradiations to $7_{TiC}/15_{matrix}$ dpa at 500 and 600°C, suggesting radiation-enhanced growth of MX-TiC precipitates occurred at elevated temperatures without helium co-injection (Figure 5.13). In contrast to the single beam conditions, the coarsening of the size distributions of the dual beam conditions at 500 and 600°C was suppressed (Figure 5.13). Hence, the co-injection of helium appears to have suppressed the radiation-enhanced growth of MX-TiC precipitates at 500 and 600°C and $7_{TiC}/15_{matrix}$ dpa.

It is hypothesized that the effects of helium co-injection on the size responses of precipitates were temperature-dependent because of its effect on diffusion. Diffusion was already suppressed

to sufficiently low values at the lower temperature in the single beam irradiations and hence a further suppression of diffusion with helium co-injection had no observable effect on the precipitate size. Whereas radiation-enhanced diffusion was operational at elevated temperatures and hence helium had noticeable effects on diffusion and therefore on precipitate sizes.

Literature shows that helium suppresses the diffusion of solutes by binding to them and increasing the activation barrier that needs to be overcome for solute diffusion to occur [4–9]. Ref. [5] discusses the interactions of helium with alloying solute atoms and interstitial carbon (C). Ref. [5] found that both Ti and C individually had significant binding (attraction) to both interstitial and substitutional helium. Though Ref. [5] did not investigate the binding of Ti-C-helium complexes, it did find that the binding of helium to $Y_2Ti_2O_7$ nanoclusters (1.8-2.5 eV) was significantly greater than the binding energy values of helium with isolated Y (1.24eV), Ti (0.34eV), and O (0.33eV) atoms. Ref. [6] found that helium-vacancy clusters also have a positive binding energy associated with them based on the number of vacancies and helium atoms present. Ref. [4] suggests that C would have an attractive binding energy with a solute-helium complexes, but the authors did not specifically study Ti as a solute. Ref. [9] discusses helium interactions with 27 substitutional solute elements in vanadium, including Ti. The authors found that Ti solute enhances the stability of helium-solute–vacancy complexes, further impeding the diffusion of the vacancy-helium clusters. Though CNA9 is primarily composed of iron and not vanadium, they are both BCC alloys and the paper can provide insights into the behavior of helium in CNA9. Particularly, there is no data to the author's knowledge on Ti-helium-vacancy binding in an iron matrix, and as such Ti-helium-vacancy binding in vanadium can shed some initial insights into how this complex may behave in iron (*i.e.,* increased binding with a vacancy). *Based on the established literature, it is assumed that helium will have a positive attraction to both Ti and C and may form stable Ti-C-helium complexes,*

most likely with vacancies as well. Table 6.2 shows the binding energies for various solute, helium, and vacancy complexes. For reference, the binding energies between He_mV_n complexes in BCC Fe are also shown. Calculations in this work will be done with a range of binding energies for helium-solute complexes that represent the low and high ends of the binding energy range in BCC systems found in literature as represented in Table 6.2. Future computational work, which would increase the fidelity of the work presented within, should focus on obtaining an accurate value for the binding energy of helium with Ti, C, and vacancy complexes in BCC FeCr alloys, but the values used here are representative of the best available data from computational literature.

Based on the previous discussion of helium binding energies, the diffusion of various migrating species in CNA9 can be calculated to better evaluate the helium suppressed coarsening observed in 500 and 600°C precipitation results. Calculations used standard diffusion theory where first the thermal diffusion of Ti solutes was determined based on the microscopic diffusion parameters [1]:

$$D_{thermal}^{Ti} = D_{v,thermal}^{Ti} C_v^0 + D_{i,thermal}^{Ti} C_i^0 \quad \text{Eq. 6.1}$$

$$D_{(v,i),thermal}^{Ti} = \alpha a^2 \upsilon exp\left(\frac{S_m^{v,i}}{k}\right) exp\left(\frac{-E_m^{v,i}}{kT}\right) \quad \text{Eq. 6.2}$$

$$C_{v,i}^0 = exp\left(\frac{S_f^{v,\mathrm{i}}}{k}\right) exp\left(\frac{-E_f^{v,\mathrm{i}}}{kT}\right) \quad \text{Eq. 6.3}$$

The diffusion of Ti under single beam irradiation was calculated from the equation for radiation-enhanced diffusion of a solute [121]:

$$D_{RED}^{Ti} = D_{v,thermal}^{Ti} \frac{C_v^{irr}}{C_v^0} + D_{i,thermal}^{Ti} \frac{C_i^{irr}}{C_i^0} \quad \text{Eq. 6.4}$$

where C_v^0, C_i^0, C_v^{irr}, and C_i^{irr} were determined in Chapter 4 (Table 4.6).

The diffusion of Ti in the presence of helium can be calculated from:

$$D_{RED,eff}^{Ti-X} = \frac{D_{RED}^{Ti}}{1+C_e exp\left(\frac{E_b^{Ti-X}}{kT}\right)} \text{ [9]} \qquad \text{Eq. 6.5}$$

where range of values was chosen for the binding energy of helium, E_b^{He}, to represent the values in Table 6.2. The values input for E_b^{Ti-X} were 0.34 eV (Ti-1NN He_{sub} in BCC Fe)($E_b^{Ti-He}, D_{RED,eff}^{Ti-He}$) and 1.3 eV (Ti-V-1NN He_{oct} in vanadium)($E_b^{Ti-He-v}, D_{RED,eff}^{Ti-He-v}$). The value of 0.34 eV (Ti-1NN He_{sub} in BCC Fe) was chosen because it is the most attractive binding energy for the simple Ti-helium complex in an Fe matrix and 1.3 eV (Ti-V-1NN He_{oct} in vanadium) was chosen to represent an upper limit on the effects of helium on diffusion found in literature – but, it is recognized this value is derived from a different materials system and thus may not be fully accurate for the system studied within. In future sections, E_b^{Ti-He}=0.34 eV may be referred to as "weak" binding and $E_b^{Ti-He-v}$=1.3 eV may be referred to as "strong" binding. The descriptive words of "weak" and "strong" serve to compare the binding effects between E_b^{Ti-He} and $E_b^{Ti-He-v}$ and not to describe them as the weakest or strongest binding found in literature.

The diffusion of Ti was used because it is assumed to govern the evolution of the TiC precipitates as the rate-limiting species. This was determined by calculating the diffusivities (product of diffusion and concentration of the species) of both Ti and C. Ti had a smaller diffusivity than C, and hence is considered the rate-limiting species. For a full analysis, see Appendix E.

Figure 6.1 plots the calculated diffusion values for all temperatures tested. The orange line in Figure 6.1 represents the radiation-enhanced diffusion under single beam conditions (D_{RED}^{Ti}), the black line represents thermal diffusion (D_{th}^{Ti}), and the blue lines represent radiation-enhanced diffusion under dual beam conditions accounting for the effects of helium ($D_{RED,eff}^{Ti-He}, D_{RED,eff}^{Ti-He-v}$). Figure 6.1 then shows that helium can suppress the diffusion of Ti complexes as shown by the blue curves ($D_{RED,eff}^{Ti-He}, D_{RED,eff}^{Ti-He-v}$) being pushed to lower diffusion values beneath the orange curve

(D_{RED}^{Ti}). If only weak binding is present (represented by $D_{RED,eff}^{Ti-He}$ with E_b^{Ti-He}=0.34 eV), then the diffusion of Ti under dual beam irradiation is nearly the same as under single beam irradiation. Strong binding is represented in Figure 6.1 by $D_{RED,eff}^{Ti-He-v}$ with $E_b^{Ti-He-v}$=1.3 eV. The filled-in gray area between the two blue curves represents the possible values of diffusion under dual beam conditions, as the blue curves represent the extreme low and high regimes of helium solute binding from literature. Note, that the diffusion for a dual beam condition at 300°C is not shown because a dual beam irradiation was not completed in this work. Thus, there is no data on cavities at 300°C to be used in determining C_v^{irr} and C_i^{irr} and in determining diffusion.

The values of C_v^{irr} and C_i^{irr} used in the diffusion calculations are dependent on the dislocation line and loop densities, since the dislocation lines and loops represent the greatest sink in the material (Figure 4.17). These values were ascertained from literature (Section 4.9). As such, it is important to understand if a variation in dislocation line and loop densities would alter the results of the diffusion calculations. An analysis was conducted that varied the dislocation line and loop densities by 10× less than or 10× greater than the values from literature given in Section 4.9. It was concluded that a variation in dislocation line and loop densities did not alter the conclusions presented within. See Appendix F for details.

The suppression of Ti diffusion resulting from the binding of Ti with helium complexes (possibly containing C and vacancies) is hypothesized to explain the reduced growth of the MX-TiC precipitate size distributions in the elevated temperature (≥500°C) dual beam conditions. Binding with helium renders Ti solutes and Ti solute complexes less likely to partake in the back diffusion necessary for precipitate growth. The helium-solute binding was not enough to prevent some growth of the precipitates at 600°C due to the greater radiation-enhanced diffusion over the lower temperature irradiations. There was, however, a 20% reduction in the maximum MX

precipitate size, a 25% reduction in the mean MX precipitate size, and 25% reduction in the upper quartile of the size distribution in the dual beam condition over the single beam condition at 600°C, indicating that helium solute binding was still significant at 600°C.

By looking at Figure 6.1, the thermal diffusion of Ti under single beam irradiation and the radiation-enhanced diffusion of Ti are very similar at 600°C, with the thermal diffusion only slightly greater. This is due to the thermal concentration of vacancies being nearly equal to those produced from radiation damage at 600°C. The thermal vacancy concentration at 600°C is 4.3×10^{20} vac/m^3, the concentration under single beam irradiation is $(6.1\pm0.2)\times10^{19}$ vac/m^3, and the concentration under dual beam irradiation is $(3.2\pm0.2)\times10^{19}$ vac/m^3. However, under thermal annealing conditions at 600°C for the same amount of time as it took to reach $7_{TiC}/15_{matrix}$ dpa (~6 h), there were no significant changes in the size distribution of pre-existing TiC precipitates. Hence, it can be assumed that radiation is the main influence on the coarsening of the precipitates in the single beam 600°C irradiation, perhaps due to combined effects of ballistic dissolution increasing the solute matrix concentration and of diffusion, and that helium co-injection is the main influence on the suppression of solute species diffusivities leading to the suppression of coarsening in the dual beam 600°C irradiation.

It can be concluded that helium co-implantation reduces the growth of precipitates during ion irradiation experiments at temperatures where precipitate size distributions are controlled by diffusion-mediated processes in single beam conditions (500, 600°C). This occurs by helium atoms binding to Ti solutes and suppressing the long-range motion of the helium-Ti complex. The complexes decrease the effective diffusion of Ti in the matrix, thus decreasing the contribution of thermal coarsening of precipitates under irradiation. This effect is observable at 500 and 600°C, where radiation-enhanced precipitate coarsening was either dominant or a major contribution

during single beam irradiation to precipitate evolution. This helps to explain why helium shifted TiC size distributions to lower precipitate sizes at elevated temperature and intermediate dose, before ballistic dissolution effects became dominant at higher damage levels.

It should be noted that this analysis of helium's effect on diffusion is a rather simplified analysis of very complex processes that occur simultaneously. Nevertheless, this approach garners useful information on understanding helium's effects on the microstructure. Future work should consider the effects of various sites of interstitial and substitutional helium (*i.e.*, octahedral site for an interstitial helium or second nearest neighbor of a substitutional helium) on the overall binding energy landscape, the de-trapping of helium from C-Ti-helium complexes to ascertain a dynamic understanding of helium's effects on diffusion, and how vacancies and C may affect the binding of Ti-helium complexes in BCC FeCr systems. Particularly, Ti diffuses by the vacancy mechanism so understanding how the flow of Ti in regard to vacancies changes with point defect-solute binding would be useful information. In-depth modelling studies, and likely an expansion of the experimental irradiation conditions, are needed to ascertain this information.

Future experiments could test the precipitate stability at and above $23_{TiC}/50_{matrix}$ dpa at higher temperatures to see if radiation-enhanced diffusion begins to play the dominant factor in precipitate stability at such damage levels. For instance, MX-(Ti,W,Ta)C precipitates were still present in CNA3 after dual beam irradiation to 50 dpa at 650°C [122]. But this work did not provide the damage rate used nor did it assess the stability effects at various temperatures. Hence, it is difficult to draw conclusions from this study due to the limited conditions as well the possibility of different initial MX precipitate composition, size distribution, and density. Future work could also assess if helium has effects on other diffusion-mediated mechanisms, such as radiation-induced segregation, as this would further the results of this work but was outside of its scope. In addition,

it is hypothesized that helium co-injection did not alter the number density of MX precipitates because no new MX precipitates nucleated under irradiation. This contrasts with austenitic steels, where MX precipitates may nucleate in the low dose regime under irradiation. The number density in austenitic steels is changed by helium co-implantation due to helium changing the dislocation loop structure which in turn affects MX precipitate nucleation and density [123]. Lastly, these experiments show that there is a critical dose to dissolution between $7_{TiC}/15_{matrix}$ and $23_{TiC}/50_{matrix}$ dpa. However, the determination of that critical dose value would take an excessive amount of time and resources and hence is left for future work, perhaps for in-situ irradiation experiments which are better suited to that type of experiment [124]. In addition, knowing the exact onset of dissolution is unnecessary for the practical operation of fusion power plants, as the critical dose between $7_{TiC}/15_{matrix}$ and $23_{TiC}/50_{matrix}$ dpa represents a small fraction of the expected desired lifetime of a commercial fusion power plant. Whether the precipitates dissolve at $7_{TiC}/15_{matrix}$ or $23_{TiC}/50_{matrix}$ dpa, they are not lasting the desired lifetime of the reactor, and hence from a practical aspect exact determination of the onset of dissolution is not necessary.

Table 6.2 The binding energies for various solute, helium, and vacancy complexes.

Matrix	Complex	Binding/Attraction (eV)	Reference
BCC Fe	Ti-1NN He_{sub} Ti-1NN He_{tet} C-1NN He_{sub} C-1NN He_{tet}	0.34 0.16 0.33 0.15	[5]
Vanadium	Ti-1NN He_{sub} Ti-1NN He_{tet} Ti-1NN He_{oct} He-V Ti-V-1NN He_{oct}	- 0.22 0.03 1.01 1.3	[9]
BCC Fe	He-V He_2V He_3V He_4V He_2V_4 He_3V_4 He_4V_4	2.3 1.84 1.83 1.91 3.12 3.16 3.05	[10]

Table 6.3 Variables and their values used in the diffusion calculations.

Variable [10,11]	Symbol	Value
Jump frequency	α	Vacancies: 1.6×10^{13} Hz Interstitials: 2.9×10^{12} Hz
Lattice parameter of the matrix	a	2.96 Å
Interstitial formation entropy	S_f^v	2.17 ev/K
Vacancy formation entropy	S_m^i	0 eV/K
Interstitial formation energy	E_f^v	1.6 eV
Vacancy formation energy	E_f^i	5 eV
Interstitial migration energy	E_m^v	0.62 eV
Vacancy migration energy	E_m^i	0.35 eV

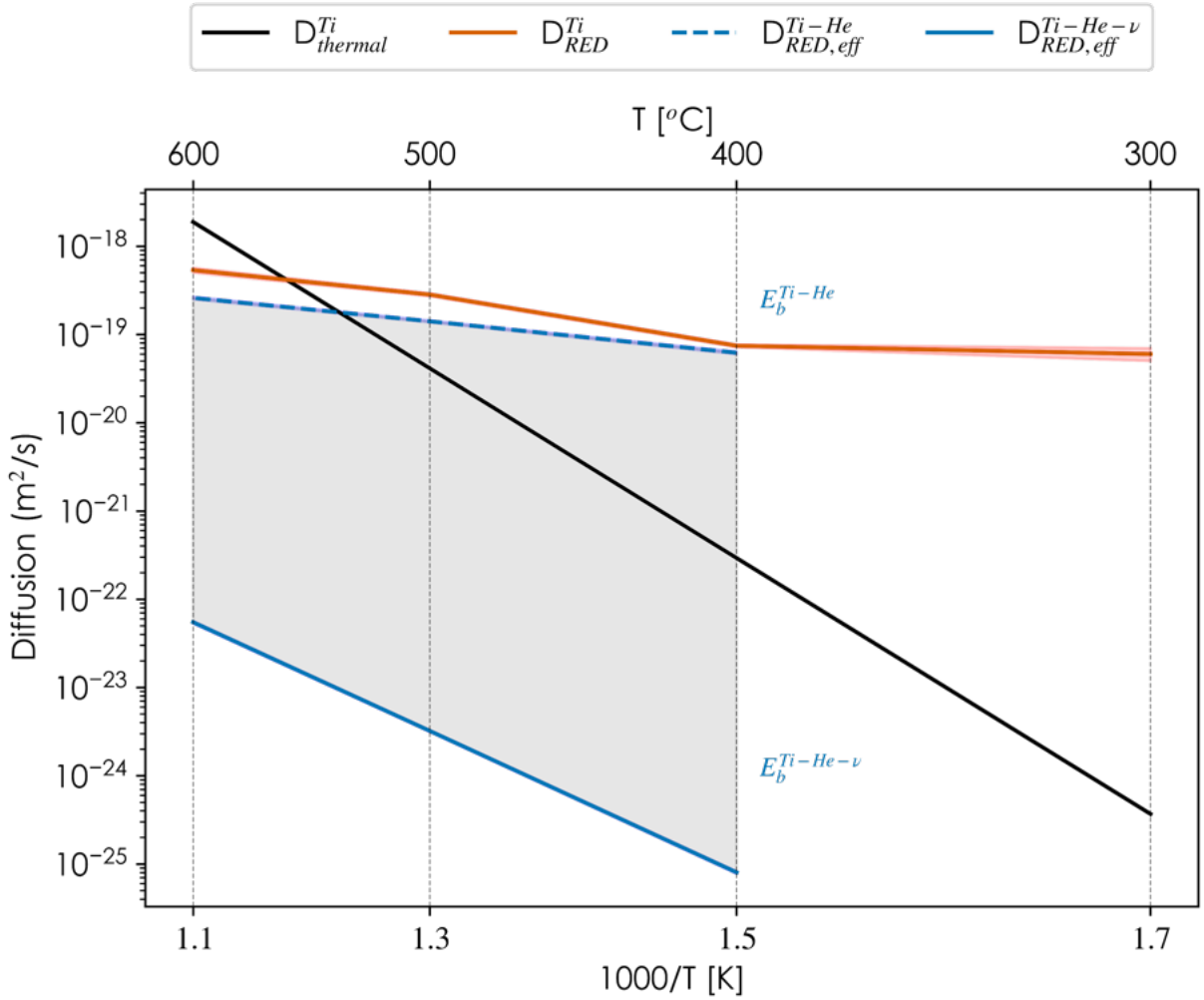

Figure 6.1 Thermal diffusion (D_{th}^{Ti}, black line), radiation-enhanced diffusion in single beam conditions (D_{RED}^{Ti}, orange line), and helium-suppressed diffusion in dual beam conditions ($D_{RED,eff}^{Ti-He}$ and $D_{RED,eff}^{Ti-He-\nu}$, blue lines). The solid blue line refers to strong Ti-helium-vacancy binding and the dashed blue line refers to weak Ti-helium binding.

6.1.2 Radiation-enhanced diffusion at intermediate damage levels

Diffusion is an important aspect to precipitate stability and coarsening, as was ascertained from the previous section. Diffusion is a determining factor of growth kinetics in a commonly observed precipitate coarsening phenomena called Ostwald ripening, by which a diffusive flux of atoms from smaller particles to larger particles results in coarsening [47]. To try to understand if the coarsening observed in the single beam $7_{TiC}/15_{matrix}$ dpa irradiations at elevated temperatures was due to diffusion-mediated radiation-enhanced Ostwald ripening, a simple analysis was performed. Ostwald ripening refers to the process by which larger particles grow at the expense of smaller ones [79]. The coarsening of particles under irradiation up to $7_{TiC}/15_{matrix}$ dpa at 500°C with no helium, with 10 appm He/dpa, and with 25 appm He/dpa was modeled using the equation for Ostwald ripening [79]:

$$r^3(t) - r_0^3(0) = \frac{8\sigma\Omega^2 D c_e}{9RT} \qquad \text{Eq. 6.6}$$

where $r_0^3(0)$ is the mean radius of the control specimen, σ is the interfacial energy (J/m^2), Ω is the molar volume of the precipitate (m^3/mol), D is the diffusion coefficient of Ti (m^2/s), C_e is the matrix concentration of Ti in equilibrium (atom fraction), R is the universal gas constant J/mol-K), and T is temperature (K). The thermal diffusion of the Ti solute atom occurs via the vacancy mechanism, and the diffusion of Ti under single beam irradiation can be calculated from the equation for radiation-enhanced diffusion of a solute given in Eq. 6.4 and the diffusion in the presence of helium was calculated with Eq. 6.5.

A range of values was chosen for the binding energy of helium, E_b^{He}, to represent the values in Table 6.2. The values input for E_b^{He} were 0.34 eV (Ti-1NN He_{sub} in BCC Fe) and 1.3 eV (Ti-V-1NN He_{oct} in vanadium). The value of 0.34 eV (Ti-1NN He_{sub} in BCC Fe) was chosen because it is the most attractive binding energy for the simple Ti-helium complex in an Fe matrix and 1.3 eV

(Ti-V-1NN He_{oct} in vanadium) was chosen to represent an upper limit on the effects of helium on diffusion.

Values for these parameters can be inputted into Eq. 6.6 to calculate the mean precipitate radius as a function of time, $r^3(t)$. A plot of $r^3(t)$ versus *t* can be seen in Figure 6.2. In this plot, time is represented by the damage level of the irradiations using a dose rate of 7×10^{-4} dpa/s. A linear dependence of the $r^3(t)$ with *t* is indicative that diffusion-controlled Ostwald ripening is occurring. A linear dependence of the $r^2(t)$ with *t* is indicative that interface-controlled Ostwald ripening is occurring. The simulated coarsening for the single beam irradiation calculated with Eq. 6.6 is shown with the dashed orange line in Figure 6.2a,b. The theoretical values of coarsening for the 10 appm He/dpa (dashed black line) and 25 appm He/dpa (dashed gray line) conditions were nearly identical, and their curves overlap in Figure 6.2a,b. The calculated values of the diffusion coefficient using 0.34 and 1.3 eV were nearly identical and also overlap for both helium co-injection rates. In addition, a linear dependence with time would be expected for the inverse of the number density of precipitates if either kind of Ostwald ripening was occurring (Figure 6.2c). The linear fits between the control specimen and the single beam $7_{TiC}/15_{matrix}$ dpa specimen for the radii and density changes are shown by the dashed blue curves.

Figure 6.2 shows that experimental values for the single beam set of irradiations to $0.5_{TiC}/1_{matrix}$, $2.3_{TiC}/5_{matrix}$, and $7_{TiC}/15_{matrix}$ dpa at 500°C (solid orange lines with markers) for the relationships of $r^3(t)$ versus t, $r^2(t)$ versus t, and ρ^{-1} versus *t* deviate from linear behavior. A decrease in the cube (Figure 6.2a) and square (Figure 6.2b) of the mean size appears to take place experimentally from the control specimen to the $0.5_{TiC}/1_{matrix}$ and $2.3_{TiC}/5_{matrix}$ dpa conditions before an increase in size is reached by $7_{TiC}/15_{matrix}$ dpa. However, the values of the mean radii at $0.5_{TiC}/1_{matrix}$ and $2.3_{TiC}/5_{matrix}$ dpa are so close to the control specimen, it was previously deduced

that irradiation had no statistically significant effect on the size distributions and number densities at these low dpa values. Indeed, the mean sizes of the $0.5_{TiC}/1_{matrix}$ and $2.3_{TiC}/5_{matrix}$ conditions are nearly within or are within the standard error bars of the means as compared to the control specimen (Figure 5.6). It is possible that re-precipitation of TiC precipitates occurred at low doses and that is the reason for the decrease in the cube and square of the mean size initially, but this was not backed up experimentally with statistically significant changes in size and density.

The cube of the mean size does increase somewhat linearly from $0.5_{TiC}/1_{matrix}$ to $2.3_{TiC}/5_{matrix}$ dpa and also from $2.3_{TiC}/5_{matrix}$ to $7_{TiC}/15_{matrix}$ dpa. However, the rate of increase is different between the values. The slope is steeper from $2.3_{TiC}/5_{matrix}$ to $7_{TiC}/15_{matrix}$ dpa. This could be a negligible artifact of the analysis, but it is possible the different slopes represent a physical change in the coarsening. The rate of coarsening is dependent on the interfacial energy, the equilibrium concentration of Ti in the matrix, and the diffusion of Ti. The interfacial energy may have changed with damage level due to coherency changes of the TiC precipitates or due to the ratio of Ti and C changing, and the concentration of Ti in the matrix may have changed with irradiation. These changes would cause deviation from the simulated coarsening of the single beam irradiations. The square of the mean size increases linearly from $0.5_{TiC}/1_{matrix}$ to $7_{TiC}/15_{matrix}$ dpa but does not have the same slope as the simulated coarsening (dashed orange line, Figure 6.2b). It is inconclusive if the behavior of precipitates is in line with radiation-enhanced Ostwald ripening for the single beam conditions, but the deviation from linear behavior suggests the coarsening was not in line with Ostwald ripening or multiple complex mechanisms including Ostwald ripening are at play.

What is conclusive from Figure 6.2a,b is that the suppressed diffusion of Ti with helium co-injection in the dual beam conditions to $7_{TiC}/15_{matrix}$ dpa caused a reduction in the simulated

Ostwald ripening. A reduction in coarsening with helium co-injection bore out with experimental results as well. The experimental radii values for the dual beam conditions in Figure 6.2a,b are also very similar to the simulated thermal coarsening. Hence, it is possible that radiation-enhanced Ostwald ripening is taking place and that helium co-injection is slowing the coarsening process by suppressing diffusivity of point defects and Ti solutes, but these results are inconclusive. Future thermal annealing experiments should be conducted to observe if Ostwald ripening happens in thermal conditions at longer annealing times than were available in this work, in excess of 100 h.

Another reason for the observed coarsening in the single beam $7_{TiC}/15_{matrix}$ dpa sample at elevated temperatures may be radiation-enhanced diffusivity. Vacancies in excess of thermal equilibrium concentration are present under irradiation in these conditions. This was shown in Table 4.6, where the vacancy concentration in the single beam irradiation at 500°C was calculated to be ~36× greater than the thermal vacancy concentration. Vacancies are known to result in faster diffusion of solute atoms [125]. In particular, Ti mainly diffuses through the vacancy-assisted mechanism and its diffusivity increases with the increase in vacancy concentration under irradiation. Hence, the greater point defect concentration and the resulting greater Ti diffusivity may have led to coarsening of the MX-TiC size distribution at $7_{TiC}/15_{matrix}$ dpa. This would also explain the reduction in mean size of the precipitates with helium co-injection, as helium would suppress Ti diffusion and possible vacancy diffusion as well and lessen the effect of radiation-enhanced point defects on the coarsening of TiC precipitates. Due to the increased sink strength under helium co-injection, the vacancy concentration was also lower in the dual beam conditions. It is assumed that radiation-enhanced diffusivity is the dominant mechanism affecting the behavior of precipitates at 600°C as well.

In addition, non-primary solute atoms segregated in MX precipitates may be of importance to morphological changes and coarsening under irradiation. Ref. [126] found that greater amounts of Mo was segregated in TiC precipitates than in NbC precipitates found in austenitic stainless steel. The TiC precipitates had a slower coarsening rate than the NbC precipitates under heavy ion irradiation to 80 dpa at 600°C due to the slow-diffusing nature of Mo. The TiC precipitates, hence, also remained spherical whereas the NbC precipitates became elongated and platelet-shaped with their growth. The level of binding of C and/or N to the main solute element in the MX precipitates (*i.e.,* Ti or Nb) may also affect the MX precipitate dissolution. Also, B additions to austenitic steel delayed the onset of morphological change in MX precipitates to higher damage levels under irradiation. Other research on $M_{23}C_6$ carbides found that B and W reduced the coarsening rate of $M_{23}C_6$ carbides by decreasing the interfacial energy and reducing diffusivities, respectively [127]. The TiC precipitates in this work were found to be enriched in W. This was not induced by radiation but rather the pre-existing precipitates contained W as well. W may have had an effect on the coarsening rate of the TiC precipitates. Future work may focus on ascertaining the effects of non-primary solute concentrations in MX precipitates on coarsening.

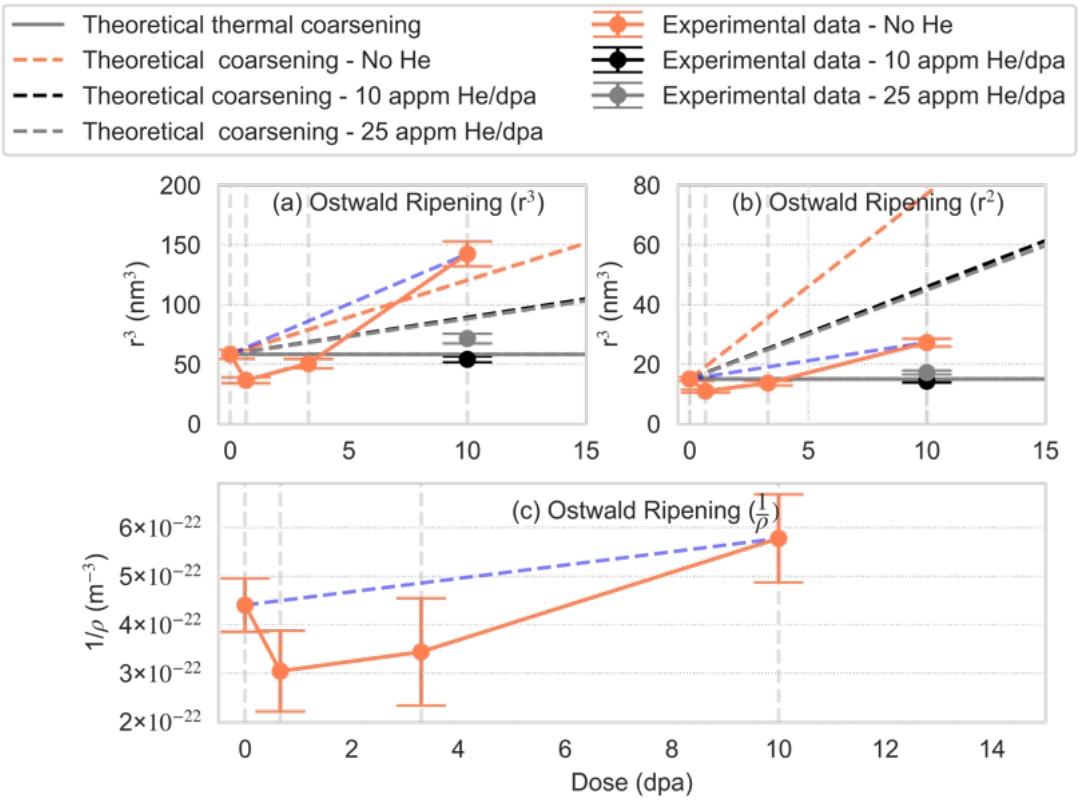

Figure 6.2 Plots for (a) r^3 versus time (diffusion-controlled Ostwald ripening), (b) r^2 versus time (interface-controlled Ostwald ripening), and (c) 1/ρ versus t (generic Ostwald ripening) for the single and dual beam conditions at 500°C.

6.1.3 Mechanisms of Precipitate Stability

As described in Section 2.5.1., Frost and Russell described a method for modelling the behavior and dissolution of precipitates under irradiation [78,128]. The model considers the competing mechanisms of resolution by radiation recoil and thermal coarsening. Resolution by radiation recoil describes the process of solute atoms in a precipitate recoiling into the matrix as a result of radiation damage, causing the eventual dissolution of the precipitate. On the other hand, thermal coarsening hastens the growth of precipitates by causing the recoiled solute atom to return to the precipitate. A steady state is reached when a balance between these two processes occurs. This model will be used to assess the mechanism of MX-TiC precipitate stability, first at

$7_{TiC}/15_{matrix}$ dpa at various temperatures with and without helium co-implantation. However, as discussed in the beginning of Chapter 5, no thermal coarsening was observed in the thermally annealed conditions. As such, it can be assumed that if coarsening is occurring in the irradiated conditions at intermediate damage level, it is due to radiation-enhanced coarsening mechanisms and not due to thermal coarsening. There are various mechanisms for radiation-enhanced coarsening, such as radiation-enhanced Ostwald ripening and enhanced coarsening due to the combined effects of solutes being ejected into the matrix from recoil resolution and enhanced solute diffusivity under irradiation (Section 6.1.2). In this analysis, if coarsening occurs it will be assumed to be radiation-enhanced coarsening and not thermal coarsening, as in the original Frost and Russell model.

The applicability of recoil resolution to precipitate behavior can be inferred from the solute matrix concentration near the precipitate interface, since dissolution and growth is dependent on the solute concentration profile:

$$c_{max}(r_p + R) = c_e + \frac{SR^2}{12D}\left(1 - \frac{R}{4r_p}\right) \qquad \text{Eq. 6.7}$$

where R is the recoil distance, S is the recoil rate (in dpa/s), D is the diffusion of the rate-limiting species (Ti in this analysis), r_p is the mean precipitate radii determined experimentally at $7_{TiC}/15_{matrix}$, and c_e is the thermal concentration (in atom fraction) of Ti calculated from Thermo-Calc. The recoil distance R refers to the distance that the recoil solute atom travels outside of the precipitate after a collision. This value was determined with SRIM. A layer of CNA9 was created in SRIM from the surface to 1200 nm below the surface followed by a small layer of 50% Ti and 50% C to model a precipitate. The TiC layer was varied from 3 to 15 nm, but no significant differences were found in the final values of the range. After the TiC layer, the final layer created in SRIM was CNA9 and went to a depth of 2.5 μm total beneath the surface. The impinging ions

were set to 9 MeV Fe^{3+} ions and a full cascade was run to obtain the range of Ti and C atoms after irradiation. The weighted average of the range distribution of Ti atoms outside of the initial TiC layer was calculated and found to be 0.7 nm. See Appendix G for full details. The recoil rate was determined by converting the displacement rate of CNA9 (7×10^{-4} dpa/s) to that for TiC. The recoil rate for TiC was determined to be 3.3×10^{-4} dpa/s (Appendix D). The diffusion of Ti used for single beam irradiations was D_{RED}^{Ti}. The diffusions of Ti used for dual beam irradiations were D_{eff}^{Ti-He} and $D_{eff}^{Ti-He-v}$ to encompass helium effects. In Figure 6.3, the matrix concentration in thermal equilibrium, c_e (black line), was plotted versus the concentration from recoil resolution, $\frac{SR^2}{12D}\left(1-\frac{R}{4r_p}\right)$ (orange line for single beam and blue lines for dual beam). Figure 6.4 plots a deconstructed version of Figure 6.3, where Figure 6.4a shows thermal equilibrium versus single beam recoil resolution concentrations and Figure 6.4b shows thermal equilibrium versus dual beam recoil resolution concentrations. In addition, Figure 6.4 only shows weak Ti-helium binding, as this best matches the experimental results, as will be discussed.

At 500 and 600°C, the magnitude of the concentration from recoil resolution for single beam irradiations (orange line) is ~2-10× less to that from the thermal equilibrium concentration (black line). This similarity in contributions to the Ti matrix concentration suggests recoil resolution as well as radiation-enhanced coarsening may be operational during single beam irradiations, but radiation-enhanced coarsening has a greater influence. The single beam experimental results at $7_{TiC}/15_{matrix}$ dpa back this modelling result up as the dominant mechanism of precipitate stability was determined to be radiation-enhanced coarsening for the 500 and 600°C for single beam conditions (Figure 5.8).

For dual beam irradiations, there is a range of possible precipitate behaviors deriving from the range of possible values of recoil resolution concentration between the bounds for strong and weak

Ti-helium binding (gray area between the solid and dashed blue lines). Though the exact binding is unknown, we can use the experimental results at dual beam conditions to help guide the interpretation of the model. Experimental results showed that the size distribution of MX-TiC precipitates underwent no significant changes with dual beam irradiation at 500°C to $7_{TiC}/15_{matrix}$ dpa and no significant changes in number density (Figure 5.12). Hence, experimental results suggest that the influence of recoil resolution and radiation-enhanced coarsening are about equal and a condition of stability has been met. For the weakest Ti-helium binding shown in Figure 6.3 and Figure 6.4b (dashed blue line), the model predicts equality of recoil resolution and radiation-enhanced coarsening influences for the 500°C dual beam condition as the concentration contributions from both are equal. This prediction from the model matches with the described experimental results. In contrast, for the strongest Ti-helium binding shown in Figure 6.3 (solid blue line), the model predicts recoil resolution dominance at the 500°C dual beam condition as the concentration from recoil resolution at this point is ~10^4 × greater than the thermal equilibrium concentration. Significant dissolution of precipitates would have been observed if this was the case, and hence strong binding is assumed to not be operational.

Experimental results showed that the size distribution of MX-TiC precipitates underwent a significant increase in average size with dual beam irradiation at 600°C to $7_{TiC}/15_{matrix}$ dpa, though the size increase was suppressed as compared to the single beam irradiation at 600°C (Figure 5.13). This would suggest that radiation-enhanced coarsening was still dominant, but that there was increased influence of recoil resolution with helium addition. The influence from recoil resolution was significant enough to suppress coarsening across the entire precipitate size distribution but not enough to cause the significant dissolution of precipitates. It may be reasonably assumed that the influence of recoil resolution is less than the influence at 500°C, in which a complete suppression

of coarsening was observed, due to the greater diffusion of solutes at 600°C. For the weakest Ti-helium binding shown in Figure 6.3 and Figure 6.4b (dashed blue line), the model predicts that both recoil resolution and radiation-enhanced coarsening are operational on precipitate behavior for the 600°C dual beam condition as the concentration from thermal equilibrium at this point is ~5 × greater than the recoil resolution concentration. The magnitude difference between the recoil resolution and thermal equilibrium concentrations is similar to the difference observed in 600°C single beam condition, but there is a slightly greater influence from recoil resolution with dual beam irradiation. This prediction matches the described experimental results for the 600°C dual beam condition (*i.e.,* partial coarsening suppression). The physical Ti-helium solute binding in the matrix is expected to be similar to the weakest binding modelled from literature (dashed blue line). In contrast, the strongest Ti-helium binding shown in Figure 6.3 (solid blue line) predicts that recoil resolution is the dominant operating mechanism for the 600°C dual beam condition as the concentration from recoil resolution concentration at this point is ~10^3 × greater than the thermal equilibrium concentration. Significant dissolution would have been observed if this was the case.

Summarizing the results at high temperatures, the modelling and experimental results indicate for both 500 and 600°C to $7_{TiC}/15_{matrix}$ *dpa that helium co-injection suppressed radiation-enhanced coarsening (i.e., increased the relative effects of recoil resolution) by suppressing diffusion of Ti solutes. It can be inferred from Figure 6.3 and Figure 6.4 that the model accurately simulates the experimental results with the use of a weak Ti-helium binding value from literature (i.e.,* $E_b^{Ti-He} = 0.34$ *eV).*

At 300 and 400°C, the magnitude of the concentration from recoil resolution for single beam irradiations (orange line) is ~5-10× greater than that from the thermal equilibrium concentration (black line). This suggests that, though both radiation-enhanced coarsening and recoil resolution

may be operating, recoil resolution is the dominant influence on particle stability. This was also seen in experimental results for the low temperature single beam irradiations to $7_{TiC}/15_{matrix}$ dpa. The precipitates in these conditions had no significant changes in size, but did have partial dissolution (*i.e.*, significant decrease in number density). Thus, modelling and experimental results suggest recoil resolution was dominant enough to prevent size changes and cause partial dissolution, but not dominant enough to completely dissolve precipitates at $(15\ \text{dpa})_{matrix}$.

At 400°C, the magnitude of the concentration from recoil resolution for dual beam irradiation using the weakest Ti-helium binding (dashed blue line) is ~5× greater to that from the thermal equilibrium concentration (black line). This similarity in contributions to the Ti matrix concentration suggests recoil resolution as well as radiation-enhanced coarsening may be operational, but recoil resolution has a greater influence. This modelling result matches with experimental results for the 400°C dual beam condition to $7_{TiC}/15_{matrix}$ dpa, where no significant changes in size but significant decreases in precipitate number density were observed. Thus, modelling and experimental results suggest recoil resolution was dominant enough to prevent size changes and cause partial dissolution, but not dominant enough to completely dissolve precipitates at $(15\ \text{dpa})_{matrix}$. In addition, the difference in magnitude between the contributions from dual beam recoil resolution and radiation-enhanced coarsening was the same as that between the contributions from single beam recoil resolution and radiation-enhanced coarsening at 400°C. Hence, identical precipitation responses are predicted by the model for the single and dual beam conditions at 400°C. As shown in Figure 5.13, this was also backed up by experimental results.

In contrast, for the strongest Ti-helium binding shown in Figure 6.3 (dashed blue line), the model predicts the complete dominance of recoil resolution, with the concentration from recoil resolution being ~10^6 × greater than the thermal equilibrium concentration. This would suggest re-

precipitation of sub-particles around the original particles to occur. This was not experimentally observed though it is possible that the sub-particles were below the STEM-EDS resolution or that the particles were constantly dissolving and re-precipitating, a dynamic process that cannot be observed via ex-situ irradiation studies. Hence, the experimentally observed precipitate behavior for the 400°C dual beam condition is best simulated with the model using the weakest Ti-helium binding.

Summarizing the results at low temperatures, the modelling and experimental results indicate that helium co-injection had no effect on the precipitate behavior. The 400°C single and dual beam irradiations had nearly the exact same precipitate responses (i.e., size, density, and volume fraction changes) (Figure 5.7). This was simulated in the model with the use of the weak Ti-helium binding, where the matrix concentration from the recoil resolution using weak binding (dashed blue line) and from recoil resolution without helium (orange line) were nearly the same.

Thus far we have accurately approximated the dominant mechanism on precipitate behavior by comparing the contributions from recoil resolution and radiation-enhanced coarsening to the solute matrix concentrations. Frost and Russell furthered the model by explicitly determining the dominant precipitate behavior operating at given irradiation conditions with the following equation:

$$S = c_e \frac{96 D \sigma V_m}{R^3 (k_b T)} \qquad \text{Eq. 6.8}$$

where σ is the surface tension of the precipitate-matrix interface and V_m is the molar volume of the precipitates. σ is taken to be the standard value of 0.5 J/m^2 [80]. This equation can be plotted as a function of temperature. The curve delineates the boundary of the dominant mechanism on precipitate behavior. If the precipitate recoil rate (S = (3.3×10^{-4} dpa/s)$_{TiC}$) is below the curve, radiation-enhanced coarsening is dominant. If the precipitate recoil rate (S = (3.3×10^{-4} dpa/s)$_{TiC}$)

is above the curve, recoil resolution is dominant. The curve is plotted in Figure 6.5 using the proper diffusion coefficients for single and dual beam conditions, as explained previously. The orange lines represent the calculations for single beam irradiations and the blue lines represent the calculations for dual beam conditions. The gray area in represents the range of recoil resolution influence during dual beam irradiation, sandwiched between the maximum and minimum effects of helium on Ti diffusion. The experimental *S* value is shown with the gray horizontal line at $(3.3\times10^{-4}\ \text{dpa/s})_{\text{TiC}}$.

Figure 6.5a predicts that radiation-enhanced coarsening is slightly dominant at 300 and 400°C during single beam irradiations, but the magnitude is so small that it can be assumed that radiation-enhanced coarsening and recoil resolution are predicted to be on par. This was not backed up with experimental results, as slight recoil resolution dominance was shown. This can be assumed to be an incorrect outcome of the model, given the experimental results. However, the precipitates are in a radiation-enhanced coarsening dominant regime in single beam irradiations (orange line) at 500 and 600°C, which is backed up by experimental results.

With weak Ti-helium binding, helium co-injection only slightly shifts the orange line down at 400, 500, and 600°C (dashed blue line, Figure 6.5b,c). The precipitates in the dual beam irradiations at these temperatures are modelled to be in a radiation-enhanced coarsening dominated regime of stability. The modelled suppression of radiation-enhanced coarsening effects while still remaining in a radiation-enhanced coarsening dominant regime was shown experimentally for the 600°C dual beam condition. However, experimental results for the 500°C dual beam condition suggest this temperature should be near the crossover point of where the dominant mode of stability changes, which is not the case with the use of the weak Ti-helium binding in the model. See Appendix F for additional discussion on the crossover point. In addition, the 400°C dual beam

condition was shown to be in a recoil resolution dominant regime experimentally. Thus, the weak Ti-helium binding does not accurately predict the behavior at the 400 and 500°C dual beam conditions.

With strong helium-solute binding, helium co-injection shifts the orange line at 400, 500, and 600°C downward and causes precipitates to enter a recoil resolution dominant regime (solid blue line in Figure 6.5b,c). The 400°C dual beam condition was shown to be in a recoil resolution dominant regime experimentally, but the conditions at 500 and 600°C were not. Neither of these results from weak or strong Ti-helium binding are entirely in line with Figure 6.3 and Figure 6.4 or satisfactorily in line with the experimental results for these dual beam conditions.

In summary, the conclusions in Section 6.1.1 were furthered with the use of the recoil resolution model. The relative influence of recoil resolution during dual beam irradiations was theoretically modelled with the strength of the binding of Ti and helium complexes and its effect on Ti solute diffusion, guided by experimental results. Through robust analyses of the modelling predictions and comparisons to experimental results, it was concluded that Ti-helium binding of the order ~0.34 eV existed during irradiations in these experiments. This binding is not expected to change significantly as a function of temperature. Rather, its influence as a function of temperature is derived from its effect on diffusion. The Ti-helium binding changed the value and slope of the diffusion curve (Figure 6.1) and also acted to affect the crossover point by which radiation-enhanced coarsening or recoil resolution became dominant. For single beam irradiation, that crossover point is approximately at 460°C (Figure 6.3, Figure 6.4a). For dual beam irradiation with E_b^{Ti-He}= 0.34 eV, the crossover point is approximately at 490°C (Figure 6.3, Figure 6.4b). This is in line with the experimental results for the 500°C dual beam condition, where the near exact contributions from recoil resolution and radiation-enhanced coarsening caused there to be

no significant changes in the precipitate size or number density. *Hence, the strength of binding determined the level of suppression of Ti back diffusion via helium-solute binding. As Ti-helium binding caused decreased diffusion, diffusion-mediated processes that were present at elevated temperatures were inhibited. Since diffusion had no minimal effects on precipitate stability at lower temperatures, helium had no effect at those conditions. Experimental results were accurately matched with the model by assessing the matrix concentration contributions from recoil resolution and thermal equilibrium (Figure 6.3, Figure 6.4), but were not accurately simulated using Eq. 6.8 (Figure 6.5).*

Thus far, this analysis taken from Frost and Russell has provided useful descriptions for the mechanisms of MX-TiC precipitate stability in CNA9 and furthered the conclusion that helium suppresses diffusion at elevated temperatures and hence decreases radiation-enhanced coarsening. There are a few shortcomings in the model though, including the assumption of perfectly homogeneous distribution of spherical particles, a stationary particle interface, and an unchanging thermal matrix solute concentration and unchanging precipitate volume fraction. In the original paper [78], the model used C to assess the effects of irradiation on TiC precipitate stability in austenite. Hence, the model may not be fully applicable in its current state to substitutional solutes and to different lattice structures. In addition, the results of the model rest heavily on the method used to calculate C_v^{ss} and C_i^{ss}, which determine the level of diffusion under irradiation. For instance, Eq. 4.10 and Eq. 4.11 used a production efficiency, ξ, of 0.1. Other production efficiency values may garner different results than found in this section (Appendix H). However, other production efficiency values for proton and electron irradiations could be used to assess precipitate stability with the Frost and Russell model as a function of cascade size. This analysis would be in line with Refs. [111,118], which performed such analyses with the NHM model. In conclusion, the

usefulness of this model is apparent in its ability to help understand the operational regime of precipitate stability and test the proposed effects of helium on microstructural development. The experimental results also served to better understand the shortcomings of the model for this system.

Another model developed by Muroga, Kitajima, and Ishino (MKI) extended Frost and Russell's work (see Section 2.5.2). The MKI model quantitatively predicts the size change and dissolution of precipitates under irradiation using recoil resolution as the guiding principle [129]. The MKI model uses computer simulations to obtain recoil range distributions from collisional cascades of primary recoils with precipitates atoms. The recoil distribution is then used to calculate the recoil resolution efficiency, ε_{res}. The recoil resolution efficiency is defined as the number of atoms moved from inside to outside the precipitate with collision cascades divided by the number of atomic displacements within the precipitate:

$$\varepsilon_{RES} = \frac{\left(-R^4/_{12} + r_p^2 R^2\right)\pi S/_R}{4\pi r_p^3 S/_3} \quad \text{Eq. 6.9}$$

$$\varepsilon_{RES} = \frac{12\left(R/_{r_p}\right) - \left(R/_{r_p}\right)^3}{16} \quad \text{Eq. 6.10}$$

The rate of change in the initial size distribution of the precipitates, assumed to be unimodal in the MKI model, can be derived from the precipitate volumetric change as a function of recoil resolution efficiency:

$$\frac{dr_p}{dt} = \frac{-r_p S \varepsilon_{RES}}{3} \quad \text{Eq. 6.11}$$

From here, the final precipitate size as a function of irradiation damage level can be calculated using integration, ensuring that ε_{RES} is a function of r_p:

$$\int_{r_0}^{r_1} \frac{1}{r_p \varepsilon_{RES}} dr_p = \int_{t_0}^{t_1} -\frac{S}{3} dt \quad \text{Eq. 6.12}$$

$$\int_{r_0}^{r_1} \frac{1}{r_p\left(\frac{12\left(R/r_p\right)-\left(R/r_p\right)^3}{16}\right)} dr_p = \int_{t_0}^{t_1} -\frac{S}{3} dt \qquad \text{Eq. 6.13}$$

This equation was solved using the solve_ivp function as part of the SciPy package in Python. The code was programmed to calculate r_p as a function of time up to a value of r_1 that corresponded to a value of t_1, the time it took to get to $47_{TiC}/100_{matrix}$ dpa. r_0 is the initial precipitate size in the control specimen. As described previously, an R value of 0.7 nm was determined with the use of SRIM. A sensitivity analysis was performed that found this value nearly the same for all precipitate sizes tested from 3 to 90 nm (Appendix G).

A more accurate model of ε_{RES} to describe precipitate dissolution via recoil resolution and growth via solute back diffusion can be developed with the use of an effective range, R_{eff}. R_{eff} takes into account the recoil range, R (solute displacements outside of the precipitates as calculated by SRIM), and the capture radius, r_{cap} (solute diffusion back to precipitate from the matrix). r_{cap} describes the likelihood of a recoiling solute to return to the original precipitate it recoiled from. If a solute recoils from the precipitate beyond the r_{cap}, the solute remains in the matrix. If a solute recoils from the precipitate wihtin the r_{cap}, the solute migrates back to the precipitate. As the MKI model is a diffusion-less model, r_{cap} represents a method to account for solute and defect migration as a function of irradiation parameters and precipitate characteristics. r_{cap} is affected by factors such as precipitate coherency (*i.e.*, stress fields) and solute matrix diffusion. For instance, if a precipitate induces a large stress in the surrounding matrix, solute and defect diffusion may be altered in localized region surrounding the precipitate and be more likely to drift to the precipitate interface. Also, if temperature is increased, the resulting increased solute and defect diffusion may cause greater amounts of solutes and/or defects to migrate to the precipitate interface as compared to a low temperature condition. The MKI model does not explicitly define how to calculate R_{eff}

from R and r_{cap}. In this work, the following relationship was assumed, graphically shown in Figure 6.6:

$$R_{eff} = R - r_{cap} \quad \text{Eq. 6.14}$$

R_{eff} is a positive value when the magnitude of r_{cap} is less than the magnitude of R, translating to a positive ε_{RES} where more solutes will leave the precipitate than are replenished and the precipitates will tend toward dissolution. R_{eff} is a negative value when the magnitude of r_{cap} is greater than the magnitude of R, translating to a negative ε_{RES} where more solutes will enter the precipitate than leave and the precipitates will tend toward growth. As R_{eff} is the effective range of recoiling precipitate solute atoms it may not at first be intuitive to have a negative range of atoms. However, forcing a negative R_{eff} with a large r_{cap} simulates coarsening by simulating a positive concentration gradient at the precipitate interface. In addition, the recoil resolution efficiency was previously defined as the number of atoms moved from inside to outside the precipitate divided by the number of atomic displacements within the precipitate. Hence, a negative value of R_{eff} predicts that more atoms from outside the precipitate are moved to within the precipitate, simulating growth.

There are various factors that affect r_{cap}, and hence R_{eff} and ε_{RES}. However, no quantitative formalisms exist in literature to determine the values of r_{cap} based on the various factors. As such, survey calculations of different values of physically relevant R_{eff} were chosen to simulate the effect of r_{cap} on ε_{RES}. Then, an analysis of the effects on precipitate stability from literature and their possible relationships to r_{cap} on ε_{RES} will be discussed to understand the results.

Values of R_{eff} were chosen to encompass different behaviors of precipitates:

- Growth of precipitates: $r_{cap} > R$ and hence R_{eff} is negative, which leads to a negative value of ε_{RES} (more solutes enter than leave the precipitate)

- Dissolution of precipitates: $r_{cap} < R$ and hence R_{eff} is positive, which leads to a positive value of ε_{RES} (more solutes leave the precipitate than are replenished)

The values of R_{eff} chosen were -0.05, -0.8, 0.05, and 0.8 nm. These values are the same order of magnitude as the values of R_{eff} used in the MKI model and represent reasonable limits of growth and dissolution for this system, based on the results. The model calculates and integrates ε_{RES} as a function of r_p.

The results are shown in Figure 6.7 with four subplots. All solid lines in all subplots represent the radius value of the precipitates, r_p, calculated with a positive R_{eff}. The black dashed lines represent R_{eff} = 0.05 nm, the gray solid lines represent R_{eff} = 0.8 nm, the black dotted lines represent R_{eff} = -0.05 nm, the gray dotted lines represent R_{eff} = -0.8 nm, and the black solid lines represent R_{eff} = 0 nm. The four subplots correspond to the different temperatures of irradiations conducted: (a) 300°C, (b) 400°C, (c) 500°C, and (d) 600°C. The box plots represent experimental data. The box plots with lighter colors represent the experimental data for the single beam conditions at that temperature and dose. The box plots with darker colors represent the range of equivalent radii for the dual beam conditions at that temperature and dose. Figure 6.7a for 300°C only has a single beam irradiation. The dissolution by $23_{TiC}/50_{matrix}$ dpa at 300 and 500°C are shown with square markers.

The MKI model does not account for differences in the initial precipitate size distribution, as it assumes a unimodal size for all precipitates. To account for this, multiple initial precipitate radii were input as r_0 into the model that correspond to the minimum, maximum, interquartile range, and mean precipitate radii calculated for the control specimen. The boxplot of the control specimen is shown in each subplot at 0 dpa (white color boxplot). While this method captures the

dissolution behavior of precipitates with different initial radii, it does not capture the physical mechanistic effects of coarsening of an initially polydisperse distribution of precipitates [79].

The value of R_{eff} = 0.05 nm (black dashed line) best simulates the precipitate size distributions and dissolution behaviors of the low temperature irradiations to $7_{TiC}/15_{matrix}$ dpa. Experimentally, the single and dual beam irradiations at 300 and 400°C irradiation did not have statistically significant changes in size distribution from the control specimen at the $7_{TiC}/15_{matrix}$ dpa mark but did display statistically significant dissolution. The value of R_{eff}= 0.05 nm corresponds to an intermediate, positive value of r_{cap} and a small, positive value of ε_{RES}, with slightly more solutes leaving the precipitate than are replenished. As such, partial dissolution of precipitates would be expected, which was experimentally observed. At low temperatures and intermediate damage level, the value of r_{cap} is hypothesized to be most influenced by low diffusion of solute atoms back to the precipitate. The value of R_{eff} is not expected to significantly change with helium co-injection at 400°C to $7_{TiC}/15_{matrix}$ dpa because diffusion is already suppressed by the low temperature, as explained in the discussion using the Frost and Russell model.

For high temperature single beam irradiations, no positive value of R_{eff} could simulate the precipitate coarsening observed at $7_{TiC}/15_{matrix}$ dpa at 500 and 600°C. A value of R_{eff} = -0.05 nm (dotted black line) appears to accurately capture the coarsening at 500°C, except for the maximum value of the control specimen. R_{eff} = -0.8 nm (dotted gray line), better captures the size change for the maximum value of the control specimen at 500°C. However, a larger magnitude of a negative value of R_{eff} is needed to simulate the greater coarsening in the 600°C condition as compared to the single beam condition at 500°C to $7_{TiC}/15_{matrix}$ dpa. R_{eff} = -0.8 nm (dotted gray line) underestimates the coarsening of the largest of initial precipitates (maximum, Q3, and mean of the control specimen) but overestimates the coarsening of the smallest of initial precipitates in the

600°C condition. R_{eff} = -0.05 nm (dotted black line) also underestimates the coarsening of the largest of initial precipitates but does accurately capture the coarsening of the smallest of initial precipitates (minimum, Q1 of the control specimen) in the 600°C condition. Hence, at high temperatures and intermediate damage level for single beam irradiations, the value of r_{cap} is hypothesized to be most greatly influenced by the high diffusion of solute atoms back to the precipitate caused by the greater diffusivity at elevated temperatures. This led to the condition of $r_{cap} > R$. This also explains why greater coarsening was observed at 600°C than at 500°C, caused by a greater diffusivity of Ti solutes as temperature increased.

For the dual beam irradiation to $7_{TiC}/15_{matrix}$ dpa at 500°C, a condition of stability is expected, as no statistically significant changes in size distribution or density with the control specimen were experimentally observed. The value of R_{eff} = 0 nm (solid black line) accurately simulates this condition, translating to $r_{cap} = R$ and $\varepsilon_{RES} = 0$. Here, r_{cap} is expected to be suppressed as compared to the single beam 500°C condition by the addition of helium to the matrix, which suppresses Ti diffusion and hence suppresses solute back diffusion to the precipitates. Thus, helium co-injection effectively decreases r_{cap} by decreasing the diffusion of solutes to the precipitate. The value of R_{eff} = 0 nm (solid black line) also accurately simulates the stable precipitation present in the single beam irradiations at 500°C to $0.5_{TiC}/1_{matrix}$ and $2.3_{TiC}/5_{matrix}$ dpa.

Just as in the dual beam condition for 500°C, helium experimentally suppressed the growth of precipitates in the dual beam condition for 600°C. However, the size distribution still coarsened in the dual beam condition for 600°C (due to the greater diffusivity of solutes at the higher temperature) and a negative value of R_{eff} with a smaller magnitude of r_{cap} as compared to the dual beam 500°C condition is more applicable to simulate the partially suppressed coarsening in the dual beam condition at 600°C. Hence, at high temperatures and intermediate damage level for dual

beam irradiations, the value of r_{cap} is hypothesized to be most influenced by helium-coinjection suppressing the diffusion of Ti solute atoms back to the precipitate, thereby decreasing the magnitude of r_{cap} as compared to the corresponding single beam conditions.

Thus far, the values of r_{cap} assessed simulate and further explain the behavior of precipitates at intermediate damage level, but none encompass the complete dissolution of precipitates by $23_{TiC}/50_{matrix}$ dpa. The dissolution of precipitates at all temperatures by $23_{TiC}/50_{matrix}$ dpa (with and without helium co-injection) is accurately captured by R_{eff} = 0.8 nm (solid gray line), corresponding to r_{cap} = 0. Hence, r_{cap} is a function of damage level at all temperatures tested and tends toward zero as damage level is increased.

This analysis suggests that with positive values of R_{eff} (whether large or small in magnitude), initially smaller precipitates dissolve before larger precipitates. This is explained by this model because smaller precipitates have greater values of ε_{RES} than larger precipitates. It is easier for solutes to be recoiled into the matrix from smaller precipitates given their smaller surface area. This is also predicted by the Gibbs-Thomson effect, which predicts that the equilibrium solute concentration in the matrix next to a particle is smaller for small particles, hence they act as solute sources for large particles [79]. In addition, solute atoms are less tightly bound to smaller precipitates and tend to diffuse to larger precipitates, leading to coarsening. However, the Frost and Russell model and the MKI model do not factor in the dissolution of smaller precipitates acting as solute sources for large particles.

In summary, the results of the model suggest that at lower temperatures (300, 400°C) to intermediate dose ($7_{TiC}/15_{matrix}$ dpa) with and without helium co-injection, a small, positive ε_{RES} (intermediate, positive r_{cap}) is operating that results in minimal changes to the original size distribution of precipitates but results in partial dissolution of precipitates. This is in line with the

Frost and Russell model, which predicted recoil resolution was dominant for these conditions. At higher temperatures (500, 600°C) to intermediate dose ($7_{TiC}/15_{matrix}$ dpa) without helium co-injection, a negative value of ε_{RES} (large r_{cap}, $r_{cap} > R$), the magnitude of which increases with increasing temperature, is operational that results in coarsening of the original size distribution of precipitates. Helium co-injection causes r_{cap} to decrease in magnitude ($r_{cap} = R$ at 500°C, $r_{cap} \rightarrow R$ at 600°C) as it suppresses diffusion and hence suppresses coarsening, causing ε_{RES} to decrease in magnitude as well. This is in line with the Frost and Russell model, which predicted radiation-enhanced coarsening was dominant for high temperature single beam irradiations, but that the coarsening was fully or partially suppressed with helium co-injection. However, at any temperature and level of helium co-injection past an intermediate damage level, all precipitates dissolve experimentally. This is modeled by $r_{cap} = 0$ which causes the ε_{RES} to become large and positive in all conditions by $23_{TiC}/50_{matrix}$ dpa. Hence, the experimental work suggests that ε_{RES} is a function of damage level, and that it reaches an asymptotic value with increasing damage level no matter the temperature tested in these experiments, which leads to the observed complete dissolution of precipitates. These results are summarized in Table 6.5. The question then, alluded to in previous sections, is why ε_{RES} changes as a function of dose. There are a few reasons this may be the case, which will now be discussed.

First, the precipitates may not be able to withstand the number of displacements per solute atom of the precipitate that occurs with increased dose. It is a well-established theory that precipitates coarsen under irradiation due to solute back diffusion, enhanced by radiation [1]. Therefore, precipitates are expected to coarsen with increasing temperature as solutes in the matrix have greater diffusivity and can reach the precipitate. It is reasonable to assume that r_{cap} would increase with increasing temperature, leading to decreased R_{eff} and ε_{RES} and increased precipitate

stability (and possibly growth). However, the diffusional recovery may not be enough to combat the displacements per the surface area of the precipitate occurring with increasing damage level, thereby outweighing the ability of the MX-TiC precipitates to remain stable. The initial influence of recoil resolution may be lower than the influence of back diffusion during single beam irradiation at elevated temperature. Precipitates may coarsen initially at elevated temperatures, though the coarsening is moderated by the effects of recoil resolution. The rate of influence of recoil resolution with dose, however, becomes steeper than that of back diffusion and recoil resolution takes over as the dominant factor in precipitate stability after an initial coarsening has taken place. The recoil resolution efficiency, therefore, increases with dose (*i.e.*, more precipitates are more likely to move from inside to outside the precipitate as the amount of dpa increases). The temperature of 500°C is not enough to bring back these displaced atoms. Future work could conduct a $23_{TiC}/50_{matrix}$ dpa irradiation at 600°C or above to see if this theory applies at higher temperatures. For instance, MX precipitates in CNA3 were stable up to 50 dpa at 650°C with a dose rate of 1×10^{-3} dpa/s [75].

The second variable to discuss is the helium concentration in the matrix. Helium co-injection increases the sink strength of materials by providing sites for point defect annihilation in the matrix, thus decreasing the point defect concentration. As previously discussed, helium can also bind with solutes and decrease their mobility. With the resulting reduction in point defect concentration and in diffusion, the capture radius is expected to effectively decrease and hence increase R_{eff} and increase the tendency for precipitates to dissolve or at least to not coarsen. However, helium concentration in the matrix seemed to only affect the coarsening behavior of precipitates at intermediate damage level and not affect the complete dissolution at high damage levels.

Another possible reason is the effect that dose has on precipitate coherency. The coherency of an interface has been hypothesized to affect the ability of the interface to sequester defects. A fully coherent interface is continuous with the surrounding lattice, typically with some strains induced to ensure lattice continuity. The lattice strains allow for long-range interaction with point defects [124]. As interstitials have a larger perturbation in the matrix, they may be more likely to interact with the coherent precipitate's strain field and be attracted to the coherent interface [124,130,131]. Coherent particles are theorized to have a high sink strength, which is the average net effect that the entire population of precipitates has on the entire population of radiation-defect concentrations in the material [86,131]. Coherent particles would, however, have a low sink efficiency, which describes the ability of one single precipitate to absorb point defects at the interface and hence alter the localized point defect concentrations. This is because coherent interfaces are thought to be trapping sites for point defects and do not absorb point defects into their atomic structure [61,132,133]. Trapping of point defects at coherent interfaces enhances recombination of point defects. On the other hand, incoherent interfaces have no continuity with the lattice. Instead of being trapping sites for point defects, incoherent interfaces have been theorized to allow for interfacial rearrangement to absorb the incoming point defects into their lattice structure. Such an interface exerts either no strain field or a minimal strain field in the matrix and is considered a neutral sink. Incoherent particles have a low sink strength but a high sink efficiency. Semi-coherent interfaces have misfitting dislocations on their interface to relieve some lattice strain at the interface. Their sink strength and sink efficiency has not been decisively documented though the misfitting dislocations on the in the semi-coherent interface are believed to be efficient defect trapping sites for point defects [61,85,131,134]. For instance, Ref. [134] found that the elastic strains induced from semi-coherent planar interfaces induce a preferential point defect drift to the

interface via a non-random walk diffusion process that increases the interface sink strength, though the work did not consider semi-coherent precipitates. The elastic strain fields from the misfit dislocations at planar interfaces acted to change the diffusivity of point defects. The diffusion of defects in a strain field is then different than diffusion in the absence of a strain field: diffusivity would then become a function of spatial location and a drift term would be added to the continuum diffusion equation. Vacancies were shown to preferentially migrates to dislocation lines and interstitials were preferentially absorbed between dislocations, but the entirety of the interface was found to interact more with interstitials. Both this work and Ref. [131] showed that elastic strains greatly influenced the sink strength of the interfaces studied, particularly the sink strength for interstitials increases with greater interfacial strains. Hence, point defect (and therefore solute) diffusion may change in the presence of precipitates based on the stress induced in the matrix lattice by the precipitate and the bias of the interface. Increasing strains around a precipitate could cause the r_{cap} to increase.

Irradiation has been shown to cause a reduction in coherency [15,32,33]. The onset to the reduction of coherency was found to be a function of the precipitate sink strength in Ref. [15] which performed in-situ ion irradiations of coherent precipitates in model Cu alloys. A greater sink strength pushed the onset of the loss of coherency to higher damage levels. Precipitates with a sink strength on the order of $\sim 10^{13}$ m^{-2} had an onset of coherency loss at 0.01 dpa, while precipitates with a sink strength on the order of $\sim 10^{14}$ m^{-2} had an onset of coherency loss at 1 dpa. Ref. [136] found that both ordered, coherent and disordered, semi-coherent precipitates lost coherency under irradiation as dose increased. Precipitates began to dissolve when the interfacial dislocation structure became unstable with increased dose levels, and this process was not dependent on temperature. Ref. [135] observed that the stability of oxide-dispersions in a 12Cr-ODS steel was

dependent on the initial interface coherency of the dispersoids. The authors observed size changes with the initially coherent ODS particles dependent on irradiation conditions but observed that initially incoherent particles dissolved at lower temperatures and shrunk in size at higher irradiation temperatures. The authors suggested the coherent particles were more stable against radiation dissolution due to their lower interfacial energy as compared to semi-coherent and incoherent particles, given identical irradiation conditions. Coherency loss of precipitates has been documented to occur via a few different mechanisms. The first is by interaction with matrix dislocations, which are attracted to the precipitate interface. The second is the formation of dislocation loops within the precipitate, and the third mechanism is prismatic punching of dislocation loops for plate-shaped coherent particles [137].

This work suggests that r_{cap} may change as a function of these precipitate characteristics under irradiation. The effects of precipitate coherency on R_{eff} are expected to change as a function of dose as increased dose causes precipitates to lose coherency and possibly decrease r_{cap}. As precipitate coherency is lost with the matrix, the effect of coherency on r_{cap} may be diminished leading to a greater R_{eff} and hence a quickened pace of dissolution. This process may have a complex interplay with the interfacial energy of the interface as well. It is possible that the misfitting dislocations at the TiC precipitate-interface remained stable to a critical dose between $7_{TiC}/15_{matrix}$ and $23_{TiC}/50_{matrix}$ dpa. The aspect ratio of the precipitates in the $7_{TiC}/15_{matrix}$ dpa and 10 appm He/dpa conditions did not significantly change as compared to the control specimen, and hence it is assumed that the coherency also did not significantly change at this irradiation condition [126]. Once the onset of the loss of these interfacial dislocations occurred, the precipitates could have rapidly dissolved. This may be because the misfitting dislocations were sources of attraction for Ti solute replenishment from the matrix, or that they changed the bias of the precipitates

(through a change in the strain energy surrounding the precipitate) such that vacancies became preferentially attracted away from the interface of the precipitate where Ti solutes could diffuse away via the vacancy mechanism to the precipitate. The loss of interfacial dislocations may have decreased r_{cap}.

While this is a possible mechanism of TiC precipitate dissolution, proving or disproving this theory is very difficult experimentally. The small size of the precipitates makes it difficult to isolate the precipitate-matrix interface from the matrix in S/TEM. Numerous attempts were made to do this but were not successful. The precipitates are fully embedded in the matrix and hence the matrix obstructs a clear view of the interfacial dislocations. Future work could focus on larger precipitates in model alloys to understand their evolution via in-situ irradiations with and without helium co-injection at various damage levels. It should be noted though that these precipitates would still need to be embedded in the matrix for in-situ experiments to avoid surface related effects, imaging the coherency of larger precipitates is still more practical than precipitates smaller than ~ 10 nm and further thinning of the TEM lamellae could occur after irradiation to image the non-embedded precipitate-matrix interface. This type of experiment could also determine if helium co-injection plays a role in the onset of coherency loss as a function of dose. Modelling would then be needed to understand the mechanisms at play, particularly to understand the dynamic bias of the precipitate interface as a function of irradiation conditions.

In addition, similar though not exact behavior of MX-TiC precipitates was reported in Ref. [59] for proton irradiated cold-worked Ti-modified 316 stainless steel. The MX-TiC precipitates were not initially formed during manufacturing, but nucleated and grew at low dose (0-10 dpa) during irradiations at 600°C, and then gradually began to dissolve between 10 and 45 dpa. The dissolution of the MX-TiC precipitates coincided with the nucleation and growth of the Ti-

containing Fe_2P phase. Hence, Ti solute redistribution was the reason for MX-TiC precipitate dissolution between intermediate and high dose. Ti solute redistribution from MX-TiC precipitates to the G phase was also reported in numerous papers, leading to MX-TiC precipitate dissolution [48]. Ref. [138] found that γ' precipitates coarsened according to Ostwald ripening under irradiation with the third power of the precipitate diameter proportional to the damage level. The γ' precipitate size reached a maximum at a certain dose once redistribution of precipitate solute atoms occurred and γ' precipitates changed morphology. Though a morphological change in the MX-TiC precipitates did not occur in this work nor did the radiation-induced nucleation of a new Ti-containing phase, a redistribution of Ti solute atoms may have occurred during irradiation that could have affected the TiC solubility limit. The dynamic nature of precipitation is based on the concentration gradients of the constituent atoms in the precipitates. As solute is depleted from the matrix, a concentration gradient is established that may cause depletion of the solutes from the precipitates back to the matrix in a dynamic environment of changing solubility limits with radiation-induced point defects and temperature affecting the evolution. If the solute concentration gradient is positive at the precipitate interface, the precipitate will be expected to grow. If the solute concentration gradient is negative at the precipitate interface, the precipitate will be expected to dissolve. A larger solute concentration gradient predicts a larger magnitude of ε_{RES}, where growth is expected for a negative ε_{RES} and dissolution for a positive ε_{RES}. However, it may be expected that the Ti and C, once diffusing away from precipitates and causing their dissolution by $23_{TiC}/50_{matrix}$ dpa, may re-precipitate at higher damage levels. This did not happen by $47_{TiC}/100_{matrix}$ dpa in these experiments, though it may occur at higher doses. The Ti may be diffusing to other features in the microstructure such as the larger TiC precipitates (which did not dissolve) or grain boundaries or remain stable in a supersaturated solid solution if the solubility limit is not reached

under irradiation. Grain boundaries were assessed for solute segregation, but no conclusive evidence of Ti segregation was found (Appendix I).

The interparticle spacing of MX-TiC precipitates are shown in Table 6.4 for all $7_{TiC}/15_{matrix}$ dpa conditions at 300, 400, 500, and 600°C along with the mean distance traveled by a point defect before being captured by a MX precipitate (k_{MX}^{-1}) or any microstructural feature (k_{tot}^{-1}). As can be seen, point defects are more likely to be trapped or absorbed by features other than precipitates due to the low density of MX precipitates leading to a high interparticle spacing. This also may have repercussions for MX-TiC precipitate dissolution, as Ti solutes are more likely to encounter other features besides MX-TiC precipitates after recoil resolution. The stability of MX-TiC precipitates may also depend on their ability to exchange Ti solutes, which would require a smaller interparticle spacing [139]. In fact, the Frost and Russell model implies that for a low volume fraction of ~10^{-3} and a precipitate displacement rate (S) of ~10^{-4} dpa/s, particles would be dissolved by ~100 dpa around 400°C [78,140]. This work may prove the effects of volume fraction, and hence interparticle spacing, are more severe than predicted as particles were observed to dissolve in these experiments at half that damage level at 500°C. Further research into the number density and interparticle spacing effects on precipitate stability is needed.

Now that the effects of precipitate interfacial characteristics, diffusion and diffusional recovery, helium concentration, solute redistribution, concentration gradients, and interparticle spacing on r_{cap} and R_{eff} have been discussed, an assessment of the likelihood of the dominant factor(s) on precipitate stability at high damage levels may be given. As precipitates dissolved at high damage levels no matter the damage rate or temperatures tested, the effects of increasing recoils within the precipitate and the effects of diffusional recovery are assumed to be secondary in the conditions tested. It is assumed that Ti solute redistribution occurred concurrently with a

loss of initial precipitate interfacial characteristics. This, combined with a high interparticle spacing, caused the dissolution of precipitates at high damage levels. Future work should focus on attempting to parse out the influence of these three effects on precipitate stability.

Lastly, the fidelity and applicability of the damage level calculations of the matrix and the MX-TiC precipitates should be discussed as the analysis of both the Frost and Russell and MKI models rests heavily on the calculated damage level. As described in 4.2.2, Chapter 6, and Appendix D, quick-KP SRIM calculations were used to ascertain the damage levels (in dpa) of both the matrix and the MX-TiC precipitates. This method has known errors associated with it, such as overpredicting the damage level and underpredicting the atomic mixing [141]. An improved method for calculating damage accounts for athermal recombination corrected dpa (arc-dpa) and atomic mixing (replacements per atoms, rpa) [141]. The arc-dpa reduces the number of point defects as compared to the SRIM-generated damage calculation. The rpa model accounts for the cascade size of damage, which can affect phase stability. Thus, how damage is calculated may affect the results of the Frost and Russell and MKI models. However, it is assumed that the general conclusions will remain the same, despite if the exact magnitude of R_{eff} may be different to match experimental results: it is assumed that R_{eff} will still change as a function of damage level and R_{eff}'s variability will still affect the growth and dissolution prediction of precipitates. It is important in future work to explain the method of damage calculation and how that might affect comparisons to this work.

In conclusion, the models employed by Frost and Russell and MKI are simple for such a complex phenomenon as precipitate evolution under irradiation. The factors discussed here (helium, precipitate interfacial characteristics, temperature, concentration gradients, solubility limits, and interparticle spacing) all change the diffusion of point defects and solutes under

irradiation, which cause a dynamic sink strength under irradiation. Table 6.5 provides a summary of the discussion on the recoil resolution model of MX-TiC precipitates in CNA9. A more comprehensive model is needed to account for these factors in a spatially sensitive manner (i.e., proximity to precipitates and the number density of all sinks) to properly account for the phenomena of precipitate coarsening and dissolution. In addition, this analysis considered Ti for MX-TiC phase stability due to Ti being the rate-limiting species. However, the loss of C to other microstructural sinks during irradiation may be a factor as well. Future work could focus on quantitatively calculating the value of r_{cap}, especially as a function of damage level. The analysis resulted in the finding that the ability of MX-TiC precipitates to resist dissolution decreased with increasing damage levels, and hence any benefit to mechanical properties or resistance to radiation damage garnered by these precipitates would be lost in the early lifetime of fusion power plants. Importantly, this analysis considered an environment free of creep, stress, and fatigue, all effects that would be operational in a power plant. The single effects of these variables under irradiation as well as their combined effects on MX-TiC precipitates are unknown.

Table 6.4 Mean MX interparticle spacing and mean distance traveled by a point defect before being captured by a MX precipitate ($\boldsymbol{k_{MX}^{-1}}$) or any microstructural feature ($\boldsymbol{k_{tot}^{-1}}$).

Condition	MX Precipitate Interparticle Spacing	$\boldsymbol{k_{MX}^{-1}}$	$\boldsymbol{k_{tot}^{-1}}$
(300°C-15 dpa-7×10^{-4} dpa/s)$_{matrix}$	180 nm	144 nm	18 nm
(400°C-15 dpa-7×10^{-4} dpa/s)$_{matrix}$	150 nm	120 nm	20 nm
(500°C-15 dpa-7×10^{-4} dpa/s)$_{matrix}$	118 nm	94 nm	52 nm
(600°C-15 dpa-7×10^{-4} dpa/s)$_{matrix}$	115 nm	92 nm	92 nm
(400°C-15 dpa-7×10^{-4} dpa/s-10 appm He/dpa)$_{matrix}$	180 nm	143 nm	19 nm
(500°C-15 dpa-7×10^{-4} dpa/s-10 appm He/dpa)$_{matrix}$	136 nm	108 nm	32 nm
(600°C-15 dpa-7×10^{-4} dpa/s-10 appm He/dpa)$_{matrix}$	119 nm	95 nm	46 nm

Table 6.5 Summary of mechanisms affecting precipitate behavior using the MKI model and literature assessments on factors affecting precipitate dissolution. The effective range, R_{eff}, is the physical range of recoiling solutes, as calculated with SRIM, minus the capture radius of the solutes, r_{cap}. R_{eff} accounts for the possible mechanisms that may change r_{cap} and hence change the diffusion of point defects and solutes to precipitates. The recoil resolution efficiency, ε_{RES}, refers to the likelihood of precipitate dissolution, with large, positive values of ε_{RES} describing more atoms leaving the precipitates than entering, leading to dissolution.

Damage Level Regime	**Temperature and Helium Regime**	**Suggested dominant mechanism affecting r_{cap}**	**Precipitate behavior**	**Capture Radius (r_{cap})**	**Effective range (R_{eff})**	**Recoil resolution efficiency (ε_{RES})**
Intermediate damage level (~5-15 dpa)	Low temperatures Single and dual beam	Low diffusion of Ti due to low temperature causing less solute migration back to precipitates	No size changes, but partial dissolution	Intermediate ($0 < r_{cap} < R$)	Small, positive	Small, positive
	High temperatures Single beam	High diffusion of Ti	Precipitate growth	Large ($r_{cap} > R$)	Large, negative	Large, negative
	High temperatures Dual beam	Lower diffusion of Ti due to helium co-injection	Complete or partially suppressed growth	Large but suppressed ($r_{cap} \rightarrow R$)	Small, positive	Small, positive
High damage level (>50 dpa)	All temperatures Single and dual beam	Ti solute redistribution, loss of initial precipitate interfacial characteristics, and high interparticle spacing	Complete dissolution	Minimum ($r_{cap} = 0$)	Large, positive	Large, positive

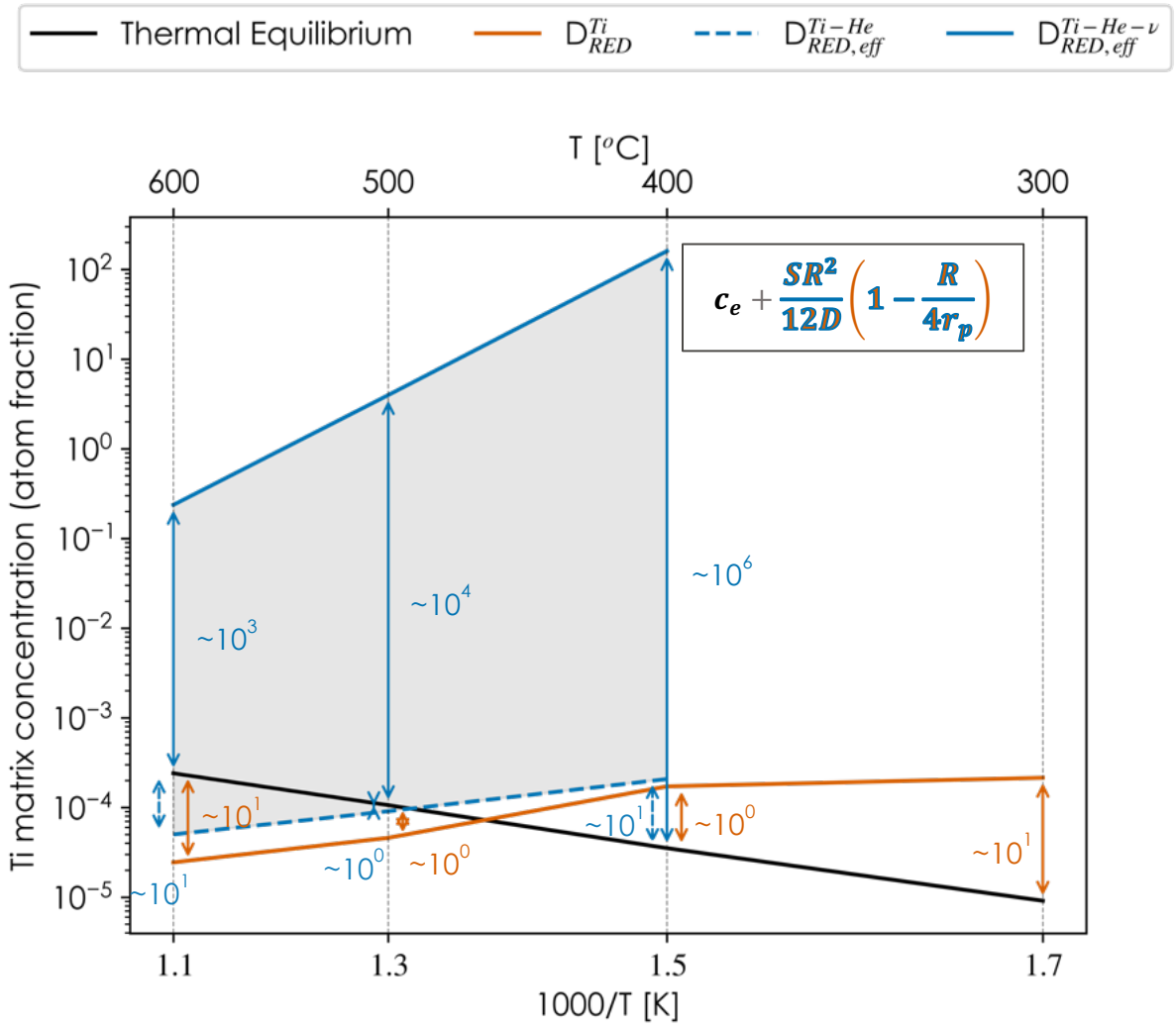

Figure 6.3 The matrix concentration in thermal equilibrium (c_e, black line) was plotted versus the concentration from recoil resolution ($\frac{SR^2}{12D}\left(1 - \frac{R}{4r_p}\right)$, orange line for single beam and blue lines for dual beam). The solid blue line refers to strong Ti-helium-vacancy binding and the dashed blue line refers to weak Ti-helium binding. The radiation-enhanced diffusion, D_{RED}^{Ti}, was used to calculated the recoil resolution contribution for single beam irradiations. The effective helium-suppressed radiation-enhanced diffusion, $D_{RED,eff}^{Ti-He}$ and $D_{RED,eff}^{Ti-He-v}$, was used to calculated the recoil resolution contribution for dual beam irradiations.

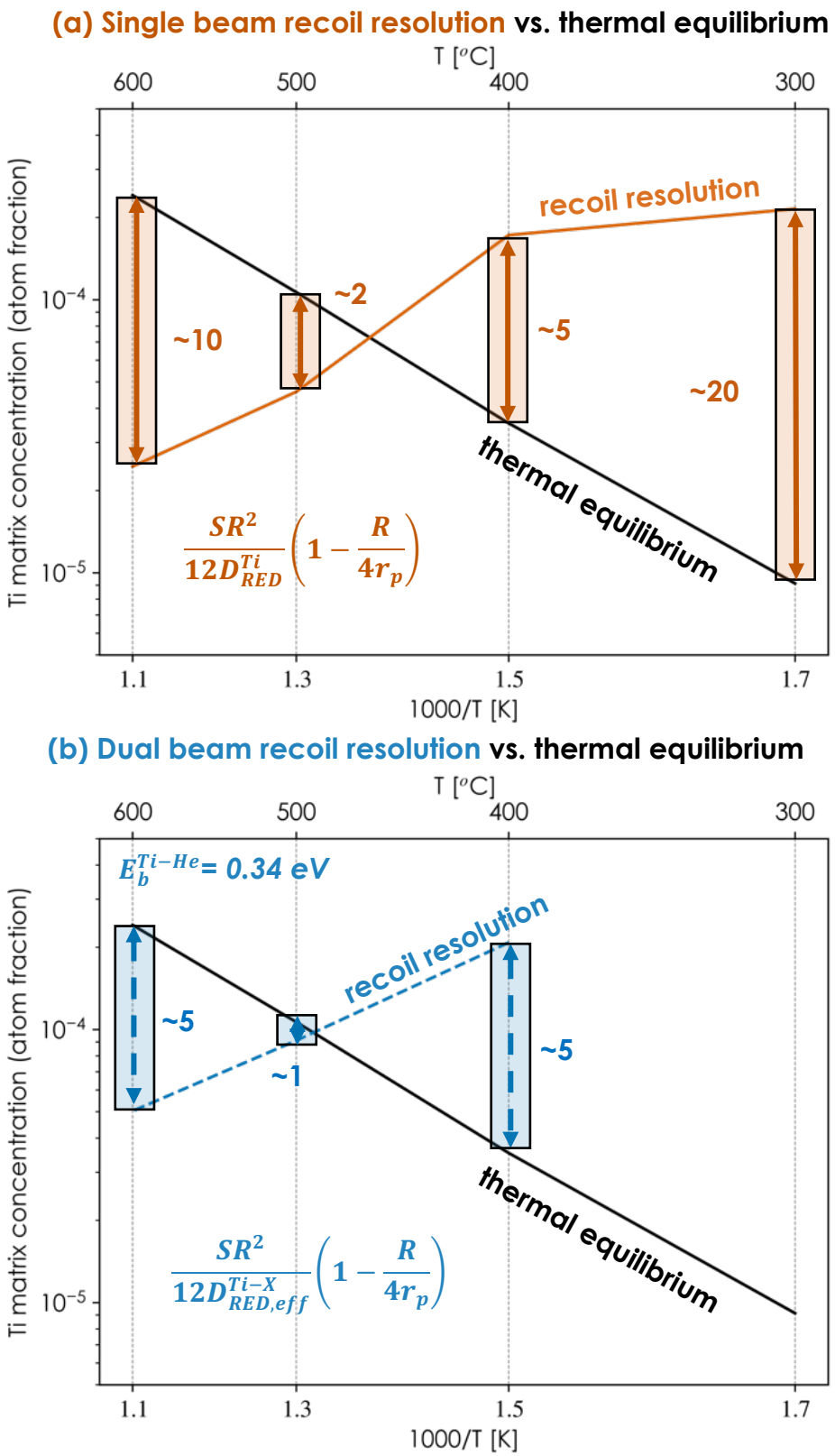

Figure 6.4 This figure is a deconstructed version of Figure 6.3. The matrix concentration in thermal equilibrium (c_e, black line) was plotted versus the concentration from recoil resolution, $\frac{SR^2}{12D}\left(1-\frac{R}{4r_p}\right)$, for (a) single beam, orange line, and for (b) dual beam, blue line. The dashed blue line refers to weak Ti-helium binding, which was found to match best with experimental results. Strong Ti-helium-vacancy binding is not shown, as in Figure 6.3.

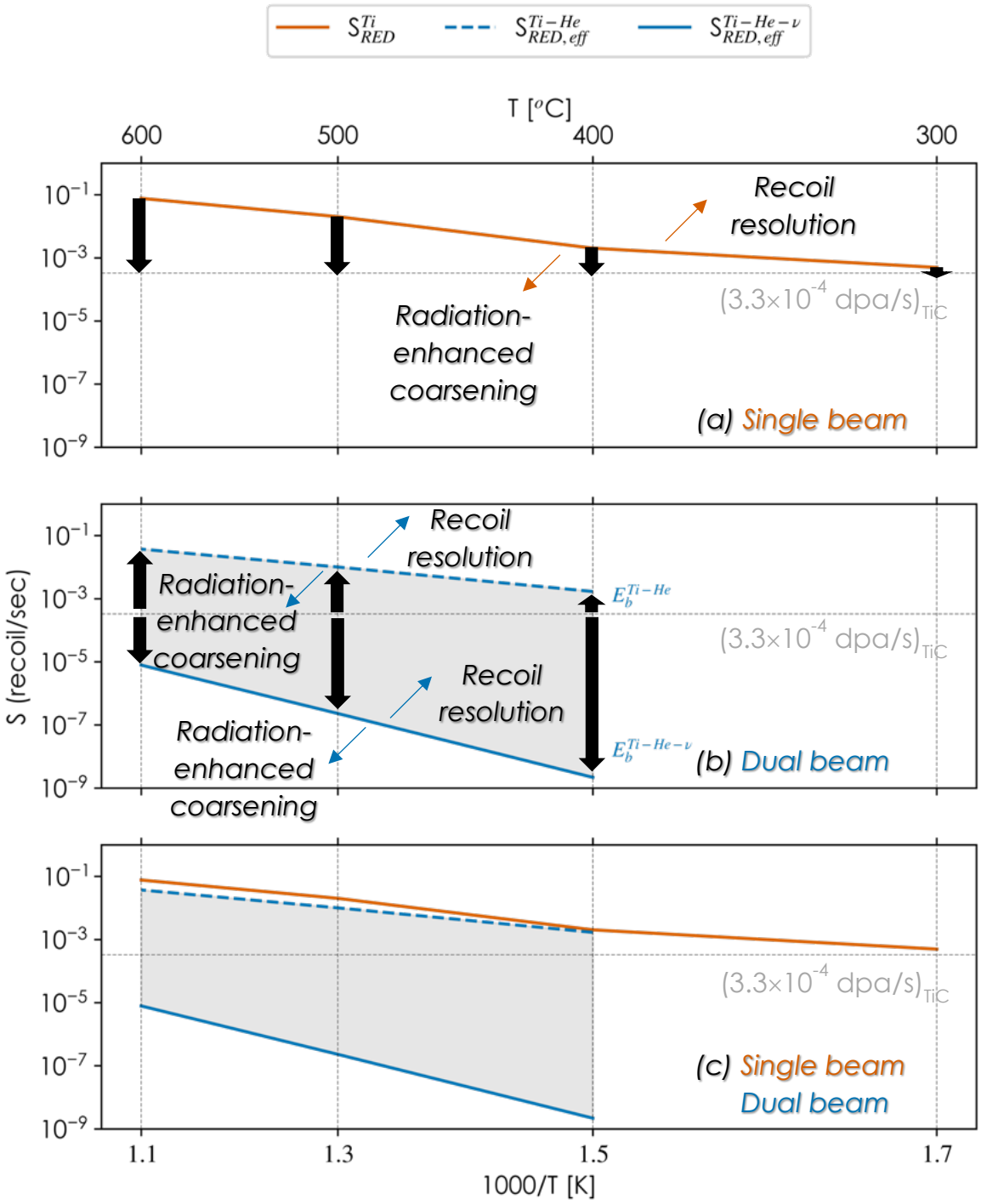

Figure 6.5 Dominant mechanisms for precipitate stability under irradiation for (a) single beam and (b) dual beam conditions. (c) Comparison of single and dual beam conditions. Recoil resolution is dominant above the dividing lines and radiation-enahnced coarsening below. The gray horizontal lines represent the recoil rate, *S*, at experimental conditions, $(3.3\times10^{-4}$ dpa/s$)_{TiC}$. The solid blue line refers to strong Ti-helium-vacancy binding and the dashed blue line refers to weak Ti-helium binding. The orange line refers to single beam conditions.

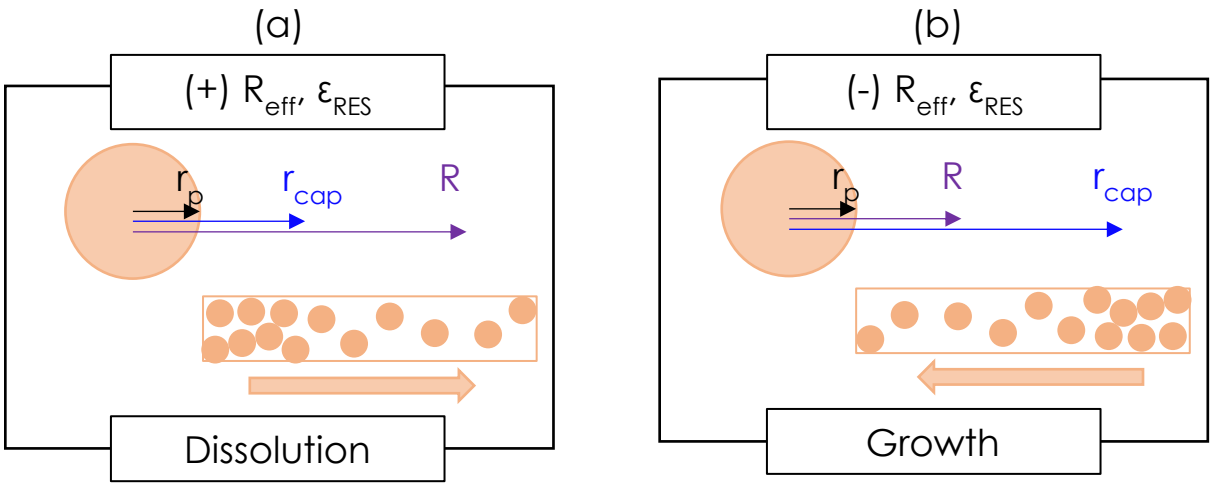

Figure 6.6 Schematic showing the relationships between the precipitate radius (r_p), the recoil distance (R), and the capture radius (r_{cap}) on the effective range (R_{eff}) and the recoil resolution efficiency (ε_{RES}). The concentration gradients are shown as well, showing the effect of Ti solute gradients at the precipitate-matrix interfaces on precipitate solute behavior.

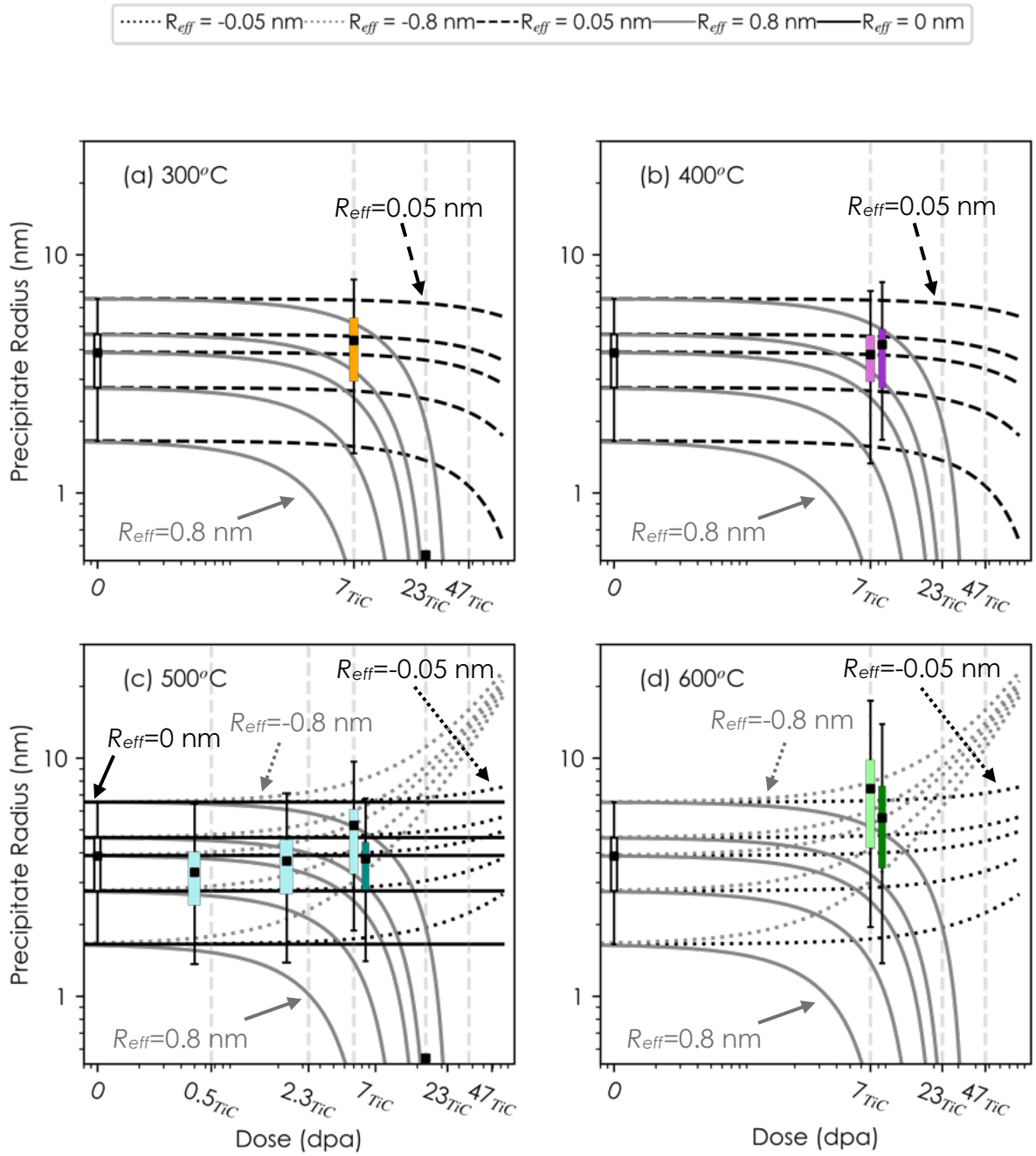

Figure 6.7 Plots showing the theoretical behavior of TiC precipitates under irradiation as modelled by the MKI model of recoil resolution. Each plot shows the same four simulated curves of coarsening or dissolution as modelled with four values of R_{eff}: -0.05 nm (dotted black line), -0.8 nm (dotted gray line), 0.05 nm (dashed black line), 0 nm (solid black line), and 0.8 nm (solid gray line). The box plot (white) showing the size distribution of the control specimen is shown on each plot at 0 dpa. The box plots for the single (lighter colors) and dual (darker colors) are shown on each plot for (a) 300, (b) 400, (c) 500, and (d) 600°C. The x axis represents the damage level received by the TiC precipitates.

6.1.4 Summary of the Results of the Scientific Objective

The scientific objective outlined in Chapter 3 sought to determine if the following hypothesis was correct:

Co-injected helium will prevent the radiation-enhanced growth of pre-existing TiC nanoprecipitation within ion irradiation environments. This will occur due to injected helium atoms binding to Ti solute atoms in the matrix.

Through detailed studies assessing the roles of damage level, damage rate, temperature, and co-injected helium on the pre-existing size distribution and number density of TiC precipitates, it can be concluded that this hypothesis was correct at elevated temperatures (500, 600°C). It can be concluded that helium co-implantation reduces the growth of precipitates during ion irradiation experiments at temperatures where precipitate size distributions are controlled by diffusion-mediated processes in single beam conditions. This occurs by helium atoms binding to Ti solutes and suppressing the long-range motion of the helium-Ti complex. The complexes decrease the effective diffusion of Ti in the matrix, thus decreasing the contribution of radiation-enhanced coarsening of precipitates under irradiation. This was simulated with the use of the recoil resolution model of precipitate stability, where helium's effects on Ti diffusion translated to a relative increase in the influence of recoil resolution on precipitates. Helium co-injection had no effect at lower temperatures (400°C) where diffusion was not a dominant process on precipitate stability.

In addition, damage level was observed to greatly influence precipitate stability, with the MX-TiC precipitates dissolving by 50 dpa_{matrix}. The influence of damage level was assessed with the recoil resolution model as well and it was concluded that the efficiency of dissolution increases with damage level. It was hypothesized that various factors caused this, but further work is needed to definitively determine the main causes of dissolution.

6.2 Helium Sequestration Ability of TiC Precipitates and its Effect on Cavity Behavior

This section will explore the effects of temperature, helium co-injection rates, and coherency on the behavior of precipitate-attached cavities and the effect of precipitates on swelling.

6.2.1 Effects of Temperature on Helium Sequestration at the TiC-Matrix Interface

The ability to sequester helium at the precipitate-matrix interface, and hence to control nucleation and subsequent growth of matrix cavities, was found to be dependent on temperature. Helium was sequestered most efficiently in the form of cavities at 500 and 600°C, whereas there were not enough cavities observed on precipitate-matrix interfaces at 400°C to be statistically relevant. It is assumed that all cavities at the precipitate-matrix interfaces are helium- filled because they are small (<5 nm) and spherical in TEM images, suggesting an over-pressurization from helium before biased-driven growth is achieved. Cavities are considered bubbles when the gas inside the cavity causes it to become spherical [1]. However, faceted cavities may look spherical in TEM images if they approach a small enough size. It is, however, common practice to assume visually small, spherical cavities are bubbles [42,142,143]. This analysis is in line with literature that describes small, spherical bubbles as being stabilized by helium gas pressure [143–146]. The size of 5 nm was chosen as the cutoff between the bimodal cavity size distributions at 500°C (Figure 5.20) [42].

As previously mentioned, a uniform distribution of small (<5 nm) helium-filled cavities were found homogeneously dispersed in the matrix in the (400°C-7 dpa-3.3×10^{-4} dpa/s-10 appm He/dpa)$_{TiC}$ / (400°C-15 dpa-7×10^{-4} dpa/s-10 appm He/dpa)$_{matrix}$ condition. There are a few possible reasons why cavities were observed to develop in the matrix but not on the precipitate-matrix interfaces. It is possible that ballistic dissolution caused the precipitate-matrix interface to become

unstable and hence no clearly defined interface was available for cavities to form. Another reason could be that helium had such a low diffusion at 400°C that it was effectively trapped within the matrix due to immobility before making it to precipitate-matrix interfaces and being able to nucleate on the interfaces. There was a significant reduction in number density of precipitates at this condition due to recoil resolution, which would further decrease the trapping ability of MX-TiC precipitates having a greater interparticle spacing.

At the conditions tested, peak swelling occurred at 500°C. Hence, the sequestration ability of the MX-TiC precipitates is most important at this temperature to prevent the negative effects of unconstrained swelling. Figure 5.17 clearly indicates helium sequestration by the MX-TiC precipitates in the (500°C-7 dpa-3.3×10^{-4} dpa/s-10 appm He/dpa)$_{TiC}$ / (500°C-15 dpa-7×10^{-4} dpa/s-10 appm He/dpa)$_{matrix}$ condition. Importantly, all cavities attached to the precipitates remained smaller than the critical bubble radius at this temperature, which was ~4 nm (see Section 4.9 for how this was determined). *This would suggest that the semi-coherent MX-TiC precipitates can act to sequester helium in FM steels before their dissolution during irradiation near the peak swelling temperature*. The MX-TiC precipitates did not act as sites of enhanced point defect collection, which would lead to precipitate-attached cavities larger than matrix cavities [56]. To the authors knowledge, this is the first work to prove helium sequestration capabilities for semi-coherent precipitates in FM steels under fusion-relevant ion irradiation conditions. The distribution of precipitate-attached bubbles and matrix cavities is shown in Figure 5.19.

The effect of the precipitates on swelling at 500°C and $7_{TiC}/15_{matrix}$ dpa may be assessed by observing the cavity distribution in grains with a higher number of MX-TiC precipitates versus grains with no precipitates. Figure 6.8 shows the size distribution of cavities, with the corresponding swelling value of matrix cavities, between various grains. As can be seen, there is

no clear trend of swelling between grains with MX-TiC precipitates (with densities ranging from 0.2 to 2.2 $\times 10^{21}$ m^{-3}) and grains with no precipitation. This is most likely because the number density of MX-TiC precipitates is still too low to have effects on the engineering level. In reviewing the available literature, Zinkle *et al.* found that oxide dispersions in ODS steels present in approximately 100× greater density than cavities result in low void swelling even up to 500 dpa (<5% volume change) in single beam ion irradiations. In addition, Zinkle *et al.* determined that an ultra-high oxide particle density of 10^{24} m^{-3} (resulting in an overall sink strength of ~10^{16} m^{-2}) was needed to suppress radiation-induced hardening. The improved radiation resistance of the oxide particles relies on their small average interparticle spacing, making point defects and helium atoms more likely to interact with a particle than with another [11]. The effect of sink strength on helium bubbles was further studied by Yan *et al.* in CNA1, CNA3, and two ODS alloys (9YWTV and 14YWTV) [77]. These materials were implanted with 7500 appm helium at 500 and 700°C. CNA1 and CNA3 contained particle densities on the order of ~10^{21}-10^{22} m^{-3}, including both MX ((V,Ta)N in CNA1 and (Ti,Ta)C in CNA3) and $M_{23}C_6$ precipitates (translating to a sink strength of ~10^{15} m^{-2}). 14YWT contained a ODS particle density on the order of ~10^{24} m^{-3} (translating to a sink strength of ~10^{16} m^{-2}). A sink strength of ~10^{16} m^{-2} was needed at peak helium effects to suppress bubble growth, leading to the conclusion that CNA1 and CNA2 did not contain enough MX precipitates to suppress peak bubble growth. Future CNAs and other advanced FM steels need to ensure a greater number density of precipitates than present in CNA9 to have an effect on properties under irradiation. In addition, MX precipitates that remain stable to damage levels at and greater than $23_{TiC}/50_{matrix}$ dpa should be assessed for their trapping ability of helium and their effect on the overall swelling at high damage levels.

The (600°C-7 dpa-3.3×10^{-4} dpa/s-10 appm He/dpa)$_{TiC}$ / (600°C-15 dpa-7×10^{-4} dpa/s-10 appm He/dpa)$_{matrix}$ condition displayed a uniform distribution of small (<5 nm) helium-filled cavities homogeneously dispersed within the matrix. However, unlike at 400°C, cavities attached to precipitate-matrix interfaces were found at this higher temperature. Like the condition at 500°C, all cavities attached to the precipitates remained smaller than the critical bubble size of 4 nm. However, cavities in the matrix also remained small and there was only a ~0.4 nm difference in the size distributions of the matrix and precipitate-attached cavities.

The size distributions between the precipitate-attached cavities in the (500°C-7 dpa-3.3×10^{-4} dpa/s-10 appm He/dpa)$_{TiC}$ / (500°C-15 dpa-7×10^{-4} dpa/s-10 appm He/dpa)$_{matrix}$ and (600°C-7 dpa-3.3×10^{-4} dpa/s-10 appm He/dpa)$_{TiC}$ / (600°C-15 dpa-7×10^{-4} dpa/s-10 appm He/dpa)$_{matrix}$ conditions will now be discussed (Figure 6.9, Figure 6.10). The matrix bubbles in the 500°C condition had an average diameter of 1.3±0.02 nm and the matrix bubbles in the 600°C condition had an average diameter of 1.2±0.02 nm. The precipitate-attached bubbles in the 500°C condition had an average diameter of 1.2±0.03 nm and the precipitate-attached bubbles in the 600°C condition had an average diameter of 1.6±0.04 nm. There is a greater size difference between the precipitate-attached bubbles at 600 and 500°C (0.4±0.05 nm) versus the size difference between matrix bubbles (-0.1±0.03 nm). In addition, there were no voids in the 600°C condition. The precipitate-attached bubbles grew to larger sizes at 600°C than at 500°C, whereas the matrix cavities shrunk to smaller sizes at 600°C than at 500°C. The larger average diameter of the precipitate-attached bubbles in the 600°C condition is reflected in the longer tail of its size distribution. This would suggest that even at 600°C the precipitate-attached bubbles were not thermally disassociating or de-trapping from the interface but that the matrix cavities were thermally disassociating at 600°C. Thermal disassociation of vacancies from matrix bubbles is predicted as temperature increases, so

it is interesting that this did not occur for the precipitate-attached bubbles [1]. This is in line with research on CNA1 and CNA3, where MX precipitates were shown to effectively trap helium at their interfaces up to 600°C under elevated temperature helium implantation [76,77]. Hence, the bubbles on the semi-coherent MX-TiC precipitate-matrix interfaces in CNA9 had greater binding for helium than matrix cavities that prevented the thermal release of helium and vacancies. Perhaps this combined with the greater diffusion of helium and vacancies at 600°C caused a slightly greater average size of precipitate-attached bubbles than at 500°C. To the author's knowledge, this is the first of a kind finding for the precipitate-matrix effect on the size of cavities.

The thermal emission probability, *P*, for a vacancy to leave a bubble is [147]:

$$P = e^{-E^B_{vac-bub}/k_bT} \quad \text{Eq. 6.15}$$

where the vacancy-bubble binding energy ($E^B_{vac-bub}$) is evaluated as the work done in emitting a vacancy and is calculated as:

$$E^B_{vac-bub} = E^f_v - \left(\frac{2\gamma_{bub}}{R} - p_1\right)\Omega \quad \text{Eq. 6.16}$$

where E^f_v is the formation energy of a vacancy in eV, γ_{bub} is the surface energy of the bubble in eV/m^2, R is the universal gas constant, p_1 is the gas pressure of the bubble determined by the Van der Waal's equation, and Ω is the atomic volume in m^3.

Hence, the probability of the thermal emission of a vacancy from a bubble is a function of temperature (in a reliance on E^f_v), γ_{bub}, and p_1. These values may have changed between the precipitate-attached cavities and the matrix cavities at 600°C. Other work calculated that high surface tension and the presence of stress fields at the precipitate interface lends to strong binding of a bubble and a precipitate [148,149]. Pressure may also have changed in the bubbles at the precipitate-matrix interfaces as the pressure of the bubble compensates for the surface energy of the precipitate. This binding may be dependent on the composition of the MX particles, and hence

modelling could be done to calculate which MX precipitates have the greatest helium binding under fusion relevant temperature conditions.

The behavior of bubbles at the precipitate-matrix interfaces can also be related to the precipitate stability mechanisms as discussed in Section 6.1. In that section, it was discussed that radiation-enhanced diffusion of Ti caused the coarsening of MX-TiC precipitates at 500 and 600°C to $7_{TiC}/15_{matrix}$ dpa under single beam irradiations. At the same conditions with 10 appm He/dpa, helium suppressed Ti diffusion through helium-Ti binding and hence suppressed the precipitate coarsening observed. Though diffusion was suppressed, helium-Ti solutes were still mobile at these elevated temperatures, as were single helium atoms and helium-vacancy clusters. The attachment of bubbles to precipitate-matrix interfaces at these elevated temperatures suggest that there was still sufficient diffusion of helium complexes to migrate and form on precipitate-matrix interfaces, though the low density of precipitates did not prevent matrix cavity development. This would suggest that diffusion at higher temperatures plays an important role in the motion of helium to precipitate-matrix interfaces as well where it becomes trapped and can accumulate into bubbles, compared to the dual beam condition at 400°C that had minimal bubble attachment to precipitates and where it was determined that helium complexes had low diffusive ability.

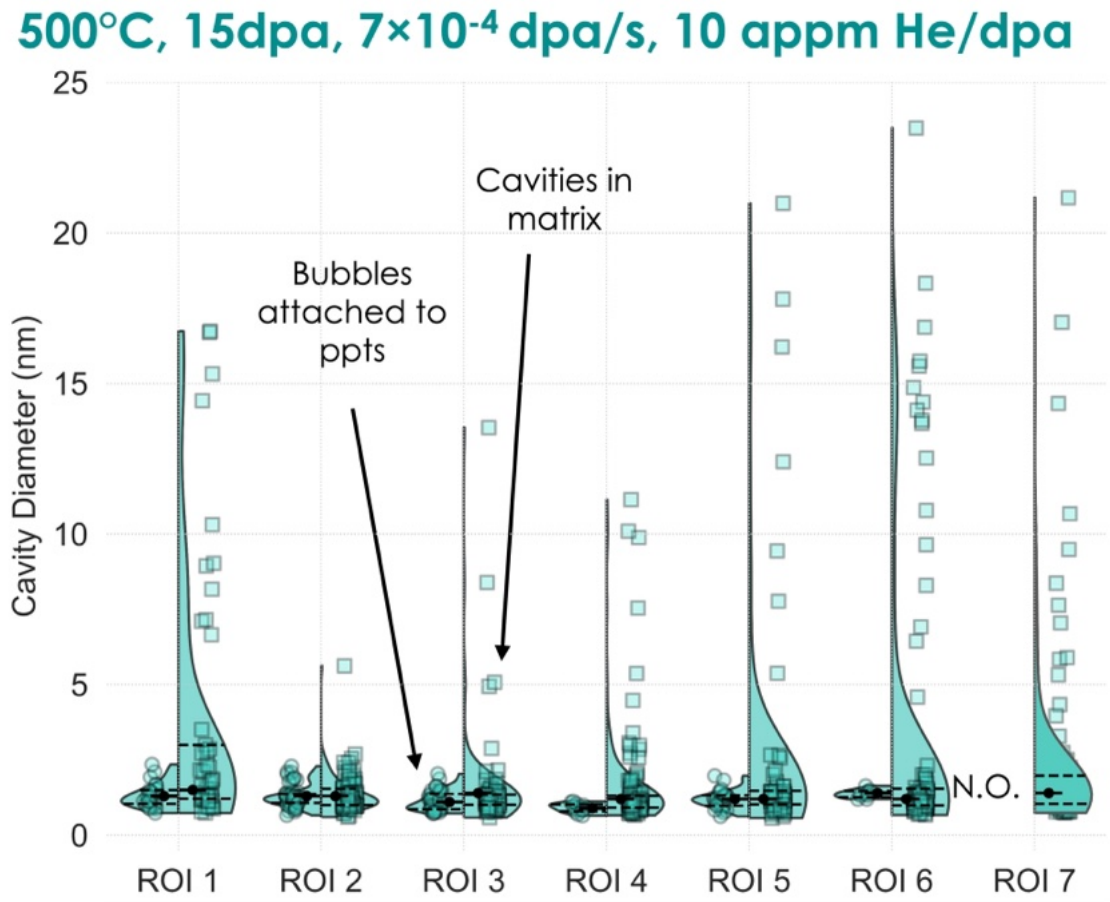

	ROI 1	ROI 2	ROI 3	ROI 4	ROI 5	ROI 6	ROI 7
Swelling (%)	0.2	0.0006	0.03	0.04	0.3	0.4	0.2
TiC Density ($\times10^{21}m^{-3}$)	1.7	2.2	2.0	0.2	1.6	0.2	N.O.

Figure 6.8 Comparison of swelling and precipitate number density in various grains in (500°C-15 dpa-7×10^{-4} dpa/s-10 appm He/dpa)$_{matrix}$ condition. No clear trend was established. The violin plots are normalized by width.

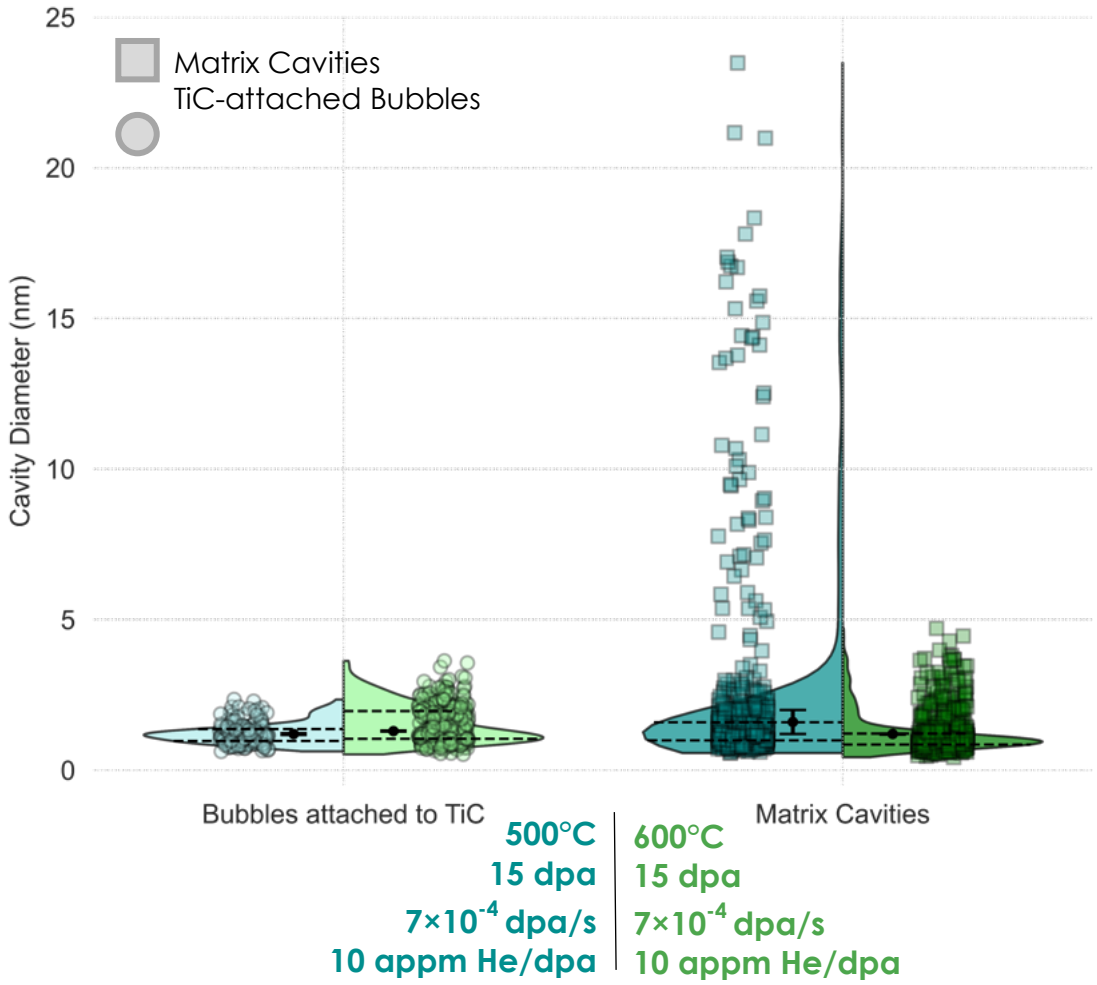

Figure 6.9 Comparison of matrix cavities (square symbols) to precipitate-attached cavities (circle symbols) for the dual beam conditions at 500 (blue) and 600°C (green).

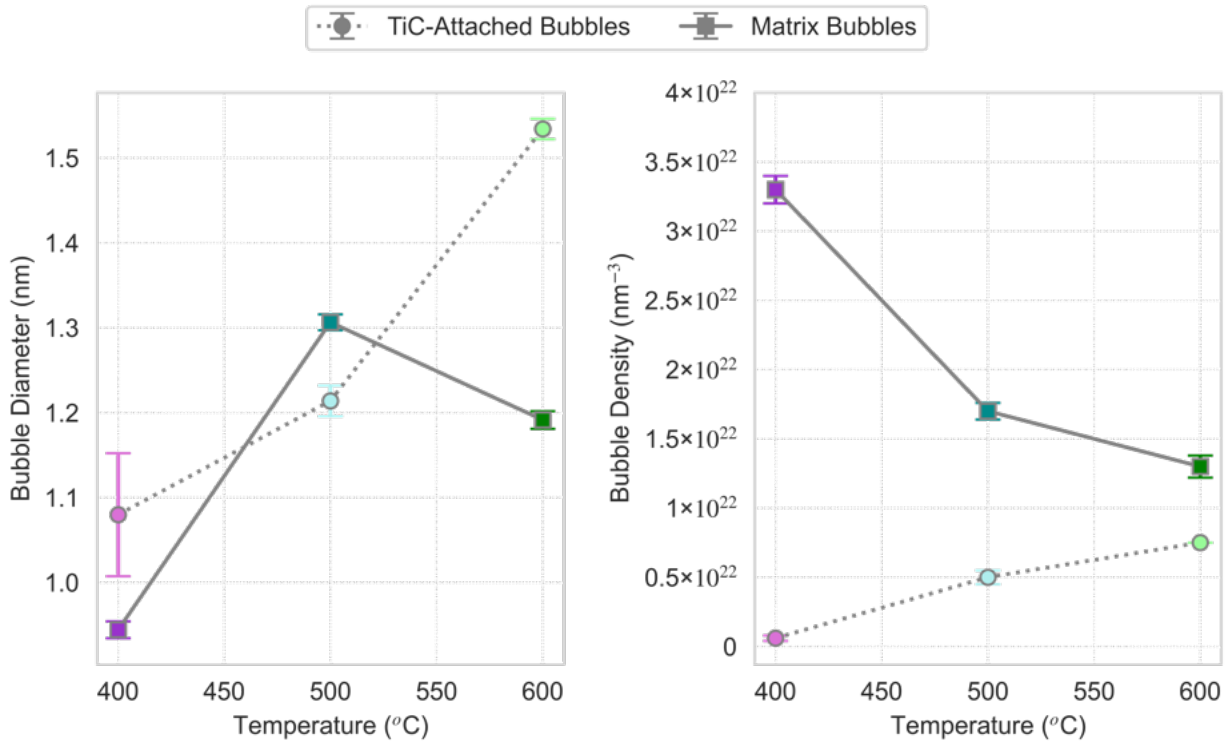

Figure 6.10 (a) Bubble diameter and (b) and bubble density of matrix bubbles (solid lines) and precipitate-attached bubbles (dotted lines) as a function of temperature for dual beam conditions.

6.2.2 Effects of Helium Co-Injection Rate on Helium Sequestration at the TiC-Matrix Interface

Figure 6.11 shows the size distributions of TiC-attached bubbles and matrix cavities in the dual beam conditions at 500°C with $(3.3\times10^{-4}$ dpa/s$)_{TiC}/(7\times10^{-4}$ dpa/s$)_{matrix}$ to $7_{TiC}/15_{matrix}$ dpa with either 10 appm He/dpa or 25 appm He/dpa. The size distributions are nearly exact.

Figure 6.12 shows the grain-to-grain variability of swelling as a function of precipitate density. No clear trend in precipitate number density and swelling could be established. In addition, Figure 6.13 shows the binned cavity density as a function of cavity diameter for both conditions and the distributions are nearly overlapping at all points, except the 25 appm He/dpa condition with went to slightly greater maximum matrix void sizes. As swelling is greatly affected by the size of cavities, this was reflected in the swelling values of the conditions. The swelling from all cavities in the 10 appm He/dpa condition was 0.2±0.01% and in the 25 appm He/dpa condition was 0.3±0.05%. the ratio of precipitate-attached bubbles to the number density of TiC precipitates for the 10 appm He/dpa condition was 5.3±0.4 and in the 25 appm He/dpa condition was 5.6±0.0.3. The fraction of precipitate-attached bubbles to the total bubble count for the 10 appm He/dpa condition was 0.3±0.03 and in the 25 appm He/dpa condition was 0.2±0.0.007. Hence, the TiC precipitates maintained a constant helium sequestration ability at the various helium co-injection rates tested and no significant differences were detected.

To the author's knowledge, no systematic studies on helium rate effects on cavities attached to precipitates have been conducted on MX precipitates in FeCr steels. However, CNA3 was irradiated to 50 dpa at 650°C with 15 appm He/dpa. CNA3 displayed a total cavity density of 5×10^{21} m^{-3}. Approximately 30% of all cavities were associated with the MX precipitates in CNA3 [122]. Approximately 22% and 38% of all cavities in the dual beam irradiations at 500 and 600°C, respectively, with 10 appm He/dpa to $7_{TiC}/15_{matrix}$ dpa were associated with the MX-TiC precipitates in CNA9. Approximately 18% of all cavities in the dual beam irradiations at 500°C with 25 appm He/dpa to $7_{TiC}/15_{matrix}$ dpa were associated with the MX-TiC precipitates in CNA9. This would suggest that temperature has a greater effect on sequestering effects for cavities in the range of 10-25 appm He/dpa of CNAs than the effect from the difference between helium co-

injection rates at 10 and 25 appm He/dpa. In addition, helium implantation studies at 500-800°C to 7500 appm helium showed that MX precipitates in CNA1 and CNA3 sequestered helium in the form of bubbles on their interfaces, but no quantification of precipitate-attached bubbles was given [77,150]. Comparatively, this work studied MX precipitate sequestration ability up to 375 appm helium at 500°C. Thus, it is shown that MX precipitates can sequester up to 7500 appm He in CNAs at elevated temperature, but the efficiency of that sequestration under irradiation is unknown above 375 appm helium.

A few studies on helium rate effects on cavities attached to oxide particles have been conducted in ODS steels. A 14YWT alloy containing oxides of various sizes was implanted to a peak implantation of ~4,000 appm helium at 700°C. Oxides of diameter ~2 nm had one attached bubble per oxide of about the same diameter. Larger oxides of diameter ~6 nm or greater had larger bubble(s) attached, either one or two in number [151]. In PM2000 and 14YW, all voids present in the materials after neutrons irradiation to <20 dpa at 500°C were associated with oxide particles [143]. To better understand these results, Emelyanova *et al.* conducted an ion irradiation study to understand the effects of helium rate on the bubble co-evolution with oxides in ODS EUROFER steel [143]. A 4 MeV Au^{2+} + 10 keV He^{+} dual ion in-situ irradiation to a damage level of ~27 dpa with a helium rate of ~354 appm He/dpa was conducted at 550°C with a damage rate of ~2.4×10^{-3} dpa/s were used. A 10 keV He^{+} single ion ex-situ irradiation was also conducted at 550°C. The damage level achieved was negligible in the ex-situ irradiation (~0.4 dpa), thus providing a significantly different He/dpa ratio than the in-situ irradiation. A one-to-one associated of bubbles with oxides was found in both irradiated samples. It was found in the single ion ex-situ irradiated sample larger oxides were associated with larger cavities, but that the oxide-attached cavities were generally smaller than the host oxides. This was typically the case for the dual ion in-situ irradiated

oxide-cavity pairs as well, though a group of oxides had voids associated with them. Hence, the oxide-attached cavities in the dual ion irradiated specimen displayed a bimodal distribution, just like matrix cavities display in high He/dpa regimes where some bubbles undergo transition to voids. Emelyanova *et al.* hypothesized that the bubble-to-void transition occurred on oxide particles because the helium bubbles on the oxide interface require less helium atoms for the transition to occur as compared to bubbles in the bulk and that the increased effective vacancy supersaturation from the increased damage rate in the dual ion irradiation condition assisted the process. However, only relatively large particles affected the critical gas content in oxide-attached bubbles, leading to the transition. The He/dpa ratio may also affect the onset of the bubble-to-void transition.

Though there are additional considerations that should be taken when interpreting these results, such as the vastly different damage levels between the in-situ and ex-situ irradiations and the viability of comparing in-situ and ex-situ irradiation results one-to-one, some insight can still be drawn for this work from the conclusions reached. One, as previously described, the He/dpa ratios may be too similar in the 10 and 25 appm He/dpa conditions at 500°C to cause any differences in the MX precipitate-attached bubbles, particularly their transition to voids. At a larger He/dpa rate with a high enough vacancy supersaturation, a bubble-to-void transition may occur on MX-TiC precipitates in CNA9. However, MX precipitate-attached bubbles were shown to be more robust against this transition than matrix bubbles with the parameters used in this work. Second, no significant average differences in the values of bubbles sequestered per precipitate were found between the 10 appm He/dpa conditions at 500 and 600°C to $7_{TiC}/15_{matrix}$ dpa, though the average precipitate sizes of precipitates differed. This may suggest that there is a critical precipitate size larger than sizes reached in this work (~35 nm) that when reached under the proper helium and

effective vacancy supersaturation conditions may promote the bubble-to-void transition. Third, the interfacial characteristics of various precipitates, such as surface energy or interfacial dislocations, may affect the critical number of helium atoms needed to promote the bubble-to-void transition. Thus, various kinds of MX precipitates may display different bubbles associations at the same irradiation conditions. This point ties back to the discussion on precipitate stability, where the precipitate interfacial characteristics may also affect the stability of the precipitates under irradiation.

Systematic studies on helium rate effects of matrix cavities have also been conducted that can be referenced. Dual ion irradiation studies of F82H and 14YWT alloys showed that a greater helium co-injection rate resulted in increased volume fraction of matrix cavities after a dose of ~30 dpa (Figure 6.14a) [152]. The matrix cavity effects were described by splitting the effects of helium rates to ranges of ~15-25 appm He/dpa, ~25-35 appm He/dpa, ~35-45 appm He/dpa, and ~45-55 appm He/dpa. Within each range, cavities followed the same trend. However, the effects of helium rates will be dependent on the sink strength of the material: with increasing sink strength, effects on matrix cavities with increasing helium rates become less noticeable (Figure 6.14b) [153]. Bhattacharya and Zinkle presented results for the dependence of swelling on helium rate in irradiated copper and irradiated austenitic stainless steel (Figure 6.15) [10]. A bell curve dependence of swelling on helium rate was found, with maximum swelling occurring at helium rates around ~10-15 appm He/dpa. In CNA9, the rates of 10 and 25 appm He/dpa did not result in any significant differences in matrix cavity sizes or densities at $7_{TiC}/15_{matrix}$ dpa. Hence, it is likely that the helium rates tested in CNA9 are within the same range and same area of the peak of the bell curve dependence and did not probe various helium rate regimes.

It is assumed that the response of MX precipitate-attached cavities in CNA9 will follow the general trend shown in literature for matrix cavities – no differences will be detected at intermediate damage levels between similar helium co-injection rates. It is possible, however, that the helium co-injection rate at which matrix cavities begin to show significant differences in behavior may be different than the critical helium co-injection rate for MX precipitate-attached cavities due to different cavity pressurization, surface energies, and binding of cavities to precipitates versus cavities in the matrix.

Thus far, analysis suggests that the microstructure of FM steels, including the MX precipitates, are robust under helium co-injection ranges relevant to fusion operation under high damage rate heavy ion irradiations. Previously in Section 6.1, it was discussed that precipitate stability may be different in fusion (or advanced fission) reactors versus ion irradiations because of the lower damage rates in reactor. Similarly, the behavior of helium sequestration may be influenced by different combinations of helium rates and damage rates during irradiation. Taller *et al.* showed that helium trapping and repartitioning at various sinks was dependent on damage rate, helium rate, and temperature in Grade 91 steel [142]. However, the saturation of traps other than cavities still occurred in both the reactor irradiated (low damage rate/low helium rate/low temperature) and ion irradiated (high damage rate/intermediate helium rate/high temperature, relative to the reactor irradiation) samples, though the saturation occurred at a higher damage level in the reactor irradiated samples. Thus, it is assumed that various combinations of damage rate, helium rate, and temperature may alter the initial partitioning of helium and point defects to sinks (including to MX precipitates), but that saturation would occur by intermediate to high damage levels. In addition, it was previously shown in Section 6.2.1 that MX precipitates had strong binding with helium bubbles up to 600°C. Thus, it is still expected that MX precipitates will sequester helium and

maintain helium-filled bubbles at their interface in other conditions, though the bubble evolution may differ.

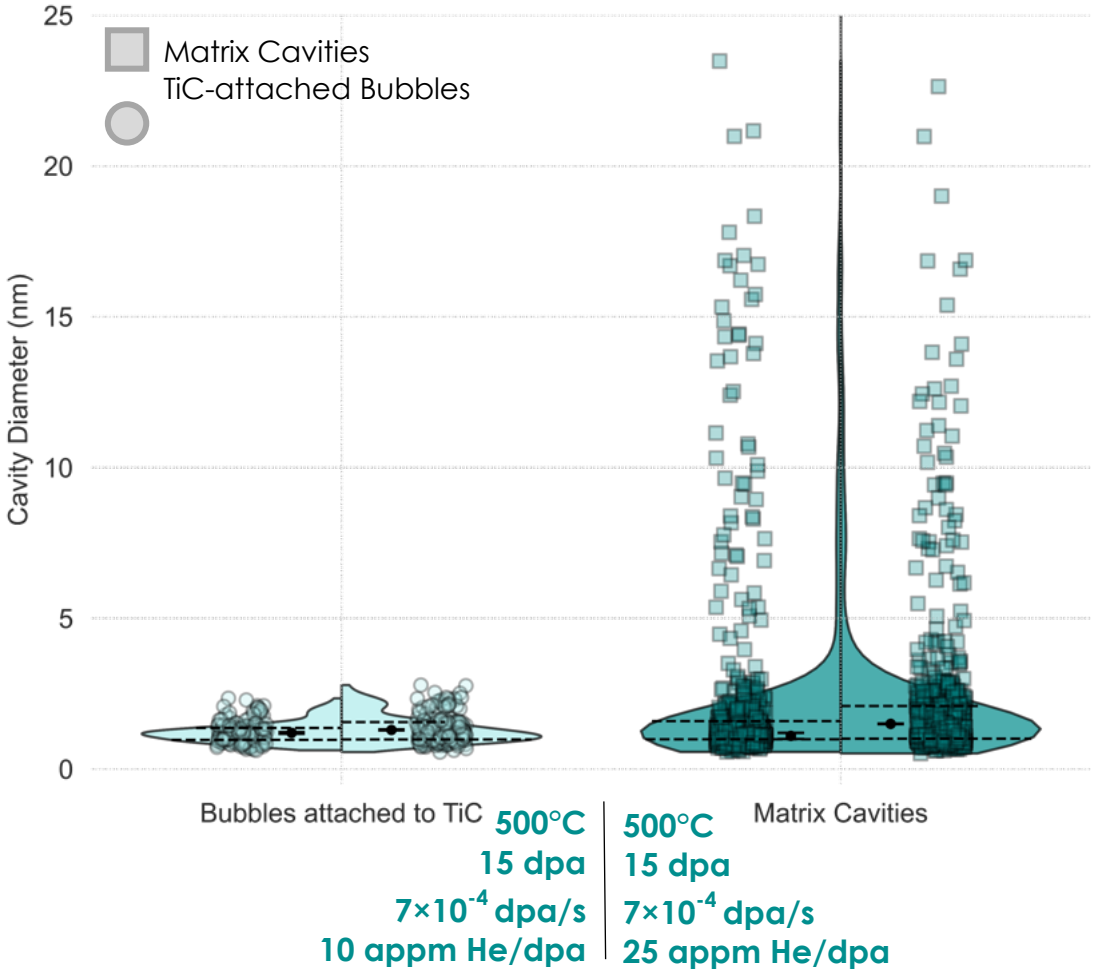

Figure 6.11 Comparison of matrix cavities (square symbols) to precipitate-attached cavities (circle symbols) for the dual beam conditions at 500°C for 10 appm He/dpa (left side of the violin plots) and 25 apppm He/dpa (right side of the violin plots).

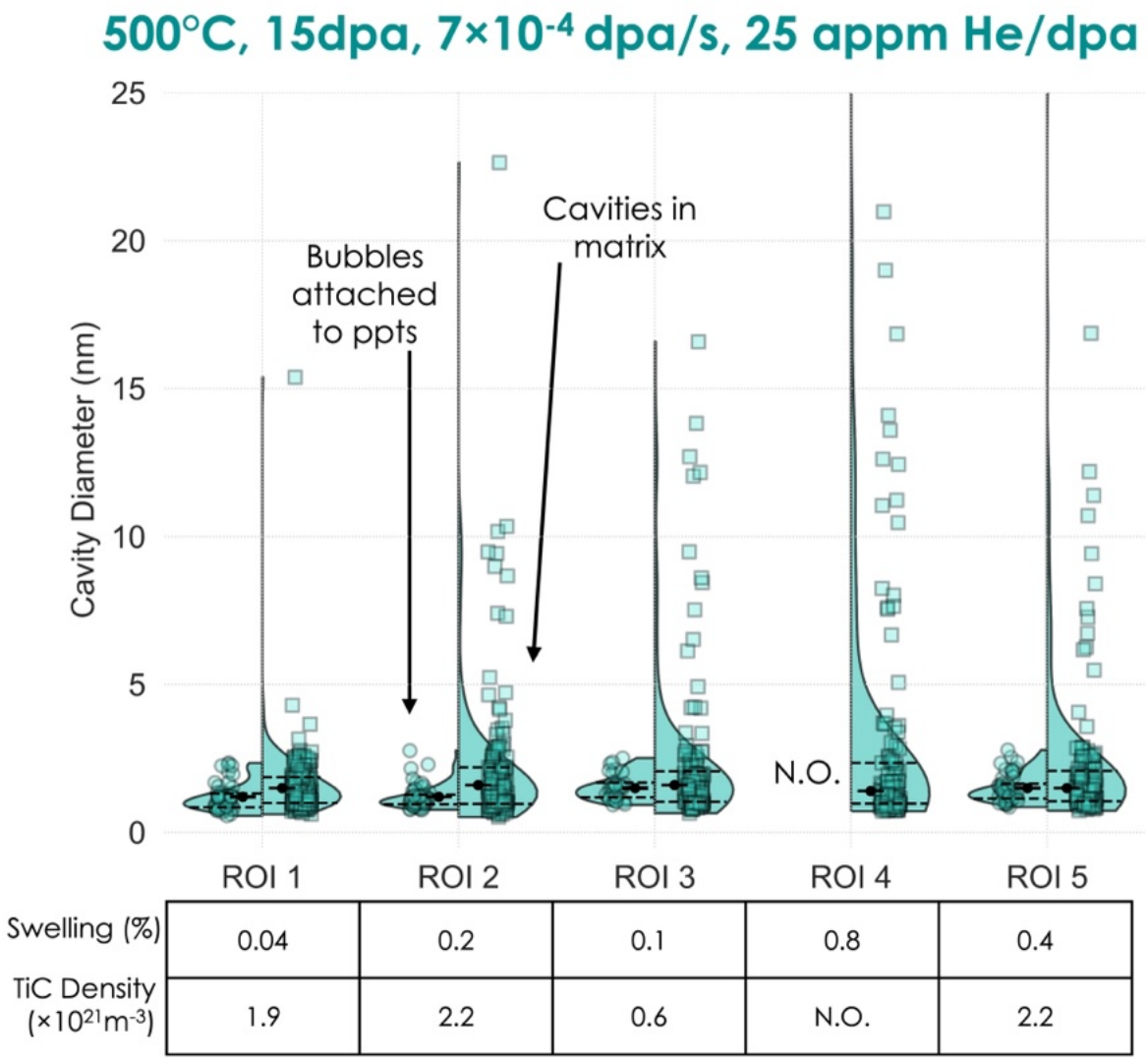

Figure 6.12 Comparison of swelling and precipitate number density in various grains in (500°C-15 dpa-7×10^{-4} dpa/s-10 appm He/dpa)matrix condition. No clear trend was established. The violin plots are normalized by width.

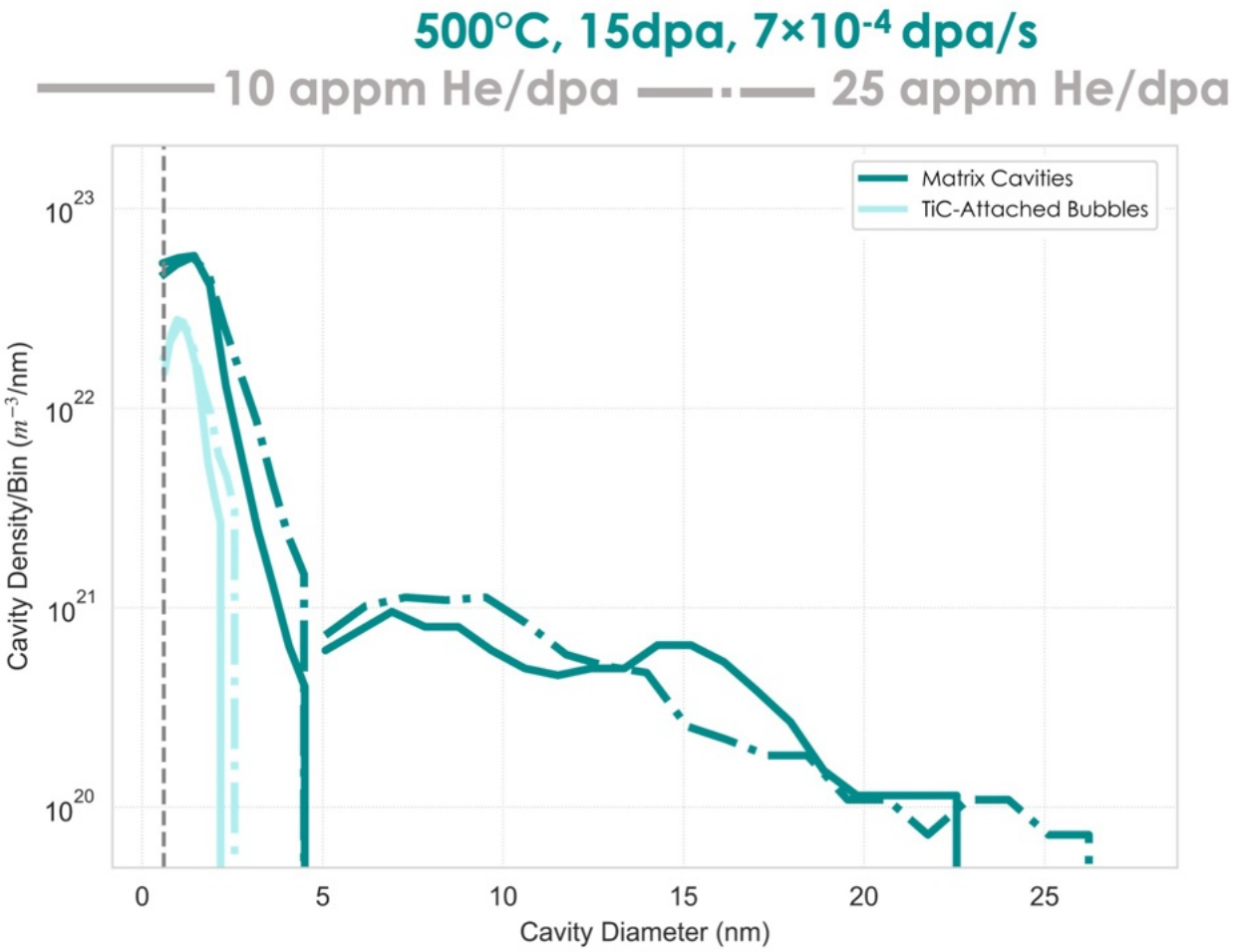

Figure 6.13 Cavity density versus cavity diameter for the 500°C dual beam conditions with 10 appm He/dpa and 25 appm He/dpa.

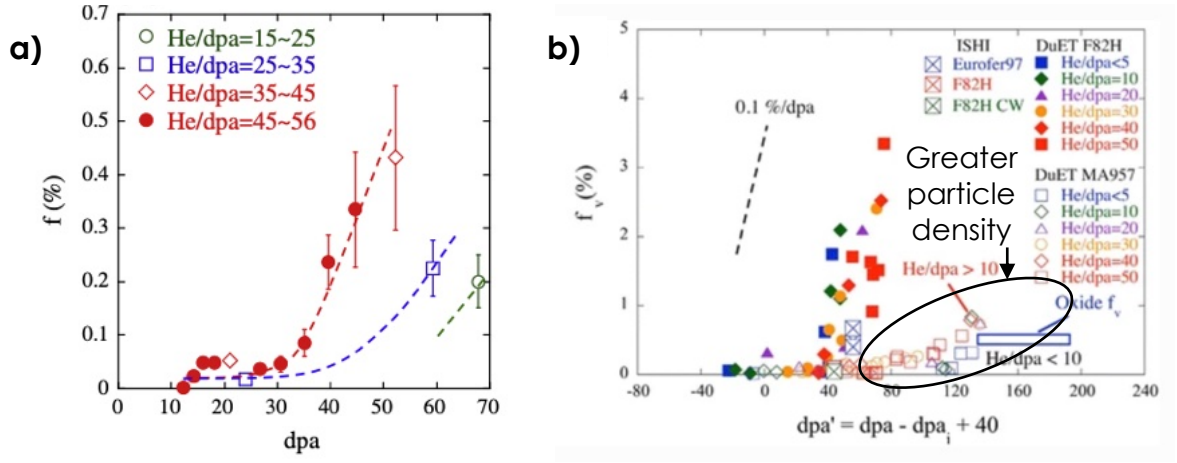

Figure 6.14 (a) The volume fraction of cavities larger than 4 nm as a function of dpa and helium co-injection rate in dual ion irradiated F82H at 500°C. Reproduced from [152]. (b) The volume fraction of cavities in Eurofer97, F82H, and MA957. MA957 contains a high density of oxide particles, with a volume fraction of particles on par with the volume fraction of cavities. Reproduced from [153].

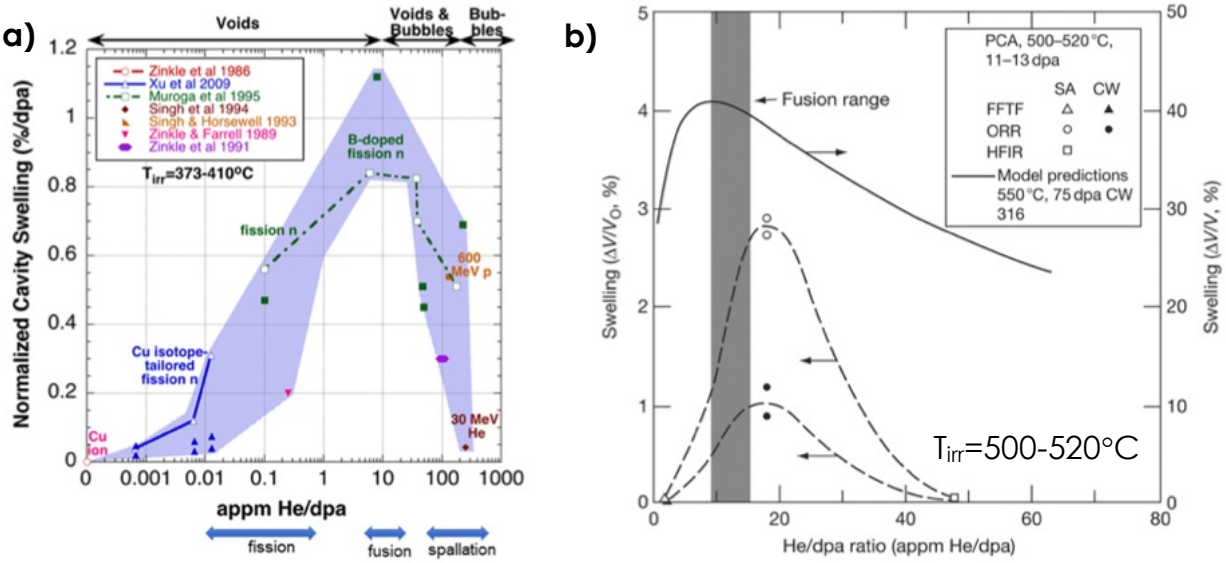

Figure 6.15 Swelling dependence on the He/dpa ratio in (a) irradiated copper (~1-10 dpa) and in (b) austenitic stainless steel. Reproduced from [10].

6.2.3 Effects of Coherency on Helium Sequestration at the TiC-Matrix Interface

Previous experimental research has shown that some types of precipitation in steel have cavities attached to their interfaces that grow larger than the matrix cavities [7,28,43,44], thus

accounting partially or for the majority of void swelling. Mansur has hypothesized that this is because these precipitates act as point defect collection sites for helium and vacancies and serve as fast pathways of diffusion for these defects along the precipitate-matrix interface to aid the accumulation of such defects into large cavities [56] (see Section 2.5.3).

Brailsford and Mansur further expounded upon this by differentiating the effects of coherent and incoherent precipitation on point defection trapping and collection [61]. The coherent interface is defined as a saturable trap, where defects are trapped and then annihilated by the anti-defects. The incoherent interface, on the other hand, is described as an unsaturable trap that acts as a site of enhanced point defect accumulation. Relatedly, the incoherent interface is assumed to be a fast diffusion pathway, like high angle grain boundaries, that serves to channel point defects collected by the interface into extended defects. Though the work underscores the importance of precipitate interfacial character to cavity development, it also concludes that experimental literature does not sufficiently back up the claim that precipitation reduces swelling.

Brailsford and Mansur also postulate that the misfitting dislocations present at semi-coherent precipitate-matrix interfaces may act as fast diffusion paths and lead to enhanced defect growth. Recent work computationally investigated the effects of semi-coherency on point defect collection and concluded that the interfacial misfitting dislocations attract point defects, namely helium, and act as stable storage sites for helium [85,86,134,155]. Shao *et al.* investigated coherency effects of oxide particles in MA956 irradiated with single ion Fe^{2+} irradiation to 60, 120, and 180 peak dpas corresponding to 10^{-3} dpa/s. All voids were found attached to the semi-coherent particle-matrix interfaces. The authors hypothesized this was due to the relatively higher strain energy of the oxides due to their larger size, resulting in point defect collection [156].

This work experimentally investigated the effects of semi-coherency on point defect collection with MX-TiC Precipitation present in CNA9. However, CNA9 also lent a natural experiment in that large, fully incoherent TiC precipitates were also present in the microstructure. By investigating the nature of the precipitate-attached cavity development on the small, semi-coherent MX-TiC precipitates and the large, fully incoherent TiC precipitates, the theorized effects of precipitate size and coherency on cavity growth can be studied.

Figure 6.16 shows the structure and corresponding diffraction pattern of the small MX-TiC precipitates. The small, semi-coherent MX-TiC precipitates have a lattice parameter twice the size of the matrix and an FCC structure that had a cube-on-cube orientation relationship with the matrix. The broad faces of the precipitate are coherent with the matrix and the edges are incoherent or semi-coherent with the matrix. The d-spacings for $d_{\{220\}}^{TiC}$ and $d_{\{110\}}^{matrix}$ were identical but the d-spacing for $d_{\{200\}}^{TiC}$ was found to be twice as large as for that of the $d_{\{200\}}^{matrix}$. Hence, the parallel planes of the $\{200\}_{\text{matrix}}$ and the $\{200\}_{\text{TiC}}$ are the incoherent or semi-coherent interfaces of the TiC nanoprecipitates and the parallel planes of the $\{110\}_{\text{matrix}}$ and the $\{220\}_{\text{TiC}}$ are the coherent interfaces. For a plate-like precipitate like the MX-TiC precipitate, the coherent edges are assumed to induce large coherency strains, but there will not be such strains at the edges [157]. The aspect ratio of the precipitates in the $7_{\text{TiC}}/15_{\text{matrix}}$ dpa and 10 appm He/dpa conditions did not significantly change as compared to the control specimen, and hence it is assumed that the coherency also did not significantly change at this irradiation condition [126]. This is a simplified analysis, and future work could assess the coherency as a function of temperature and irradiation conditions. No difference in size of the attached bubbles on the short or long sides on the precipitate was observed. The misfitting dislocations could have attracted point defects which then diffused to various atomic sites on the precipitate interface and equally grew into spherical helium bubbles. The bubbles

attached to the MX-TiC precipitates can only be assessed at $7_{TiC}/15_{matrix}$ dpa, as they dissolve at some point past this damage level. Future experiments should assess semi-coherent precipitates that are stable up to higher damage levels, or even to ~25 dpa_{matrix}, to see if the semi-coherent interfaces remain as trapping sites for helium or act as sites of enhanced cavity growth. Swelling becomes more important as damage level increases, so MX precipitate's ability to sequester helium is important to high damage levels.

The large TiC precipitates were determined to have a lattice parameter of 16.5Å and an FCC structure (Figure 6.17). Figure 6.18 shows the large non-MX TiC precipitates irradiated to $7_{TiC}/15_{matrix}$, $23_{TiC}/50_{matrix}$, and $47_{TiC}/100_{matrix}$ dpa at 500°C with 10 appm He/dpa. As expected, they remain fully incoherent after irradiation to $47_{TiC}/100_{matrix}$ dpa. The incoherent TiC precipitates remained stable at all conditions tested, unlike the smaller MX-TiC precipitates. They remain stable most likely due to their larger size shielding them from dissolution. Solutes in the precipitate are less likely to ballistically eject from the precipitate and more likely to be displaced within the precipitate at larger precipitate sizes. This translates to a smaller recoil resolution efficiency (Section 6.1.3). As can also be observed, the large TiC precipitates sequester helium at all damage levels in the form of small bubbles. As the damage level increases, so do the number of bubbles attached to the large TiC precipitate-matrix interface. However, the attached bubbles remain small ($\lesssim$1.5 nm in diameter). Instead of serving as sites of enhanced cavity growth as theory has suggested, the interface of these fully incoherent precipitates acted as traps for helium.

This work then suggests that the simplistic view of large, incoherent precipitates as enhanced point defect collection sites needs further modification for FM steels. Large TiC incoherent precipitates, though having a low overall sink strength due to their low density, appear to have a high interfacial sink efficiency that prevents the growth of large cavities on their interfaces [86].

The exact reasons for this rebuttal to previous theory on incoherent precipitation are unknown and warrant further research. One reason may be that though the large TiC incoherent precipitates in CNA9 act as point defect collection sites, the incoherent interface does not act as a fast diffusion pathway for those point defects to accumulate and grow. Another reason may be that the larger lattice parameter of the incoherent TiC precipitates may lend to more efficient helium sequestration in stable orientations (such as platelets) that are precursors to the spherical helium-filled bubbles observed in TEM. The interfacial energy and coherency have complicated interactions that produce the final cavity behavior at the interface, and this result suggests further work is needed.

In addition, Mansur's theory discusses precipitation's effects matrix cavities, but does not differentiate effects on matrix bubbles or voids. Bubbles and voids have different biases for point defects and hence may be affected differently [112]. In addition, taking the mean matrix cavity radius to include both radii from bubbles and voids skews the matrix cavity radius to larger values that are not representative of the bimodal size distribution of cavities. The theory also needs to be updated to account for a bimodal size distribution of cavities.

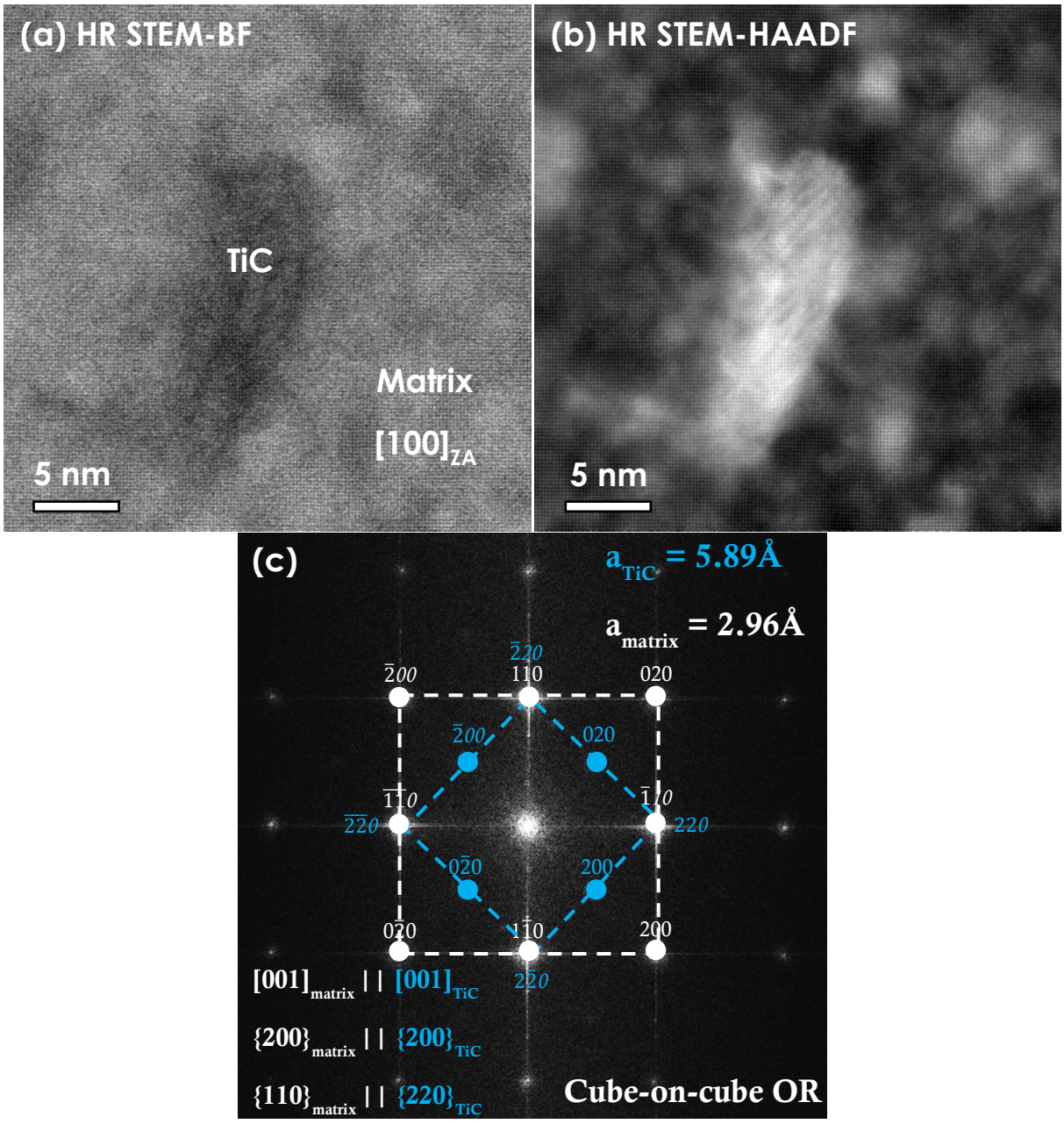

Figure 6.16 (a) HR STEM-BF image, (b) STEM-HAADF image, and (c) the diffraction pattern of a MX-TiC nanoprecipitate from the control specimen of CNA9.

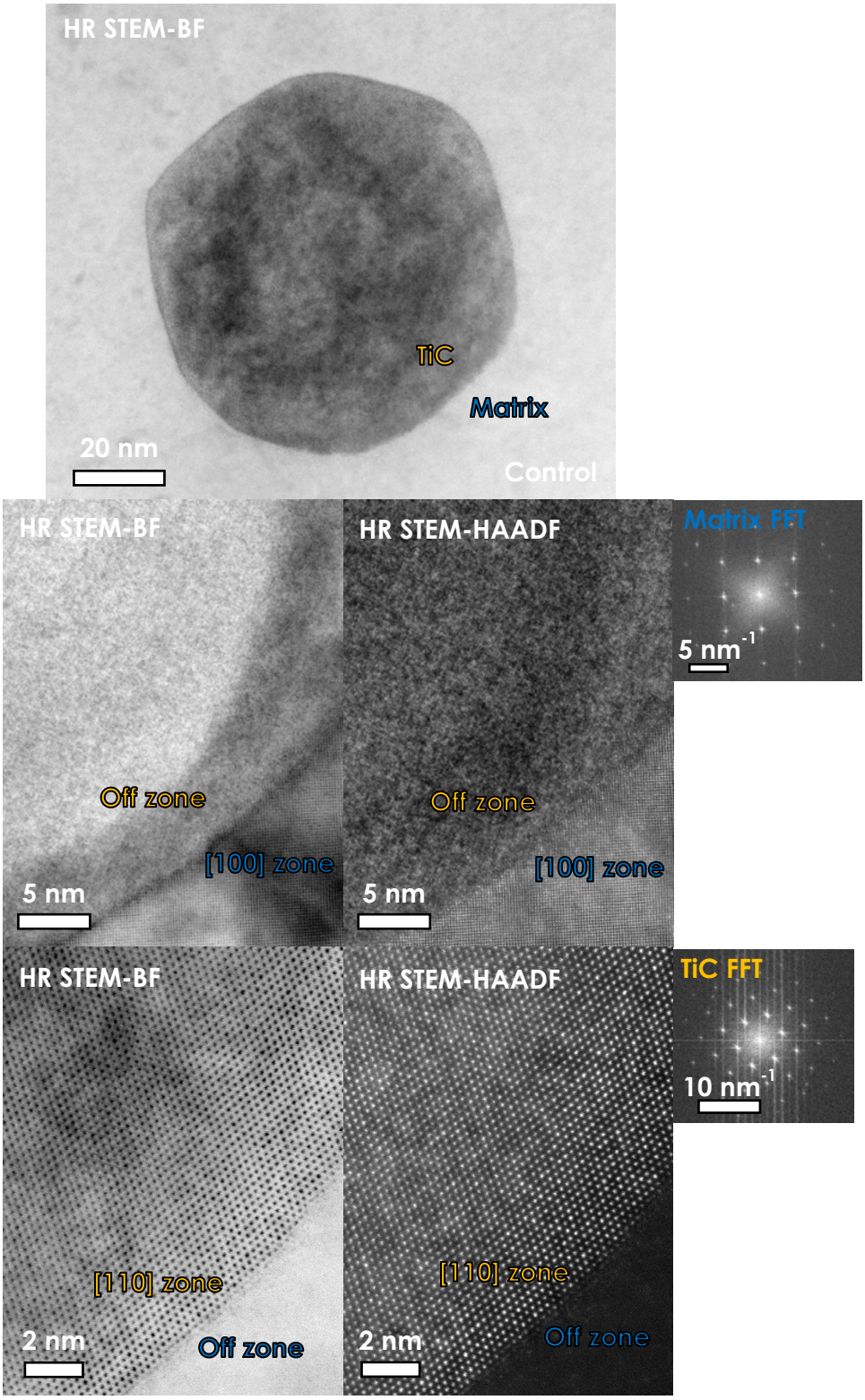

Figure 6.17 HR STEM-BF and -HAADF images with correspoinding diffraction patterns showing the incoherent nature of the large TiC precipitates.

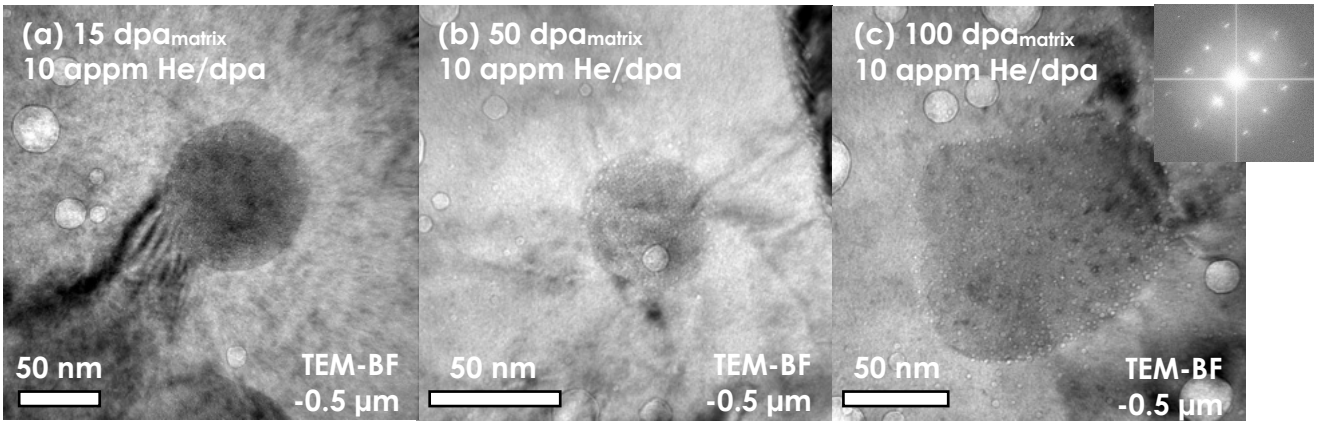

Figure 6.18 Cavities attached to large TiC precipitates at 500°C with 10 appm He/dpa for (a) 15 dpa_{matrix}, (b) 50 dpa_{matrix}, and (c) 100 dpa_{matrix}.

6.2.4 Effects of MX-TiC Precipitation on Swelling

Figure 6.19 shows the comparison of cavities for the dual beam irradiations at 500°C to $7_{TiC}/15_{matrix}$, $23_{TiC}/50_{matrix}$, and $47_{TiC}/100_{matrix}$ dpa with 10 appm He/dpa and $(3.3\times10^{-4}$ dpa/s$)_{TiC}/(7\times10^{-4}$ dpa/s$)_{matrix}$. This figure shows that the bubbles distribution was mostly unchanged by increasing damage level, but that the matrix cavities grew to larger sizes with increasing damage level which led to greater swelling. The swelling data for these conditions as well as for the (500°C-7 dpa-3.3×10^{-4} dpa/s-25 appm He/dpa)$_{TiC}$ /(500°C-15 dpa-7×10^{-4} dpa/s-25 appm He/dpa)$_{matrix}$ condition is shown along swelling data from literature for FeCr steel alloys, including RAFM steels and Grade 91, in Figure 6.20. All dpa values are considered for the matrix. Numerical data for literature values shown in Figure 6.20 are tabulated in Table 6.6.

Dual and triple ion beam irradiations produced greater amounts of swelling than single ion beam irradiations. The model Fe-9Cr alloy swelled more at 50 dpa than the other steels, regardless of irradiation type. Dual ion irradiated CNA3 and CNA9 had similar swelling values at 50 dpa, despite differences in irradiation temperature. CNA9 remained on the lower end of swelling as

compared to the other alloys by 50 dpa, and from 50 to 100 dpa displayed a swelling rate of 0.03%/dpa. This value is higher than observed for neutron irradiated Grade 91 steel (~ 0.01%/dpa), but lower than JLF-1 steel that underwent dual ion irradiation. It is also lower than the generally accepted post-transient steady-state swelling in neutron irradiated FM steels of 0.2%/dpa [158]. Overall, CNA9 displays similar swelling behavior to traditional FM steels and RAFM steels based on the limited swelling data of CNA9. CNA9 had a swelling value of ~0.2% at both 15 and 50 dpa_{matrix}, and a swelling value of ~2% at 100 dpa_{matrix}.

CNA9 remained in the incubation and transient regimes at a damage level of $23_{TiC}/50_{matrix}$ dpa, even though the MX-TiC precipitates had dissolved. The dissolution of the precipitates before $23_{TiC}/50_{matrix}$ dpa does not appear to have triggered steady-state swelling at this damage level in CNA9. This may be because the precipitates represent only a miniscule fraction of the total sink strength of CNA9. For example, the condition at $7_{TiC}/15_{matrix}$ dpa at 500°C with 10 appm He/dpa, the MX precipitates only represent ~5% of the entire sink strength (Table 4.8). Xiu showed that the steady-state swelling changes as a function of the sink strength of the material, both the onset of steady-state swelling and the steady-state swelling rate [159]. Xiu's work used the same ion irradiation facility and the same damage rate used in this study of 7×10^{-4} dpa/s_{matrix} Data points from Ref. [159] for three HT9 materials are shown in the Figure 6.20 (orange lines). The HT9 materials had different processing histories which led to different starting sink strengths and hence different sink strengths under irradiation. At 100 dpa, ASB-HT9 had a sink strength of ~1.1×10^{16} m^{-2} and swelling rate of 0.002%/dpa (though ASB-HT9 was most likely still in the incubation and transient regime), FCRD-HT9 had a sink strength of ~7.1×10^{15} m^{-2} and swelling rate of 0.003%/dpa, and ACO3-HT9 had a sink strength of ~6.3×10^{15} m^{-2} and swelling rate of 0.02%/dpa. Hence, a greater sink strength was shown to translate to lengthened onset to steady-state swelling

and smaller swelling rate values. As the precipitates in CNA9 represent such a small fraction of the overall sink strength than this, their dissolution is assumed to not significantly affect the overall sink strength of CNA9 and does not alter the cavity development with increasing damage level. However, this analysis is based on only three data points for CNA9, and a finer resolution of damage levels would be needed for a full assessment. In addition, it is possible that the precipitates dissolved close to 50 dpa_{matrix} and hence there was not enough time for the onset of steady-state swelling to begin and be observed in the 50dpa_{matrix} condition.

Another assessment of the effect of MX precipitate density on sink strength was completed. Ref. [160] suggests that a dramatic reduction in void swelling for fission reactors occurs when the average spacing between matrix cavities is greater than 10 × the average spacing between defect sinks. The average spacing between defect sinks is calculated as one over the square root of the total sink strength and represents the mean distance a free defect travels before becoming trapped. This analysis was carried out for the (500°C-7 dpa-3.3×10^{-4} dpa/s-10 appm He/dpa)$_{TiC}$ /(500°C-15 dpa-7×10^{-4} dpa/s-10 appm He/dpa)$_{matrix}$ condition and is shown in

Table 6.7. The analysis was conducted using three different values for precipitate number density: no precipitates, the density observed experimentally, and an ultra-high density of 10^{24} m^{-3} [11,12]. The calculated average spacing between matrix cavities is 5-7 × less than 10× the average spacing calculated with conditions of no precipitate density and the experimentally observed

density. There are no significant differences between these precipitate number densities on the average spacing between defect sinks. This suggests that precipitates present experimentally are not enough to suppress void swelling. However, if the average spacing between defect sinks was calculated using an ultra-high number density of 10^{24} m^{-3} MX precipitates, then the calculated average spacing between matrix cavities is on par with 10× the average spacing between defect sinks (

Table 6.7).

As can be seen, sink strength is greatly tied to swelling. As FM steels have a high overall sink strength, precipitates are theorized to only significantly affect swelling (either through a lengthened transient regime or a slower rate of steady-state swelling) if they represent a large percentage of the overall sink strength (~50%). This analysis suggests that for fusion reactors, a greater sink strength derived from precipitates is needed versus what is needed for fission reactors. This analysis is similar to that conducted in Ref. [77], which suggested that a sink strength of ~10^{16} m^{-2} derived from precipitates is needed for optimal resistance to swelling in extreme conditions. A shortcoming of this analysis is that the matrix bubble density was unchanging as the precipitate density was changed. Importantly, these precipitates would need to remain stable to damage levels above 100 dpa in order to provide swelling resistance during the lifetime of the fusion power plant, and the MX-TiC precipitates were shown to dissolve before that point.

The prior simple analysis has showed that an ultra-high density of 10^{24} m^{-3} precipitates is optimal to suppress swelling. However, one more value should be calculated to understand the full effect of precipitates on swelling. Mansur also theorized that the swelling rate of materials under irradiation could be calculated as the ratio of the sink strength of dislocations to that of cavities:

$$Q = \frac{k_d^2}{k_c^2} \quad \text{Eq. 6.17}$$

As pointed out in Ref. [159], this analysis does not consider other important microstructural features, such as precipitates and grains boundaries, nor does it differentiate between the interstitial-biased bubbles and the neutral-biased voids. Hence, the Q value was calculated as the ratio of the total interstitial sink strength to the total vacancy sink strength:

$$Q = \frac{k_i^2}{k_v^2} \quad \text{Eq. 6.18}$$

The Q value was calculated for the hypothetical condition of an ultra-high precipitate density of 10^{24} m^{-3} assuming the precipitates have no bias, have a 10% bias for interstitials, and assuming the precipitates have a 10% bias for vacancies. The results are shown in

Table 6.8. Mansur hypothesized that a Q value of ~1, when biased and neutral sink strengths are approximately equal, results in the maximum swelling. A Q value less than or greater than 1 results in less swelling due to the reduction in the super saturation of vacancies in the matrix. A Q value of 1 is achieved when the ultra-high density of precipitates was assumed to be neutral sinks, but a Q value deviating from 1 is achieved when the precipitates are biased toward interstitials or vacancies. This analysis is simply to show that designing a high amount of precipitates to occur in a material may not be enough to limit swelling. Rather, the interface itself may need to be

engineered in order to maintain a particular flow of point defects. The bias of precipitates is an important factor. It may be possible to have a lower density of precipitates that have a high bias and hence effectively separate helium from vacancies and prevent their evolution into voids. Ultimately, the lowered concentration of freely migrating helium and vacancies and the disparate partitioning of helium and vacancies to different sinks are desired.

This section has concluded that the MX-TiC precipitates in CNA9 were not present in high enough density to prevent matrix swelling at intermediate damage levels at the peak swelling temperature assessed for fusion-relevant helium co-injection rates. The precipitates were not able to capture all of the freely migrating helium and prevent their agglomeration together and with vacancies in the matrix. However, the MX-TiC precipitates may be able to prevent unconstrained matrix swelling in advanced fission reactor relevant conditions. Advanced fission reactor operation will cause a helium generation rate of about 0.2 appm He/dpa, though Taller found that a helium co-injection rate of ~4 appm He/dpa (using the same ion irradiation facility and the same damage rate used in this study of 7×10^{-4} dpa/s_{matrix}) was needed in ion irradiated Grade 91 steel to simulate the matrix cavity behavior observed in neutron irradiated Grade 91 [142]. In advanced fission-relevant ion irradiation conditions with ~4 appm He/dpa, the MX-TiC precipitates in CNA9 may be able to sequester enough helium at their interfaces to lower the overall free helium concentration in the matrix, preventing the association of helium and vacancies together that leads to matrix cavity growth. Hence, the MX precipitates in CNA9 may play a key role for mitigating swelling at lower helium rates. Section 6.2.2 discussed the possible effects of different helium rates and damage rates in more detail.

Table 6.6 Literature data shown in Figure 6.20 for swelling behavior in FeCr FM alloys under various irradiation conditions.

Ref.	Material	Type	Swelling	Damage and Implantation Rates	Temperature (°C)	Damage Level (dpa)
[161]	F82H	Dual Ion 10.5 MeV Fe^{3+} 1.05 MeV He^{+}	470°C: 0.1% 510°C: 0.05%	1.6×10^{-3} dpa/s 18 appm He/dpa 70 appm H/dpa	470 510	50
	F82H	Triple Ion 10.5 MeV Fe^{3+} 1.05 MeV He^{+} 0.38 MeV H^{+}	470°C: 3.2% 510°C: 0.14%			
[74]	F82H	Single Ion 5 MeV Fe^{2+}	0%	1×10^{-3} dpa/s 10 appm He/dpa 40 appm H/dpa	500	50
	F82H	Dual Ion 5 MeV Fe^{2+} 2.85 MeV He^{2+}	0.7%			
	F82H	Dual Ion 5 MeV Fe^{2+} 0.4 MeV H^{+}	0.04%			
	F82H	Triple Ion 5 MeV Fe^{2+} 2.85 MeV He^{2+} 0.4 MeV H^{+}	0.9%			
[162]	F82H	Reactor FFTF	0.1%		430	67
[163]	F82H	Reactor HFIR	0.52%	1.1×10^{23} n/cm^2 0.5 appm He/dpa	400	51
	F82H	Reactor HFIR+^{10}B	1.1%	1.1×10^{23} n/cm^2 6.5 appm He/dpa		
	F82H	Reactor HFIR+^{58}Ni	0.002%	1.1×10^{23} n/cm^2 9.9 appm He/dpa		
[74]	Fe8Cr2W	Single Ion 5 MeV Fe^{2+}	0.19%	1×10^{-3} dpa/s 10 appm He/dpa 40 appm H/dpa	500	50
	Fe8Cr2W	Dual Ion 5 MeV Fe^{2+} 2.85 MeV He^{2+}	0.69%			
	Fe8Cr2W	Dual Ion 5 MeV Fe^{2+} 0.4 MeV H^{+}	1.04%			
	Fe8Cr2W	Triple Ion 5 MeV Fe^{2+} 2.85 MeV He^{2+}	2.62%			

		0.4 MeV H^+				
[164]	Fe-9Cr	Single Ion 10.5 MeV Fe^{3+}	510°C: 0.5%	1.6×10^{-3} dpa/s 10 appm He/dpa 40 appm H/dpa	470 510	50
		Dual Ion 10.5 MeV Fe^{3+} 1.05 MeV He^+	510°C: 0.1%			
		Dual Ion 10.5 MeV Fe^{3+} 0.38 MeV H^+	510°C: 5%			
		Triple Ion 10.5 MeV Fe^{3+} 1.05 MeV He^+ 0.38 MeV H^+	510°C: %			
[165]	JLF-1 (9Cr– 2.0W– V,Ta)	Single Ion 6.4 MeV Fe^{3+} 1.0 MeV He^+	40: 0.3% 50: 1.5% 62: 3.2% 79: 2.3%	1×10^{-3} dpa/s 15 appm He/dpa	470	40-79
[74]	CNA3	Single Ion 5 MeV Fe^{2+}	0.02%	1×10^{-3} dpa/s 10 appm He/dpa 40 appm H/dpa	500	50
		Dual Ion 5 MeV Fe^{2+} 2.85 MeV He^{2+}	0.5%			
		Dual Ion 5 MeV Fe^{2+} 0.4 MeV H^+	0%			
		Triple Ion 5 MeV Fe^{2+} 2.85 MeV He^{2+} 0.4 MeV H^+	1.6%			
[75]	CNA3	Dual Ion 6.4 MeV Fe^{2+} He	N.R.	5.2×10^{20} Fe^{3+}/ m^2 15 appm He/dpa	650	50
[10]	Grade 91	Reactor	35: 0.5% 185: 1.6% 205: 1.8% 210: 1.9% 210: 2.0% 210: 2.5% 210: 2.6%		400-420	
[10]	Grade 91	Dual Ion 5 MeV Fe^{2+} 3.42 MeV He^{2+}	0.004%	7×10^{-4} dpa/s 4 appm He/dpa	480	16.6
[159]	ASB- HT9	Dual Ion 5 MeV Fe^{2+}	16.6: 0% 50: 0%	5.8×10^{-4} dpa/s 4 appm He/dpa	445	16.6 50

		3.42 MeV He^{2+}	75: 0% 100: 0.01% 150: 0.11% 250: 0.15%			75 100 150 250
	FCRD-HT9		16.6: 0.01% 50: 0.15% 75: 0.08% 100: 0.51% 150: 0.64% 250: 0.74%			
	ACO3-HT9		16.6: 0.07% 50:0.48 % 75: 0.25% 100: 0.40% 150: 1.54% 250: 4.51%			

Table 6.7 The relationship between sink strength of precipitates, overall sink strength of CNA9, cavity development, and average distance travelled by defects.

Condition	Experimental average spacing between cavities in the matrix ($\boldsymbol{\rho_{cav}^{-1/3}}$)	ρ_{MX}	$\boldsymbol{k_{MX}^2}$	$\boldsymbol{k_{tot}^2}$	Percentage of sink strength from precipitates	$\boldsymbol{10 \times k_{tot}^{-1}}$
Simulated values for MX Precipitates	38.8 nm	0	0	1.4×10^{15} m^{-2}	0%	264 nm
Experimental values for MX Precipitates		1.8×10^{21} m^{-3}	8.5×10^{13} m^{-2}	1.7×10^{15} m^{-2}	5%	243 nm
Simulated values for MX Precipitates		10^{24} m^{-3}	4.8×10^{16} m^{-2}	1.0×10^{17} m^{-2}	48%	31 nm

Table 6.8 Relationship between neutral and biased sinks on swelling behavior as a function of three different precipitate number density.

Simulated – 10^{24} m^{-3} of MX Precipitates, No Bias			Simulated – 10^{24} m^{-3} of MX Precipitates, Interstitial Bias of 10%			Simulated – 10^{24} m^{-3} of MX Precipitates, Vacancy Bias of 10%		
k_{is}^{-1} (nm)	k_{vs}^{-1} (nm)	Q = k_{is}^2/k_{vs}^2	k_{is}^{-1} (nm)	k_{vs}^{-1} (nm)	Q = k_{is}^2/k_{vs}^2	k_{is}^{-1} (nm)	k_{vs}^{-1} (nm)	Q = k_{is}^2/k_{vs}^2
4.4±0.03	4.4±0.03	1.0±0.00008	4.2±0.03	4.4±0.03	1.1±0.001	4.4±0.03	4.2±0.03	0.9±0.001

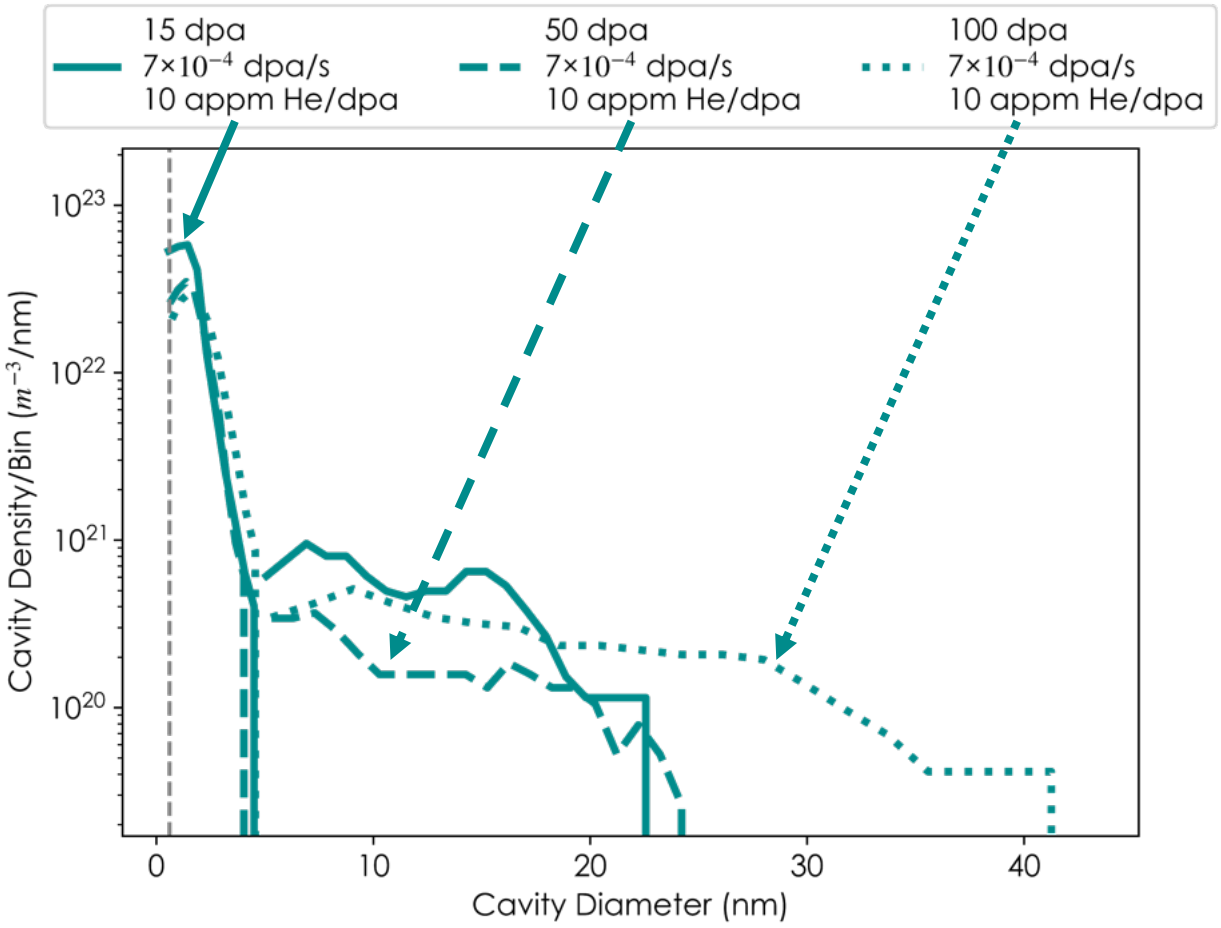

Figure 6.19 Cavity density versus cavity diameter for the 500°C dual beam conditions with 10 appm He/dpa at (a) 15 dpa_{matrix}, (b) 50 dpa_{matrix}, and (c) 100 dpa_{matrix}.

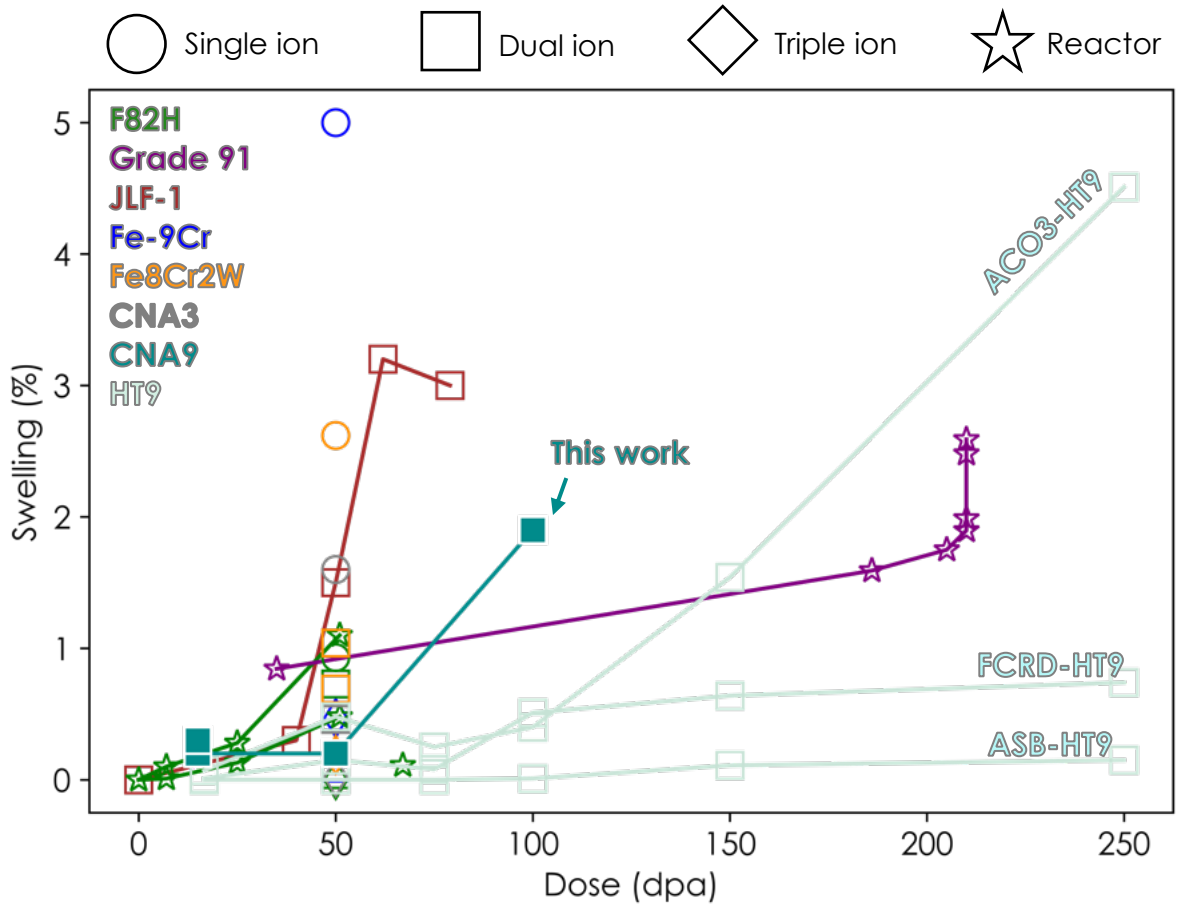

Figure 6.20 Comparison of swelling as a function of damage level (dpa) for FM and RAFM steels, including CNA9 irradiated in this work. See Table 6.6 for references. Adapted from Ref. [12].

6.2.5 Summary of the Results of the Engineering Objective

The engineering objective outlined in Chapter 3 sought to determine if the following hypothesis was correct:

Precipitates will sequester helium atoms during irradiations with co-injected helium in the form of individual nano-scale bubbles on the precipitate-matrix interface as a function of temperature, coherency, and level of helium co-implantation. However, the relatively low density of pre-existing TiC precipitates is hypothesized to not prevent the overall un-constrained helium-driven swelling in the matrix.

It was found that precipitates effectively sequestered helium in the form of nanoscale helium-filled bubbles at 500 and 600°C but not at 400°C, most likely due to the diffusion of helium being too low at 400°C for helium to migrate to the precipitate-matrix interfaces. It was also found that both the semi-coherent MX-TiC precipitates and the incoherent TiC sequestered nanoscale helium-filled bubbles, though the exact reasons why the different interfaces displayed similar behavior could not be determined and warrants further work. Further experimental work is also needed to assess if the misfitting dislocations at the interface of the precipitates are serving as helium sequestration sites. Additionally, it was found that the two helium co-injection rates assessed did not caused any significant different in the precipitates' ability to sequester helium. Most likely this was because the helium co-injection rates used were too similar to warrant different responses.

Importantly, the hypothesis that the relatively low density of pre-existing TiC precipitates will not prevent the overall un-constrained helium-driven swelling in the matrix was also proven correct. The precipitates also dissolved at intermediate damage level and hence could not provide any sites for helium trapping to high damage levels.

Chapter 7 Conclusions and Future Work

The following conclusions have been reached in this work:

Radiation-enhanced diffusion is the dominant mechanism affecting MX-TiC precipitate stability at elevated temperatures and intermediate damage level ($7_{TiC}/15_{matrix}$ dpa), while ballistic dissolution is dominant at low temperatures and intermediate damage level. Radiation-enhanced diffusion led to precipitate coarsening at elevated temperatures before ballistic dissolution became the dominant mechanism at higher damage levels.

Ballistic dissolution is the dominant mechanism affecting MX-TiC precipitate stability at high damage levels ($\geq 23_{TiC}/50_{matrix}$ dpa), no matter the temperature or damage rate tested. The dissolution of precipitates was theorized to occur from a complicated combination of effects such as the back diffusion of solutes, precipitate interparticle spacing, precipitate coherency and interfacial dislocation structure, and solute concentration gradients at the precipitate-matrix interfaces. It is unknown if the MX-TiC precipitate dissolution under irradiation will also occur with other types of MX precipitates in FM steels, such as VN precipitates. This is because morphology and composition differences of the precipitates will alter interfacial characteristics such as interfacial energy and misfitting dislocation structures, lattice strains, coarsening rates, solute recoil distances, interparticle spacing, binding between the constituent atoms of the precipitate, and solute solubility limits under irradiation. Future work could focus on narrowing down the most important effects on the stability of various MX precipitates.

Helium co-injection influenced the precipitate size evolution when diffusion-assisted growth of precipitates was on par with or more significant than ballistic dissolution during single beam irradiation at the same conditions. Thus, helium co-injection caused a reduction in radiation-enhanced precipitate growth at elevated temperatures and intermediate damage level by suppressing radiation-enhanced diffusion but had no effect at low temperatures. Further modelling work is necessary, though, to understand exactly how helium is binding with solutes, interstitials, and vacancies in FeCr steels with MX precipitates.

The mechanistic roles of ballistic dissolution and radiation-enhanced diffusion were mapped out with accuracy at using the recoil resolution model of precipitate stability under irradiation. Further modeling studies are needed to accurately predict precipitate coarsening and dissolution under irradiation. Experimental studies on semi-coherent precipitates in model alloy systems could also occur simultaneously with modelling studies to inform models on why precipitates dissolve under irradiation. Future work could also assess precipitate behavior as a function of other variables in the model, such as precipitate interfacial energy effects on dissolution and coarsening.

The co-injection of helium is not needed to ascertain the complete dissolution of precipitates under high dose and high dose rate ion irradiation conditions. Helium co-injection had no effect on the complete precipitate dissolution or on precipitate number density. As the stability of the MX precipitates are paramount to the properties of structural materials for fusion plants, their complete dissolution is the important factor to understand. However, future work is needed to understand if helium affects the onset of precipitate dissolution in high sink strength FM steels and if helium and hydrogen have combined effects on precipitate stability. In addition, the precipitates in neutron irradiated CNA9 should be characterized and compared to this work to

better understand the differences in precipitate stability under ion versus neutron irradiation. Importantly, this work also did not assess the stability of nanoprecipitates under creep, fatigue, or cycling conditions. Such work should be conducted as these environmental factors may have significant influences on precipitate behavior.

Semi-coherent MX-TiC precipitates can act to effectively sequester helium in FM steels before their dissolution during irradiation at the peak swelling temperature at fusion relevant ion irradiations conditions. MX-TiC precipitates in CNA9 were found to sequester ~5 helium-filled bubbles per precipitate at peak swelling temperature with 10 and 25 appm He/dpa before their dissolution. The precipitate-attached bubbles remained smaller than the critical bubble radius, proving the MX precipitates to elongate the incubation and transient regime of swelling for the precipitate-attached cavities versus the matrix cavities. However, future work could focus on similar precipitates that remain stable to higher damage levels in order to understand if MX precipitates are able to effectively sequester helium to high damage levels.

Large, incoherent TiC precipitates were found to have a high sink efficiency. These precipitates sequestered large amounts of helium in the form of nanoscale bubbles that remained smaller than the critical bubbles radius. Hence, the theory that large and incoherent precipitates are sites for enhanced cavity growth is incomplete. Future work is needed to understand what governs the nucleation and growth of precipitate-attached cavities in complex FM steels. The diffusion of helium on the precipitate-matrix interface, the ability of the lattice of the precipitate to accommodate irradiation-induced point defects, and the interfacial characteristics including interfacial energy and misfitting dislocation arrays are expected to impact the sink efficiency of the precipitation and cavity development on the precipitate-matrix interface.

The MX-TiC precipitates did not affect the overall swelling behavior of CNA9 due to their low sink strength derived from a low number density of ~10^{21} m^{-3}. To lengthen the onset of steady-state swelling and to decrease the steady-state swelling rate, an ultra-high density of precipitates ~10^{24} m^{-3} is needed for future RAFM steels for fusion applications. Future work should be conducted to understand if such a high density of precipitates is feasible to create with traditional manufacturing methods and what consequences such a high density of precipitates may have on the hardening and creep behavior of the steel. In addition, engineering a high density of precipitates that remain stable to high damage levels is key to garnering the benefits of nanoprecipitation for helium mitigation during the lifetime of a fusion power plant.

Appendices

Appendix A: $M_{23}C_6$ Precipitates in CNA8 and CNA9

Due to having twice the amount of carbon, CNA8 contained $M_{23}C_6$ precipitation whereas CNA9 did not. Appendix Figure A.1 shows SEM micrographs and STEM-EDS composition maps from Oak Ridge National Laboratory [38]. No $M_{23}C_6$ precipitates are present in CNA9.

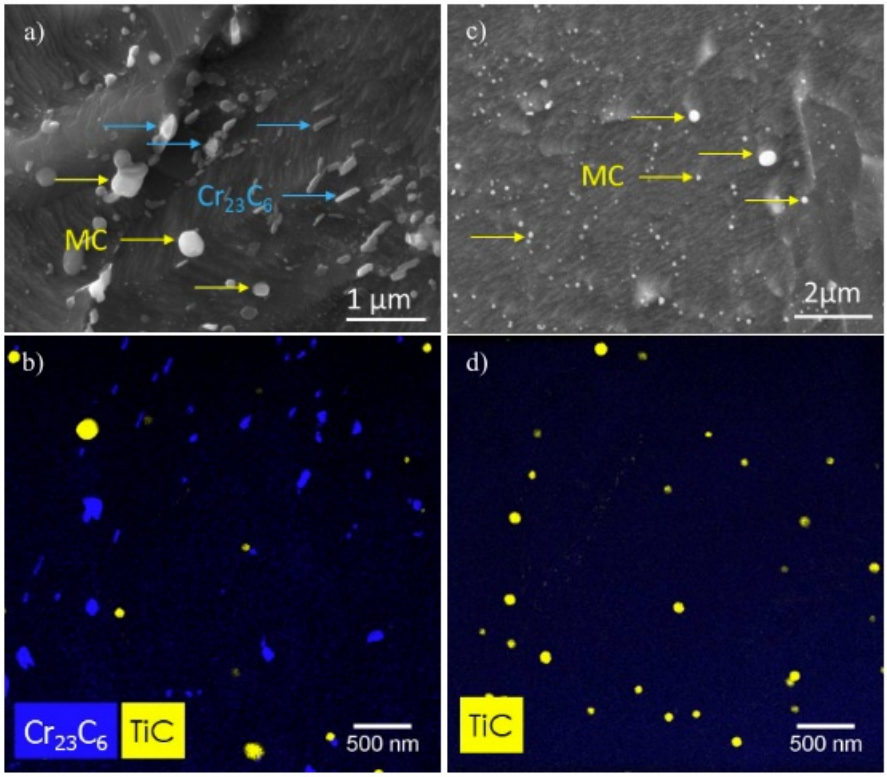

Appendix Figure A.1 SEM micrographs in (a) CNA8 and (c) CNA9. STEM-EDS composition maps of (b) CNA8 and (d) CNA9.

Appendix B: Ex-Situ Irradiation Data

Section 4.2 described the irradiation parameters that were measured during experiments and how they were measured. Chamber pressure history, thermocouple (TC) history, and Fe^{3+} stage current histories for single beam irradiations are shown in Appendix Figure B.1. Chamber pressure history, thermocouple (TC) history, Fe^{3+} stage current, and He^{2+} stage current histories for dual beam irradiations are shown in Appendix Figure B.2. Refer Table 4.3 to for the irradiation parameters for each experiment. Data for irradiations C6 and C8 are not shown because these irradiations were conducted by another person and data could not be recovered at the time of reporting.

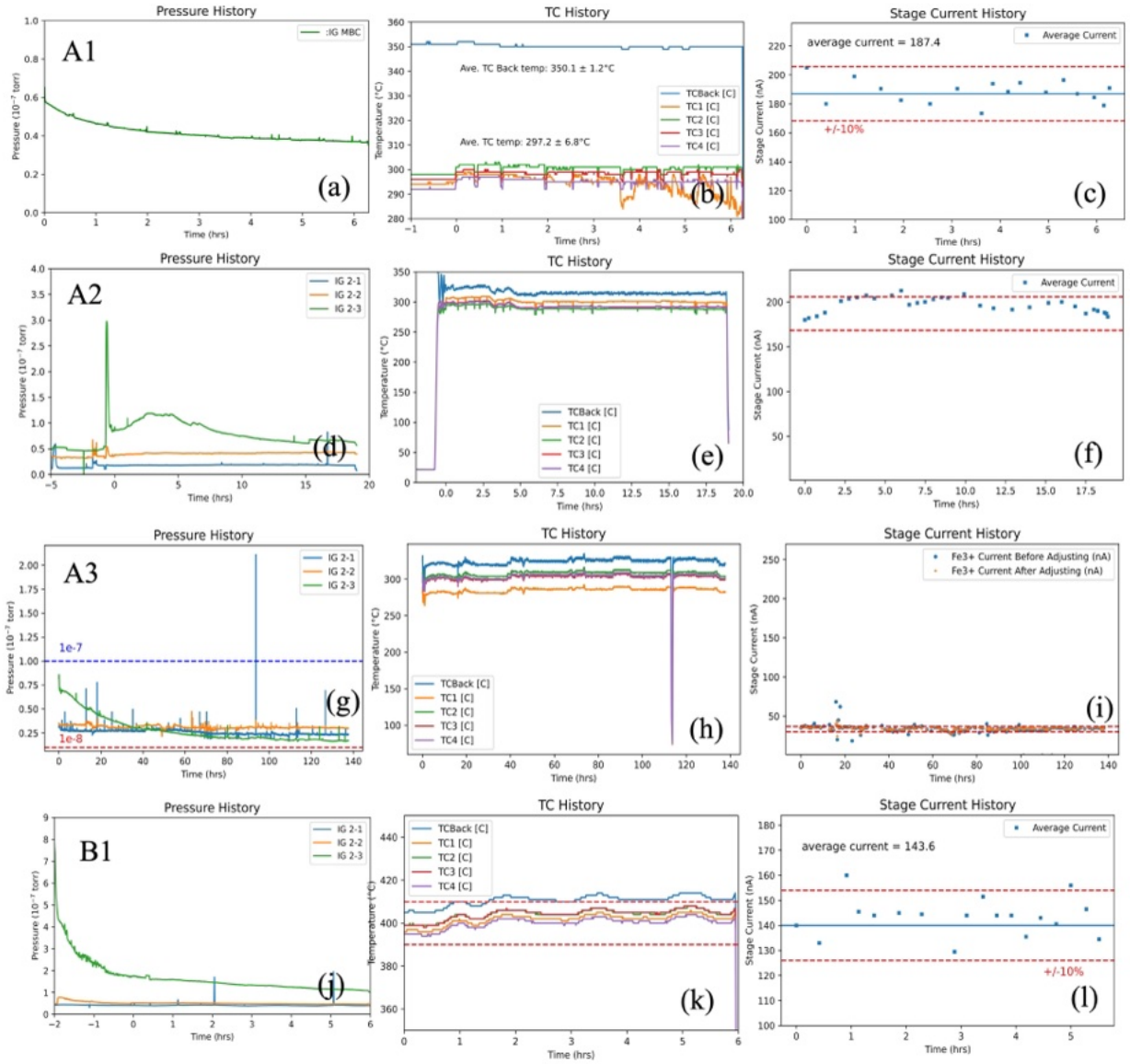

Appendix Figure B.1 Pressure (left column), temperature (middle column), and Fe^{3+} current histories for irradiations A1 (a-c), A2 (b-f), A3 (g-i), and B1. (j-l)

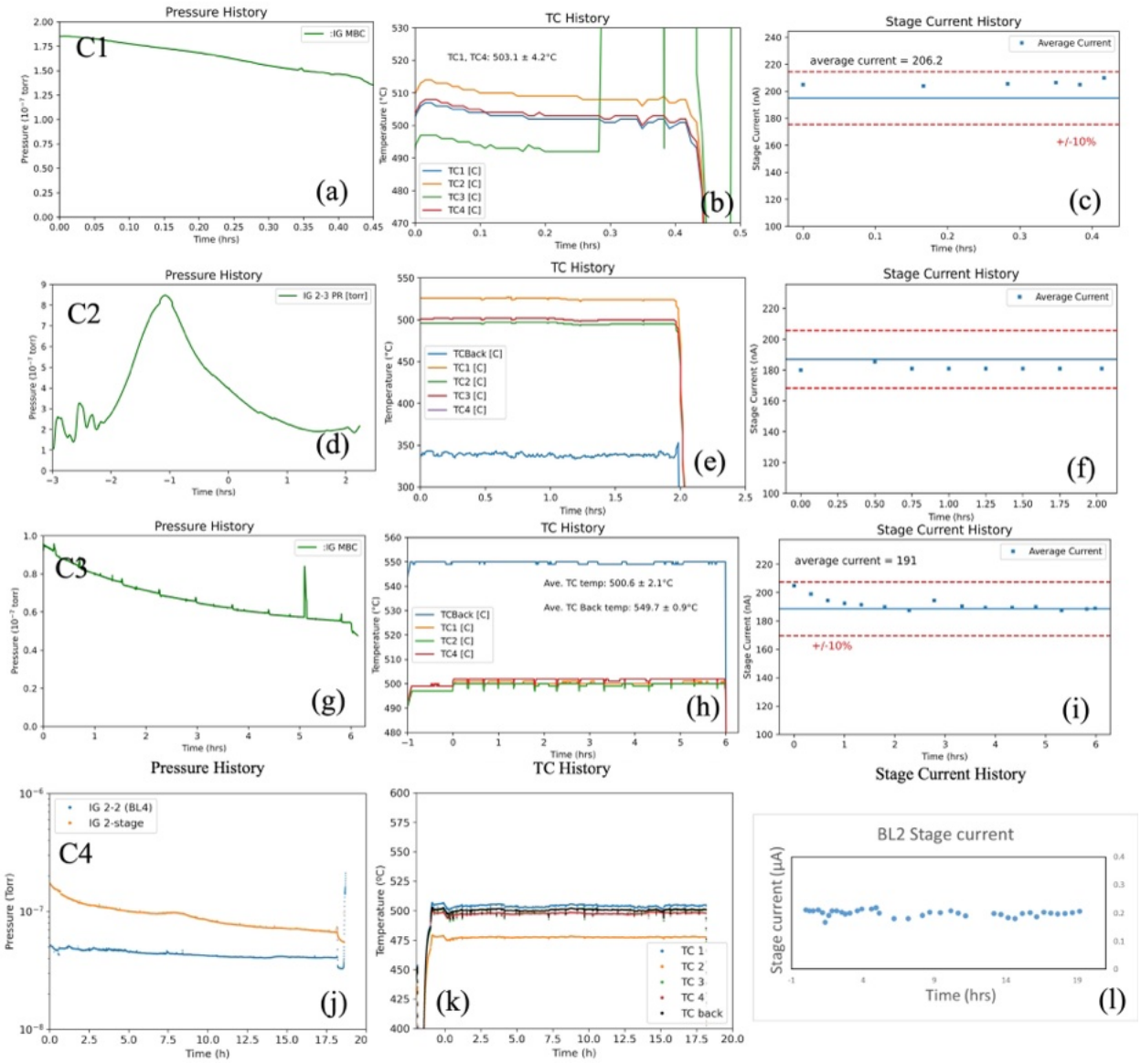

Appendix Figure B.2 Pressure (left column), temperature (middle column), and Fe^{3+} current histories for irradiations C1 (a-c), C2 (d-f), C3 (g-i), and C4 (j-l).

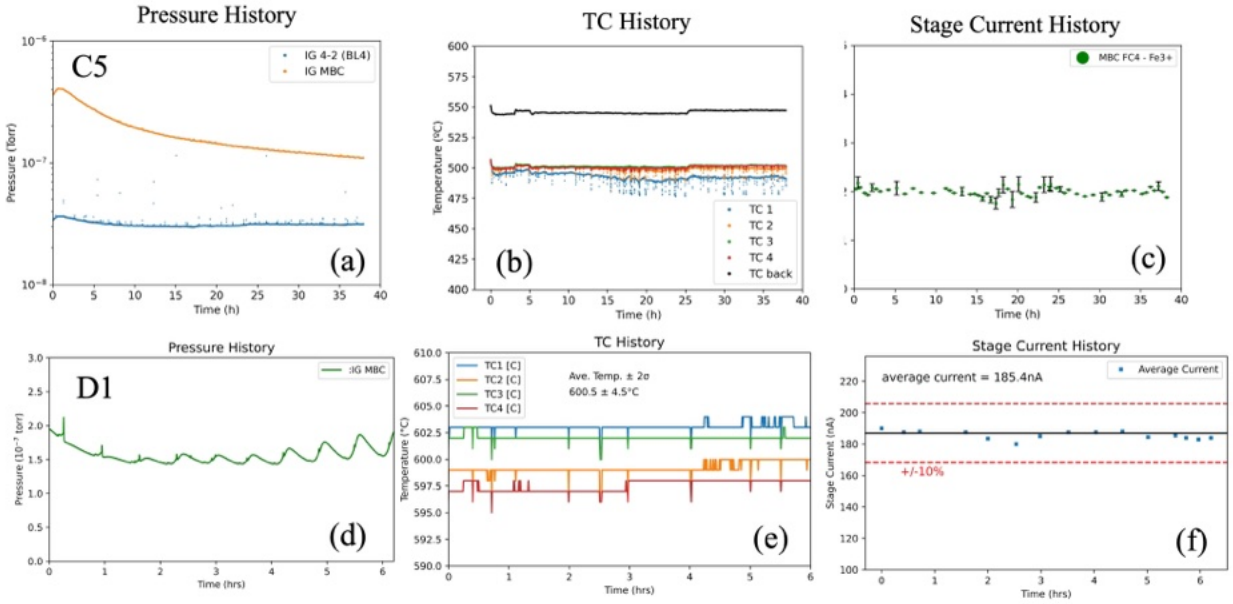

Appendix Figure B.3 Pressure (left column), temperature (middle column), and Fe^{3+} current histories for irradiations C5 (a-c) and D1 (d-f).

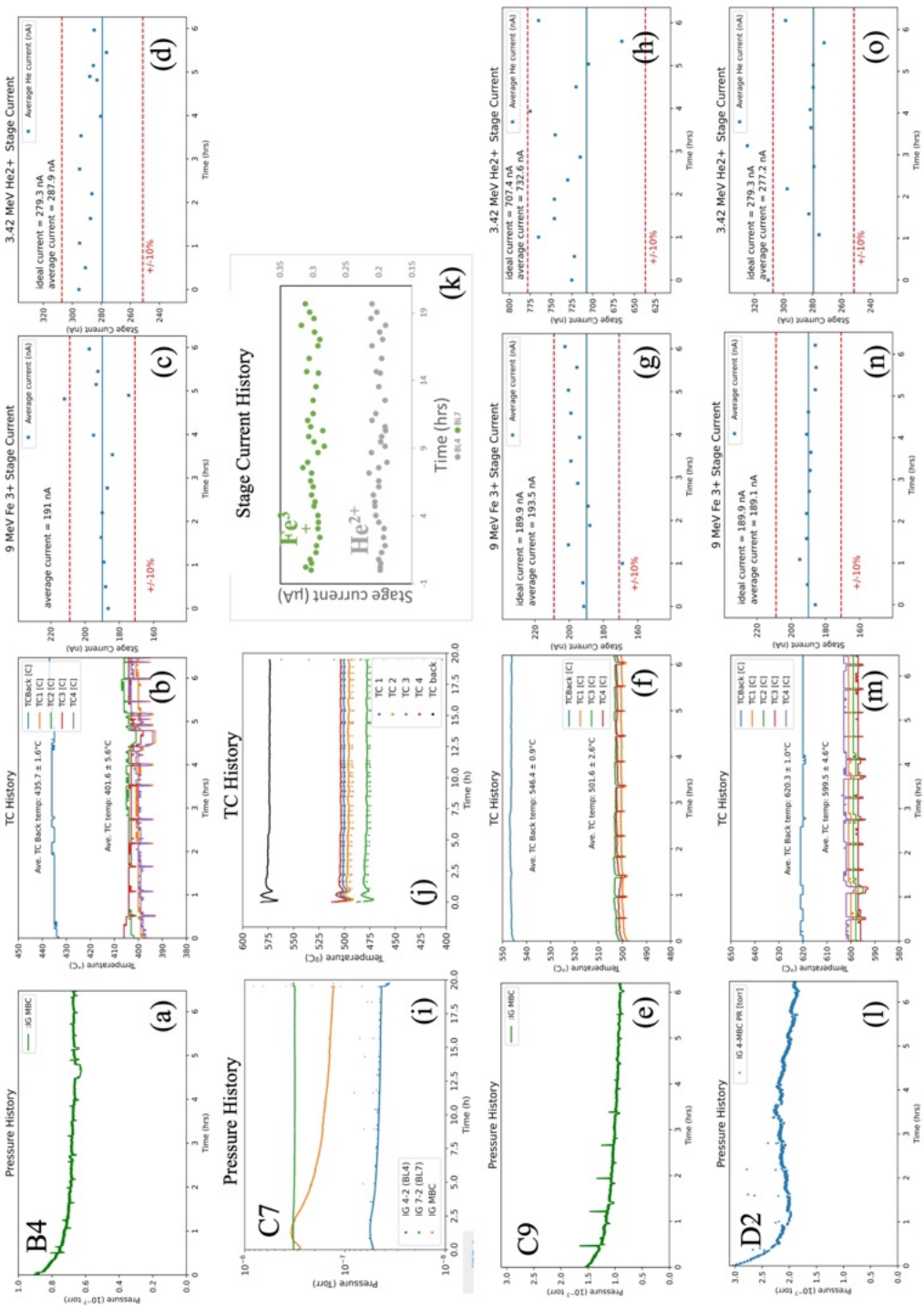

Appendix Figure B.4 Pressure (left column), temperature (middle-left column), Fe^{3+} current (middle-right column), and He^{2+} current histories for irradiations B4 (a-d), C7 (i-k), C9 (e-h), and D2 (l-o).

Appendix C: Precipitate Data

This appendix provides the data on the number of liftouts taken, the number of STEM-EDS maps taken, the number of precipitates counted, the number density of precipitates, the equivalent diameters of precipitates, and the volume fraction of precipitates for each irradiation condition in Table 4.3.

Appendix Table C.1 Data on the number of liftouts taken, the number of STEM-EDS maps taken, the number of precipitates counted (N), the number density of precipitates (ρ), the equivalent diameters of precipitates (d_{eq}), and the volume fraction of precipitates (f) for each irradiation condition.

Sample ID	# of Liftouts Taken	# of EDS Maps Taken	N	ρ (m^{-3})	d_{eq}(nm)	f
Control	1	5	90	$(2.3\pm0.3)\times10^{21}$	7.8±0.3	$(6.8\pm0.6)\times10^{-4}$
A1	3	11	49	$(0.9\pm0.2)\times10^{21}$	8.7±0.6	$(3.9\pm1.0)\times10^{-4}$
A2	1	5	N.O.	N.O.	N.O.	N.O.
A3	1	4	N.O.	N.O.	N.O.	N.O.
B1	3	9	67	$(1.5\pm0.2)\times10^{21}$	7.6±0.4	$(4.4\pm0.9)\times10^{-4}$
B4	2	9	56	$(0.9\pm0.2)\times10^{21}$	8.4±0.4	$(3.8\pm0.9)\times10^{-4}$
C1	1	5	106	$(3.3\pm0.9)\times10^{21}$	6.6±0.4	$(6.9\pm0.2)\times10^{-4}$
C2	1	5	86	$(2.9\pm0.9)\times10^{21}$	7.4±0.4	$(9.3\pm3.4)\times10^{-4}$
C3	3	12	109	$(1.7\pm0.3)\times10^{21}$	10.4±0.9	$(11.1\pm2.3)\times10^{-4}$
C4	2	9	N.O.	N.O.	N.O.	N.O.
C5	2	6	N.O.	N.O.	N.O.	N.O.
C6	2	11	122	$(1.8\pm0.1)\times10^{21}$	7.6±0.4	$(5.3\pm0.5)\times10^{-4}$
C7	1	4	N.O.	N.O.	N.O.	N.O.
C8	2	4	N.O.	N.O.	N.O.	N.O.
C9	2	7	63	$(1.5\pm0.2)\times10^{21}$	8.3±0.4	$(6.1\pm1.1)\times10^{-4}$
D1	3	9	69	$(1.3\pm0.2)\times10^{21}$	14.9±2.2	$(42.0\pm11.0)\times10^{-4}$
D2	4	14	142	$(1.6\pm0.2)\times10^{21}$	11.2±1.2	11.2±1.2

Appendix D: Determination of Recoil Rate (dpa/s) of TiC Precipitates Under Irradiation

The recoil rate was determined by converting the displacement rate of CNA9 (7×10^{-4} dpa/s) to that for TiC. A quick KP calculation in SRIM was run with 5,000 ions into CNA9. A layer of CNA9 was simulated from the surface of the bulk sample to 1200 nm beneath the surface of the bulk sample. Then a layer of TiC was simulated, the layer having a width of 20 nm. Another Layer of CNA9 was simulated from the end of the TiC layer to 2500 nm beneath the surface. The results of this calculation are shown in Appendix Figure D.1. The damage for the TiC layer is ~7 dpa and the damage for the CNA9 matrix is ~15 dpa around the nominal damage region. This translates to a 0.467 difference between the damage levels of the TiC precipitates and the CNA9 matrix. This ratio can be used to estimate the equivalent damage rate for the TiC precipitates as well. The matrix had a damage rate of 7×10^{-4} dpa/s, which translates to 3.3×10^{-4} dpa/s for the TiC precipitates.

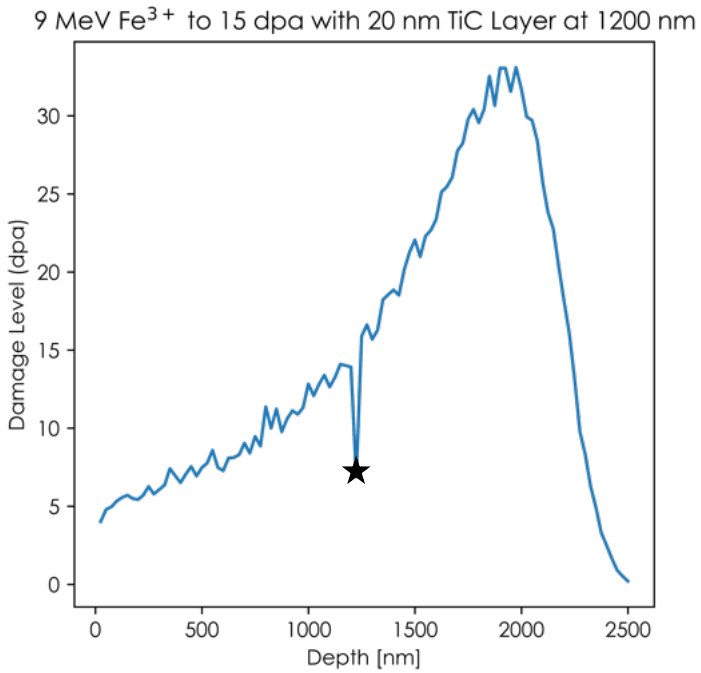

Appendix Figure D.1 SRIM calculation of damage into CNA9 with a layer of Ti and C at 1200 nm, simulating the damage that would occur in a TiC precipitate (star).

Appendix E: Titanium and Carbon Diffusivities

The diffusivities of Ti and C were determined to find the rate-limiting species for TiC precipitate evolution under irradiation. Appendix Table E.1 shows the calculations of the diffusivities of Ti and C as a function of temperature. The amount of Ti and C in the BCC CNA9 matrix were calculated from Thermo-Calc. Calculations were made assuming the amount of Ti and C in the matrix does not significantly alter under irradiation. Radiation-enhanced diffusion will increase the diffusion of Ti versus thermal conditions because it diffuses as a substitutional solute. However, radiation will not affect C as C is an interstitial and already diffuses quickly [128]. The diffusion of Ti was calculated using the equations outlined for single beam and dual beam irradiations in Eq. 6.1-Eq. 6.5. Since a range of D_{eff}^{Ti} values were calculated, as explained in the preceding paragraphs, the average value of $D_{eff,ave}^{Ti}$ was used. The diffusion of C in single beam irradiations was calculated using:

$$D_{thermal}^{C} = D_0^C exp\left(-\frac{\Delta H_D}{k_b T}\right) \text{[9]} \qquad \text{Eq. E.0.1}$$

where D_0^C is the frequency factor of diffusion of C atoms equal to 6.2×10^{-7} m^2/s and ΔH_D is the carbon diffusion activation energy equal to 80 kJ/mol. The diffusion of C in dual beam irradiations was calculated using:

$$D_{eff}^{C} = \frac{D_{thermal}^{C}}{1 + C_e exp\left(\frac{E_b^{C-He}}{kT}\right)} \qquad \text{Eq. E.0.2}$$

The value of 0.33 eV (C-1NN He_{sub} in BCC Fe) was chosen for E_b^{C-He} because it is the most attractive binding energy for the simple C-He complex and hence the most conservative. Diffusivity was calculated as the diffusion of the diffusing species (Ti or C) multiplied by its concentration in the matrix. As Appendix Table E.1 shows, the diffusivity values at all conditions for Ti are significantly lower than those of C. Hence, using the diffusion values for Ti instead of for C are justified.

Appendix Table E.1 This table shows the diffusivity calculations for Ti and C. Refer to the text for the equations used to calculate the values. This table justifies the use of Ti, as the rate-limiting species, for diffusion calculations regarding precipitate stability in the proceeding sections.

Temperature (°C)	C concentration in the matrix (atom fraction)	Ti concentration in the matrix (atom fraction)	D_C in the matrix ($\times 10^{-7}$ m^2/s)		D_{Ti} in the matrix ($\times 10^{-19}$ m^2/s)		Diffusivity of C in the matrix (m^2/s)		Diffusivity of Ti in the matrix ($\times 10^{-22}$ m^2/s)	
			SI ($D_{thermal}^{C}$)	DI (D_{eff}^{C})	SI (D_{RED}^{Ti})	DI ($D_{eff,ave}^{Ti}$)	SI	DI	SI	DI
300	3×10^{-12}	9.14×10^{-6}	6.1	-	5.1±0.09	-	1.8×10^{-18}	-	0.05±0.00009	-
400	1.21×10^{-9}	3.53×10^{-5}	6.1	5.9	8.8±0.02	3.5±0.02	7.4×10^{-16}	7.1×10^{-16}	0.3±0.001	0.1±0.0007
500	9.75×10^{-8}	1.06×10^{-4}	6.1	6.0	13.4±0.1	.0±0.02	6.0×10^{-14}	5.8×10^{-14}	1.4±0.01	0.5±0.002
600	2.22×10^{-6}	2.41×10^{-4}	6.1	6.1	12.3±0.4	5.3±0.1	1.4×10^{-12}	1.3×10^{-12}	3.0±0.09	1.3±0.03

Appendix F: The Effects of Dislocation Line and Loop Densities on Diffusion and Recoil Resolution Calculations

An analysis was conducted that varied the dislocation line and loop densities by 10× less than or 10× greater than the values given in Section 4.9 to understand how dislocation density affected the calculated values of C_v^{irr} and C_i^{irr}. The values of C_v^{irr} and C_i^{irr} are used in the calculations of diffusion and hence also in the recoil resolution calculations. This appendix provided the results of the diffusion and recoil resolution calculations with varied dislocation line and loop densities.

Appendix Table F.1 shows the dominant mechanism of precipitate stability predicted using the Frost and Russell model of precipitate stability with the various dislocation densities.

Appendix Table F.2 shows the crossover temperature by which the dominant mechanism of precipitate stability changes as a function of dislocation line and loop densities. Appendix Figure F.1 shows the calculated values of diffusion with the varied dislocation line and loop densities. Appendix Figure F.2a shows the Ti matrix concentration values calculated with the varied dislocation line and loop densities.

Using the low dislocation density of 10× less than used in Section 4.9 (Appendix Figure F.2b) causes the single beam recoil resolution concentration to be less dominant at 300 and 400°C. The low dislocation density also causes the dual beam recoil resolution with weak Ti-helium binding to be lower than the single beam recoil resolution at all temperatures, which would affect the analysis of the relative influence of recoil resolution with helium. Using the high dislocation density (Appendix Figure F.2c) causes the single beam recoil resolution concentration to be more

dominant at 300, 400, and 500°C. The effects of dual beam recoil resolution with weak binding became less significant at 500 and 600°C, also affecting the analytical results discussed in Chapter 6. Both high and low dislocation densities change the crossover temperature by which the dominant mechanism of stability changes. However, the best match to experimental results was obtained with the literature values of dislocation densities used in the text.

Overall, variations in the dislocation density do affect the results of the Frost and Russell model. However, it is not expected that the dislocation density varies as much as 10× less or more than the values used from literatures and most likely the effects are minimal on the analysis. However, the best matches between the model and experimental data are obtained using the dislocation density values given in Section 4.9.

Appendix Table F.1 The dominant mechanism on precipitate stability using the Frost and Russell model of precipitate stability with dislocation line and loop densities derived from literature as well as 10× greater than and 10× less than this densities. Red text indicates a different dominant mechanism than predicted using the dislocation densities from literature.

	Dominant mechanism					
	400°C		500°C		600°C	
	Single beam	Dual beam (E_b^{Ti-He})	Single beam	Dual beam (E_b^{Ti-He})	Single beam	Dual beam (E_b^{Ti-He})
Dislocation density used	***Recoil resolution***	***Recoil resolution***	***Thermal equilibrium***	***Equal***	***Thermal equilibrium***	***Thermal equilibrium***
10× less than dislocation density	**Equal (~4× smaller)**	**Thermal equilibrium (~20× smaller)**	Thermal equilibrium	**Thermal equilibrium (~10× smaller)**	Thermal equilibrium	Thermal equilibrium
10× greater than dislocation density	Recoil resolution	Recoil resolution	**Equal (~10× greater)**	**Thermal equilibrium (~4× smaller)**	Thermal equilibrium	Thermal equilibrium

Appendix Table F.2 The crossover temperature by which the dominant mechanism of precipitate stability changes as a function of dislocation line and loop densities. Red text indicates a different dominant mechanism than predicted using the dislocation densities from literature.

	Crossover point	
	Single beam	Dual beam (E_b^{Ti-He})
Dislocation density used	***~460°C***	***~490°C***
10× less than dislocation density	**~410°C**	**~300°C**
10× greater than dislocation density	**~500°C**	**~415°C**

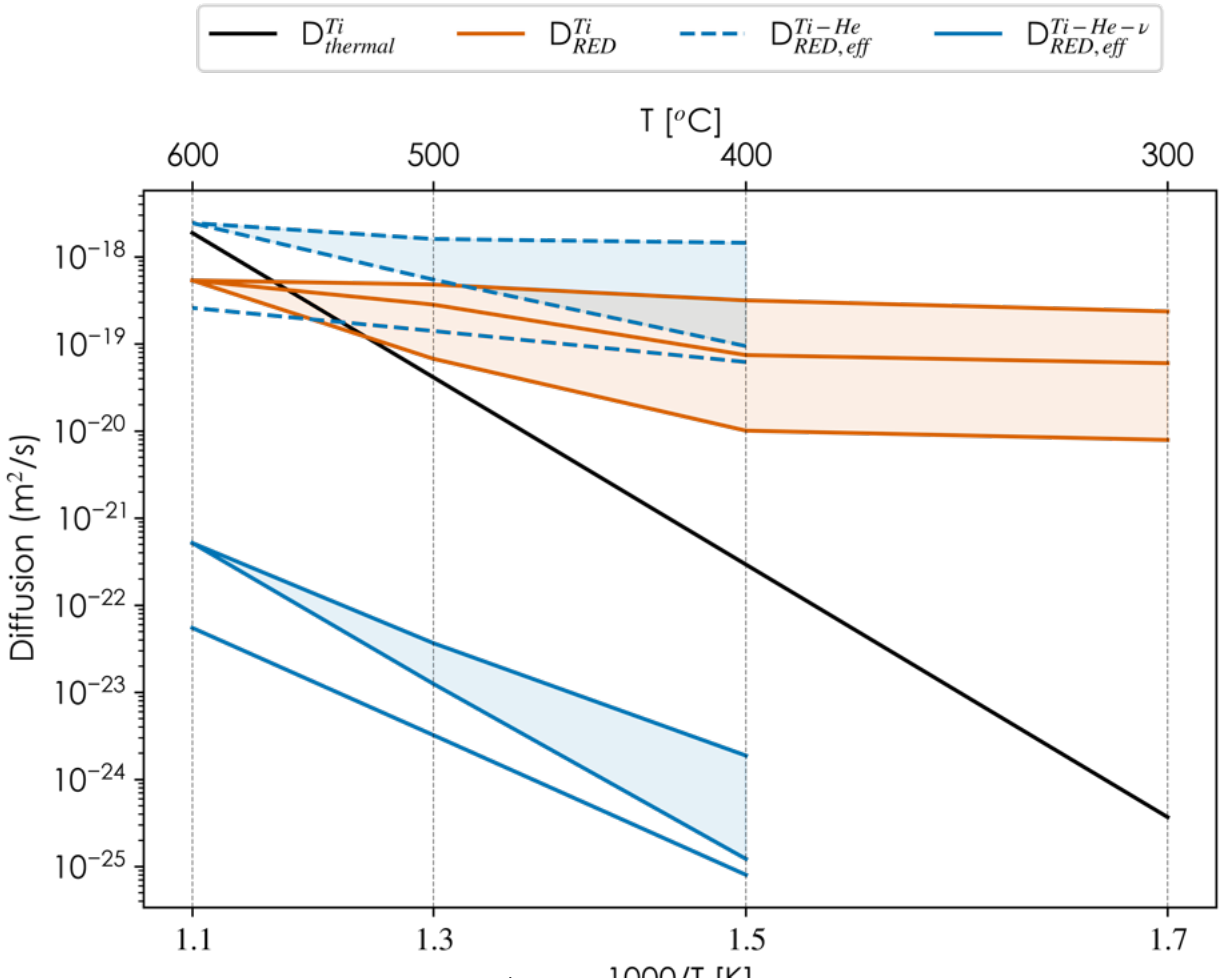

Appendix Figure F.1 Thermal diffusion (D_{th}^{Ti}, black line), radiation-enhanced diffusion in single beam conditions (D_{RED}^{Ti}, orange line), and helium-suppressed diffusion in dual beam conditions ($D_{RED,eff}^{Ti-He}$ and $D_{RED,eff}^{Ti-He-\nu}$, blue lines). Three lines are shown for each type of diffusion that corresponds to low, nominal, and high dislocation density.

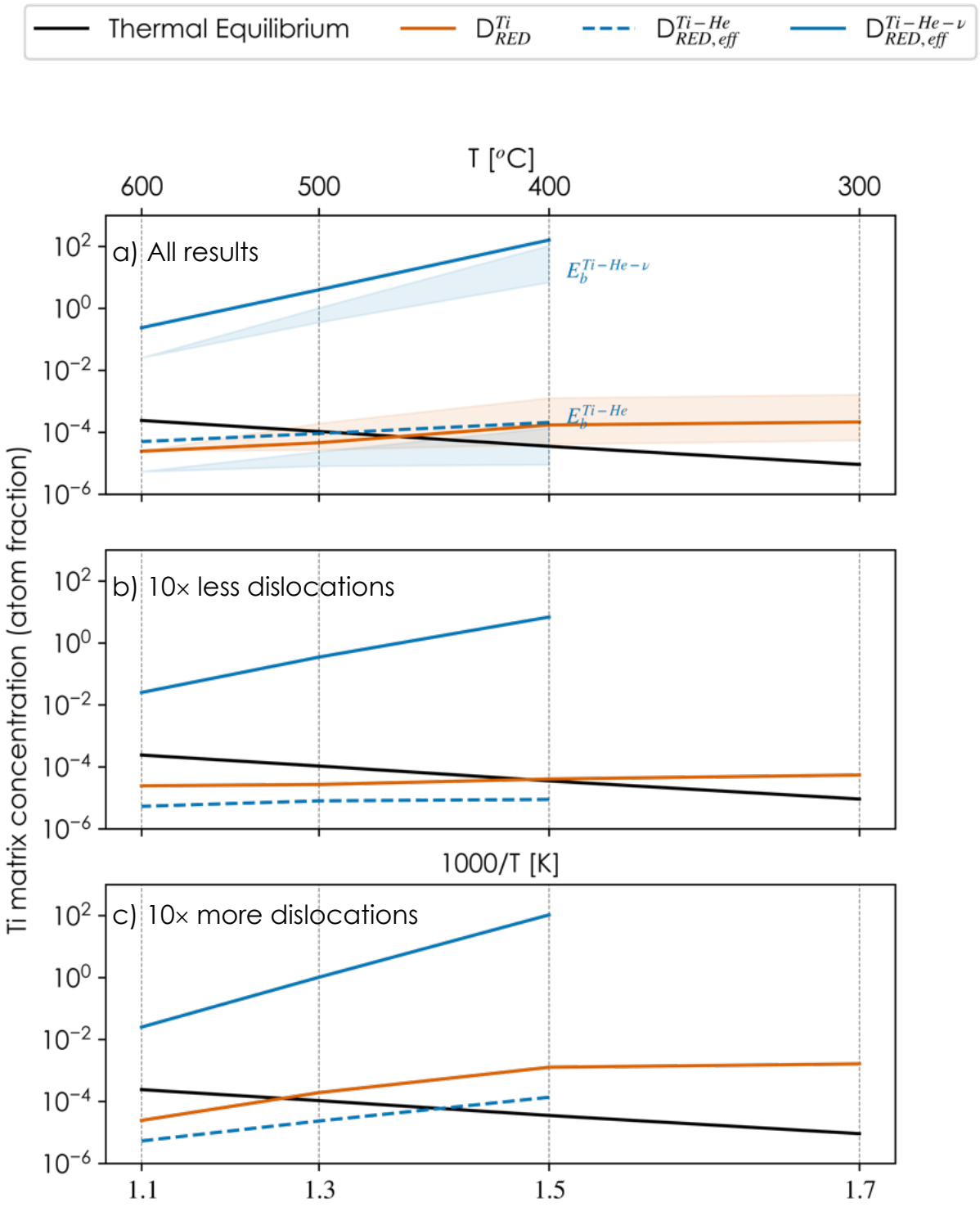

Appendix Figure F.2 The matrix concentration in thermal equilibrium (c_e, black line) was plotted versus the concentration from recoil resolution, $\frac{SR^2}{12D}\left(1-\frac{R}{4r_p}\right)$, orange line for single beam and blue lines for dual beam. (a) The results using the dislocation values given in Chapter 4 are shown with the darker blue and orange lines. This plot was shown in Figure 6.3. The filled in blue and orange areas represent the results of using 10× more or less than the dislocation density values used in Chapter 4. (b) The lines now represent the calculations using the low dislocation density (10× less than the dislocation density values used in Chapter 4). (c) The lines now represent the calculations using the high dislocation density (10× more than the dislocation density values used in Chapter 4).

Appendix G: Recoil Range Calculation of Ti Atoms from TiC Precipitates and Recoil Rate of TiC Precipitates using SRIM

To estimate the recoil range of Ti atoms from TiC precipitates under irradiation, a SRIM analysis was performed. Multiple SRIM calculations were run to estimate recoil ranges of Ti atoms from various sized precipitates and precipitates located in different areas of the nominal damage region. The TiC precipitates were modelled as layers of Ti and C atoms. The nominal damage region occurred 1100-1300 nm beneath the surface of the bulk sample of CNA9, with the exact nominal damage and damage rate occurring at 1200 nm beneath the surface. The "Detailed Calculation with Full Damage Cascades" mode of SRIM with 1,000 ions was used in order to obtain the range of Ti atoms from the TiC layer. The displacement energies of atoms were listed in Section 4.2.2.

First, a sensitivity analysis of the range dependence on TiC precipitate size was calculated. The SRIM calculation was set up as follows. A layer of CNA9 was simulated from the surface of the bulk sample to 1200 nm beneath the surface of the bulk sample. Then a layer of TiC was simulated, the layer having a width of 3, 5, 7, 10, or 90 nm. Another Layer of CNA9 was simulated from the end of the TiC layer to 2500 nm beneath the surface, where the 9 MeV Fe^{3+} ions were shown to come to rest (Figure 4.4). A TiC precipitate was modelled as a layer of 40% Ti and 60% C atoms. The ratio of Ti and C atoms in the layer was garnered from Thermo-Calc estimations of the ratio of Ti and C in the precipitates. The various widths simulated precipitates of various sizes. The values were chosen to represent the observed sizes for the MX-TiC and non-MX TiC precipitates in the control specimen.

The weighted average recoil range was then calculated from the SRIM results from each SRIM run. The weighted average of the recoil distance of a Ti solute outside of a TiC layer was calculated as follows, using a TiC layer located at 1200-1205 nm as an example:

$$R = \frac{\sum_{i=depth\ of\ 1205nm}^{depth\ at\ end\ of\ Ti\ range} counts\ in\ each\ bin/100 \times (bin - 1205nm)}{\sum_{i=depth\ of\ 1205nm}^{depth\ at\ end\ of\ Ti\ range} counts\ in\ each\ bin/100} \qquad \text{Eq. G.1}$$

The counts represent the percentage of Ti in a bin. The bin represents the depth, and subtracting 1205 nm from the bin will obtain the projected range from the edge of the precipitate. The bin resolution was set by the viewing window parameter in SRIM and was equal to 0.3 nm. This way, the amount of Ti atom recoils within and outside the precipitate edge are calculated. As such, R represents the range outside the precipitate edge.

Appendix Table G.1 summarizes the results of this analysis. Appendix Figure G.1 shows the distributions of Ti atoms as a function of depth for TiC layers of 3, 5, 7, 10, and 90 nm. The weighted recoil ranges are approximately 0.5-0.7 nm. The recoil resolution efficiency was calculated as the ratio of the number of Ti atoms that recoiled outside the precipitate to those that recoiled within. As the MKI model suggests, this value increases for decreasing precipitate sizes (see Section 6.1.3). A layer of 7 nm was then chosen to continue with, as the ranges did not significantly change between the various layers and because the 7 nm represents the average size of the MX-TiC precipitates in the control specimen best, thus providing an average estimate of the range for MX-TiC precipitates.

Second, a sensitivity analysis of the range dependence on the location of the TiC layer was calculated. A 7 nm layer of TiC was placed at 1100-1107, 1200-1207, and 1293-1300 nm to cover the full range of the nominal damage region. Appendix Table G.2 and Appendix Figure G.2 display the results of these calculations. The weighted recoil ranges 0.9, 0.5, and 0.7 nm for layers at 1100-

1107, 1200-1207, and 1293-1300 nm, respectively. The average of these values is 0.7 nm. This is the final value used for the range in the calculations for Chapter 6.

A final analysis was completed to understand how helium bubbles attached to the MX-TiC precipitate interface might affect the range of recoiling Ti solutes. Another SRIM calculation with the same parameters as previously described was run with a 1200 nm layer of CNA9, followed by a 1.5 nm layer of helium, followed by a 7 nm layer of TiC, followed by another 1.5 nn layer of helium, and finally a 1290 nm layer of CNA9. The widths of the helium layers were chosen to be 1.5 nm as this was about the average size of the helium bubbles attached to the MX-TiC precipitate-matrix interfaces for the 500 and 600°C conditions with 10 appm He/dpa to $7_{TiC}/15_{matrix}$ dpa with 3.3×10^{-4} dpa/s_{TiC} and 7×10^{-4} dpa/s_{matrix} (Table 5.3). The average weighted recoil range was found to be ~2.2 nm (Appendix Figure G.3). A larger range than the previous calculations is expected, as helium has a lower density than TiC and CNA9 and thus a recoiling Ti solute will travel further outside the initial TiC layer if helium is surrounding it. Using this range value of 2.2 nm, it can be calculated that a recoiling Ti solute would travel through the surrounding 1.5 nm layer of helium and then the average weighted distance travelled in the CNA9 matrix would be 0.7 nm. This value of 0.7 nm travelled in the matrix, after travelling through the helium layer, is equal to the average weighted range in the previous calculations without helium. The density of CNA9 was 7.8 g/cm^3, of TiC was 2.06 g/cm^3, and of helium was 0.18×10^{-3}g/cm^3. This range value of 2.2 nm was not used in calculations, as it was found from experimental observations (Figure 5.16, Figure 5.17, Figure 5.18) that the entirety of the MX-TiC precipitate interfaces were not surrounded by helium bubbles and hence this represents a conservative case for the upper limit of the range value. Rather, this calculation could be used in future work to assess the effects of different range values on precipitate stability and also shows how helium can alter solute behavior in complicated ways.

Appendix Table G.1 Summary of results from SRIM calculations to obtain the recoil distance of Ti atoms from different sized precipitates under irradiation in CNA9.

Width of TiC Layer	Location of Layer	Weighted Recoil Distance	Recoil Resolution Efficiency
3 nm	1200-1203 nm	0.6 nm	20.7%
5 nm	1200-1205 nm	0.7 nm	11.3%
7 nm	1200-1207 nm	0.5 nm	10.1%
10 nm	1200-1210 nm	0.5 nm	8.7%
90 nm	1200-1290 nm	0.5 nm	2.8%

Appendix Table G.2 Summary of results from SRIM calculations to obtain the dependence of the recoil distance of Ti atoms from same sized precipitates located at different locations in the nominal damage region under irradiation in CNA9.

Width of TiC Layer	Location of Layer	Weighted Recoil Distance	Recoil Resolution Efficiency
7 nm	1100-1107 nm	0.9 nm	15.2%
7 nm	1200-1207 nm	0.5 nm	10.1%
7 nm	1293-1300 nm	0.7 nm	17.5%

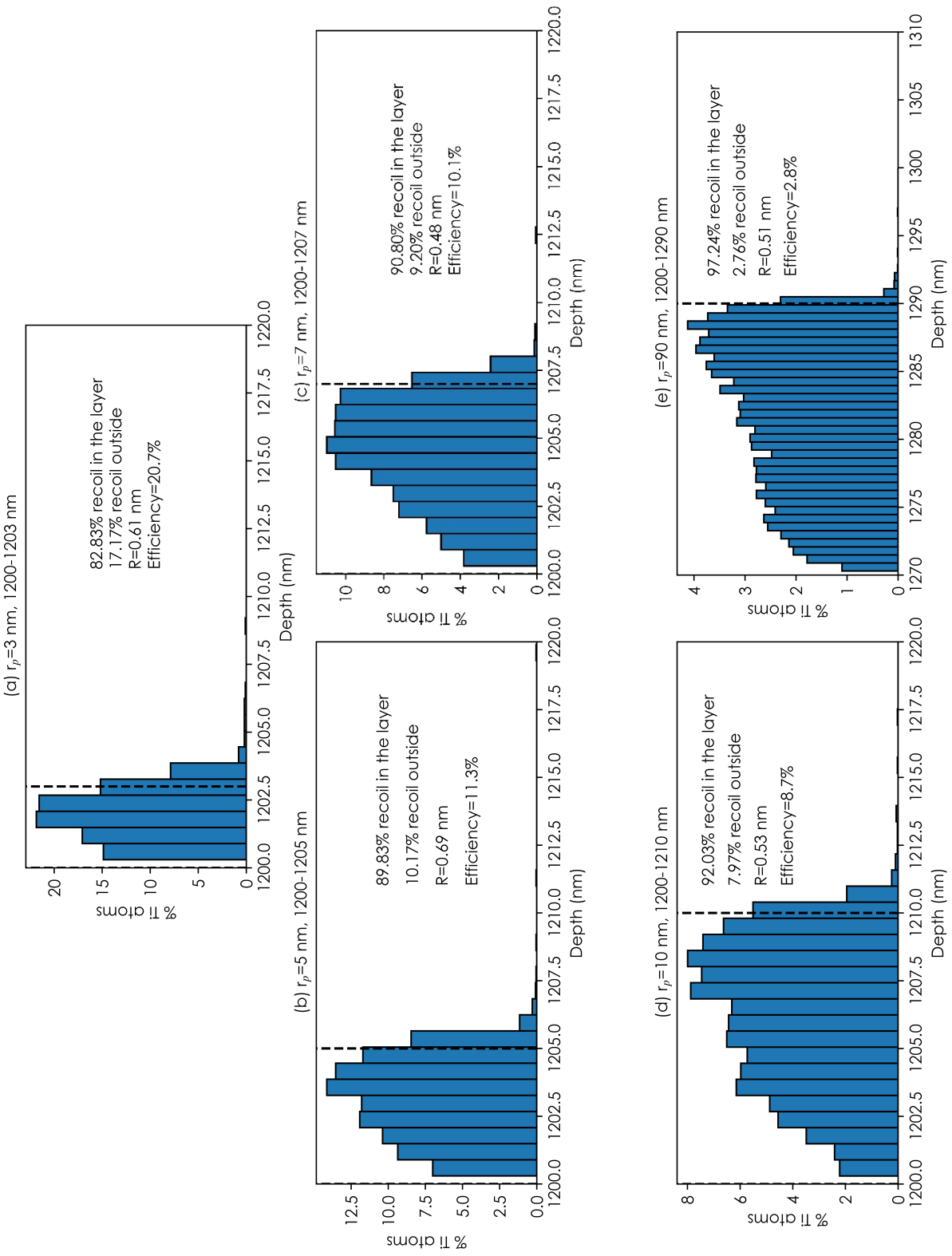

Appendix Figure G.1 SRIM analysis of recoiling Ti atoms from a TiC layer with widths of (a) 3nm, (b) 5nm, (c) 7 nm, (d) 10 nm, and (e) 90 nm.

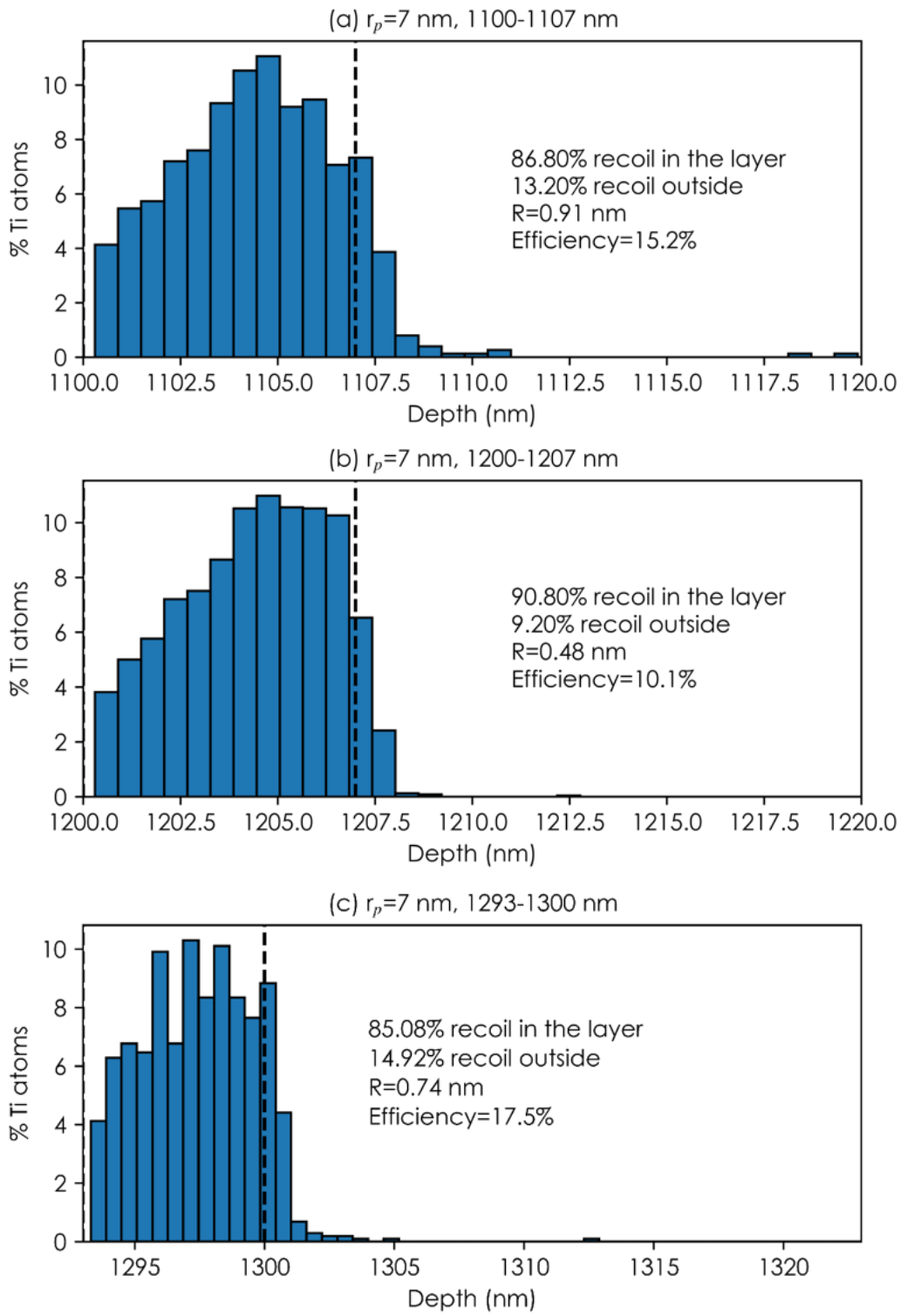

Appendix Figure G.2 SRIM analysis of 7 nm layers of TiC located at positions of (a) 1100-1107 nm, (b) 1200-1207 nm, and (c) 1293-1300 nm.

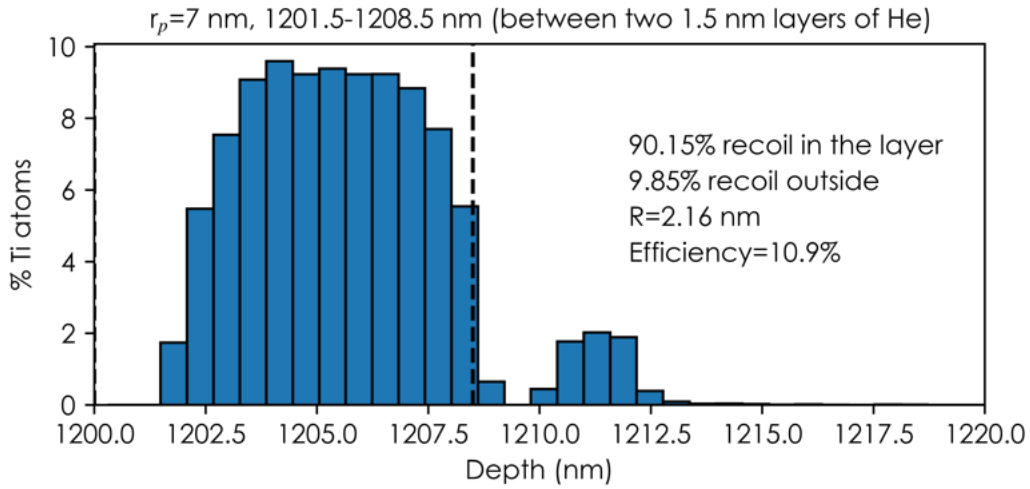

Appendix Figure G.3 SRIM analysis of a 7 nm layer of TiC located at a position of 1201.5-1208.5 nm, sandwiched between two 1.5 nm layers helium.

Appendix H: Effect of Production Efficiency on Results of Frost and Russell Model of Precipitate Stability

As described in Section 4.9, the production efficiency, ξ, is used to describe the freely migrating defects during irradiation as a function of irradiation type. For heavy ion irradiations, ξ is typically equal to ~0.1, which was used in Section 4.9 to calculate the concentrations of interstitials and vacancies under irradiation. However, this value will affect the results of the Frost and Russell model presented in Section 6.1.3 by affecting the diffusion of Ti solutes under irradiation. To assess the sensitivity of the Frost and Russell analysis to ξ, two values of ξ were compared: $\xi = 0.1$, typical value for heavy ion irradiations, and $\xi = 1$, typical value for electron irradiations [111]. A greater value of ξ corresponds to less freely migrating defects, and hence lower diffusion. As can be seen in Appendix Figure I.1, $\xi = 0.1$ leads to greater relative influences of recoil resolution than $\xi = 1$. This analysis shows that the choice for the value of ξ will determine the results of the Frost and Russell model, and that the Frost and Russell model can be used to assess mechanisms of precipitate stability between different kinds of irradiations.

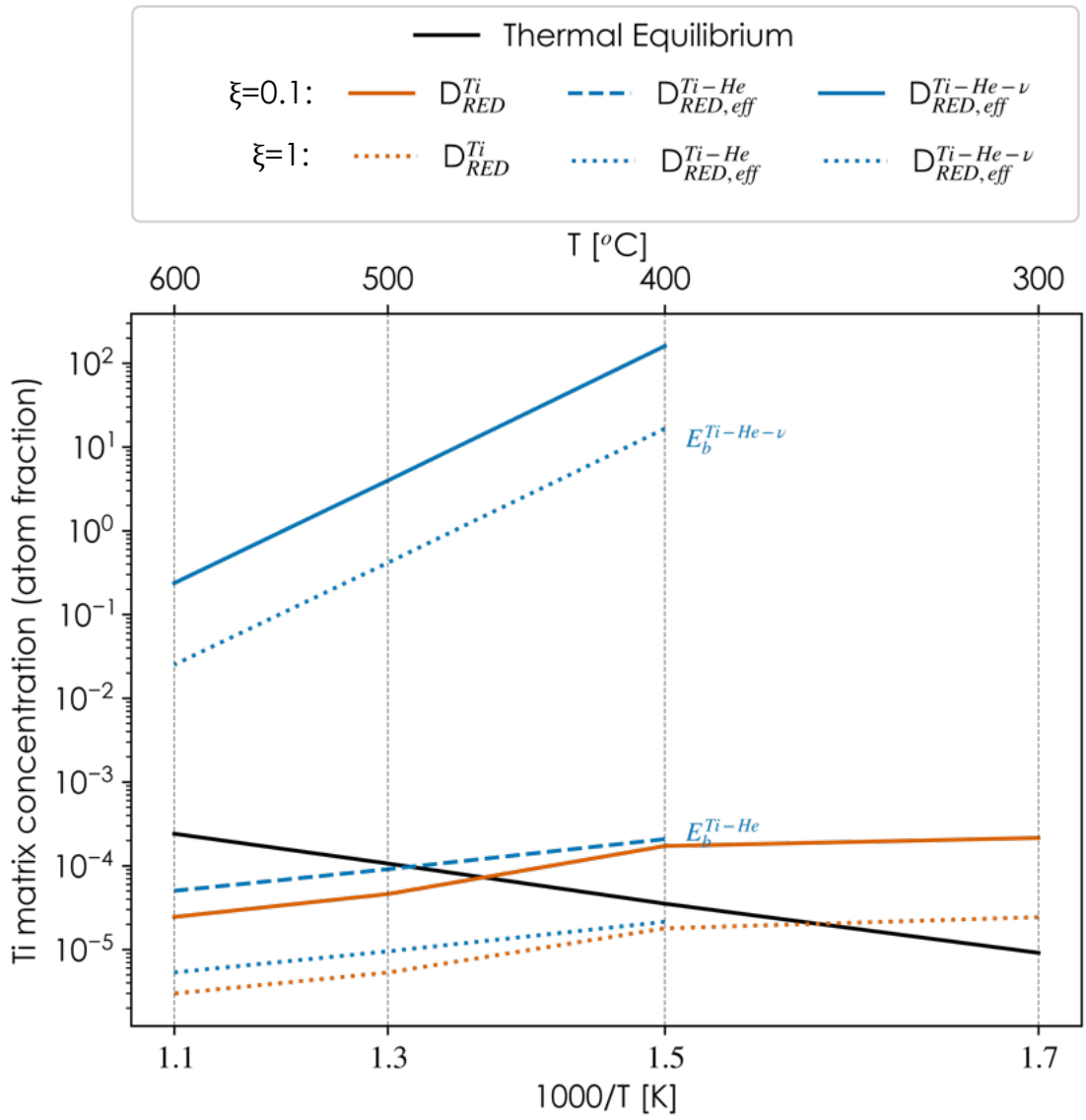

Appendix Table H.1 The matrix concentration in thermal equilibrium (c_e, black line) was plotted versus the concentration from recoil resolution ($\frac{SR^2}{12D}\left(1-\frac{R}{4r_p}\right)$, orange lines for single beam and blue lines for dual beam). The dotted lines represent the calculations using a value for defect production efficiency of ξ=1. The dashed and solid lines represent the calculations using a value for defect production efficiency of ξ=0.1, which was used in the thesis work.

Appendix I: Segregation at Grain Boundaries

Grain boundaries were assessed for segregation by observing solute behavior at grain boundaries present in EDS maps that had been taken to understand precipitate behavior. As such, the grain boundaries were not in the ideal condition for segregation assessment, *i.e.*, they were not edge-on and magnified on. However, the maps were assessed to try to understand if radiation-induced segregation (RIS) was taking place under irradiation. Cr and W appeared to have been depleted from grain boundaries in the dual beam conditions. In addition, W was found in the MX-TiC precipitates, but that was not caused by irradiation as the control specimen displayed this as well. It is possible that dual beam irradiation conditions caused Cr and W depletion at grain boundaries, but this analysis is inconclusive.

Appendix Table I.1 Summary of grain boundary segregation results.

	400°C	**500°C**	**600°C**
Unirradiated	No enrichment/depletion at GBs		
15 dpa$_{matrix}$	No enrichment/depletion at GBs W segregation at MX-TiC precipitates		
15 dpa$_{matrix}$ **10 appm He/dpa**	Minimal Cr, W depletion at GBs Minimal Cr, W segregation at MX-TiC precipitates		
15 dpa$_{matrix}$ **25 appm He/dpa**	Not conducted	Minimal Cr, W depletion at GBs Minimal Cr, W segregation at MX-TiC precipitates	Not conducted

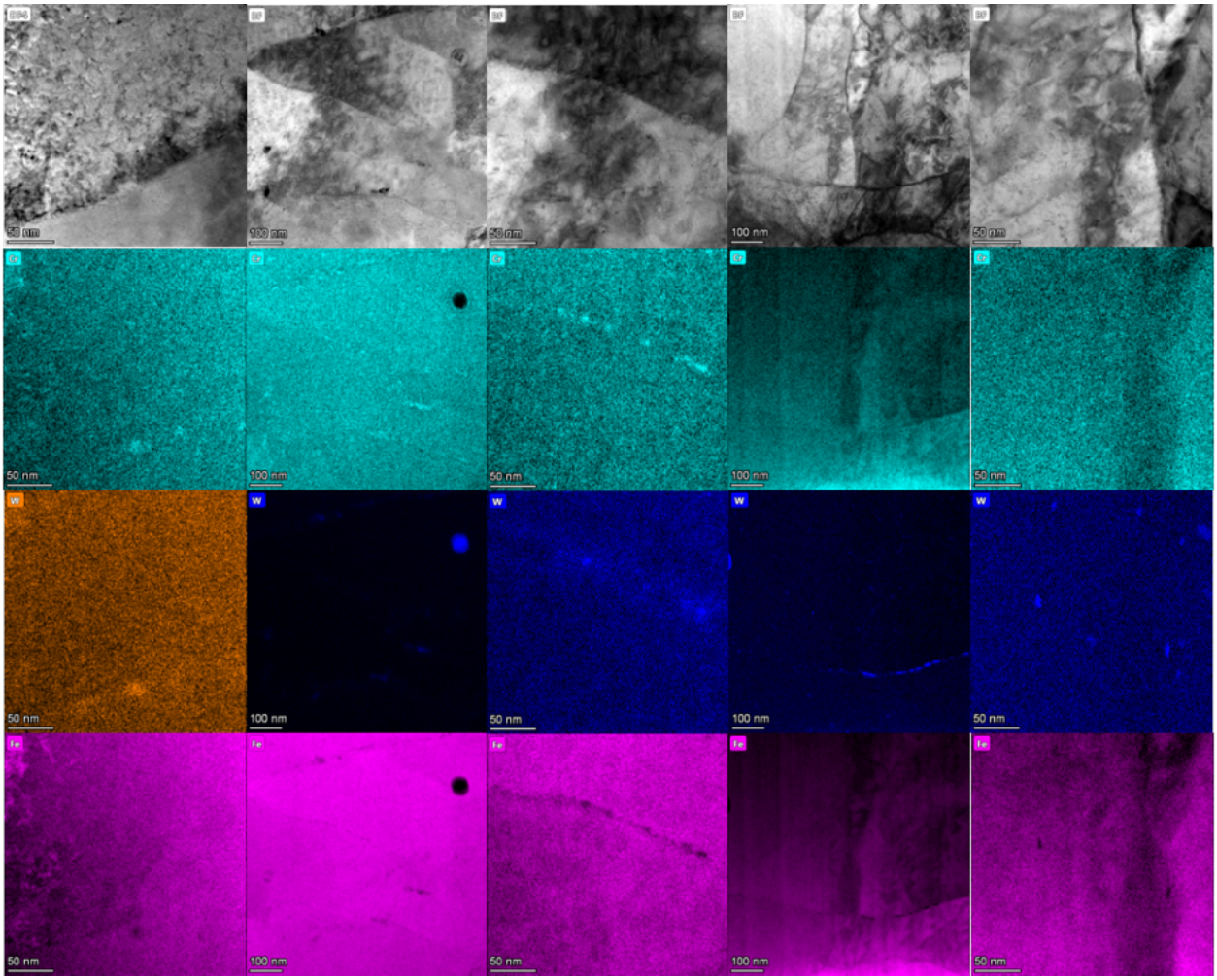

Appendix Figure I.1 STEM-EDS maps encompassing the nominal damage region in the (400°C-15 dpa-7×10^{-4} dpa/s)$_{matrix}$ condition.

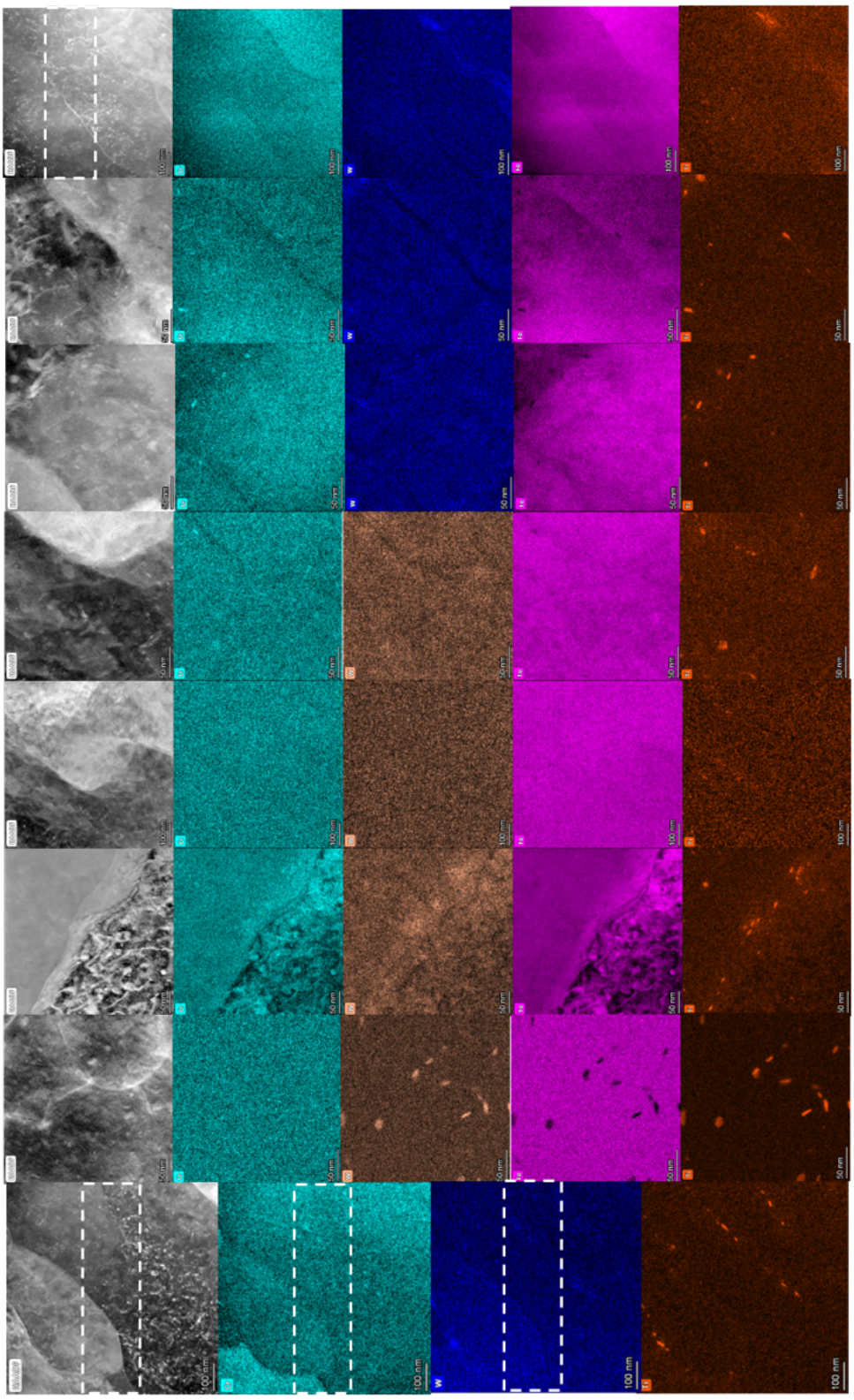

Appendix Figure I.2 STEM-EDS maps encompassing the nominal damage region in the (400°C-15 dpa-7×10^{-4} dpa/s-10 appm He/dpa)$_{matrix}$ condition.

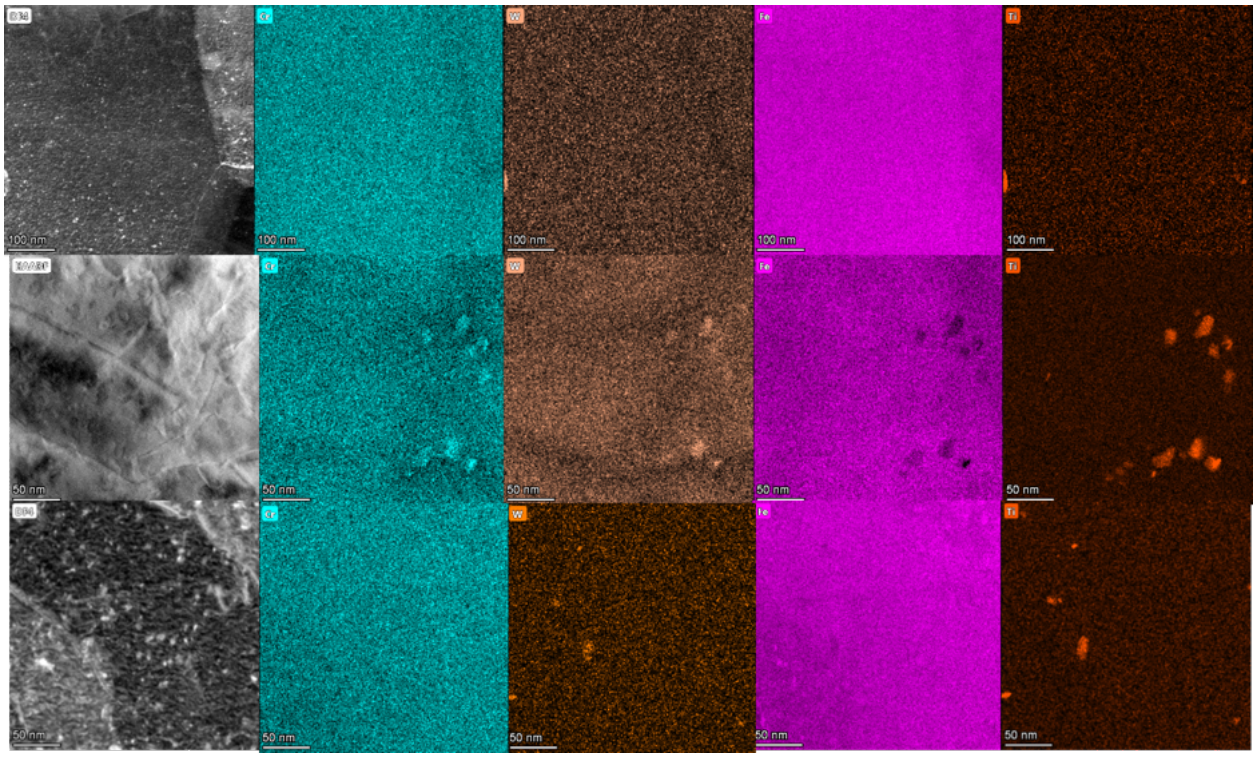

Appendix Figure I.3 STEM-EDS maps encompassing the nominal damage region in the (500°C-15 dpa-7×10^{-4} dpa/s)$_{matrix}$ condition.

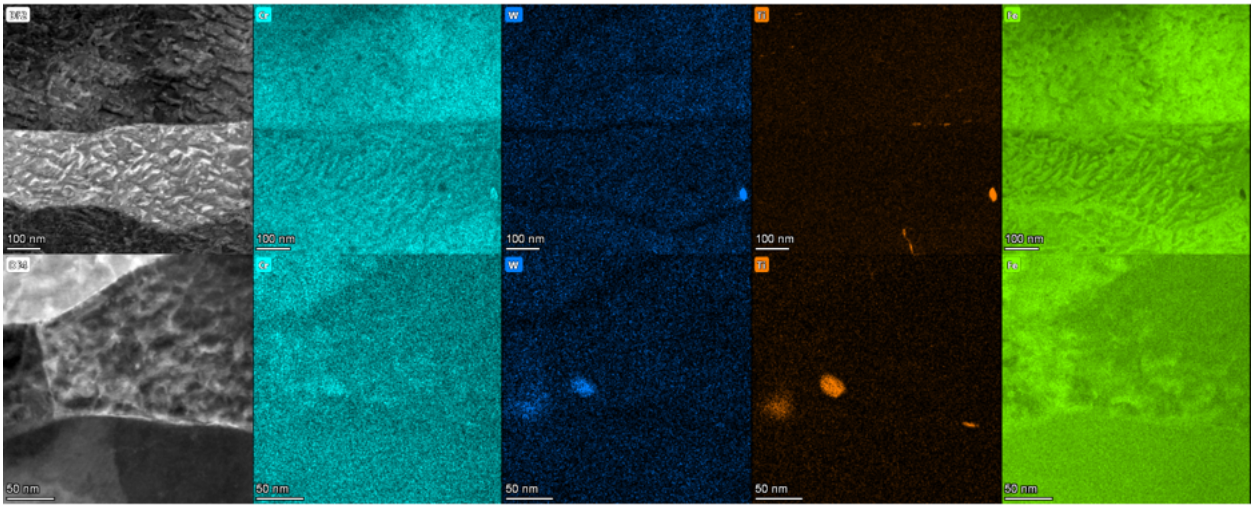

Appendix Figure I.4 STEM-EDS maps encompassing the nominal damage region in the (500°C-15 dpa-7×10^{-4} dpa/s-10 appm He/dpa)$_{matrix}$ condition.

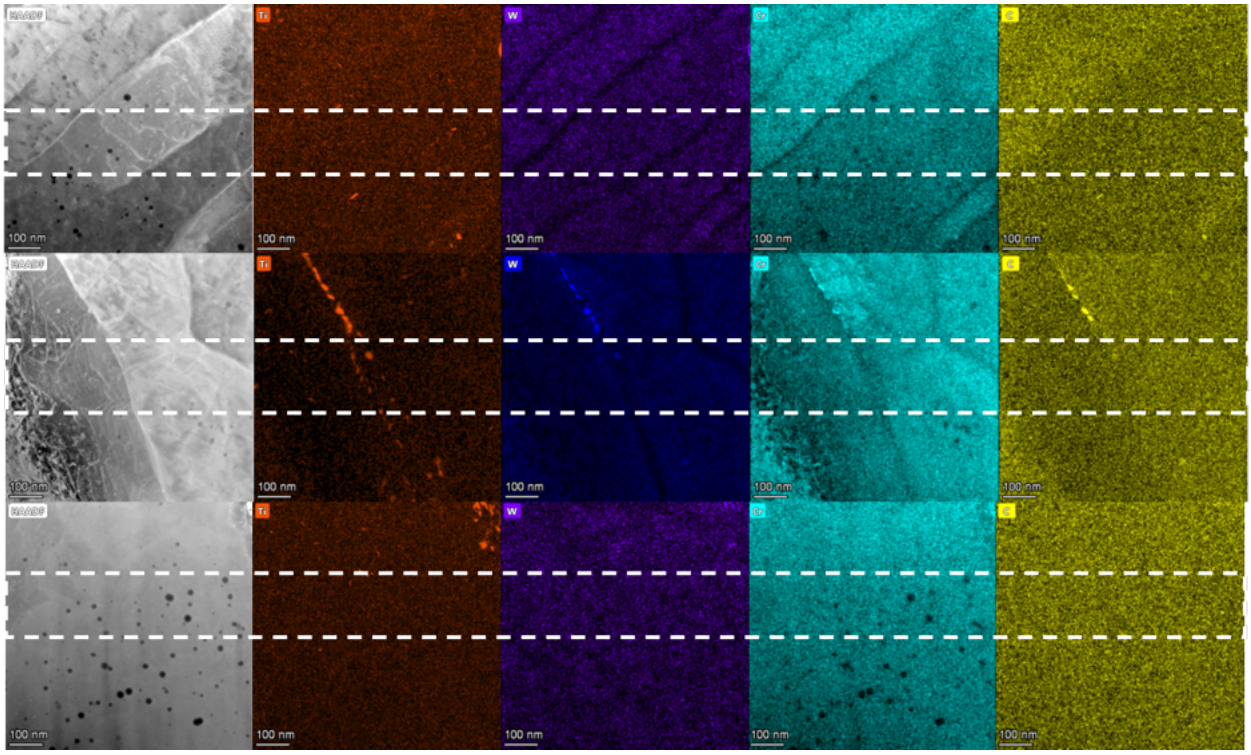

Appendix Figure I.5 STEM-EDS maps encompassing the nominal damage region in the (500°C-15 dpa-7×10^{-4} dpa/s-25 appm He/dpa)$_{matrix}$ condition.

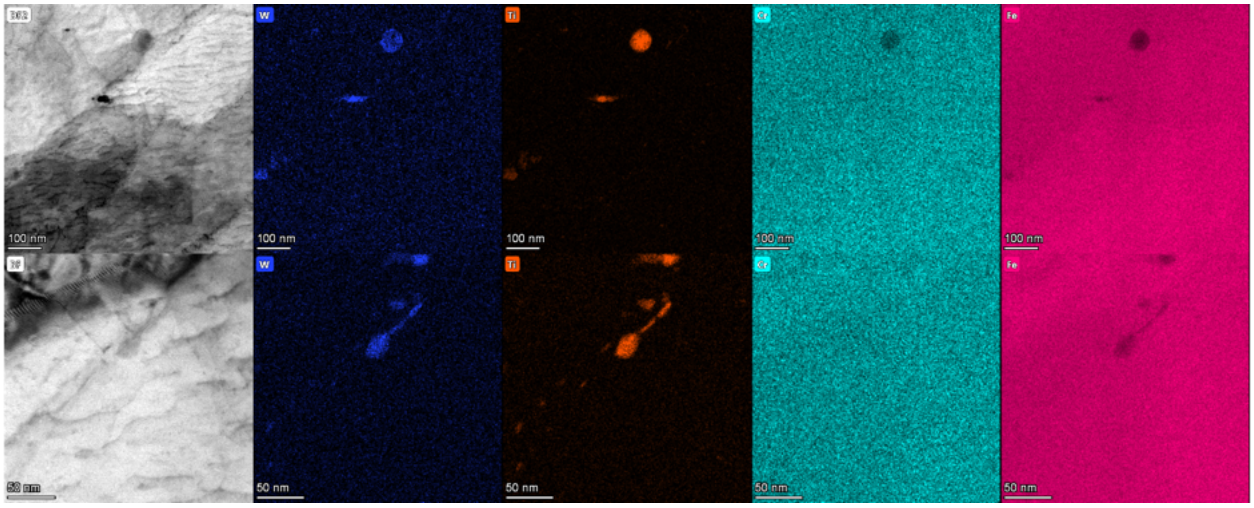

Appendix Figure I.6 STEM-EDS maps encompassing the nominal damage region in the (600°C-15 dpa-7×10^{-4} dpa/s)$_{matrix}$ condition.

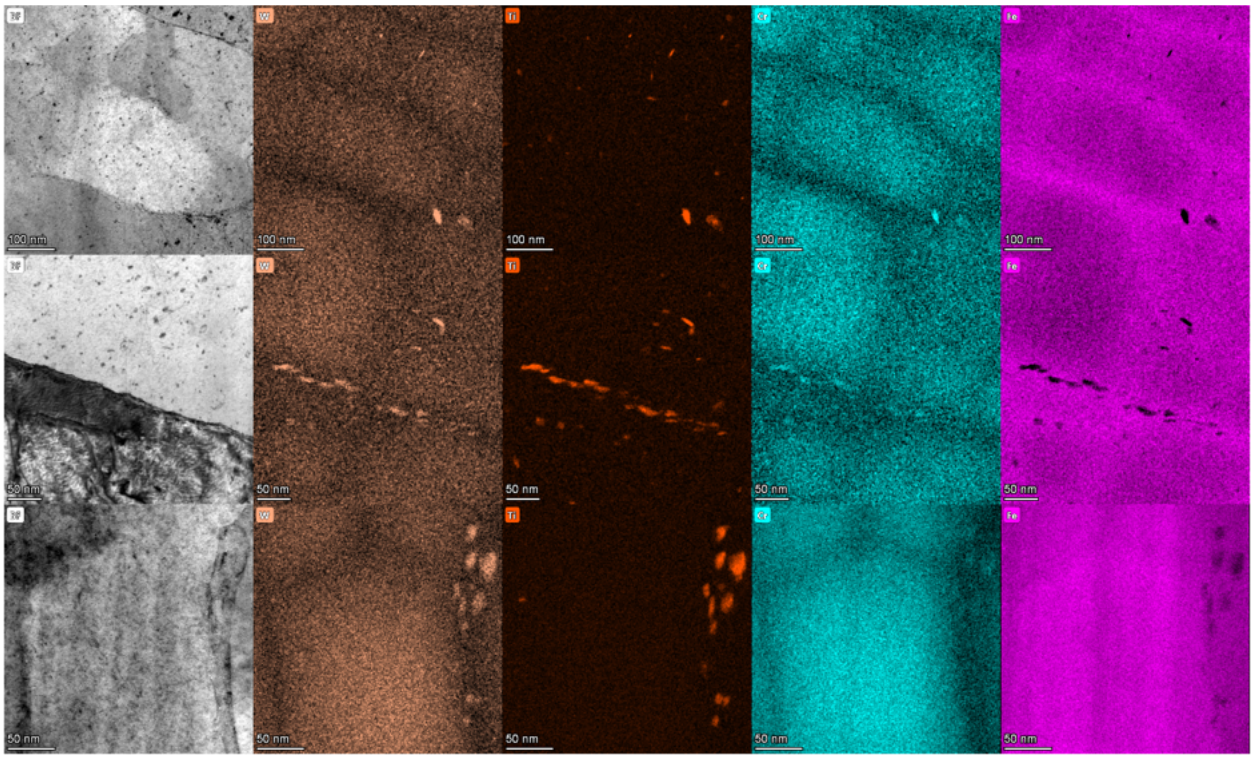

Appendix Figure I.7 STEM-EDS maps encompassing the nominal damage region in the (600°C-15 dpa-7×10^{-4} dpa/s-10 appm He/dpa)$_{matrix}$ condition.

Bibliography

[1] G.S. Was, Fundamentals of Radiation Materials Science Metals and Alloys, 2nd ed., Springer, 2017. https://doi.org/10.1007/978-1-4939-3438-6.

[2] K. Farrell, P.J. Maziasz, E.H. Lee, L.K. Mansur, Modification of radiation damage microstructure by helium, in: Radiat Eff, 1983: pp. 277–295. https://doi.org/10.1080/00337578308207378.

[3] L.K. Mansur, W.A. Coghlan, Mechanisms of helium interaction with radiation effects in metals and alloys: a review, Journal of Nuclear Materials. 119 (1983) 1–25.

[4] J. Ding, P. Zhang, D. Sun, Y. Wang, S. Huang, J. Zhao, Energetics of helium-vacancy complexes in Fe-9Cr alloys from first-principles calculations, Journal of Nuclear Materials. 513 (2019) 143–151. https://doi.org/10.1016/j.jnucmat.2018.10.031.

[5] K.C. Pitike, H. Ke, D.J. Edwards, W. Setyawan, Helium interaction with solutes and impurities in neutron-irradiated nanostructured ferritic alloys: A first principles study, Journal of Nuclear Materials. 566 (2022). https://doi.org/10.1016/j.jnucmat.2022.153771.

[6] P.J. Maziasz, Helium trapping at Ti-rich particles in Ti-modified austenitic stainless steel, Oak Ridge National Laboratory, 1980.

[7] L.K. Mansur, E.H. Lee, P.J. Maziasz, A.P. Rowcliffe, Control of helium effects in irradiated materials based on theory and experiment, Journal of Nuclear Materials. (1986) 633–646.

[8] S.H. Kim, J. Clarke, J. Edmonds, The economic value of fusion energy, 96551. https://ieeexplore.ieee.org/stamp/stamp.jsp?arnumber=553802 (accessed October 25, 2023).

[9] S. Sojak, J. Degmova, P. Noga, V. Krsjak, V. Slugen, T. Shen, Bubble swelling in ferritic/martensitic steels exposed to radiation environment with high production rate of helium, Materials. 14 (2021). https://doi.org/10.3390/ma14112997.

[10] A. Bhattacharya, S.J. Zinkle, Cavity Swelling in Irradiated Materials, in: Comprehensive Nuclear Materials: Second Edition, Elsevier, 2020: pp. 406–455. https://doi.org/10.1016/B978-0-12-803581-8.11599-1.

[11] S.J. Zinkle, A. Möslang, T. Muroga, H. Tanigawa, Multimodal options for materials research to advance the basis for fusion energy in the ITER era, Nuclear Fusion. 53 (2013). https://doi.org/10.1088/0029-5515/53/10/104024.

[12] S.J. Zinkle, J.L. Boutard, D.T. Hoelzer, A. Kimura, R. Lindau, G.R. Odette, M. Rieth, L. Tan, H. Tanigawa, Development of next generation tempered and ODS reduced activation ferritic/martensitic steels for fusion energy applications, Nuclear Fusion. 57 (2017) 92005. https://doi.org/10.1088/1741-4326/57/9/092005.

[13] F. Abe, Precipitate design for creep strengthening of 9% Cr tempered martensitic steel for ultra-supercritical power plants, Sci Technol Adv Mater. 9 (2008). https://doi.org/10.1088/1468-6996/9/1/013002.

[14] S.J. Zinkle, A. Quadling, Extreme materials environment of the fusion “fireplace,” MRS Bull. 47 (2022) 1113–1119. https://doi.org/10.1557/s43577-022-00453-9.

[15] L. Chen, I. Sukuba, M. Probst, A. Kaiser, Beryllium, tungsten and their alloys Be2W and Be12W: Surface defect energetics from density functional theory calculations, Nuclear Materials and Energy. 16 (2018) 149–157. https://doi.org/10.1016/j.nme.2018.06.021.

[16] H. Tanigawa, E. Gaganidze, T. Hirose, M. Ando, S.J. Zinkle, R. Lindau, E. Diegele, Development of benchmark reduced activation ferritic/martensitic steels for fusion energy applications, Nuclear Fusion. 57 (2017). https://doi.org/10.1088/1741-4326/57/9/092004.

[17] A.K. Suri, N. Krishnamurthy, I.S. Batra, Materials issues in fusion reactors, in: J Phys Conf Ser, Institute of Physics Publishing, 2010. https://doi.org/10.1088/1742-6596/208/1/012001.

[18] R.L. Klueh, D.R. Harries, High-Chromium Ferritic and Martensitic Steels for Nuclear Applications, ASTM Stock Number: MONO3, 2001. https://doi.org/10.1520/MONO3-EB.

[19] A. V Sverdlin, A.R. Ness, Chapter 3 Fundamental Concepts in Steel Heat Treatment, in: Totten G.E. (Ed.), Steel Heat Treatment: Metallurgy and Technologies, 1st ed., 2006. https://doi.org/https://doi-org.proxy.lib.umich.edu/10.1201/NOF0849384523.

[20] J.M. Vitek, R.L. Klueh, Precipitation reactions during the heat treatment of ferritic steels, Metallurgical Transactions A. 14 (1983) 1047–1055. https://doi.org/10.1007/BF02670443.

[21] A. Alamo, J.C. Brachet, A. Castaing, C. Lepoittevin, F. Barcelo, Physical metallurgy and mechanical behaviour of FeCrWTaV low activation martensitic steels: Effects of chemical composition, Journal of Nuclear Materials. 258–263 (1998) 1228–1235.

[22] P. Dubuisson, D. Gilbon, J.L. Séran, Microstructural evolution of ferritic-martensitic steels irradiated in the fast breeder reactor Phénix, Journal of Nuclear Materials. 205 (1993) 178–189. https://doi.org/10.1016/0022-3115(93)90080-I.

[23] R.L. Klueh, A.T. Nelson, Ferritic/martensitic steels for next-generation reactors, Journal of Nuclear Materials. 371 (2007) 37–52. https://doi.org/10.1016/j.jnucmat.2007.05.005.

[24] R.L. Klueh, Elevated-Temperature Ferritic and Martensitic Steels and Their Application To Future, ORNL/TM-2004/176, 2004.

[25] E.A. Little, D.R. Harries, F.B. Pickering, S.R. Keown, Effects of heat treatment on structure and properties of 12%Cr steels, Metals Technology. 4 (1977) 205–217. https://doi.org/10.1179/030716977803292060.

[26] C. Wassilew, K. Ehrlich, Effect of neutron irradiation on the dynamic fracture behaviour of the 12% Cr steel MANET-I investigated using subsize V-notch specimens, Journal of Nuclear Materials. (1992) 850–854.

[27] L. Tan, L.L. Snead, Y. Katoh, Development of new generation reduced activation ferritic-martensitic steels for advanced fusion reactors, Journal of Nuclear Materials. 478 (2016) 42–49. https://doi.org/10.1016/j.jnucmat.2016.05.037.

[28] Y. Du, X. Li, X. Zhang, Y.W. Chung, D. Isheim, S. Vaynman, Design and Characterization of a Heat-Resistant Ferritic Steel Strengthened by MX Precipitates, Metall Mater Trans A Phys Metall Mater Sci. 51 (2020) 638–647. https://doi.org/10.1007/s11661-019-05525-1.

[29] M. Taneike, F. Abe, K. Sawada, Creep-strengthening of steel at high temperatures using nano-sized carbonitride dispersions, Nature. 424 (2003) 294–296. https://doi.org/10.1038/nature01740.

[30] K. Maruyama, K. Sawada, J.I. Koike, Strengthening mechanisms of creep resistant tempered martensitic steel, ISIJ International. 41 (2001) 641–653. https://doi.org/10.2355/isijinternational.41.641.

[31] L. Tan, Y. Katoh, A.A.F. Tavassoli, J. Henry, M. Rieth, H. Sakasegawa, H. Tanigawa, Q. Huang, Recent status and improvement of reduced-activation ferritic-martensitic steels for high-temperature service, Journal of Nuclear Materials. 479 (2016) 515–523. https://doi.org/10.1016/j.jnucmat.2016.07.054.

[32] F. Abe, Coarsening behavior of lath and its effect on creep rates in tempered martensitic 9Cr-W steels, Materials Science and Engineering: A. 387–389 (2004) 565–569. https://doi.org/10.1016/j.msea.2004.01.057.

[33] T.M.K. Green, N. Sridharan, X. Chen, K.G. Field, Effect of N2- and CO2-containing shielding gases on composition modification and carbonitride precipitation in wire arc additive manufactured grade 91 steel, Addit Manuf. 56 (2022). https://doi.org/10.1016/j.addma.2022.102854.

[34] L. Tan, Y. Katoh, L.L. Snead, Development of castable nanostructured alloys as a new generation RAFM steels, Journal of Nuclear Materials. 511 (2018) 598–604. https://doi.org/10.1016/j.jnucmat.2018.05.024.

[35] L. Tan, T. Graening, X. Hu, W. Zhong, Y. Yang, S.J. Zinkle, Y. Katoh, Effects of carbonitrides and carbides on microstructure and properties of castable nanostructured alloys, Journal of Nuclear Materials. 540 (2020). https://doi.org/10.1016/j.jnucmat.2020.152376.

[36] L. Tan, Y. Katoh, L.L. Snead, Stability of the strengthening nanoprecipitates in reduced activation ferritic steels under Fe2+ ion irradiation, Journal of Nuclear Materials. 445 (2014) 104–110. https://doi.org/10.1016/j.jnucmat.2013.11.003.

[37] L. Tan, T.S. Byun, Y. Katoh, L.L. Snead, Stability of MX-type strengthening nanoprecipitates in ferritic steels under thermal aging , stress and ion irradiation, Acta Mater. 71 (2014) 11–19. https://doi.org/10.1016/j.actamat.2014.03.015.

[38] F.W. Wiffen, Y. Katoh, S. Melton, Fusion Materials Research at Oak Ridge National Laboratory in Fiscal Year 2018, ORNL/TM-2018/1072, 2018.

[39] Melton, Stephanie, Fusion Materials Semiannual Progress Report for the Period Ending December 31, 2020, Oak Ridge National Laboratory, 2020.

[40] Fusion Materials Semiannual Progress Report for the Period Ending December 31, 2021, 2021.

[41] H. Ullmaier, The influence of helium on the bulk properties of fusion reactor structural materials, Nuclear Fusion. 24 (1984) 1039.

[42] S. Taller, The Role of Damage Rate on Cavity Nucleation with Co-Injected Helium in Dual Ion Irradiated T91 Steel, University of Michigan-Ann Arbor, 2020.

[43] E. Getto, Z. Jiao, A.M. Monterrosa, K. Sun, G.S. Was, Effect of pre-implanted helium on void swelling evolution in self-ion irradiated HT9, Journal of Nuclear Materials. 462 (2015) 458–469. https://doi.org/10.1016/j.jnucmat.2015.01.045.

[44] S.J. Zinkle, L.L. Snead, Opportunities and limitations for ion beams in radiation effects studies: Bridging critical gaps between charged particle and neutron irradiations, Scr Mater. 143 (2018) 154–160. https://doi.org/10.1016/j.scriptamat.2017.06.041.

[45] G.S. Was, Z. Jiao, E. Getto, K. Sun, A.M. Monterrosa, S.A. Maloy, O. Anderoglu, B.H. Sencer, M. Hackett, Emulation of reactor irradiation damage using ion beams, Scr Mater. 88 (2014) 33–36. https://doi.org/10.1016/j.scriptamat.2014.06.003.

[46] K.C. Russell, Phase stability under irradiation, Prog Mater Sci. 28 (1984) 229–434.

[47] J. Ribis, Phase Stability in Irradiated Alloys, in: Comprehensive Nuclear Materials: Second Edition, Elsevier, 2020: pp. 265–309. https://doi.org/10.1016/B978-0-12-803581-8.11647-9.

[48] A.F. Rowcliffe, E.H. Lee, High temperature radiation damage phenomena in complex alloys, Journal of Nuclear Materials. 108–109 (1982) 306–318.

[49] T. Muroga, M. Gasparotto, S.J. Zinkle, Overview of materials research for fusion reactors, Fusion Engineering and Design. 61–62 (2002) 13–25. www.elsevier.com/locate/fusengdes.

[50] A. Aitkaliyeva, L. He, H. Wen, B. Miller, X.M. Bai, T. Allen, Irradiation effects in Generation IV nuclear reactor materials, in: Structural Materials for Generation IV Nuclear Reactors, Elsevier Inc., 2017: pp. 253–283. https://doi.org/10.1016/B978-0-08-100906-2.00007-0.

[51] L.K. Mansur, M.R. Hayns, E.H. Lee, Mechanisms affecting swelling in alloys with precipitates, Oak Ridge National Laboratory, 1980.

[52] A.F. Rowcliffe, E.H. Lee, HIGH TEMPERATURE RADIATION DAMAGE PHENOMENA IN COMPLEX ALLOYS *, 1982.

[53] P.J. Maziasz, Formation and stability of radiation-induced phases in neutron-irradiated austenitic and ferritic steels, Journal of Nuclear Materials. 169 (1989) 95–115. https://doi.org/10.1016/0022-3115(89)90525-4.

[54] E.H. Lee, A.F. Rowcliffe, L.K. Mansur, Precipitation and Cavity Formation in Austenitic Stainless Steels during Irradiation, Journla of Nuclera Materials. 104 (1981) 1475–1480.

[55] E.H. Lee, A.F. Rowcliffe, L.K. Mansur, Precipitation and cavity formation in austenitic stainless steels during irradiation, Journal of Nuclear Materials. 103 & 104 (1981) 1475–1480.

[56] L.K. Mansur, Theoretical Evaluation of a Mechanism of Precipitate-enhanced Cavity Swelling during Irradiation, Philosophical Magazine A. 44 (1981) 867–877. https://doi.org/10.1080/01418618108239554.

[57] W. Kesternich, Helium trapping at dislocation, precipitates, and grain boundaries, in: Radiat Eff, 1983: pp. 261–273. https://doi.org/10.1080/00337578308207376.

[58] E.H. Lee, N.H. Packan, L.K. Mansur, Effects of pulsed dual-ion irradiation on phase transformations and microstructure in ti-modified austenitic alloy, Journal of Nuclear Materials. 117 (1983) 123–133.

[59] T. Kimoto, H. Shiraishi, Void swelling and precipitation in a titanium-modified austenitic stainless steel under proton irradiationIRRADIATION, Journal of Nuclear Materials. 132 (1985) 266–276.

[60] R. E. Stoller, G. R. Odette, The effect of helium on swelling in stainless steel: Influence of cavity density and morphology, in: Effects of Radiation on Materials Proceedings of the Eleventh International Symposium, 1982: pp. 275–294.

[61] A.D. Brailsford, L.K. Mansur, The Effect of Precipitate-Matrix Interface Sinks on the Growth of Voids in the Matrix, Journal of Nuclear Materials. 103 & 104 (1981) 1403–1408.

[62] L. Cui, Y. Dai, S.S.A. Gerstl, M.A. Pounchon, APT characterization of irradiation effects on MX phase in reduced-activation ferritic/martensitic steels, Journal of Nuclear Materials. 573 (2023). https://doi.org/10.1016/j.jnucmat.2022.154121.

[63] M. Tamura, H. Sakasegawa, A. Kohyama, H. Esaka, K. Shinozuka, Creep deformation of iron strengthened by MX type particles, Journal of Nuclear Materials. 329–333 (2004) 328–332. https://doi.org/10.1016/j.jnucmat.2004.04.046.

[64] P.J. Maziasz, R.L. Klueh, J.M. Vitek, Helium effects on void formation in 9Cr-1MoVW irradiated in HFIR, Journal of Nuclear Materials. (1986) 929–937.

[65] B.H. Sencer, F.A. Garner, D.S. Gelles, G.M. Bond, S.A. Maloy, Microstructural evolution in modified 9Cr-1Mo ferritic/martensitic steel irradiated with mixed high-energy proton and neutron spectra at low temperatures, n.d. www.elsevier.com/locate/jnucmat.

[66] H. Tanigawa, H. Sakasegawa, H. Ogiwara, H. Kishimoto, A. Kohyama, Radiation induced phase instability of precipitates in reduced-activation ferritic/martensitic steels, Journal of Nuclear Materials. 367-370 A (2007) 132–136. https://doi.org/10.1016/j.jnucmat.2007.03.155.

[67] H. Tanigawa, H. Sakasegawa, R.L. Klueh, Irradiation Effects on Precipitation in Reduced-Activation Ferritic/Martensitic Steels, Mater Trans. 46 (2005) 469–474.

[68] H. Abe, T. Ishizaki, S. Kano, F. Li, Y. Satoh, H. Tanigawa, D. Hamaguchi, T. Nagase, H. Yasuda, Mechanism of instability of carbides in Fe-TaC alloy under high energy electron irradiation at 673 K, Journal of Nuclear Materials. 455 (2014) 695–699. https://doi.org/10.1016/j.jnucmat.2014.08.032.

[69] H. Abe, T. Ishizaki, F. Li, S. Kano, Y. Li, Y. Satoh, T. Nagase, H. Yasuda, New approach to in situ observation experiments under irradiation in high voltage electron microscopes, Mater Trans. 55 (2014) 423–427. https://doi.org/10.2320/matertrans.MD201315.

[70] S. Kano, H. Yang, J. Shen, Z. Zhao, J. McGrady, D. Hamaguchi, M. Ando, H. Tanigawa, H. Abe, Instability of MX and M23C6 type precipitates in F82H steels under 2.8 MeV

Fe2+ irradiation at 673 K, Nuclear Materials and Energy. 17 (2018) 56–61. https://doi.org/10.1016/j.nme.2018.08.001.

[71] C. Dethloff, E. Gaganidze, J. Aktaa, Quantitative TEM analysis of precipitation and grain boundary segregation in neutron irradiated EUROFER 97, Journal of Nuclear Materials. 454 (2014) 323–331. https://doi.org/10.1016/j.jnucmat.2014.07.078.

[72] C. Dethloff, E. Gaganidze, J. Aktaa, Microstructural defects in EUROFER 97 after different neutron irradiation conditions, Nuclear Materials and Energy. 9 (2016) 471–475. https://doi.org/10.1016/j.nme.2016.05.009.

[73] H. Yan, X. Liu, L. He, J. Stubbins, Phase stability and microstructural evolution in neutron-irradiated ferritic-martensitic steel HT9, Journal of Nuclear Materials. 557 (2021). https://doi.org/10.1016/j.jnucmat.2021.153252.

[74] L.N. Clowers, Z. Jiao, G.S. Was, Synergies between H, He and radiation damage in dual and triple ion irradiation of candidate fusion blanket materials, Journal of Nuclear Materials. 565 (2022). https://doi.org/10.1016/j.jnucmat.2022.153722.

[75] C.M. Parish, K.A. Unocic, L. Tan, S.J. Zinkle, S. Kondo, L.L. Snead, D.T. Hoelzer, Y. Katoh, Helium sequestration at nanoparticle-matrix interfaces in helium + heavy ion irradiated nanostructured ferritic alloys, Journal of Nuclear Materials. 483 (2017) 21–34. https://doi.org/10.1016/j.jnucmat.2016.10.038.

[76] Y.R. Lin, W.Y. Chen, L. Tan, D.T. Hoelzer, Z. Yan, C.Y. Hsieh, C.W. Huang, S.J. Zinkle, Bubble formation in helium-implanted nanostructured ferritic alloys at elevated temperatures, Acta Mater. 217 (2021). https://doi.org/10.1016/j.actamat.2021.117165.

[77] Z. Yan, Y. Lin, The effect of sink strength on helium bubble formation at elevated temperatures, Nuclear Analysis. 1 (2022) 100003. https://doi.org/10.1016/j.nucana.2022.100003.

[78] H.J. Frost, K.C. Russell, Particle Stability with Recoil Resolution, Acta Metallurgica. 30 (1982) 953–960.

[79] A. Baldan, Progress in Ostwald ripening theories and their applications to the γ-precipitates in nickel-base superalloys Part II Nickel-base superalloys, J Mater Sci. 37 (2002) 2379–2405.

[80] J.H. Jang, C.-H. Lee, N. Han, H.K.D.H. Bhadeshia, D.-W. Suh, Modelling the coarsening behaviour of TiC precipitates in high-strength, low-alloy steels, Materials Science and Technology,. 29 (2013) 1074–1079.

[81] T. Muroga, K. Kitajima, S. Ishino, Computer Simulation of Precipitate Recoil Resolution by Energetic Collision Cascades, in: Radiation-Induced Changes in Microstructure: 13th International Symposium (Part I) ASTM STP 955, ASTM International, 1987: pp. 834–846. www.astm.org.

[82] Y. Zhang, Y.W. You, Y. Xu, C.S. Liu, J.L. Chen, G.N. Luo, Effect of carbon and alloying solute atoms on helium behaviors in α-Fe, Journal of Nuclear Materials. 484 (2017) 103–109. https://doi.org/10.1016/j.jnucmat.2016.11.023.

[83] P. Olsson, T.P.C. Klaver, C. Domain, Ab initio study of solute transition-metal interactions with point defects in bcc Fe, Phys Rev B Condens Matter Mater Phys. 81 (2010). https://doi.org/10.1103/PhysRevB.81.054102.

[84] P. Zhang, X. Wang, M. Wei, Y. Wang, T. Zou, Interaction between helium and transition metals in vanadium: A first-principles investigation, Nuclear Materials and Energy. 31 (2022). https://doi.org/10.1016/j.nme.2022.101189.

[85] A. Kashinath, A. Misra, M.J. Demkowicz, Stable storage of helium in nanoscale platelets at semicoherent interfaces, Phys Rev Lett. 110 (2013). https://doi.org/10.1103/PhysRevLett.110.086101.

[86] I.J. Beyerlein, M.J. Demkowicz, A. Misra, B.P. Uberuaga, Defect-interface interactions, Prog Mater Sci. 74 (2015) 125–210. https://doi.org/10.1016/j.pmatsci.2015.02.001.

[87] Fusion Materials Semiannual Progress Report for the Period Ending June 30, 2021, 2021.

[88] Fusion Materials Semiannual Progress Report for the Period Ending December 31, 2022, 2023.

[89] L. Tan, T. Chen, Y. Yang, Development of Nanoprecipitates- Strengthened Advanced Ferritic Alloys for Nuclear Reactor Applications, Oak Ridge National Laboratory, 2019.

[90] L. Tan, T. Chen, Y. Yang, L. He, K. Sridharan, Report on The Down-Selected Advanced Ferritic Alloys for Nuclear Reactor Applications, Oak Ridge National Laboratory, 2019.

[91] L. Tan, T. Chen, Y. Yang, L. He, K. Sridharan, Mechanical Properties and Radiation Resistance of Nanoprecipitates-Strengthened Advanced Ferritic Alloys, Oak Ridge National Laboratory, 2017.

[92] L. Tan, C.M. Parish, X. Hu, Microstructure and property tailoring of castable nanostructured alloys through thermomechanical treatments, Journal of Nuclear Materials. 509 (2018) 267–275. https://doi.org/10.1016/j.jnucmat.2018.07.012.

[93] A.M. Monterrosa, The Role of Pre-Implanted Helium and Carbon on Cavity Evolution in Ion-Irradiated T91, The University of Michigan, 2018.

[94] S.J. Zinkle, J.T. Busby, Structural materials for fission & fusion energy, Materials Today. 12 (2009) 12–19. https://doi.org/10.1016/S1369-7021(09)70294-9.

[95] L.K. Mansur, A.F. Rowcliffe, R.K. Nanstad, S.J. Zinkle, W.R. Corwin, R.E. Stoller, Materials needs for fusion, Generation IV fission reactors and spallation neutron sources - Similarities and differences, in: Journal of Nuclear Materials, 2004: pp. 166–172. https://doi.org/10.1016/j.jnucmat.2004.04.016.

[96] G.S. Was, D. Petti, S. Ukai, S. Zinkle, Materials for future nuclear energy systems, Journal of Nuclear Materials. 527 (2019). https://doi.org/10.1016/j.jnucmat.2019.151837.

[97] Elizabeth Margaret Getto, The co-evolution of microstructure features in self-ion irradiated ht9 at very high damage levels, University of Michigan-Ann Arbor, 2016. https://doi.org/10.1017/CBO9781107415324.004.

[98] S.J. Zinkle, L.L. Snead, Opportunities and limitations for ion beams in radiation effects studies: Bridging critical gaps between charged particle and neutron irradiations, Scr Mater. 143 (2018) 154–160. https://doi.org/10.1016/j.scriptamat.2017.06.041.

[99] Y.R. Lin, A. Bhattacharya, S.J. Zinkle, Analysis of position-dependent cavity parameters in irradiated metals to obtain insight on fundamental defect migration phenomena☆, Mater Des. 226 (2023). https://doi.org/10.1016/j.matdes.2023.111668.

[100] J.F. Ziegler, M.D. Ziegler, J.P. Biersack, SRIM - The stopping and range of ions in matter (2010), Nucl Instrum Methods Phys Res B. 268 (2010) 1818–1823. https://doi.org/10.1016/j.nimb.2010.02.091.

[101] R.E. Stoller, M.B. Toloczko, G.S. Was, A.G. Certain, S. Dwaraknath, F.A. Garner, On the use of SRIM for computing radiation damage exposure, Nucl Instrum Methods Phys Res B. 310 (2013) 75–80. https://doi.org/10.1016/j.nimb.2013.05.008.

[102] M.I. Norgett, M.T. Robinson, I.M. Torrens, A proposed method of calculating displacement dose rates, Nuclear Engineering and Design. 33 (1975) 50–54.

[103] H. Benfu, H. Kinoshita, H. Takahashi, Damage behavior in an electron/helium dual-beam irradiated Fe-Cr-Mn(W,V) alloy, Journal of Nuclear Materials. 258–263 (1998) 1708–1712.

[104] M. Li, W.Y. Chen, P.M. Baldo, In situ transmission electron microscopy with dual ion beam irradiation and implantation, Mater Charact. 173 (2021). https://doi.org/10.1016/j.matchar.2021.110905.

[105] S. Taller, D. Woodley, E. Getto, A.M. Monterrosa, Z. Jiao, O. Toader, F. Naab, T. Kubley, S. Dwaraknath, G.S. Was, Multiple ion beam irradiation for the study of radiation damage in materials, Nucl Instrum Methods Phys Res B. 412 (2017) 1–10. https://doi.org/10.1016/j.nimb.2017.08.035.

[106] E. Getto, Z. Jiao, A.M. Monterrosa, K. Sun, G.S. Was, Effect of irradiation mode on the microstructure of self-ion irradiated ferritic-martensitic alloys, Journal of Nuclear Materials. 465 (2015) 116–126. https://doi.org/10.1016/j.jnucmat.2015.05.016.

[107] J. Bentley, Energy-Filtered Imaging: A Tutorial, Microscopy and Microanalysis. 6 (2000) 1186–1187. https://doi.org/10.1017/s1431927600038423.

[108] T. Malis, S.C. Cheng, R.F. Egerton, EELS log-ratio technique for specimen-thickness measurement in the TEM, J Electron Microsc Tech. 8 (1988) 193–200. https://doi.org/10.1002/jemt.1060080206.

[109] M.C. Jones, J.S. Marron, S.J. Sheather, A brief survey of bandwidth selection for density estimation, J Am Stat Assoc. 91 (1996) 401–407. https://doi.org/10.1080/01621459.1996.10476701.

[110] T. Malis, S.C. Cheng, R.F. Egerton, EELS log-ratio technique for specimen-thickness measurement in the TEM, J Electron Microsc Tech. 8 (1988) 193–200. https://doi.org/10.1002/jemt.1060080206.

[111] K.N. Thomas, Effect of Cascade Size and Damage Rate on α' Precipitate Stability on Fe-15Cr, University of Michigan-Ann Arbor, 2022.

[112] A.A. Kohnert, M.A. Cusentino, B.D. Wirth, Molecular statics calculations of the biases and point defect capture volumes of small cavities, Journal of Nuclear Materials. 499 (2018) 480–489. https://doi.org/10.1016/j.jnucmat.2017.12.005.

[113] J. Duan, H. Wen, L. He, K. Sridharan, A. Hoffman, M. Arivu, X. He, R. Islamgaliev, R. Valiev, Effect of grain size on the irradiation response of grade 91 steel subjected to Fe ion irradiation at 300 °C, J Mater Sci. 57 (2022) 13767–13778. https://doi.org/10.1007/s10853-022-07480-6.

[114] Y. Chen, Irradiation effects of HT-9 martensitic steel, Nuclear Engineering and Technology. 45 (2013) 311–322. https://doi.org/10.5516/NET.07.2013.706.

[115] A. Bhattacharya, J. Henry, B. Décamps, S.J. Zinkle, E. Meslin, Helium causing disappearance of a/2<111> dislocation loops in binary Fe-Cr ferritic alloys, Journal of Nuclear Materials. 556 (2021). https://doi.org/10.1016/j.jnucmat.2021.153213.

[116] N.H. Packan, K. Farrell, Simulation of first wall damage: effects of the method of gas implantations, Journal of Nuclear Materials. 85 (n.d.) 677–681.

[117] J.J. Kai, G.L. Kulcinski, 14 MeV nickel-ion irradiated HT-9 ferritic steel with and without helium pre-implantation, Journal of Nuclear Materials. 175 (1990) 227–236. https://doi.org/10.1016/0022-3115(90)90211-5.

[118] K.N. Thomas, G.S. Was, Effect of cascade size and damage rate on α' precipitate stability in Fe-15Cr, Journal of Nuclear Materials. 585 (2023). https://doi.org/10.1016/j.jnucmat.2023.154615.

[119] D. Vizoso, C. Deo, R. Dingreville, The effects of dose, dose rate, and irradiation type and their equivalence on radiation-induced segregation in binary alloy systems via phase-field simulations, Journal of Nuclear Materials. 569 (2022). https://doi.org/10.1016/j.jnucmat.2022.153924.

[120] S.M. Levine, C. Pareige, Z. Jiao, P.D. Edmondson, G.S. Was, S.J. Zinkle, A. Bhattacharya, Phase instabilities in austenitic steels during particle bombardment at high and low dose rates, Mater Des. 217 (2022). https://doi.org/10.1016/j.matdes.2022.110588.

[121] Arthur T. Motta, Donald R. Olander, Chapter 24 Phase Transformations Under Irradiation, in: Light Water Reactor Materials, Volume 1, 2017: p. 1090.

[122] C.M. Parish, K.A. Unocic, L. Tan, S.J. Zinkle, S. Kondo, L.L. Snead, D.T. Hoelzer, Y. Katoh, Helium sequestration at nanoparticle-matrix interfaces in helium + heavy ion irradiated nanostructured ferritic alloys, Journal of Nuclear Materials. 483 (2017) 21–34. https://doi.org/10.1016/j.jnucmat.2016.10.038.

[123] E.A. Kenik, E.H. Lee, INFLUENCE OF INJECTED HELIUM ON THE PHASE INSTABILITY OF ION-IRRADIATED STAINLESS STEEL, CONF-801072-1, 1980.

[124] L. Wang, D. Martin, W.Y. Chen, P.M. Baldo, M. Li, B.D. Wirth, S.J. Zinkle, Effect of sink strength on coherency loss of precipitates in dilute Cu-base alloys during in situ ion irradiation, Acta Mater. 210 (2021). https://doi.org/10.1016/j.actamat.2021.116812.

[125] Y.F. Yin, R.G. Faulkner, Z. Lu, Irradiation-induced precipitation modelling of ferritic steels, Journal of Nuclear Materials. 389 (2009) 225–232. https://doi.org/10.1016/j.jnucmat.2009.02.006.

[126] Voyevodin V.N., Zelensky V.F., Neklyudov I.M., Variations of Phase and Structure in Austenitic Stainless Steel Under Heavy Ion Irradiation, in: Effects of Radiation on Materials: 14th International Symposium, 1983: pp. 198–207.

[127] J.P. Sanhueza, D. Rojas, J. García, M.F. Melendrez, E. Toledo, C. Montalba, M.I. Alvarado, A.F. Jaramillo, Computational modeling of the effect of B and W in the phase transformation of M23C6 carbides in 9 to 12 pct Cr martensitic/ferritic steels, Mater Res Express. 6 (2019). https://doi.org/10.1088/2053-1591/ab500c.

[128] Frost H.J., Russell K.C., Recoil resolution and particle stability under irradiation, Journal of Nuclear Materials. 103 & 104 (1981) 1427–1432.

[129] T. Muroga, K. Kitajima, S. Ishino, Computer Simulation of Precipitate Recoil Resolution by Energetic Collision Cascades, in: Radiation-Induced Changes in Microstructure: 13th International Symposium (Part 1), ASTM International, 1987: pp. 834–846. www.astm.org.

[130] W.G. Wolfer, M. Ashkin, Stress-induced diffusion of point defects to spherical sinks, J Appl Phys. 46 (1975) 547–557. https://doi.org/10.1063/1.321679.

[131] M. Mock, P. Stein, C. Hin, K. Albe, Modeling the influence of strain fields around precipitates on defect equilibria and kinetics under irradiation in ODS steels: A multi scale approach, 2019. https://doi.org/https://doi.org/10.1016/j.jnucmat.2019.151807.

[132] A.D. Brailsford, R. Bullough, The Rate Theory of Swelling in Irradiated Metals, Journal of Nuclear Materials. 44 (1972) 121–135.

[133] A.D. Marwick, Solute segregation and precipitate stability in irradiated alloys, Nuclear Instruments and Methods. 182 (1981) 827–843.

[134] A. Vattré, T. Jourdan, H. Ding, M.C. Marinica, M.J. Demkowicz, Non-random walk diffusion enhances the sink strength of semicoherent interfaces, Nat Commun. 7 (2016). https://doi.org/10.1038/ncomms10424.

[135] T. Chen, J.G. Gigax, L. Price, D. Chen, S. Ukai, E. Aydogan, S.A. Maloy, F.A. Garner, L. Shao, Temperature dependent dispersoid stability in ion-irradiated ferritic-martensitic dual-phase oxide-dispersion-strengthened alloy: Coherent interfaces vs. incoherent interfaces, Acta Mater. 116 (2016) 29–42. https://doi.org/10.1016/j.actamat.2016.05.042.

[136] W. V Vaidya, Modification of the precipitate interface under irradiation and its effect on the stability of precipitates, Journal of Nuclear Materials. 83 (1979) 223–230.

[137] T. Le Cheng, Y.H. Wen, Phase-field model of precipitation processes with coherency loss, Computational Materials. 7 (2021). https://doi.org/10.1038/s41524-021-00503-x.

[138] D.I. Potter, H. Wiedersich, Mechanisms and kinetics of precipitates restructuring during irradiation, Journal of Nuclear Materials. 83 (1979) 208–213.

[139] M.L. Lescoat, J. Ribis, A. Gentils, O. Kaïtasov, Y. De Carlan, A. Legris, In situ TEM study of the stability of nano-oxides in ODS steels under ion-irradiation, in: Journal of Nuclear Materials, 2012: pp. 176–182. https://doi.org/10.1016/j.jnucmat.2011.12.009.

[140] K.C. Russell, Phase instability under cascade damage irradiation, Journal of Nuclear Materials. 206 (1993) 129–138.

[141] K. Nordlund, S.J. Zinkle, A.E. Sand, F. Granberg, R.S. Averback, R. Stoller, T. Suzudo, L. Malerba, F. Banhart, W.J. Weber, F. Willaime, S.L. Dudarev, D. Simeone, Improving

atomic displacement and replacement calculations with physically realistic damage models, Nat Commun. 9 (2018). https://doi.org/10.1038/s41467-018-03415-5.

[142] S. Taller, G. VanCoevering, B.D. Wirth, G.S. Was, Predicting structural material degradation in advanced nuclear reactors with ion irradiation, Sci Rep. 11 (2021). https://doi.org/10.1038/s41598-021-82512-w.

[143] O. Emelyanova, A. Gentils, V.A. Borodin, M.G. Ganchenkova, P. V. Vladimirov, P.S. Dzhumaev, I.A. Golovchanskiy, R. Lindau, A. Möslang, Bubble-to-void transition promoted by oxide nanoparticles in ODS-EUROFER steel ion implanted to high He content, Journal of Nuclear Materials. 545 (2021). https://doi.org/10.1016/j.jnucmat.2020.152724.

[144] A. Hishinuma, L.K. Mansur, Critical radius for bias-driven swelling - a further analysis and its application to bimodal cavity size distributions, Journal of Nuclear Materials. 118 (1983) 91–99.

[145] W.A. Coghlan, L.K. Mansur, Critical radius and critical number of gas atoms for cavities containing a van der waals gas, Journal of Nuclear Materials. 122 (1984) 1.

[146] R.E. Stoller, G.R. Odette, Analytical solutions for helium bubble and critical radius parameters using a hard sphere equation of state, Journal of Nuclear Materials. 131 (1985) 11–125.

[147] N.M. Ghoniem, J.N. Alhajji, The effect of helium clustering on its transport to grain boundaries, Journal of Nuclear Materials. 136 (1985) 192–206.

[148] S. Kenneth, Helium bubbles in Niobium and Niobium-Zirconium Alloys, University of Surrey, 1979.

[149] A.J. Markworth, E.M. Baroody, On the binding between inert-gas bubbles and rigid precipitate particles, Journal of Nuclear Materials. 39 (1971) 348–349.

[150] Z. Yan, T. Yang, Y. Lin, Y. Lu, Y. Su, S.J. Zinkle, Y. Wang, Effects of temperature on helium bubble behaviour in Fe–9Cr alloy, Journal of Nuclear Materials. 532 (2020). https://doi.org/10.1016/j.jnucmat.2020.152045.

[151] T. Stan, Y. Wu, J. Ciston, T. Yamamoto, G.R. Odette, Characterization of polyhedral nano-oxides and helium bubbles in an annealed nanostructured ferritic alloy, Acta Mater. 183 (2020) 484–492. https://doi.org/10.1016/j.actamat.2019.10.045.

[152] T. Yamamoto, Y. Wu, G. Robert Odette, K. Yabuuchi, S. Kondo, A. Kimura, A dual ion irradiation study of helium-dpa interactions on cavity evolution in tempered martensitic steels and nanostructured ferritic alloys, Journal of Nuclear Materials. 449 (2014) 190–199. https://doi.org/10.1016/j.jnucmat.2014.01.040.

[153] G.R. Odette, Recent Progress in Developing and Qualifying Nanostructured Ferritic Alloys for Advanced Fission and Fusion Applications, JOM. 66 (2014) 2427–2441. https://doi.org/10.1007/s11837-014-1207-5.

[154] L.K. Mansur, Theory and experimental background on dimensional changes in irradiated alloys, Journal of Nuclear Materials. 216 (1994) 97–123.

[155] M.J. Demkowicz, A. Misra, A. Caro, The role of interface structure in controlling high helium concentrations, Curr Opin Solid State Mater Sci. 16 (2012) 101–108. https://doi.org/10.1016/j.cossms.2011.10.003.

[156] L. Shao, F. Gao, F.A. Garner, Final report for Development of high performance ODS alloys, n.d. https://doi.org/doi:10.2172/1419659.

[157] Porter D.A., Easterling K.E., Phase Transformations in Metals and Alloys, 2nd ed., 1992. https://doi.org/10.1007/978-1-4899-3051-4.

[158] T. Allen, Generation-IV Reactors, Fuels and Fuel Cycles Scientific Issues & Technological Challenges in the Development of Materials, Journal of Nuclear Materials. 78 (2011) 156–160. https://doi.org/10.1007/s11661-012-1565-y.

[159] P. Xiu, Effects of Sink Strength and Irradiation Parameters on Defect Evolution in Additively Manufactured HT9, University of Michigan-Ann Arbor, 2022.

[160] S.J. Zinkle, Advanced Structural Materials for Non-Light Water Reactors Workshop on Advanced Non-Light Water Reactors: Materials and Component Integrity Nuclear Regulatory Commission, in: 2019. www.nrc.gov/docs/ML2003/ML20030B792.pdf.

[161] E. Wakai, K. Kikuchi, S. Yamamoto, T. Aruga, M. Ando, H. Tanigawa, T. Taguchi, T. Sawai, K. Oka, S. Ohnuki, Swelling behavior of F82H steel irradiated by triple/dual ion beams, in: Journal of Nuclear Materials, 2003: pp. 267–273. https://doi.org/10.1016/S0022-3115(03)00122-3.

[162] T. Morimura, A. Kimura, H. Matsui, Void swelling of Japanese candidate martensitic steels under FFTF/MOTA irradiation, Journal of Nuclear Materials. 239 (1996) 18–125.

[163] E. Wakai, N. Hashimoto, Y. Miwa, J.P. Robertson, R.L. Klueh, K. Shiba, S. Jistukawa, Effect of helium production on swelling of F82H irradiated in HFIR, Journal of Nuclear Materials. 283–287 (2000) 799–805. www.elsevier.nl/locate/jnucmat.

[164] T. Tanaka, K. Oka, S. Ohnuki, S. Yamashita, T. Suda, S. Watanabe, E. Wakai, Synergistic effect of helium and hydrogen for defect evolution under multi-ion irradiation of Fe-Cr ferritic alloys, in: Journal of Nuclear Materials, 2004: pp. 294–298. https://doi.org/10.1016/j.jnucmat.2004.04.051.

[165] H. Ogiwara, H. Sakasegawa, H. Tanigawa, M. Ando, Y. Katoh, A. Kohyama, Void swelling in reduced activation ferritic/martensitic steels under ion-beam irradiation to high fluences, n.d. www.elsevier.com/locate/jnucmat.